

POWER ELECTRONIC CONVERTERS FOR INTERFACING TO DC MICROGRID

THESIS

SUBMITTED IN PARTIAL FULFILLMENT OF THE REQUIREMENTS
FOR THE AWARD OF THE DEGREE
OF
DOCTORATE OF PHILOSOPHY

Submitted by:

SHIRISH RAIZADA

2K17/PhD/EE/11

Under the supervision of

PROF. VISHAL VERMA

EED. DTU



**DEPARTMENT OF ELECTRICAL ENGINEERING
DELHI TECHNOLOGICAL UNIVERSITY**

(Formerly Delhi College of Engineering)

Bawana Road, Delhi-110042

DECLARATION

I, SHIRISH RAIZADA (2K17/PhD/EE/11) hereby declare that the work, which is being presented in the thesis entitled, “**POWER ELECTRONIC CONVERTERS FOR INTERFACING TO DC MICROGRID**” submitted in partial fulfillment of the requirements for the award of the degree of Doctor of Philosophy is an authentic record of my own work carried out under the able guidance of Prof. VISHAL VERMA, EED, DTU. The matter embodied in the dissertation work has not been plagiarized from anywhere and the same has not been submitted for the award of any other degree or diploma in full or in part.

Submitted by:-

SHIRISH RAIZADA

(2K17/PhD/EE/11)

Electrical Engineering Department

DEPARTMENT OF ELECTRICAL ENGINEERING
DELHI TECHNOLOGICAL UNIVERSITY
(Formerly Delhi College of Engineering)



CERTIFICATE

This is to certify that the thesis entitled, “**POWER ELECTRONIC CONVERTERS FOR INTERFACING TO DC MICROGRID**”, submitted by Mr. **SHIRISH RAIZADA**, Roll No. 2K17/PhD/EE/11, research scholar Electrical Engineering Department, Delhi Technological University (Formerly Delhi College of Engineering), is a dissertation work carried out by him under my guidance during session 2017-2024 towards the partial fulfillment of the requirements for the award of degree of Doctor of Philosophy.

The uniqueness of the thesis pertains to detailed analysis, design and development, and performance of current-fed high gain isolated interfacing DC / DC converter topologies which has not been reported elsewhere.

I wish him all the best in his endeavors.

Prof. Vishal Verma
Professor EED, DTU
Supervisor

ACKNOWLEDGMENT

It is a great pleasure to express my gratitude to all those who have contributed towards the successful completion of my Ph.D. work. I would like to extend my sincere gratitude to my supervisor, Prof. Vishal Verma for his invaluable guidance and firm support during the course of my research work. It has been a privilege to work under his able supervision and an experience to cherish forever.

I would like to further extend my thanks to Prof. Rachna Garg, Head of the Department of Electrical Engineering at Delhi Technological University (DTU), Delhi for her support. I am also thankful to all the faculty, staff members and research scholars of Electrical Engineering Department for their assistance from time to time. I would like to convey my sincere appreciation to my seniors and colleagues in Lab including Mr. Anil Butola, Dr. Ramesh Singh, Dr. Amritesh Kumar, Dr. Ritka Gour, Ms. Vandana Arora, Mr. Aditya Narula and Ms. Pankhuri Asthana for their constant help and support during my research work in the laboratory.

I want to express my deepest appreciation to my parents Mrs. Roli Raizada and Dr. Sumesh Raizada for their unconditional love, support, patience, and encouragement. I owe a debt of gratitude to my grandparents for their constant motivation and encouragement. I also want to appreciate the constant support of my brother Mr. Aditya Raizada. Lastly, I would like to thank my wife for her love and support.

POWER ELECTRONIC CONVERTERS FOR INTERFACING TO DC MICROGRID

ABSTRACT

With rapid depletion of fossil fuel reserves and widespread environmental concerns, the global adoption of renewable energy sources is being highly encouraged. Solar energy is one of the most prominent renewable energy sources and offers numerous advantages. However, the adoption of photovoltaic (PV) systems in different applications is primarily limited due to high intermittency. Furthermore, conventional string PV system is highly susceptible to partial shading conditions while also witnessing poor reliability, poor robustness, and single point failure. Conversely, module level PV system (MLPS) offers highly flexible architecture with superior power utilization, reliability and robustness under different operating conditions while also achieving smooth system operation during the outage of a section due to bypassing provided by the diode. MLPS also utilizes distributed power generation controllers for evacuating maximum power from each panel. However, the integration of individual low voltage PV panel with high voltage DC microgrid is a major challenge in MLPS and requires high gain module level interfacing converter (MLIC) and multi-input module interfacing converter (MMIC). The lack of topological viability of conventional boost converter for MLIC due to its inability to operate at high gain with high efficiency prompted extensive research on the family of high gain DC/DC converters.

This thesis focusses on investigating different novel high gain DC/DC converter topologies for MLIC and MMIC to integrate MLPS with DC microgrid. Comprehensive literature review of different DC/DC converter topologies and their comparative study is presented to affirm the viability of proposed converter topologies for MLIC and MMIC. The thesis

presents modeling, steady state analysis, design methodology and loss distribution of proposed current-fed high gain isolated interfacing converter (CF-HGIIC) topology for MLIC and investigates its simulated performance on MATLAB Simulink environment and further through experimental investigation on the developed hardware prototype. Moreover, modified CF-HGIIC (MCF-HGIIC) topology for MLIC offering notable topological improvements over CF-HGIIC is proposed in the thesis and its modeling and steady-state analysis has been carried out. The simulated and experimental performance of MCF-HGIIC has also been investigated. The thesis also presents the novel multi-input CF-HGIIC (MI-CF-HGIIC) topology for MMIC and discusses its modeling, steady-state analysis, and simulated performance.

The system integration of MLPS with DC microgrid for different system architectures of MLPS utilizing proposed converter topologies has been discussed in the thesis while also exploring several applications of MLPS. The concept and challenges of dynamic shading and the failure of conventional MPPT controller to track such fast dynamics has been discussed. Different power generation control algorithms offering features like flexible power generation capability and fast dynamical response during dynamic shading conditions are also discussed to enhance the overall system performance under various operating conditions. The performance of different system architectures under diverse operating conditions such as source perturbations are evaluated using MATLAB Simulink environment to validate the efficacy of system and its salient features viz, modularity, robustness, plug-and-play operation etc. Moreover, the experimental performance of system under various source perturbations and the effectiveness of proposed converter in integrating MLPS with DC microgrid are also investigated in the thesis.

TABLE OF CONTENTS

	Declaration	i
	Certificate	iii
	Acknowledgment	v
	Abstract	vii
	Table of Contents	ix
	List of Figures	xv
	List of Tables	xxv
	Abbreviations	xxvii
CHAPTER 1	INTRODUCTION	
1.1	Background	1
1.2	Renewable Energy Sources	3
1.2.1	Advantages of Renewable Energy Sources	3
1.2.2	Challenges of Renewable Energy Sources	5
1.2.3	Types of Renewable Energy Sources	6
1.3	Photovoltaic System	9
1.3.1	Advantages of Solar Energy Sources and Photovoltaic Systems	9
1.3.2	Challenges of Solar Energy Sources and Photovoltaic Systems	11
1.3.3	Opportunities of Solar Energy in India	12
1.3.4	Key Applications of Solar Energy	13
1.3.5	Major Environmental Factors Contributing to the Intermittency of PV Panels	13
1.3.6	Components of PV System	15
1.3.7	Classification of PV System	16
1.4	DC Microgrid	19
1.4.1	Advantages of DC Microgrid	20
1.4.2	Challenges in DC Microgrid	20

1.4.3	Architectures and Applications of DC Microgrid	21
1.4.4	Integration of Module Level PV System with DC Microgrid	22
1.5	Power Electronics	23
1.5.1	Power Electronics for the Interfacing Converters	23
1.6	Scope of Work	25
1.7	Organization of Thesis	26
CHAPTER 2	LITERATURE SURVEY	
2.1	General	29
2.2	Performance Issues in the PV System	29
2.3	Review of Algorithms for Power Generation Control	33
2.3.1	Maximum Power Point Tracking Algorithms	33
2.3.2	Flexible Power Point Tracking Algorithms	36
2.4	Configurations of PV System	39
2.5	DC Microgrid	42
2.6	Interfacing Converters for MLPS	45
2.6.1	Survey of Topologies for MLIC	46
2.6.2	Survey of Topologies for MMIC	61
2.7	Identified Research Gaps	64
2.8	Research Objectives	68
CHAPTER 3	FRONT-END CURRENT-FED HIGH GAIN ISOLATED INTERFACING CONVERTER	
3.1	General	69
3.2	Proposed Converter Topology	70
3.3	Topological Modes of Operation	72
3.3.1	Mode 1	74

3.3.2	Mode 2	74
3.3.3	Mode 3	74
3.3.4	Mode 4	75
3.4	Mathematical Modeling of Converter	75
3.4.1	Static Voltage Gain of Converter	75
3.4.2	Steady-State Operation Analysis	77
3.5	Steady-State Converter Analysis	79
3.5.1	Input Current Ripple Analysis	79
3.5.2	Leakage Current Modeling	81
3.5.3	Component Stress	83
3.6	Design Considerations of Converter	85
3.6.1	Design of Input Inductor	85
3.6.2	Selection of HF Transformer Turns Ratio	85
3.6.3	Design of Coupling Capacitors	86
3.6.4	Selection of Devices	89
3.6.5	Design of Output Capacitor	89
3.7	Theoretical Loss Distribution of Converter	90
3.8	Comparative Study of the State-of-the-art Topologies	91
3.9	Results and Discussions	95
3.9.1	Simulation Results	95
3.9.2	Experimental Results	101
3.10	Conclusion	107
CHAPTER 4	TOPOLOGICAL MODIFICATIONS AND PERFORMANCE ENHANCEMENTS	
4.1	General	111
4.2	Improvements in the Existing Topology	112
4.3	Proposed Converter Topology	113
4.4	Topological Modes of Operation	115
4.4.1	Mode 1	116

	4.4.2	Mode 2	116
	4.4.3	Mode 3	116
	4.4.4	Mode 4	117
	4.4.5	Mode 5	117
	4.4.6	Mode 6	117
4.5		Mathematical Modeling of Converter	120
	4.5.1	Steady-State Operational Analysis	120
4.6		Results and Discussions	123
	4.6.1	Simulation Results	123
	4.6.2	Experimental Results	129
4.7		Conclusion	139
CHAPTER 5		MULTI-INPUT CONFIGURATION OF CURRENT-FED HIGH GAIN ISOLATED INTERFACING CONVERTER	
5.1		General	141
5.2		Proposed Converter Topology and Modulation Scheme	142
	5.2.1	Proposed Converter Topology	142
	5.2.2	Modulation Scheme	145
5.3		Topological Modes of Operation of Converter	145
	5.3.1	Mode 1	146
	5.3.2	Mode 2	146
	5.3.3	Mode 3	146
	5.3.4	Mode 4	147
5.4		Mathematical Modeling of Converter	149
	5.4.1	Steady-State Operational Analysis	149
5.5		Design Considerations of Converter	151
5.6		Results and Discussions	152
5.7		Conclusion	166

CHAPTER 6	SYSTEM INTEGRATION AND PERFORMANCE UNDER VARIABLE INSOLATION AND SHADING CONDITIONS	
6.1	General	169
6.2	System Architecture	170
	6.2.1 Merits of MLPS	170
	6.2.2 MLPS based System Architecture	171
6.3	Applications of MLPS	173
	6.3.1 Off-Grid EV Charging Infrastructure	173
	6.3.2 Floating PV system	175
	6.3.3 Rooftop MLPS on Train	177
6.4	Concept of Dynamic Sub-Panel Shading	178
6.5	Power Generation Control Algorithms	180
	6.5.1 CPG-InC Flexible Power Point Tracking Algorithm	180
	6.5.2 Fast-MPPT Algorithm	185
6.6	Results and Discussions	187
	6.6.1 Simulation Results	187
	6.6.2 Experimental Results	214
6.7	Integration of Proposed Converters with DC Microgrid	225
6.8	Conclusion	226
CHAPTER 7	CONCLUSION AND FUTURE WORK	
7.1	Main Conclusion	229
7.2	Future Scope of Work	233
	References	235
	List of Publications	263

LIST OF FIGURES

Fig. No.	Figure Name	Page No.
Fig. 1.1	CO ₂ emissions in different sectors in India	2
Fig. 1.2	Cumulative installed capacities of different RES in India	8
Fig. 2.1	Overview of high gain DC-DC converter topologies	46
Fig. 3.1	Topological structure of CF-HGIIC	70
Fig. 3.2	Analytical waveforms of CF-HGIIC	72
Fig. 3.3	Topological operating modes of proposed converter	73
Fig. 3.4	Static voltage gain of CF-HGIIC	77
Fig. 3.5	Normalized inductor and input current ripple vs duty cycle (d) for CF-HGIIC	81
Fig. 3.6	Leakage current model of CF-HGIIC	83
Fig. 3.7	3-D plot of voltage gain (m) vs duty cycle (d) vs turns ratio (n)	86
Fig. 3.8	Voltage ripple (ΔV_C) of coupling capacitor vs (a) Input current (b) Duty cycle (d)	88
Fig. 3.9	Simulated waveform of inductor currents I_{L1} , I_{L2} (A), input current I_{IN} (A), voltage across coupling capacitors V_{C1} , V_{C2} (V), coupling diode voltages V_{D1} , V_{D2} (V) and currents I_{D1} , I_{D2} (A), rectifier diode voltages V_{D3} (V_{D6}), V_{D4} (V_{D5}) (V) and currents I_{D3} (I_{D6}), I_{D4} (I_{D5}) (A) (a) Input power of 500W (b) Input power of 325W.	97
Fig. 3.10	Simulated waveform of gating signals of switches, leakage current through HF transformer into ground ($I_{G,lk}$) and leakage current at output ($I_{O,lk}$)	98
Fig. 3.11	Simulated waveform of voltages and currents of primary winding V_P (V) and I_{LK1} , I_{LK2} (A) and secondary winding V_{SEC} (V) and I_{SEC} (A) of HF transformer (a) Input power of 500W (b) Input power of 325W	99

Fig. 3.12	Simulated waveform of gating signals of switches V_{GS1} - V_{GS4} (V), voltages: V_{DS1} , V_{DS2} (V) and currents: I_{S1} , I_{S2} (A) in S_1 and S_2 and voltages: V_{DS3} , V_{DS4} (V) and currents: I_{S3} , I_{S4} (A) in S_3 and S_4 (a) Input power of 500W (b) Input power of 325W	100
Fig. 3.13	Simulated waveform of voltages of input V_{IN} (V) and output V_O (V) and currents of input I_{IN} (A) and output I_O (A) (a) Input power of 500W (b) Input power of 325W	101
Fig. 3.14	Hardware prototype of CF-HGIIC (a) Gen 1 (b) Gen 2 (c) Gen 3 (latest)	102
Fig. 3.15	Waveform of coupling capacitor voltage V_{C1} (V), drain to source voltage of switch S_1 : V_{DS1} (V) and S_2 : V_{DS2} (V) and inductor current I_{L1} (A) for input power of 125W (a) Experimental result (b) Simulated result	103
Fig. 3.16	Waveform of coupling capacitor voltage V_{C1} (V), drain to source voltage of switch S_1 : V_{DS1} (V) and S_2 : V_{DS2} (V) and inductor current I_{L1} (A) for input power of 85W (a) Experimental result (b) Simulated result	104
Fig. 3.17	Waveform of voltage across primary winding V_P (V) and secondary winding V_{SEC} (V) for input power of 125W (a) Experimental result (b) Simulated result	105
Fig. 3.18	Experimental performance (a) Efficiency of CF-HGIIC for variation in input power (b) Loss analysis of converter for input power of 125W	106
Fig. 4.1	Topological structure of MCF-HGIIC	112
Fig. 4.2	Analytical waveforms of MCF-HGIIC	115
Fig. 4.3	Topological operating modes of proposed converter	118
Fig. 4.4	Simulated waveform of inductor currents I_{L1} , I_{L2} (A), input current I_{IN} (A), voltage across coupling capacitors V_{C1} , V_{C2} (V), coupling diode voltages V_{D1} , V_{D2} (V) and currents I_{D1} , I_{D2} (A), rectifier diode voltages V_{D3} (V_{D6}), V_{D4} (V_{D5}) (V) and currents I_{D3} (I_{D6}), I_{D4} (I_{D5}) (A) (a) Input voltage of 30V (b) Input voltage of 20V.	124

Fig. 4.5	Simulated waveform of voltages and currents of primary winding V_P (V) and I_{LK1} , I_{LK2} (A) and secondary winding V_{SEC} (V) and I_{SEC} (A) of HF transformer (a) Input voltage of 30V (b) Input voltage of 20V	125
Fig. 4.6	Simulated waveform of gating signals of switches V_{GS1} - V_{GS4} (V), voltages: V_{DS1} , V_{DS2} (V) and currents: I_{S1} , I_{S2} (A) in S_1 and S_2 and voltages: V_{DS3} , V_{DS4} (V) and currents: I_{S3} , I_{S4} (A) in S_3 and S_4 (a) Input voltage of 30V (b) Input voltage of 20V	126
Fig. 4.7	Simulated waveform of voltages of input V_{IN} (V) and output V_O (V) and currents of input I_{IN} (A) and output I_O (A) (a) Input voltage of 30V (b) Input voltage of 20V	127
Fig. 4.8	MCF-HGIIC (a) 3-D PCB design (b) Hardware prototype	129
Fig. 4.9	Waveform of inductor currents I_{L1} , I_{L2} (A) coupling capacitor voltage V_{C1} (V), drain to source voltage of switch S_1 : V_{DS1} (V) for input voltage of 26V (a) Experimental result (b) Simulated result	133
Fig. 4.10	Waveform of inductor currents I_{L1} , I_{L2} (A) coupling capacitor voltage V_{C1} (V), drain to source voltage of switch S_1 : V_{DS1} (V) for input voltage of 18V (a) Experimental result (b) Simulated result	133
Fig. 4.11	Waveform of voltage V_{SEC} (V) and current in secondary winding I_{SEC} (A) and voltage across primary winding V_P (V) for input voltage of 26V (a) Experimental result (b) Simulated result	134
Fig. 4.12	Waveform of voltage V_{SEC} (V) and current in secondary winding I_{SEC} (A) and voltage across primary winding V_P (V) for input voltage of 18V (a) Experimental result (b) Simulated result	134
Fig. 4.13	Waveform of voltage across coupling diodes V_{D1} , V_{D2} (V) for input voltage of 26V (a) Experimental result (b) Simulated result	135
Fig. 4.14	Waveform of voltage across coupling diodes V_{D1} , V_{D2} (V) for input voltage of 18V (a) Experimental result (b) Simulated result	135
Fig. 4.15	Waveform of gating signals of S_3 : V_{GS3} (V) and S_1 : V_{GS1} (V), switch S_3 voltage V_{DS3} (V) and current I_{S3} (A) for input voltage of 26V (a) Experimental result (b) Simulated result	136

Fig. 4.16	Waveform of gating signals of S_3 : V_{GS3} (V) and S_1 : V_{GS1} (V), switch S_3 voltage V_{DS3} (V) and current I_{S3} (A) for input voltage of 18V (a) Experimental result (b) Simulated result	137
Fig. 4.17	Experimental efficiency of MCF-HGIIC for variation in input power at (a) Input voltage of 26V (b) Input voltage of 18V	138
Fig. 4.18	Loss analysis of MCF-HGIIC for rated power of 190W and input voltage of 26V	138
Fig. 5.1	Topological structure of MI-CF-HGIIC	142
Fig. 5.2	Modulation scheme of MI-CF-HGIIC	145
Fig. 5.3	Analytical waveforms of MI-CF-HGIIC	147
Fig. 5.4	Topological operating modes of proposed converter	148
Fig. 5.5	Simulated waveform of input voltages of each module (V), output voltage (V), input currents of each module (A), output current (A)	154
Fig. 5.6	Simulated waveform of input current (A), inductor currents (A), voltage across coupling capacitors (V), coupling diode voltages (V) and currents (A), blocking diode voltages (V) and currents (A) during symmetric converter operation (a) Module 1 (b) Module 2.	157
Fig. 5.7	Simulated waveform of gating signals $V_{GS1} - V_{GS6}$ (V) of switches $S_1 - S_6$ (A), voltage V_{DS1} , V_{DS2} (V) and current I_{S1} , I_{S2} (A) in switches S_1 , S_2 , voltage V_{DS3} , V_{DS4} (V) and current I_{S3} , I_{S4} (A) in switches S_3 , S_4 , voltage V_{DS5} , V_{DS6} (V) and current I_{S5} , I_{S6} (A) in switches S_5 , S_6 during symmetric operation	158
Fig. 5.8	Simulated waveform of primary V_P (V) and secondary V_{SEC} (V) winding voltages of HF transformer and primary I_{LK1} , I_{LK2} (A) and secondary winding I_{SEC} (A) currents during symmetric operation	159
Fig. 5.9	Simulated waveform of rectifier diode voltages V_{D9-D12} (V) and currents I_{D9-D12} (A) during symmetric operation	159
Fig. 5.10	Simulated waveform of input voltages of each module (V), output voltage (V), input currents of each module (A), output current (A) (a) Current based asymmetric converter operation (b) Voltage based asymmetric converter operation	160

Fig. 5.11	Simulated waveform of input current (A), inductor currents (A), voltage across coupling capacitors (V), coupling diode voltages (V) and currents (A), blocking diode voltages (V) and currents (A) during current based asymmetric converter operation (a) Module 1 (b) Module 2.	161
Fig. 5.12	Simulated waveform of input current (A), inductor currents (A), voltage across coupling capacitors (V), coupling diode voltages (V) and currents (A), blocking diode voltages (V) and currents (A) during voltage based asymmetric converter operation (a) Module 1 (b) Module 2.	162
Fig. 5.13	Simulated waveform of gating signals $V_{GS1} - V_{GS6}$ (V) of switches $S_1 - S_6$ (A), voltage V_{DS1} , V_{DS2} (V) and current I_{S1} , I_{S2} (A) in switches S_1 , S_2 , voltage V_{DS3} , V_{DS4} (V) and current I_{S3} , I_{S4} (A) in switches S_3 , S_4 , voltage V_{DS5} , V_{DS6} (V) and current I_{S5} , I_{S6} (A) in switches S_5 , S_6 during (a) Current based asymmetric converter operation (b) Voltage based asymmetric converter operation	163
Fig. 5.14	Simulated waveform of primary V_P (V) and secondary V_{SEC} (V) winding voltages of HF transformer and primary I_{LK1} , I_{LK2} (A) and secondary winding I_{SEC} (A) currents during (a) Current based asymmetric converter operation (b) Voltage based asymmetric converter operation	164
Fig. 5.15	Simulated waveform of rectifier diode voltages V_{D9-D12} (V) and currents I_{D9-D12} (A) during (a) Current based asymmetric converter operation (b) Voltage based asymmetric converter operation	165
Fig. 6.1	MLPS system architecture	172
Fig. 6.2	Applications of MLPS	172
Fig. 6.3	MLPS based off-grid EV charging infrastructure	174
Fig. 6.4	MLPS based floating PV system	176
Fig. 6.5	Rooftop MLPS on train	176
Fig. 6.6	PV Panel with bypass diode operation (a) Unshaded PV cells (b) Shaded PV cells	178

Fig. 6.7	Concept of dynamic sub-panel shading as train is moving (a) No panel is shaded (b) Stationary pole shades some section of PV Panel 1 as it crosses the pole (c) Stationary pole then shades some section of PV panel 2 as it crosses the pole	179
Fig. 6.8	Flexible power generation (a) Basic concept (b) Flowchart of flexible power point tracking algorithm	182
Fig. 6.9	Block diagram of current control	183
Fig. 6.10	Operation of PV panel under sub-panel shading with I-V curve having (a) No shading (b) One-third shading	183
Fig. 6.11	Flowchart of fast MPPT algorithm	184
Fig. 6.12	Case 1: Simulated operation of MLIC system under uniform insolation variation from 1000W/m^2 to 750W/m^2 from $t=0.015\text{s}$ till $t=0.025\text{s}$ and vice versa from $t=0.035\text{s}$ till $t=0.045\text{s}$ and further outage of PV panel 2 at $t=0.05\text{s}$ and its reinsertion at $t=0.07\text{s}$ (a) Profile of PV panels with their powers P_{PV1} and P_{PV2} (W), PV current I_{PV1} and I_{PV2} (A) and PV voltage V_{PV1} and V_{PV2} (V) (b) Output profile with current of MLICs I_{O1} and I_{O2} (A), current in the DC microgrid I_{DC} (A) and output voltages of MLICs V_{O1} and V_{O2} (V)	190
Fig. 6.13	Case 2: Simulated operation of MLIC system under partial shading with insolation variation from 1000W/m^2 to 800W/m^2 in panel 1 and 600W/m^2 in panel 2 from $t=0.025\text{s}$ till $t=0.045\text{s}$ (a) Profile of PV panels with their powers P_{PV1} and P_{PV2} (W), PV current I_{PV1} and I_{PV2} (A) and PV voltage V_{PV1} and V_{PV2} (V) (b) Output profile with current of MLICs I_{O1} and I_{O2} (A), current in the DC microgrid I_{DC} (A) and output voltages of MLICs V_{O1} and V_{O2} (V)	192
Fig. 6.14	Case 3: Simulated operation of MLIC system under uniform insolation variation from 1000W/m^2 to 600W/m^2 from $t=0.015\text{s}$ till $t=0.025\text{s}$ and vice versa from $t=0.045\text{s}$ to $t=0.055\text{s}$ and addition of new panel (PV3) at $t=0.03\text{s}$ (a) Profile of PV panels with their powers P_{PV1} , P_{PV2} and P_{PV3} (W), PV current I_{PV1} , I_{PV2} and I_{PV3} (A) and PV voltage V_{PV1} , V_{PV2} and V_{PV3} (V) (b) Output profile with current of MLICs I_{O1} , I_{O2} and I_{O3} (A), current in the DC microgrid I_{DC} (A) and output voltages of MLICs V_{O1} , V_{O2} and V_{O3} (V)	194
Fig. 6.15	Case 4: Simulated operation of MLIC system under sub-panel shading in panel 1 at $t=0.02\text{s}$ and panel 2 at $t=0.03\text{s}$ and removal of shade in panel 1 at $t=0.05\text{s}$ and panel 2 at $t=0.06\text{s}$ (a) Profile of PV	196

panels with their powers P_{PV1} and P_{PV2} (W), PV current I_{PV1} and I_{PV2} (A) and PV voltage V_{PV1} and V_{PV2} (V) (b) Output profile with current of MLICs I_{O1} and I_{O2} (A), current in the DC microgrid I_{DC} (A) and output voltages of MLICs V_{O1} and V_{O2} (V)

- Fig. 6.16 Case 5: Simulated flexible power operation of MLIC system under insolation variation from 500W/m^2 to 1000W/m^2 from $t=0.02\text{s}$ to $t=0.03\text{s}$, then from 1000W/m^2 to 900W/m^2 from $t=0.04\text{s}$ to $t=0.05\text{s}$ and finally from 900W/m^2 back to 500W/m^2 from $t=0.06\text{s}$ to $t=0.07\text{s}$ (a) Profile of PV panels with their powers P_{PV1} and P_{PV2} (W), PV current I_{PV1} and I_{PV2} (A) and PV voltage V_{PV1} and V_{PV2} (V) (b) Output profile with current of MLICs I_{O1} and I_{O2} (A), current in the DC microgrid I_{DC} (A) and output voltages of MLICs V_{O1} and V_{O2} (V) 198
- Fig. 6.17 Case 6: Simulated flexible power operation of MLIC system under insolation variation from 600W/m^2 to 850W/m^2 from $t=0.03\text{s}$ till $t=0.04\text{s}$ and the outage of PV panel 2 at $t=0.06\text{s}$ (a) Profile of PV panels with their powers P_{PV1} and P_{PV2} (W), PV current I_{PV1} and I_{PV2} (A) and PV voltage V_{PV1} and V_{PV2} (V) (b) Output profile with current of MLICs I_{O1} and I_{O2} (A), current in the DC microgrid I_{DC} (A) and output voltages of MLICs V_{O1} and V_{O2} (V) 200
- Fig. 6.18 Case 7: Simulated flexible power operation of MLIC system under partial shading with insolation variation from 1000W/m^2 to 850W/m^2 in panel 1 and 600W/m^2 in panel 2 from $t=0.025\text{s}$ till $t=0.045\text{s}$ (a) Profile of PV panels with their powers P_{PV1} and P_{PV2} (W), PV current I_{PV1} and I_{PV2} (A) and PV voltage V_{PV1} and V_{PV2} (V) (b) Output profile with current of MLICs I_{O1} and I_{O2} (A), current in the DC microgrid I_{DC} (A) and output voltages of MLICs V_{O1} and V_{O2} (V) 202
- Fig. 6.19 Case 1: Simulated operation of MMIC system under partial shading with insolation variation from 1000W/m^2 to 750W/m^2 in panel 1 and 400W/m^2 in panel 2 from $t=0.04\text{s}$ till $t=0.0408\text{s}$ (a) Profile of PV panels with their powers P_{PV1} and P_{PV2} (W), PV current I_{PV1} and I_{PV2} (A) and PV voltage V_{PV1} and V_{PV2} (V) (b) Output current I_O (A) and output voltage V_O (V) of MMIC 205
- Fig. 6.20 Case 2: Simulated operation of MMIC system under insolation change in PV panel 1 from 1000W/m^2 to 750W/m^2 from $t=0.04\text{s}$ till $t=0.05\text{s}$ and outage of PV panel 2 at $t=0.03\text{s}$ and its reinsertion at $t=0.05\text{s}$ (a) Profile of PV panels with their powers P_{PV1} and P_{PV2} (W), 207

	PV current I_{PV1} and I_{PV2} (A) and PV voltage V_{PV1} and V_{PV2} (V) (b) Output current I_O (A) and output voltage V_O (V) of MMIC	
Fig. 6.21	Case 3: Simulated operation of MMIC system with PV panel 1 operation at 1000W/m^2 while sub panel shading of PV panel 2 at $t=0.03$ and removal of shade at $t=0.05\text{s}$ (a) Profile of PV panels with their powers P_{PV1} and P_{PV2} (W), PV current I_{PV1} and I_{PV2} (A) and PV voltage V_{PV1} and V_{PV2} (V) (b) Output current I_O (A) and output voltage V_O (V) of MMIC	209
Fig. 6.22	Case 4: Simulated operation of MMIC system with dynamic sub panel shading in PV panel 1 and panel 2 (a) Profile of PV panels with their powers P_{PV1} and P_{PV2} (W), PV current I_{PV1} and I_{PV2} (A) and PV voltage V_{PV1} and V_{PV2} (V) (b) Output current I_O (A) and output voltage V_O (V) of MMIC	211
Fig. 6.23	Comparative performance of conventional InC MPPT algorithm and fast MPPT algorithm under dynamic sub-panel shading	212
Fig. 6.24	Experimental hardware setup of MLIC based MLPS system architecture interfacing the PV simulator with the section of DC microgrid	213
Fig. 6.25	Experimental operation of CF-HGIIC based MLIC integrating PV simulator with section of 170V DC microgrid (a) DC bus voltage V_{BUS} (V), PV voltage V_{PV} (V) and PV current I_{PV} (A) (b) Load current I_{LOAD} (A), DC bus current I_{BUS} (A) and converter output current I_O (A)	215
Fig. 6.26	Experimental starting dynamics of system with integration of PV simulator with the section of 170V DC microgrid using CF-HGIIC at $t=25\text{s}$ having load current I_{LOAD} (A), DC bus current I_{BUS} (A) and converter output current I_O (A)	216
Fig. 6.27	Experimental flexible power generation using CF-HGIIC based MLIC integrating PV simulator with section of 170V DC microgrid under insolation variation from 600W/m^2 to 850W/m^2 from $t=5\text{s}$ till $t=30\text{s}$ (a) PV voltage V_{PV} (V), PV power P_{PV} (W) and PV current I_{PV} (A) (b) Converter output current I_O (A), DC bus current I_{BUS} (A) and load current I_{LOAD} (A)	217

Fig. 6.28	Tracking accuracy of InC MPPT and CPG-InC FPPT implemented on dsPIC33FJ16GS502 during different operating conditions.	218
Fig. 6.29	Efficiency of CF-HGIIC based MLIC under different operating conditions	219
Fig. 6.30	Experimental operation of MCF-HGIIC based MLIC integrating PV simulator with section of 270V DC microgrid under insolation variation from 1000W/m^2 to 700W/m^2 from $t=10\text{s}$ till $t=20\text{s}$ and vice versa from $t=30\text{s}$ till $t=40\text{s}$ with waveforms of output voltage V_O (V) and current I_O (A) of converter and PV current I_{PV} (V) and voltage V_{PV} (V)	220
Fig. 6.31	Experimental operation of MCF-HGIIC based MLIC integrating PV simulator with section of 270V DC microgrid under sub-panel shading at $t=15\text{s}$ and $t=45\text{s}$ and removal of shade at $t=30\text{s}$ with waveforms of output voltage V_O (V) and current I_O (A) of converter and PV current I_{PV} (V) and voltage V_{PV} (V)	221
Fig. 6.32	Experimental operation of MCF-HGIIC under insolation variation from 1000W/m^2 to 800W/m^2 from $t=10\text{s}$ till $t=20\text{s}$ and subsequent sub panel shading at $t=30\text{s}$ with waveforms of output voltage V_O (V) and current I_O (A) of converter and PV current I_{PV} (V) and voltage V_{PV} (V)	222
Fig. 6.33	Experimental starting dynamics of system with integration of PV simulator with the section of 270V DC microgrid using MCF-HGIIC at $t=25\text{s}$ with waveforms of output voltage V_O (V), output current I_O (A), input current I_{IN} (A) and input Voltage V_{IN} (V) of converter	223
Fig. 6.34	Tracking accuracy of InC MPPT implemented on dsPIC33FJ16GS502 during different operating conditions	224
Fig. 6.35	Efficiency of MCF-HGIIC based MLIC under different operating conditions	225
Fig. 6.36	DC microgrid architecture with integration of proposed converters	226

LIST OF TABLES

Table No.	Title	Page No.
Table 2.1	State-of-the-art Isolated Current-Fed Converter Topologies	50
Table 3.1	Parametric notations of CF-HGIIC	71
Table 3.2	Loss equations of proposed converter	90
Table 3.3	Comparative study of state-of-the-art topologies	92
Table 3.4	Simulated converter specifications	96
Table 3.5	Simulated converter design parameters	96
Table 3.6	Experimental converter specifications	102
Table 3.7	Experimental converter design parameters	102
Table 4.1	Parametric notations of MCF-HGIIC	113
Table 4.2	Simulated converter specifications	123
Table 4.3	Simulated converter design parameters	123
Table 4.4	Experimental converter specifications	130
Table 4.5	Experimental converter design parameters	130
Table 5.1	Parametric notations of MI-CF-HGIIC	143
Table 5.2	Simulated converter specifications	153
Table 5.3	Simulated converter design parameters	153
Table 6.1	Simulated system parameters	187

Table 6.2	Simulated operating conditions for MLIC	188
Table 6.3	Simulated operating conditions for MMIC	203
Table 6.4	Experimental parameters of CF-HGIIC based MLIC for MLPS system architecture	214
Table 6.5	Experimental parameters of MCF-HGIIC based MLIC for MLPS system architecture	220

ABBREVIATIONS

3D	:	Three Dimension
A	:	Amperes
AC	:	Alternating Current
ADC	:	Analog to Digital Converter
ANFIS	:	Adaptive Neuro Fuzzy Inference System
ANN	:	Artificial Neural Network
CBC	:	Conventional Boost Converter
CCM	:	Continuous Conduction Mode
CF	:	Current-Fed
CF-HGIIC	:	Current-Fed High Gain Isolated Interfacing Converter
CPG	:	Constant Power Generation
DC	:	Direct Current
DCM	:	Discontinuous Conduction Mode
DERs	:	Distributed Energy Resources
DSO	:	Digital Storage Oscilloscope
DSP	:	Digital Signal Processor
EMI	:	Electromagnetic Interference
ESR	:	Equivalent Series Resistance
ESS	:	Energy Storage System
FPPT	:	Flexible Power Point Tracking
FPV	:	Floating Photovoltaic System
GMPP	:	Global Maximum Power Point
GMPPT	:	Global Maximum Power Point Tracking

HF	:	High Frequency
InC	:	Incremental Conductance
I _M	:	Magnetizing Current
KCL	:	Kirchhoff's Current Law
MATLAB	:	Matrix Laboratory
MCF-HGIIC	:	Modified Current-Fed High Gain Isolated Interfacing Converter
MI-CF-HGIIC	:	Mult-Input Current-Fed High Gain Isolated Interfacing Converter
MLIC	:	Module Level Interfacing Converter
MLPS	:	Module Level Photovoltaic System
MMIC	:	Multi-Input Module Interfacing Converter
MPG	:	Maximum Power Generation
MPP	:	Maximum Power Point
MPPT	:	Maximum Power Point Tracking
PI	:	Proportional Integral
PGC	:	Power Generation Control
P&O	:	Perturb and Observe
PV	:	Photovoltaic
P _{PV}	:	PV Panel Power
PWM	:	Pulse Width Modulation
RES	:	Renewable Energy Sources
RMS	:	Root Mean Square
s	:	seconds

SMLPS	:	Sub-Module Level PV System
SPS	:	String Photovoltaic System
SWG	:	Standard Wire Gauge
V	:	Voltage
VF	:	Voltage-Fed
V_P	:	PV Panel Voltage
V_{MPP}	:	Voltage corresponding to MPP
W	:	Watt
ZVS	:	Zero Voltage Switching
ZCS	:	Zero Current Switching

CHAPTER 1

INTRODUCTION

1.1. Background

The industrial revolution is commonly recognized as a pivotal point in human history, serving as the cornerstone for the remarkable expansion of technological progress. Since the advent of the second Industrial Revolution, electricity has played a central role in facilitating industrialization and has made a profound impact on technological and economic advancement. The adoption of electricity has led to a substantial increase in industrial productivity, thanks to enhanced machinery and more efficient processes. This, in turn, has spurred rapid urbanization and infrastructure development, necessitating significant improvements in transportation for quicker commutes and reduced travel times.

Over the past century, the energy sector has rapidly emerged as a crucial indicator of a country's development, with fossil fuels serving as the primary source. In the current landscape, thermal power plants, heavily reliant on coal reserves (a fossil fuel) play the most substantial role in electricity generation when compared amongst all sources. Similarly, in the transportation sector, vehicles fueled by oil (another fossil fuel) dominate the landscape. The continuous increase in energy demands within the industrial, urban, and transportation sectors has led to widespread fossil fuel consumption, resulting in a significant depletion of their reserves. Consequently, this depletion has had a profound impact on the overall progress and economies of nations.

According to the United Nations-Climate Action reports, fossil fuels such as coal, oil, and gas are the largest contributors to global warming, accounting for over 75% of total

greenhouse gas (GHG) emissions and nearly 90% of global carbon dioxide (CO₂) emissions [1]. The escalating emissions of greenhouse gases have raised concerns among international environmental agencies due to their role in causing abrupt changes in the global climate, exacerbating issues like global warming and the greenhouse effect. These factors have led to alterations in weather patterns, an increase in global average temperatures, rising sea levels, severe environmental consequences, exacerbation of existing human health concerns, and significant economic repercussions. According to the International Energy Agency (IEA), India ranks as the third-largest global emitter of CO₂, despite having relatively low per capita CO₂ emissions. Figure 1.1 depicts a pie chart illustrating the CO₂ emissions in various energy sectors in India for the year 2019 [2]-[3]. In this chart, the power sector in India, primarily reliant on coal-based power plants, stands out as the major contributor to CO₂ emissions, followed by the industrial and transportation sectors. These limitations and the severe consequences associated with fossil fuels have acted as a driving

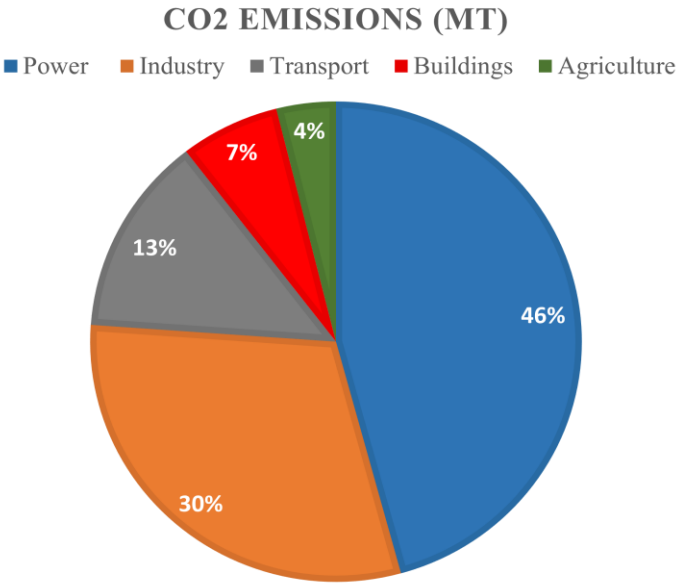


Fig.1.1. CO₂ emissions in different sectors in India

force for significant reforms in the energy sector and the adoption of cleaner, more sustainable energy solutions.

1.2. Renewable Energy Sources

Over the last decade, there has been a paradigm shift towards more environmentally friendly and sustainable energy solutions. The future energy infrastructure demands a system that is both eco-friendly and sustainable, capable of achieving carbon neutrality, possessing ample reserves, ensuring energy security, and mitigating the negative impacts associated with fossil fuels [3]. Renewable energy sources (RES) have emerged as a prominent and viable solution, attracting extensive research to assess their feasibility, potential, and technological means of implementation. The advantages, challenges, and different types of RES are discussed in the following sub-sections [4]-[7].

1.2.1. Advantages of Renewable Energy Sources

- **Environmental Sustainability and minimal carbon footprints-** The primary advantage of renewable energy sources is their minimal impact on the environment as they don't generate greenhouse gas emissions, unlike fossil fuels. Additionally, their adoption will aid in combating climate change and global warming.
- **Inexhaustible Energy Reserves-** Renewable energy sources offer vast inexhaustible reserves of energy.
- **Energy Security-** Fossil fuels demonstrate limited energy security due to their high sensitivity to the supply chain demand and global energy market price. In contrast, RES offers notably robust and superior energy security, enabling power

generation utilizing local energy reserves and reducing vulnerability to disruption in the supply chain and global price fluctuations.

- **Economic Enabler** - RES is becoming a major driver for the economic growth of the nations. The cheaper cost of renewable energy, with lower operational expenses, when compared to fossil-fuel based thermal power plants translates to substantial long-term cost savings for the consumers. This positive impact of RES extends beyond the operational and manufacturing sectors, encompassing the domains of installation and research as well. The governments are actively encouraging extensive investments in RES and fostering different innovative start-ups. Several countries are offering energy subsidies to incentivize their population to adopt renewable energy sources. Furthermore, they are boosting their economy with revenue generation by selling the excess energy generated from the RES to other power deficit countries. This approach reduces the overreliance on the import of fossil fuels, thereby contributing to greater energy sovereignty.
- **Opportunity for development of Innovative Technologies** - The focus on renewable energy sources offers vast prospects for efficient tapping of renewable energy and improvements in the existing technologies. This motivates significant research on innovation and technological advancements. Innovative technologies have the potential to improve the operational performance, efficiency, cost-effectiveness, and reliability of RES.
- **Community Benefits**- The adoption of RES ensures its installation in remote areas where electrification is not viable. Moreover, it can expand energy access to

nearby local communities, improving their quality of life. Furthermore, it provides opportunities for the locals to generate revenue by leasing their property for the installation of RES and accommodating the workforce.

- Future-Proofing- The vast energy reserves of RES ensure future-proofing of energy needs and provide long-term energy sustainability.

1.2.2. Challenges of Renewable Energy Sources

- Intermittency- Some renewable energy sources such as Solar and Wind are highly intermittent. The variability in their power generation is attributed to the fluctuation in the operating environmental conditions. The intermittency also affects the sizing and operational performance of RES.
- Integration with Existing Power Grid - The integration of RES with the existing power grid is a critical challenge with a high risk of power fluctuations, significant failures, and power blackouts. The existing grid requires major upgrades for seamless integration with RES.
- Additional Storage System – The incorporation of the energy storage system is imperative for mitigating the intermittency of RES. However, the storage system is significantly bulky, has higher installation costs, and requires frequent maintenance, leading to increased expenses for the upkeep of the overall system.
- Higher Penetration of RES in the existing power grid - The higher penetration of RES in the existing power grid can pose challenges due to issues like reverse power flow and overvoltage in the grid, which may result in grid instability and overloading.

- Regional variance of resources - There exists a disparity in the accessibility and availability of RES, influenced by geographical location. The wind energy systems are well-suited for coastal regions but are not feasible for urban areas due to constraints like limited available land and less favorable wind conditions.
- Higher initial cost - The installation and deployment of RES is a cost-intensive and high upfront investment, posing a challenge for a seamless transition to RES.
- Resource / Capital Intensive (Requirement of Land) - The installation of RES such as wind farms are resource-intensive project and necessitates extensive land use, which could otherwise be allotted for other developmental activities.
- Supply Chain Vulnerabilities - The supply chain for renewable energy technologies such as rare earth metals can be highly price sensitive and prone to disruptions.
- Dependence on Regulation and Policies of Government - The RES sector is highly influenced by government policies, incentives, and regulation which can create uncertainties amongst investors and companies and impact the development of the projects.

1.2.3. Types of Renewable Energy Sources

- Solar Energy - Solar energy stands out as one of the most promising and readily available RES. The solar energy is harnessed by photovoltaic panels and converted into electricity. The lower capital investment, smaller form factor, and ease of installation and maintenance make the photovoltaic (PV) system a viable solution for residential and commercial applications. Additionally, large solar plants are installed both on land and water. However, solar energy faces major

drawbacks, including its intermittent power generation and lower conversion efficiency of PV panels.

- Wind energy – Wind energy taps the kinetic energy of moving air and converts it into electricity using a wind turbine. These turbines are equipped with blades that convert the wind energy into rotational motion, subsequently powering generators to produce electricity. Wind energy systems face challenges such as intermittency and significant high capital intensive. The onshore wind farms, typically located on land, are most prevalently used owing to their higher reliability and efficiency. In contrast, offshore wind power is installed on water bodies with access to stronger winds but incurs significantly higher installation and maintenance costs.
- Hydropower – Hydropower harnesses the kinetic energy of running water and generates electricity. The hydroelectric dam stores water in the reservoirs and the released water through the turbines generates electricity with consistent power generation. However, hydropower is highly capital intensive and has large installation and maintenance expenses and the construction of hydropower dam displaces the communities.
- Tidal / Wave Energy - The tidal power captures the energy during the crest and trough of the tides. Moreover, wave energy technology harnesses the energy of ocean waves, transforming the mechanical energy into electricity. Wave energy is effective in regions with strong ocean wave currents. Both tidal and wave energy systems come with steep upfront costs for installation and maintenance, demanding significant capital investment and the use of advanced and expensive technology.

- **Geothermal Energy** - Geothermal energy utilizes the internal heat of the earth (earth's crust) for electricity generation, heating, and cooling applications. The geothermal power plants make use of steam extracted from geothermal reservoirs to drive the turbines and generate electricity.
- **Biomass Energy** – Biomass energy converts organic materials like wood, crop residues, and waste products to electricity. The biomass power plants operate by burning organic materials to produce steam which powers the turbine to generate electricity. Biomass power plants are highly versatile and accept a wide range of organic materials.

Fig.1.2 displays the cumulative installed capacity of RES in India from 2012-2023, as reported by MNRE and CEA [8]-[9]. Over this period, there has been a remarkable growth in renewable energy capacity, with a compound annual growth rate (CAGR) of 16.13%.

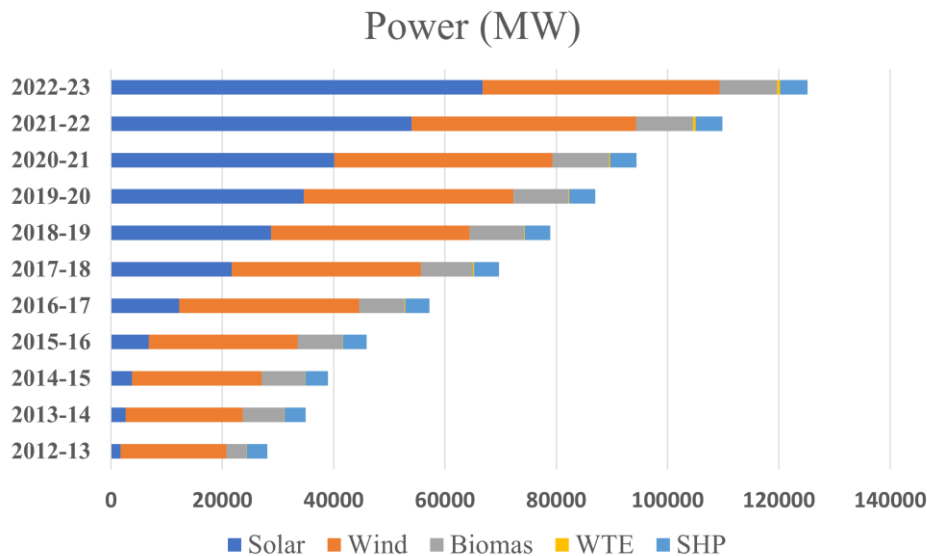


Fig.1.2. Cumulative installed capacities of different RES in India

Notably, solar has witnessed unprecedented growth among all RES, boasting of dramatically higher CAGR of 44.47%. Moreover, the share of solar in overall renewable

installed capacity has surged considerably, rising from 6.01% in 2012-2013 to a notable 53.33% in 2022-2023. This underscores the exceptional growth of solar energy in India and its dominant position in the renewable energy sector. These statistics also suggest a major uptrend in the Indian solar market, driven by favorable government policies and advancements in technology, thus enabling a smoother transition to solar energy.

1.3. Photovoltaic System

India is endowed with massive potential for solar energy as many regions receive more than 300 sunny days. Moreover, solar is a major resource surplus in India with about 5000 trillion kWh per year of energy incident over the area and most regions receiving 4-7kWh per square meter per day [10]. The impact of solar in the Indian renewable energy sector has become increasingly evident in recent years, and the rapid rise in the installed solar capacity over a decade is attributed to the key advantages of solar outlined below [11]-[12]:

1.3.1. Advantages of Solar Energy and Photovoltaic Systems

- **Sustainable and Clean Source of Energy-** Solar is a sustainable energy source with minimal carbon footprints and does not emit greenhouse gases. It primarily reduces the reliance on fossil fuels and helps in addressing the problems posed by climate change.
- **Smaller form factor –** The compact size of photovoltaic (PV) panels makes it possible to achieve a smaller form factor of PV systems and facilitate their installations in urban areas, particularly on the rooftops where the space is limited.
- **Low installation and operating cost-** The installation process and its associated expenses in PV system is comparatively cheaper than capital-intensive RES like

wind-based system. After the installation, the recurring operating and maintenance expenses are also relatively lower, owing to reduced maintenance requirements when compared to other RESs.

- Scalable Architecture – The PV system achieves highly flexible and scalable architecture well suited for a diverse array of applications based on the power demand ranging from small residential setups to large utility-scale solar farms.
- Longevity- The typical warranty on PV panels is 25 years or longer, which improves the longevity of the entire PV system and further reduces the need for frequent panel replacement and the associated expenses.
- Proximity to the Load Centers - The PV system offers the major advantage of facilitating local power generation near the load center and subsequently reducing transmission losses and costs. Furthermore, multiple clusters of PV system functions as distributed energy resources (DERs) and seamlessly integrates with the grid while catering to the demands of local loads.
- Remote Power Generation – The PV system can be deployed in remote and off-grid areas devoid of conventional power infrastructure for electrification of these regions.
- Energy Access - Solar energy offers the quickest restoration of electricity for critical services like hospitals in case of natural calamities and emergencies such as floods.

1.3.2. Challenges of Solar Energy and Photovoltaic Systems

Despite the numerous merits of solar energy, it faces different challenges that impede its widespread adoption for different applications and integration with existing grid infrastructure [13]-[14].

- Intermittency- The power generation from PV panels is highly intermittent and dependent on the environmental conditions, weather patterns, and time of the day. Moreover, ensuring stable and continuous power throughput to the grid is a challenging task, particularly with the power fluctuations impacting the operation and stability of the grid.
- Higher PV penetration in the existing grid - With the major thrust on solar, there is a manifold increase in the installation of PV systems. The increasing penetration of PV systems in the existing grid can cause severe problems like overvoltage and reverse power flow in the grid which can lead to grid overloading.
- Low conversion efficiency of PV panels - Presently, the commercially available PV panels have dramatically poor conversion efficiency, and hampers their power generation capability despite the abundance of solar influx.
- Integration of Energy Storage System – The energy storage system is necessary to mitigate the intermittency of the PV system and ensure a stable power supply to the grid. The current state of the battery storage system has several drawbacks viz, limited life cycles, low energy density, high installation and recurring maintenance cost, and requirement of larger space.
- Material availability for PV panels – There is a surge in the market of PV systems with an exponential increase in the demand for PV panels. However, procurement

of specific materials required for the PV panels is a challenge due to their limited availability, thereby causing frequent disruptions and delays in the manufacturing.

1.3.3. Opportunities of Solar Energy in India

As solar energy is becoming increasingly prominent, massive opportunities are being created in countries like India, which are discussed below [15].

- The solar energy market has the potential to create significant employment opportunities, spanning from the manufacturing of PV panels and their components to the installation, maintenance, operation, and research.
- Rural electrification is a massive opportunity for the Indian solar market due to the critical role of solar energy in electricity generation in the rural and remote areas of India. Furthermore, it helps in bridging the energy gap and enriching the quality of life of millions of people.
- India is attracting substantial domestic and foreign investment prospects in the renewable energy sector, markedly in the solar sector. These investments are broadly in the areas of manufacturing, research and development, and product development.
- The thrust on solar energy is motivating major interest in the research and development of innovative and advanced technologies for the economical and enhanced operational performance of PV systems.
- India has the potential to become a major exporter in the solar market for equipment and technology, thereby boosting its economy.
- The limited available space in urban areas can be a deterrent to the installation of different RES. Nonetheless, the PV system with rooftop installation capability

presents a major opportunity for deployment in urban environments, both residential and commercial sectors.

- For effective solar energy utilization, the net metering will provide incentives to the consumer to earn revenue by selling excess generated power back to the grid and thereby reducing the recurrent electricity bill.
- The utilization of solar energy for diverse sectors such as transportation, residential, commercial, industrial, and agriculture can significantly alleviate their dependence on fossil fuel-based power plants.

1.3.4. Key Applications of Solar Energy

- Utility-scale Solar Power Plants and Solar Farms
- Rural and Off-Grid Electrification
- EV charging infrastructure
- Telecom sector: Solar-powered telecom towers and rooftop PV systems in Data Centers
- Transportation
- Rooftop and Building Integrated Systems
- Solar Pumps and streetlights

1.3.5. Major Environmental Factors Contributing to the Intermittency of PV panels

The environmental conditions are primarily responsible for the intermittency of PV panels and introduce source-side perturbations in the PV system. The major environmental factors are discussed below [16]-[18].

- **Insolation Variations** - The insolation profile is highly variable due to the gradual shifts in the solar influx throughout the day. The power generation of PV panels is highly correlated with the insolation profile. The variations in insolation affects the generated current from the PV panel, thereby making it highly intermittent.
- **Shading Conditions** - The shading on the PV panels is a major challenge for the PV system causing variations in the generated PV power and severely affecting the voltage during shading conditions leading to significant power and voltage fluctuations. These fluctuations impact the operation of the PV system and in extreme cases, render them inoperable. The shading conditions are broadly classified into partial shading of PV panels and sub-panel shading. During the partial shading conditions, non-uniform insolation is incident on the PV panels with different panels receiving different insolutions at the same time. Meanwhile, sub-panel shading occurs due to localized shading on a section of the PV panel. Furthermore, the dynamic shading of panels, such as PV panels installed on the roof of locomotives introduces a novel challenge of moving shade on the PV panels and exhibits dynamically fast shading variations. Dynamic shading is a more severe problem in comparison to stationary shading condition.
- **Dust and Soiling** - The accumulation of dust and soiling of PV panels reduces the glass transmittance of panels and decreases the amount of insolation reaching the PV cells, thereby reducing the PV power generation.
- **Temperature** - The variation in the temperature affects the power generation of PV panels. The hotter regions experience substantially lower power generation in

comparison to the cooler regions. Moreover, the dynamics of temperature variation are significantly slower in comparison to shading.

1.3.6. Components of PV System

The Photovoltaic (PV) system is critical for harnessing solar energy and transforming it into electricity. The major components of PV system are [19]:

- **Photovoltaic Panels** - Photovoltaic (PV) panels are the fundamental component of the PV system and responsible for converting solar energy into electricity. The PV panels are constructed by connecting PV cells in series, which upon exposure to the solar influx generates current. Moreover, the PV panel is installed with the bypass diodes in parallel with 12-15 cells, typically to prevent the formation of hot spots on the cells. The PV panels are further categorized into Monocrystalline Silicon, Polycrystalline Silicon, Thin-film, and Bifacial. Monocrystalline PV panels achieve superior efficiency compared to polycrystalline panels with enhanced longevity, better space efficiency, and performance at higher temperatures and low lights but are notably expensive. The PV panels exhibit non-linear power-voltage (P-V) and current-voltage (I-V) curve profiles and even slight disturbances in the operating conditions displace the operating point. This limitation of PV panels requires robust power generation control for sustained operation at the maximum power point (MPP) irrespective of the operating conditions and PV side disturbances such as insolation changes, shading conditions, and temperature variations.
- **Power Generation Control** - The evacuation of maximum power from the non-linear profile of PV panels requires power generation control viz, maximum

power point tracking (MPPT) algorithms. The MPPT algorithm ensures the operation of the PV panel at maximum power point (MPP) during variations in the environmental conditions such as insolation, temperature changes, and the shading conditions. Furthermore, a new concept of flexible power generation in the PV system is recently being explored where the PV power generation transitions between maximum power generation and constant power generation depending on the operating conditions. The flexible power generation is deployed to counter the high PV penetration in the existing system and support the battery storage system in mitigating intermittency. The control-based techniques such as flexible point tracking (FPPT) algorithms are employed to achieve flexible power generation in the PV system.

- **Interfacing Converter** - Different applications of the PV system require the integration of low-voltage PV panels with high-voltage loads / DC bus. The considerable difference in the operating voltages of PV and load / DC bus necessitates the use of interfacing converters to enable seamless integration of PV panels. Moreover, such converters also help optimize the evacuation of maximum power from the PV panel under different operating conditions.

1.3.7. Classification of PV System

The PV systems are broadly classified into various configurations [20]-[22]:

- **String PV system** – Traditionally, the string PV system has widely been adopted in several applications owing to their simpler configuration, lower cost, and need for fewer electronic components. The string configuration of the PV system consists of multiple PV strings where each PV string consists of the series

connected PV panels. The higher terminal voltage of the PV string eases the demand for voltage conversion gain from the interfacing converter, enabling its interfacing with the load / DC bus. Additionally, a centralized MPPT controller is employed to harness the maximum generated power from the PV string.

However, the limitations of string PV system becomes evident during shading conditions where shading of PV panel(s) causes severe power fluctuations and can destabilize the entire system under extreme cases. The lack of independent power control over the individual PV panel impacts the system performance with the conventional MPPT algorithms getting stuck at one of the local power maxima and exhibiting sub-optimal performance. Furthermore, the complex and computation-intensive global maximum power point (GMPPT) algorithms are utilized for evacuating the maximum power from the entire PV string during shading. The performance of the string PV system is further exacerbated during dynamic shading conditions where fast shading variations significantly impair the tracking performance of the GMPPT controller. Another major drawback of string PV system is its single point failure where the system outage due to the malfunctioning of even a single PV panel or breakdown of an interfacing converter will render the entire string inoperable and lead to significant loss of electricity production. This also highlights the poor reliability and poor robustness of string PV systems with expensive and recurring maintenance, complex repairability, lack of modularity, and operational flexibility.

- **Module Level PV System** – The recent advances in power electronic technologies have opened fresh opportunities for the PV system and significantly heightened the interest in new PV configurations that can alleviate the constraints of

traditional string PV systems. The researchers and industry experts are actively investigating the concept of module-level PV systems (MLPS), conducting in-depth studies to assess their operational viability weighing on the decreasing cost of power electronics and associated electronics. The module-level PV system incorporates multiple units of PV panels where each PV panel has its own distributed MPPT controller and is discretely integrated with the load / DC bus. Furthermore, MLPS demonstrates superior power utilization owing to its greater degree of control of power generation over each panel, thereby allowing the evacuation of maximum available power from each panel. MLPS also exhibits excellent reliability and robustness with the smooth operation of the entire system during the outage of a section, malfunctioning of a PV panel(s), or maintenance process carried out in any part of the plant thereof. This also highlights the simple and low-cost maintenance of MLPS with easy repairability, higher modularity, and operational flexibility. The MLPS offers a highly scalable architecture with plug-and-play operation and can dynamically and seamlessly increase the power capacity.

- Sub-Module Level PV System – The recent advances in power electronics have spurred the exploration of the concept of sub-module PV systems. In a sub-module level PV system, the bypass diodes connected in parallel with a few PV cells are replaced by the DC/DC converters, thereby facilitating optimal power evacuation from each sub-module of PV panel. This approach dramatically enhances the performance of the PV system but substantially increases the implementation cost and has limited viability in a commonly used PV

applications. This configuration is well suited for critical applications where high performance is crucial.

The salient features of module-level PV systems highlight their advantages over string PV systems and can be a sustainable solution for several applications.

1.4. DC Microgrid

The traditional centralized energy grids are facing increasing challenges, including limited ability to adapt to the increasing integration of renewable energy sources and their outdated energy infrastructure. The emergence of microgrids offers a promising solution due to its decentralized structure, which provides greater resiliency and sustainability. A microgrid is a small-scale autonomous energy system which can operate both in grid-connected and islanded mode. It incorporates distributed energy resources (DERs) viz, solar, wind, and energy storage systems. The microgrid is well suited for the integration of renewable energy sources due to its decentralized approach, where it enables local power generation and its consumption. Furthermore, it can effectively manage the intermittency and higher penetration of RES by seamlessly integrating the energy storage system. It also enhances grid resiliency, facilitates electrification of rural and remote areas, supply power to the local communities, and ensure uninterrupted operation of the critical systems during grid outages and blackouts.

Conventionally, AC microgrids have been in existence for years and their technology has reached a level of maturity with standardized equipment and universally accepted electrical standards. However, the increasing pervasiveness of DC sources and loads in the system has garnered significant interest in DC microgrids, which are relatively new

infrastructure. The DC microgrids are becoming an attractive solution due to their following advantages [23].

1.4.1. Advantages of DC Microgrids

- The DERs such as solar and battery storage system are typically DC power sources. Their integration with the DC microgrid eliminates the need for additional inversion or conversion stage. Moreover, as the majority of electronic loads are also DC, their integration with the DC microgrid removes the requirement of the rectifier stage (AC/DC). Consequently, the adoption of a DC microgrid reduces the number of conversion stages and significantly improves the overall efficiency of the system.
- The DC microgrid does not have any issues involving reactive power, power quality problems and other which dramatically impacts the AC microgrids. Moreover, there are no such problems of voltage sag and swell, harmonics, and imbalances.
- There is no requirement for synchronization with the utility grid and frequency regulation.
- The DC currents eliminate the problem of skin effect in the distribution cable, thereby reducing losses.
- DC microgrid has higher reliability and resiliency.

1.4.2. Challenges in DC Microgrid

The DC microgrids have multiple benefits but also have different challenges [24].

- The DC microgrids are significantly costlier as compared to the AC microgrids.

- Lack of readiness amongst manufacturers and consumers to transition from conventional AC infrastructure. Moreover, retrofitting the existing AC infrastructure to enable its compatibility with DC microgrid infrastructure is a daunting task and expensive.
- Lack of standardisation
- The system protection in DC microgrid is underdeveloped and is expensive.

1.4.3. Architecture and Application DC Microgrid

The DC microgrids have different types of architectures such as single bus topology (radial topology), ring topology, and mesh topology [25]-[27]. Single bus topology is the simplest and requires a single DC bus where all power generation sources such as RES, battery storage system, and loads are connected through a single pair of lines. This topology requires minimal upkeep with a modest initial capital investment. Moreover, the DC microgrids are further classified into unipolar and bipolar configurations. The unipolar configuration is simple and requires only two wires (+VDC and GND) to which all generation sources, energy storage systems, and loads can be connected.

The 380V DC microgrid is an industry standard and is widely accepted for residential and commercial applications [28]. The power generated from the RES integrated with the 380V DC microgrid drives the popular community loads such as EV charging centers, data centers, etc., besides its use as an intermediary DC bus for AC loads such as motor drives and UPS.

A few key applications where DC microgrid is suitable are electric vehicle charging infrastructure, rural and remote electrification, renewable energy parks, transportation such

as ship, train, and aerospace, data centers, residential and commercial applications, and infrastructure sector [29]-[30].

1.4.4. Integration of Module Level PV System with DC Microgrid

Relatively newer technologies like the DC microgrid and module-level PV system are currently undergoing extensive research and investigation [31]. There is a growing interest in integrating the MLPS as the front-end section of the DC microgrid as both systems are decentralized. Additionally, MLPS has a modular and scalable architecture with operational flexibility, thereby enhancing the power generation capability of DC microgrid. Furthermore, it allows for better power utilization of power generated from the PV panels and contributes to increased robustness and reliability.

However, the efficacy in the interconnection of sources and loads in DC microgrid and their power utilization is primarily limited by the power conversion interfacing system. It is pertinent to note that the integration of MLPS with the DC microgrid is extremely critical to ensure the proper operation and performance of the system. The integration is a major challenge because the individual low-voltage PV panels within the MLPS configuration must be interfaced with the high-voltage DC microgrid. Consequently, there is a heightened need for interfacing converters (module-level interfacing converters and multi-input module interfacing converters), with the capability to achieve higher voltage gain while maintaining high efficiency. These converters must exhibit their ability to integrate each PV panel safely and seamlessly with the DC microgrid. Also, achieving the optimal power generation during the integration is another challenge and requires the development of power generation control algorithms which can deliver superior performance during different operating conditions. For the typical master-slave configuration of the DC

microgrid, the module-level interfacing converters (MLIC) and multi-input module interfacing converters (MMIC) are required to operate as slaves.

1.5. Power Electronics

Power electronics is a rapidly developing interdisciplinary field that is playing a pivotal role in different applications of Electrical Engineering. In the present scenario, it has become indispensable and finds widespread utility in diverse applications like motor drives, RES, microgrids, electric vehicles, switched-mode power supplies, and many more. The evolution of power electronics is also correlated with advancements in other domains such as magnetics, semiconductor technologies, and control [32]. The extensive improvements in the fabrication technology and materials have remarkably enhanced the performance of semiconductor devices while also making them more cost-effective, thereby improving the affordability and performance of power electronics. Currently, power electronics is transitioning towards high-frequency operation to reduce the overall size of systems [33]. However, major bottlenecks are the performance of magnetics, increased switching losses, and thermal designs. The prevailing trend in power electronics is focused on the high power density of converters, efficient power conversion, superior reliability, and utilization of wide-bandgap devices viz, Gallium Nitride and Silicon Carbide devices, which are notably superior to the Silicon devices [34].

1.5.1. Power Electronics for the Interfacing Converters

DC/DC converter is a class of power electronic converter which is widely popular and used in different applications. The interfacing converter utilizes different topologies of DC/DC converters for integrating various sources and loads in the DC microgrid and

facilitates efficient power conversion. For the integration of string PV system with the DC microgrid, conventional DC/DC converter topology like boost converter is widely utilized as the interfacing converter. The conventional boost converter has a simple structure with moderate voltage gain capability, which is sufficient for a string PV system [35]. However, the conventional boost converter fails to operate at high voltage gain which becomes essential during the integration of MLPS with DC microgrid, and experiences dramatic degradation of its efficiency with severe recovery losses in diodes at higher operating duty cycles.

The power electronics play a vital role in ensuring the seamless integration of MLPS with the DC microgrid. Extensive research has been conducted on the family of high-gain DC/DC converter topologies to cater to the demand for high voltage gain [36]-[38]. The high-gain DC/DC converters exhibit large voltage gain capability while ensuring highly efficient power conversion. These converters should have smaller input current ripple, low EMI issues and circulating currents, higher power density, and fast dynamics. It is pertinent to note that the current-fed topologies of high-gain DC/DC converters are well suited for MLPS applications due to their natural boosting capability which allows higher voltage gain, smaller input current ripple, and inherent short circuit protection [39]-[40]. Consequently, the single-input current-fed high gain converter topologies are ideal for module-level interfacing converters (MLIC) while their multi-input topologies are tailor-made for multi-input module interfacing converters (MMIC). Both MLIC and MMIC facilitate the smooth integration of MLPS with the DC microgrid.

1.6. Scope of Work

Considering the rising popularity of solar energy and the increased focus on its incorporation into the existing power system, it is necessary to extensively investigate the integration of module-level PV systems with the DC microgrid. The scope of research work is presented below:

- Investigate the string PV system and module level PV system (MLPS) to evaluate the merits of the MLPS and its feasibility for different applications. Moreover, the suitability of MLPS as the front-end section of DC microgrid for different applications needs to be comprehensively studied.
- Study on high gain current-fed DC/DC converters with single input topologies for module-level interfacing converter and multi-input topologies for multi-input module interfacing converter.
- Mathematical modeling and operating modes of high gain current-fed DC/DC converters.
- Steady-state analysis and designing of the converters.
- Investigate the simulated performance of the converters and further validate their performance experimentally.
- Study different power generation control algorithms and evaluate their performance for various operating conditions.
- Study the system integration of MLPS with the DC microgrid and further investigate the performance of the entire system under different operating conditions on MATLAB simulated environment and experimental hardware setup.

1.7. Organization of Thesis

The thesis is organized into different chapters to meet the research objectives. The outline and overview of each chapter are as follows:

- **Chapter 2:** The chapter presents a comprehensive literature review about the photovoltaic (PV) system and its challenges, and different methodologies adopted for the interfacing between the PV system and DC microgrid. The overview of string PV and module-level PV system and their comparative study are also discussed in this chapter. The chapter further presents an exhaustive survey of different topologies of power electronic DC/DC converters for module-level interfacing converter (MLIC) and multi-input module interfacing converter (MMIC). Moreover, various power generation control algorithms viz, maximum power point tracking (MPPT), global maximum power point tracking (GMPPT), and flexible power point tracking (FPPT) and their performance under different operating conditions are also discussed. The research gaps are then elucidated, followed by formulating the research objectives.
- **Chapter 3:** The chapter investigates the topology of a front-end current-fed high gain isolated interfacing converter. The modeling, steady-state analysis, design methodology, and loss distribution of the converter are presented in this chapter. Different state-of-the-art power electronic converter topologies are comparatively studied for analyzing the suitability of the proposed converter for the module-level interfacing converter. The simulated performance of the converter is analyzed using MATLAB simulation environment and further validated experimentally by developing the hardware prototype.

- **Chapter 4:** In this chapter, improvements, and modifications in the current-fed high-gain converter topology introduced in chapter 3 are investigated. The salient feature of the modified converter is discussed in the chapter. The modeling and steady-state analysis of the modified converter topology are presented. The chapter highlights and quantifies the improvements in the performance of the modified converter. The MATLAB Simulink environment is used for evaluating the simulated performance of the modified converter topology while experimental performance is also investigated using the hardware prototype.
- **Chapter 5:** This chapter studies the multi-input topological configuration of the current-fed high gain converter described in Chapter 3 and investigates its candidacy for a multi-input module interfacing converter (MMIC). The operating topological modes of the proposed converter and its steady-state analysis are presented in the chapter. The chapter evaluates the performance of the converter using a MATLAB simulation environment.
- **Chapter 6:** The chapter studies the system integration of a module-level PV system (MLPS) with the DC microgrid and analyses its performance under various operating conditions. The system architectures of MLPS utilizing different proposed topologies of interfacing converters from the previous chapters for integration with the DC microgrid are investigated. Several applications of MLPS are explored in the chapter. The concept and challenges of dynamic shading are discussed, and various power generation control algorithms are studied to enhance the system's performance. The performance of different system architectures is evaluated using MATLAB simulation environment under various

source perturbations and other operating conditions. The efficacy of the system and its salient features like modularity, robustness, plug-and-play operation, etc, are evaluated from the simulated results. Furthermore, the experimental performance of the system under diverse source perturbations is analyzed in the chapter. The effectiveness of the proposed interfacing converter for integrating MLPS with the DC microgrid is also investigated from the results.

- **Chapter 7:** In this chapter, thesis research work and its contribution, challenges, opportunities, and the future direction of work are summarized.

CHAPTER 2

LITERATURE SURVEY

2.1. General

The rapid degeneration of fossil fuel reserves and increasing CO₂ emission has motivated the transition to a cleaner energy solution. Photovoltaic (PV) generation has gained widespread popularity due to its sustainability, abundant energy reserves, low capital investment, ease of installation and maintenance, and proximity to the load centers. However, the wider adaptation of PV systems is creating pressure on the existing grid infrastructure, thereby encouraging the deployment of microgrids to effectively meet the energy demands of the local loads. The PV generation is highly intermittent due to its source-side disturbances and requires power generation control to ensure optimal power generation. Additionally, the integration of PV system with microgrid is a critical challenge and require suitable interfacing converters. In this chapter, the discussion on performance issues in PV systems, a review of different power generation control algorithms, a study on different PV systems, a brief on the DC microgrid architecture, and an insight view on different state-of-the-art DC/DC converter topologies for the interfacing converter is presented to formulate and pinpoint the research objectives.

2.2. Performance Issues in the PV System

The performance of PV panels is dependent on the prevailing operating conditions, with variations in the power generation experienced due to the changes in the conditions. It is reported that the PV panel is degraded when its power capacity drops below 80% of its rated power and major factors influencing the panel deterioration are temperature, humidity,

insolation, and mechanical shock [41]. The intermittency is a major limitation of the PV system and is responsible for the fluctuations in the power, significantly impacting the overall system performance [42]. The source side disturbances along with the environmental conditions particularly play a prime role in introducing intermittency in the generation of power by the PV system [43].

Throughout the day, fluctuations in solar radiation due to the shift in the position of the sun are observed, resulting in a significantly variable insolation profile [44]. The insolation profile is greatly dependent on several factors like weather patterns, seasonal changes, duration of the day, azimuth angle, and geographical locations [45]. The PV panel harnesses the solar radiation primarily originating from the direct sunlight along with the contribution from the diffused sunlight, which is caused by the scattering of light from sky, ground, or objects. The power generation from the PV panel is contingent on the amount of solar radiation received by the panel, with higher insolation increasing its power generation output [46]. Furthermore, the PV panel current has a direct correlation with the insolation conditions as lower insolation results in a smaller PV current.

Shading is another major contributor to intermittency in PV panels and significantly impacts their performance [47]-[49]. During the shading condition, some cells of the PV panel get shaded and cannot produce current while the non-shaded cells continue to generate current. This forces the shaded cells to dissipate power and operate as load and create hot spots, thereby severely degrading the performance and health of PV panel [50]. The hot spots on the PV panels are mitigated by installing the bypass diodes in parallel with the section of the PV panel and completely bypassing the shaded cells [51]. This prevents the degradation of the PV panel and enhances its life but at the cost of reduced power

generation and voltage output from the PV panel, inducing severe voltage and power fluctuations in the PV system. The shading is further categorized into two types: partial shading and sub-panel shading. During partial shading conditions, the insolation profile is non-uniform and various PV panels experience different insolation [52]-[54]. This is a common occurrence during cloudy conditions where few PV panels are partially shaded while others continue to receive more insolation. In the string PV system with series connected PV panels experiencing partial shading, the occurrence of multiple local power peaks is observed leading to sub-optimal power generation. The sub-panel shading condition is characterized by localized shading on a section of PV panel [55]. Dynamic sub-panel shading is another type of shading introduced due to the installation of PV panels on moving locomotives, posing a unique challenge with the panels experiencing fast shading variations [56]-[57].

The performance of PV panels is also impacted by the accumulation of dust and soiling of panels as the conversion efficiency of the panels degrades [58]. The accumulation of a thick layer of dust on the surface of the PV panel blocks the solar insolation from reaching the PV cells, further reducing the amount of solar radiation captured by the panel. Several factors viz, wind velocity, rainfall, dust particles, humidity, and regional topography affect dust accumulation [59]. Furthermore, the problem of dust accumulation is more severe in desert areas where the density of dust is higher and rainfall precipitation is lower. The power generation of a PV panel is severely affected without regular cleaning with a reported 50% drop in the power generation [60]. The accumulation of dust for 45 days experiences a reduction in the glass transmittance by 20% [61]. Furthermore, the soiling is caused by dust accumulation in humid environments [62]. The capillary bridges are formed between dust

particles and the surface of PV panels due to the vapor condensation, which generates large meniscus force and aids dust buildup. Soiling is also one of the factors responsible for the shading of panels. Moreover, the geographical locations also influence the loss of power generation in the PV panels.

The temperature is another vital factor impacting the power generation of PV panels [63]-[64]. The temperature increase degrades the conversion efficiency and power output of PV panels due to the strong relationship between the bandgap energy of PV cells and temperature, with greater temperature typically reducing the band-gap energy. Moreover, a slight increase in the PV panel current is observed leading to a drop in its open circuit voltage and further decreasing the fill factor of the PV cell [65]-[66]. According to the studies, the operating temperature of the silicon cell affects its conversion efficiency with a drop in cell efficiency by 3.13% for the operating cell temperature of 56°C at an insolation of 1000W/m² and even further by 69% at 64°C [67]-[68].

The mismatch in the operating characteristics of PV panels during manufacturing creates hotspots in the panels and impacts the overall PV system performance [69]. The PV system is also sensitive to leakage currents which can accelerate the corrosion process in the supporting metallic structures as well as other metallic infrastructure near the PV installation [70]. These consequences are far more adverse in the floating PV applications and severely affect the operating performance of the entire system [71]. Frequent outages due to recurring faults in the PV panel and the interfacing converter significantly impact the electricity generation and drastically increase the maintenance expenses.

2.3. Review of Algorithms for Power Generation Control

The power generation control is necessary for facilitating maximum power / constant power generation from the PV panels during the source side disturbances and different operating conditions. The insolation variations and shading conditions primarily contribute to the source side disturbances and need to be monitored due to their substantially faster dynamics in comparison to the temperature variations. Different types of power generation control and their performance under different operating conditions are reviewed in the following sub-sections.

2.3.1. Maximum Power Point Tracking Algorithms

The maximum power point tracking algorithms facilitate the evacuation of maximum power from the PV panels under different operating conditions viz, insolation variations and shading conditions. The fractional open circuit voltage and fractional short-circuit current algorithms are primitive MPPT techniques offering simple and cost-effective approach but suffers from poor tracking performance with their inability to sustain the maximum power point (MPP) operation [72]-[73]. The perturb & observe (P&O) / hill climbing algorithm is one of the widely popular MPPT techniques due to its simple and computationally inexpensive implementation on low-cost controllers [74]-[75]. However, there is a trade-off between the tracking speed and accuracy of the algorithm due to its dependence on the perturbation step size, with larger step size enables faster convergence of the algorithm but increases the steady-state power oscillations and power loss. The variable step-size P&O algorithm improvises the classical P&O algorithm by utilizing the adaptive step size [76]. The LCASF MPPT algorithm employs the adaptive step size of 4% to improve the tracking accuracy to 91% from 88% observed for the conventional P&O

[77]. The incremental conductance (InC) MPPT algorithm is also extensively adopted technique due to its simple and computationally inexpensive implementation on low-cost controllers [78]-[79]. Additionally, it demonstrates more robust operation with improved tracking speed and accuracy in comparison to the P&O algorithm.

The shading on PV panels in the string PV configuration observes multiple power peaks in the P-V curve and highlights the inability of the conventional MPPT algorithms to detect and track the global maximum power point (GMPP) while getting stuck on the local maximum power point (LMPP), thereby experiencing power loss [80]. To improve the performance of PV systems during shading, the global maximum power point tracking (GMPPT) algorithms have been widely investigated [81]-[82]. The earlier GMPPT techniques focussed on the scanning of the entire P-V curve regularly to detect the global peak and subsequently upon detection, facilitate the operation at GMPP with the evacuation of the global maximum power using conventional MPPT techniques [83]-[84]. However, these algorithms experience unreasonably higher utilization of the resources from the controller during normal operation due to continuous scanning. Also, the slower scanning of these algorithms fails to detect GMPPT during fast shading variations and dynamic shading, causing higher power loss. Intelligent MPPT algorithms are also actively being researched because of their robust implementation and improved performance during different operating conditions. The neuro-fuzzy algorithm incorporates a hybridized technique for improving the tracking performance, but the major bottleneck for its implementation is higher computation complexity and a greater degree of dependency on fuzzy logic control efficiency on the optimal selection of the membership function [85]. The hybrid ANFIS technique improves the tracking speed and accuracy while increasing

the complexity, thereby inhibiting its implementation on low-cost controllers [86]. The artificial neural network-based MPPT algorithms do not need comprehensive system information and mathematical modeling and are capable of handling complex problems using different parameters and learning processes [87]. Yet, the realization of ANN-based MPPT techniques is expensive and requires sophisticated controllers. Sliding mode controller-based MPPT algorithm on the other hand has two operating modes, i.e., approaching mode and sliding mode, and achieves independence to the type and the size of PV configuration [88]. Moreover, the technique is robust and achieves faster tracking of MPP with lower power ripple but with significant control complexity and implementation cost. During the fast-shading variations and dynamic shading conditions, the performance of intelligent MPPT algorithms are impacted considerably. The metaheuristic approach to MPPT algorithms using soft computing techniques for optimally searching the GMPP is comprehensively being investigated. Several metaheuristic MPPT algorithms are reported in the literature utilizing techniques like the artificial bee colony, particle swarm optimization, differential algorithm, cuckoo search, gray wolf optimization, and Jaya algorithm [89]-[94]. Fundamentally, these algorithms require the complete scanning of the P-V curve before converging to the GMPP. Conversely, metaheuristic methods with a notably slower response due to the random search process limit their suitability for dynamic shading conditions [95]. Hybrid MPPT techniques combining the metaheuristic and conventional algorithms improve the tracking performance of MPPT with faster tracking speed [96]-[97]. Nevertheless, they are still comparatively slower than the conventional MPPT algorithms, thereby reducing their operational performance under dynamic shading conditions and further discouraging their use for the distributed MPPT controllers. Recently, there has been a strong focus on fast GMPPT techniques to address the issue of

fast shading changes in string PV systems [98]-[101]. These algorithms swiftly detect the GMPP during rapid changes in the shading but are computationally expensive and require memory and computation-intensive controllers. Furthermore, these techniques are only suitable for string PV systems employing individual MPPT controllers for each PV string and where the accurate detection of GMPP is critical to maximum power generation during partial shading conditions.

2.3.2. Flexible Power Point Tracking Algorithms

The adverse impacts of higher PV penetration in the existing grid system viz, grid overloading are compelling the researchers to adopt the constant power generation (CPG) from the PV panels [102]. The utilization of an energy storage system (ESS) is a capital and space-intensive solution which increases the complexity of the entire system [103]-[104]. Moreover, limited life cycles of batteries with poor energy density, sensitivity to the temperature, and higher safety constraints necessitate frequent maintenance, thereby impacting their operational performance. The control-based constant power generation techniques are gaining popularity due to no requirement of additional storage systems, further minimizing the frequent upkeep of the system and overall expenses. The research on CPG and FPPT techniques is relatively in the nascent stages and is comprehensively being investigated [105]-[106]. The advanced FPPT algorithms can detect the available MPP and calculate the available power reserve [107]-[109]. Moreover, they are typically suitable for large capacity of grid-connected centralized PV plants where the accuracy of power generation control and constant power generation is critical. However, for comparatively smaller capacity PV systems, the conventional FPPT algorithms offer cost-effective and simpler implementation with no need for MPP detection. The fundamental

operating principle of flexible power generation is discussed in the literature where the algorithm seamlessly tracks the power setpoints by accurately predicting the voltage references corresponding to the power setpoints and estimating the available maximum power point (MPP) [110]-[111]. This enables the operation of the PV panel below its MPP and ensures constant power generation. The FPPT algorithm achieves CPG operation in the PV system by utilizing different parametric controls like closed loop power control, PV current control, and conventional MPPT techniques-based control [112]-[113]. The research on flexible power point tracking (FPPT) algorithm employs the PI controller and P&O method for tracking the PV voltage, thus curtailing the power generation in the PV system [114]. The comparative study of different FPPT algorithms reported in the literature underlines the efficacy of P&O-based FPPT techniques in achieving superior robustness with lower computational complexity [115]. The major challenge for the P&O-based FPPT methods is the trade-off between mitigating the steady state power oscillations and fast tracking speed and requires the appropriate selection of the step size. The research on the adaptive FPPT algorithm highlights its superior robustness and improved transient performance [116]. However, the algorithm is prone to overshoots with large power oscillations around the set point and needs further parametric tuning. The FPPT algorithm discussed in the research articles offers a cost-effective and intuitive solution where the algorithm selects the operating mode i.e., MPPT mode or CPG mode based on the conditions [117]. The binary search-based FPPT algorithm proposed in the literature utilizes non-linear search [118]. Furthermore, as compared to linear search-based algorithms like P&O, it performs logarithmic search on the sorted data and achieves minimal steady-state oscillations, thereby reducing power loss. The major downside is the notable increase in memory requirement for the controller, necessitating a more advanced

and costly controller. Also, it requires parametric tuning and a separate algorithm for determining and setting the search boundary. The secant method-based FPPT algorithm achieves a faster settling time in comparison to the P&O-based FPPT algorithms and tracks the set power reference accurately with minimal power oscillations [119]. The algorithm further does not need any parametric tuning. However, it requires the calculation of initial parameters and boundary conditions for search. The Newton method-based FPPT algorithm demonstrates faster convergence than the secant-based FPPT algorithm with minimal power oscillation and further eliminates the requirement of initial parametrization and needs a single search parameter instead of the entire search boundary [120]. Nevertheless, there is a need for parametric tuning with a major challenge in the calculation of the slope. Recently, there also has been an increased research focus on the global FPPT algorithms under partial shading conditions for string PV systems [121]-[123]. The impact of the FPPT algorithm in minimizing the requirement of an energy storage system for a standalone DC microgrid is deeply studied in the literature [124]-[125]. Additionally, the paper highlights the ability of the FPPT algorithm to prolong the life of the battery storage system by seamlessly supporting it in mitigating the intermittency of the PV system. The FPPT algorithms have been developed primarily for centralized and string PV systems but the contribution for decentralized architectures like module-level PV systems has been very limited and requires extensive study. The significantly smaller power capacity of MLPS with independent distributed controllers necessitates the power generation control such as MPPT and FPPT algorithms to be cost-effective and computationally less expensive with low memory requirements.

2.4. Configurations of PV System

The PV system is an integral part of the modern power system with continuous research on newer technologies being conducted to improve its performance. The major research on PV systems is focused on improving the PV panel efficiency, configurations of PV systems, interfacing converters, and power generation control. As the improvements in conversion efficiency of PV panel is highly dependent on materials, the current research trend is optimizing the generated PV power under different operating conditions, thereby necessitating the investigation of different configurations of the PV system. The PV system is broadly classified into three configurations, viz, string PV system (SPS), module level PV system (MLPS), and sub-module level PV system (SMLPS) [126]-[128].

The string PV system incorporates multiple PV strings where each PV string consists of a series connected PV panels [129]. The higher terminal voltage of the PV string alleviates the voltage gain requirement from the string interfacing converters while integrating with the microgrids, but substantially increases the converter power rating due to aggregation of power from all panels. The string interfacing converters are sub-categorized into full power converters and partial power converters. The full power converters process the entire generated power from the PV string and employ conventional boost-derived and buck-boost-derived power electronic converters [130]-[131]. Partial power converters are an emerging technology offering improvements in power conversion efficiency while integrating PV string with the microgrid and further reducing the converter size, losses, and ratings considerably in comparison to full power converters [132]-[133]. These converters utilize a fraction of power to stabilize the source voltage. However, the operational performance of partial power converters is poor during the shading conditions.

The module-level PV system incorporates multiple PV panels where each low voltage PV panel is directly interfaced with the DC microgrid using a module-level interfacing converter (MLIC) / multi-input module interfacing converter (MMIC) and utilizes distributed power MPPT controller [134]-[135]. Furthermore, module-level interfacing converters require boost-derived high-gain converters for facilitating seamless PV integration with the microgrid [136].

The sub-module level PV system enhances the tolerance to the shading conditions by directly interfacing each submodule of the panel with the microgrid and avoiding using the bypass diode, thereby demonstrating superior power utilization from the panel under different operating conditions [137]. However, this approach has a major limitation of significantly increasing the component count, complexity, and overall cost of the entire system.

Traditionally, the SPS and MLPS have been widely adopted in AC microgrids using string inverters and microinverters respectively. Since both these PV systems are natively DC in nature, they can be seamlessly integrated with the DC microgrid. The fundamental concept of string inverters and microinverters can be easily extended to the string converters and MLIC / MMIC. The comparative study of both SPS and MLPS is reported in the literature and further highlights the merits of MLPS [138]-[141]. The MLPS achieves better power utilization per panel due to its greater control over the power generation owing to the independent distributed MPPT controller, thereby enabling optimized power generation from each panel [140]-[141]. It compensates for up to 2.5% mismatches in the PV panels and presents newer and decoupled orientations of panels, allowing architectural flexibility [142]. Moreover, MLPS also demonstrates higher tolerance to the shading conditions [143]-

[144]. SPS exhibits poor tolerance to the shading conditions as it can only control the power generation from the entire string and not from each PV panel [145]. Furthermore, during shading conditions, the string experiences multiple power peaks which increases the power loss in the SPS. The distributed MPPT controller in MLPS utilizes conventional MPPT algorithms with lower computation and simpler implementation for tracking the MPP while SPS requires global MPPT algorithms with increased complexity and higher computational requirements to track the GMPP [146]-[148]. It is reported in the literature that under fast-changing shading conditions, parallel connected PV systems should be utilized instead of the string PV system, highlighting the suitability and efficacy of MLPS to seamlessly operate under fast shading conditions [149]. In case of a fault in the PV panel or converter, the MLPS can bypass them and ensure continuous operation, though at reduced capacity, thus demonstrating the redundancy of PV panels / interfacing converters and increased fault tolerance [150]. This is not viable in the SPS where the fault in a single PV panel or converter will render the entire string inoperable and create a severe loss of electricity generation. Safety of the system during the installation or maintenance is enhanced in MLPS where each converter can isolate the connected PV panel from the microgrid and ensure proper procedure. The superior scalability of the architecture of MLPS, higher robustness, and flexible operation are other merits of the MLPS [151]-[152]. Furthermore, the MLPS requires power electronic converters with substantially lower power ratings as compared to the SPS, thereby considerably reducing the size of the converters and overall system.

It is pertinent to note that the salient features of MLPS with its superior performance and numerous merits over SPS highlight its viability as the front-end section of PV-based DC microgrid.

2.5. DC Microgrid

The proliferation of RES, energy storage systems, and various electronic loads have driven the requirement for DC microgrids. The research on DC microgrids has attracted significant interest among researchers owing to their numerous advantages in comparison to the AC microgrids [153]-[154]. The major benefit of DC microgrid is the reduction in the number of conversion stages (AC/DC and DC/AC) due to the integration of DC sources and DC loads, which makes the power conversion highly efficient with greater reliability, robustness, and resiliency [155]-[157]. Moreover, it circumvents the problems of harmonics, synchronization issues, reactive power flow, skin effect in wires, and unbalances [158]-[159].

Different architectures are discussed in the literature for establishing the DC microgrid [160]. The single bus topology is the simplest and integrates all sources and loads on the single bus [161]-[163]. Moreover, it is characterized by low capital investment and maintenance requirements. The single bus architecture is further sub-categorized into unipolar and bipolar configurations. The unipolar bus configuration requires two poles (+VDC, GND) on which all sources and loads are interfaced [164]. Moreover, the bipolar configuration is more complex with the requirement of three poles (+VDC, GND, -VDC), where sources and loads have the flexibility to connect to different poles [165]. The bipolar configuration presents greater reliability, higher count of voltage levels, improved power supply quality, and superior efficiency. However, it suffers from the problem of voltage

imbalance between the bipolar terminals, which becomes more severe during the connection of different loads or generators at a terminal. The multi-bus architectures viz, radial, ring, mesh, and interconnected are reported in the literature [166]-[169]. Different voltage levels and standards of the DC microgrid are reported, with 380V DC being an industry standard for DC microgrid [160],[170]. The decentralized master-slave configuration is reported for the microgrids incorporating distributed generation sources (DGs) and loads operating in the grid-connected and islanded mode where under islanded operation, master DGs operate as a voltage source with voltage mode control while slave DGs operate as a current source with current mode control [171]. The concept of master-slave configuration is further extended to hybrid AC and DC microgrids [172]-[173].

The major challenges associated with DC microgrids are the higher installation cost, increased complexity, lower maturity in technology, involved expenses in retrofitting the existing AC infrastructure for DC microgrids, lack of standardization, and primitive and expensive protection system [174]. The DC microgrid offers a diverse range of applications such as commercial and residential infrastructure, RES parks, electrification in remote and rural areas, industrial applications like integration of motor drives on common DC links, data centers, telecommunication systems, electric vehicle charging infrastructure, ship, and train networks [175]-[183].

The photovoltaic (PV) based DC microgrids are gaining widespread attention and increased research focus owing to the sustainable and clean energy generation and the utilization of PV systems as a core source of generation [184]. The challenges pertaining to the control and stability while integrating the PV system with DC microgrids are discussed in the literature [185]. The operation and performance of PV-based DC microgrid utilizing

the cascaded PV modules during partial shading conditions and the connection/disconnection of modules are studied and reported in the literature [186]. The performance of PV-integrated DC microgrids for rural electrification is investigated with a detailed analysis of the power flow, system losses, and efficiency [187]. Further research on rural electrification using PV-based microgrids is presented in [188]. The energy management strategy for the PV-based DC community grid is discussed in the article [189]. The residential DC microgrid with a PV system as the primary generation source is an emerging technology with an eco-friendly implementation and sustainable solution for energy requirement benefitting the community, but the major impediments to its full-scale adoption are higher overall cost, maintenance requirements, and poor reliability [190]. The power electronic interfacing converters have a major impact on the operational performance of the PV system integrated with the DC microgrid, significantly affecting the efficiency, reliability, robustness, and cost-effectiveness of the entire system. Future research on PV technologies like thin films, and bifacial PV systems will further enhance the operability and adoption of the residential DC nanogrids / microgrids.

The critical aspect of the DC microgrid is the interfacing converter which is required to integrate sources and loads seamlessly and facilitate optimal power flow with higher conversion efficiency and greater reliability. Furthermore, the deployment of MLPS in the PV-based DC microgrid is a major challenge due to the need for direct integration of low-voltage PV panels with the DC microgrid, thereby increasing the importance of power electronic converters required for the interfacing converters. It is vital to properly select the converter topology as its operational characteristics dramatically impact the overall performance of the MLPS and PV-based DC microgrid.

2.6. Interfacing Converters for MLPS

The recent advances and major breakthroughs in power electronic technologies have made the interfacing converters for MLPS a viable solution. The interfacing converters for MLPS have a primary requirement of large voltage gain for seamless integration of low-voltage PV panels directly with the DC microgrid with high efficiency. The interfacing converters for MLPS employ different topologies of DC/DC power electronic converters. The selection of the converter topology should be based on the high voltage gain capability, minimal topological bottleneck to the performance of power generation controllers, superior power conversion efficiency, low ripple component in input current drawn from the PV panels, wide operating range for the input variations, and high modularity, scalability, and operational flexibility in the topological structure [191]. Based on the number of input ports in the converter topological structure and the count of PV panels simultaneously integrated with the DC microgrid using a single converter unit, the interfacing converters for MLPS are further categorized into module-level interfacing converter (MLIC) and multi-input module interfacing converter (MMIC) having a single input port and multiple input ports respectively. Moreover, both MLIC and MMIC should demonstrate the voltage step-up capabilities owing to the substantially lower input voltage when compared to the output voltage.

The conventional boost converter is a popular DC/DC converter topology with a wider range of applications owing to its simpler architecture and design with a smaller component count. However, the major limitation of a conventional boost converter (CBC) is its inability to operate at higher duty cycles with severe diode recovery losses and power losses in switches, thereby demonstrating drastic efficiency degradation at higher voltage gain

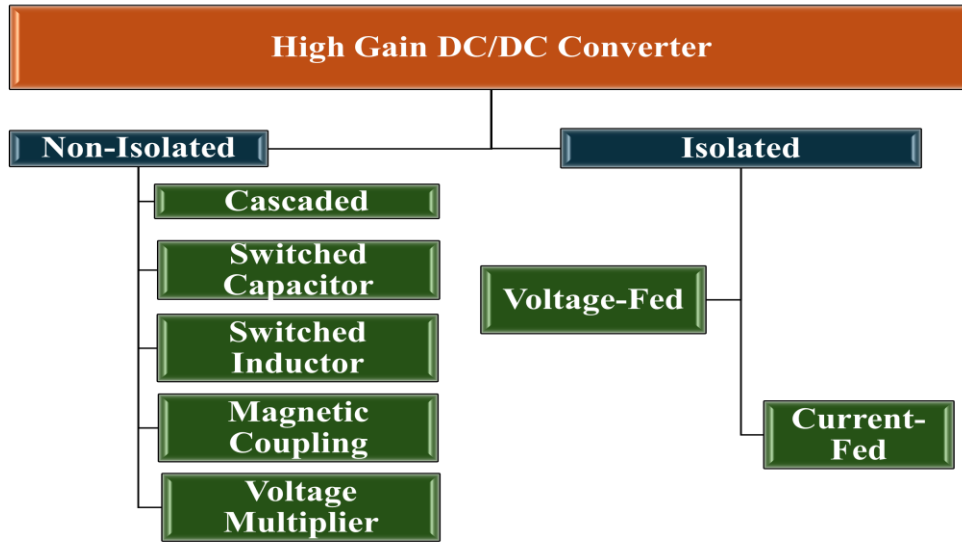


Fig.2.1. Overview of high gain DC-DC converter topologies

[192]. The drawbacks of CBC motivated the researcher to investigate the family of high-gain converters which exhibit seamless operation at higher voltage gain without sacrificing the converter efficiency [193]-[195]. The overview of high gain DC-DC converter topologies is shown in Fig.2.1. Different topologies of high-gain DC/DC converters are investigated for module-level interfacing converter (MLIC) and subsequently for multi-input module interfacing converter (MMIC).

2.6.1. Survey of Topologies for MLIC

The non-isolated topologies of high gain converters are extensively used in industries for a wide range of applications and offer cost-effective and simple architecture with lower design constraints and higher power density and efficiency [196]-[197]. For enhancing the voltage gain capability of the non-isolated topologies, they utilize different techniques viz, magnetics, cascading of converters, switched capacitors, switched inductors, and voltage multiplier. The coupled inductor-based non-isolated converter topologies reported in the

literature offer improvement in the voltage gain capability with the reduction in the input current ripple depending on the winding orientation and further reduce the printed circuit board (PCB) size with the reduced count of magnetic components [198]-[199]. However, the major drawback of such converters is significantly higher voltage spike on switches and the requirement of additional passive and active clamping circuits. The cascaded converter studied in the papers improves the voltage gain by increasing the number of cascading converter stages [200]. The cascaded boost topology utilizes two cascaded boost stages for increasing the boosting range and exhibits lower stress on components of the first stage [201]. However, the second stage experiences significantly higher stress with greater switching losses and as a result must operate at a lower switching frequency, thereby compromising on the power density. The quadratic boost converter achieves higher gain but loses independent control over each stage [202]. Furthermore, the efficiency of cascaded converters typically degrades dramatically with the increase in the number of cascaded stages. The switched capacitor (SC) is a popular voltage-boosting technique utilizing capacitive power transfer and achieves significantly higher power density and structural modularity [203]. Different types of switched capacitor techniques such as Dickson SC, Makowski SC, and Fibonacci SC, and their merits are studied in the literature [204]-[206]. The major challenge with the switched capacitor-based high gain converters is the higher current spikes which can damage the devices and require additional circuits which has a detrimental effect on the overall efficiency and power density of the converter. Meanwhile, improving the voltage gain capability of the converter utilizing switched inductors is reported in the literature [207]-[208]. However, such converters suffer from higher input current ripple and require larger value of input capacitor, while compromising on the power density. The voltage multiplier techniques are widely embraced and being employed in

various high gain converters due to their simpler structure and design, low device count, and seamless integration with the existing converter topologies [209]-[211]. The voltage multiplier technique utilized in the non-isolated high gain converter demonstrates a lower switch rating and zero current switching of the power switch while alleviating the reverse recovery problem in diodes [212]. The high gain capability of the proposed converter is enhanced by using a capacitor-diode voltage multiplier cell which exhibits reduced switching losses in the MOSFETs using zero voltage switching operation while further mitigating the stress on the devices and reverse recovery losses in diodes [213].

However, the non-isolated topologies have limited suitability for MLIC during the integration of the PV panel with the DC microgrid, and the isolated high gain converter topologies are dominantly used owing to the cancellation of leakage currents and better safety [190]. Moreover, the safety standards require galvanic isolation between the input and output of the converter for the grid-connected / microgrid applications and sensitive loads viz, military, medical, and avionics, and further utilizes the high-frequency transformer to achieve reliable power transfer with lower noise and EMI issues [193]. The isolated high-gain converters are further segmented into voltage-fed and current-fed converters with their merits and challenges discussed in the literature [214]-[215]. The voltage-fed converters have inherent buck-derived characteristics and rely on the turns ratio of high frequency (HF) transformer to furnish higher voltage gain. The flyback-forward derived voltage fed isolated converter utilizes an HF transformer for galvanic isolation and demonstrates soft switching of devices to mitigate the switching losses [216]. However, such converters are suitable for low-power applications with the requirement of the auxiliary circuit for mitigating voltage spikes in the devices and suffers from higher input

current ripple. Whereas, flyback topology utilizing an active leakage recovery network operating on leakage energy getting transferred to the output while reducing the conduction losses without any auxiliary switching network and further achieving soft switching of devices [217]. However, such converters are inherently prone to magnetic core saturation with moderate gain capability and high input current ripple and is suitable for sub-100W applications. The voltage-fed push-pull derived topologies are popular and widely employed in different applications [218]-[219]. The push-pull DC/DC converter mitigates the switching loss in devices using zero voltage switching operation and reduces the voltage spike in switches by recycling the leakage energy [220]. However, the converter suffers from larger input current ripple with the susceptibility to magnetic core saturation due to flux walking and further requires an additional active clamp circuit. The isolated high step-up converter utilizing push-pull topology is presented in the literature and achieves enhanced efficiency over a wide range of input and output while ensuring the ZVS operation of primary switches and ZCS operation of secondary diodes [221]. The major limitation of the converter is the larger input current ripple and the sensitivity to flux walking. Moreover, the utilization of bidirectional switches in the resonant tank requires expensive devices which significantly inflates the overall converter cost. The bridge-derived voltage-fed converters reported in the literature utilize a large turns ratio of HF transformer for furnishing high voltage gain but suffer from higher stress on the transformer and further use high side switches with complex gate drive design. Several topological variations of the bridge-derived converter with soft switching and active clamping are reported [222]-[226]. The bridge-derived voltage-fed converters have bidirectional power transfer capability and are typically employed for battery applications [227]-[228]. However, such converters are not suitable for MLIC due to the requirement of unidirectional power transfer and further

TABLE 2.1: State-of-the-art Isolated Current-Fed Converter Topologies		
Converter Reference	Topological Structure	Efficiency
Passive Snubber based Isolated Current Fed Converter		
[237]		92%
[240]		
[242]		93%
Active Clamping based Isolated Current Fed Converter		
[244]		88.5%
[245]		93.7%

[246]		
[247]		94.5%
[250]		96%
[251]		93.2%
[252]		90%
[253]		96.6%

[257]		94.52%
[258]		95.3%
[260]		97.8%
[263]		94%
[266]		90%
[268]		97.29%

Snubberless / Natural Voltage Clamping Isolated Current Fed Converter		
[277]		92.9%
[278]		93%
[280]		95.8%
[282]		94%
[283]		97.2%
*All the converter topological figures have been taken from the references cited alongside		

experience substantially higher conduction losses due to increased circulating currents when operated in parallel. The increased demand for power-dense and highly efficient solutions has focussed the research on the resonant converters with LLC converter being one of the most popular and extensively adopted in different domains of power electronic industries [229]. The different configurations of LLC converter are presented in the literature [230]-[233]. The LLC converter mitigates the switching loss, maintains higher efficiency near full load conditions, and experiences low EMI noise. Nonetheless, it has complex and involved converter design which impacts its performance and needs careful consideration in designing and selecting components of the resonant tank for achieving optimized performance. Furthermore, the converter demonstrates poor performance when the source and load perturbs to lower power as its gain also reduces, making it ineffective for PV applications. Further, the utilization of frequency modulation makes the power flow control complex. It is pertinent to observe that voltage-fed converters have inherent limitations of high input current ripple and are not suitable for MLIC.

The current-fed isolated converter is a promising research topic and is extensively being investigated [234]. The current-fed converters are inherently boost-derived topologies with natural voltage boosting capability which alleviates the burden of voltage gain from the HF transformer and further reduces its turns ratio [235]. Moreover, these converters have natural short-circuit protection. However, the major limitation of the current-fed converters is the large turn-off voltage spike on switches which necessitates the requirement of snubbers to mitigate the spike. Different current-fed isolated converter topologies along with their efficiencies have been tabulated in Table 2.1.

A. Passive Snubbers

Early research on the current-fed converter topologies employed passive dissipative snubbers to alleviate the turn-off voltage spike in switches [236]-[238]. The conventional RCD snubber having a combination of resistor, capacitor, and diode is a type of passive snubber used in the converter [239]-[240]. The snubber mitigates the voltage spike in switches by storing the leakage energy in the capacitor and further dissipating it into the resistor but with a notable increase in the snubber losses and degradation of the overall efficiency. The lossless snubbers viz, LC snubber and flyback snubber improve the efficiency by transferring the leakage energy to the input or output but increase the design complexity and PCB size [241]-[243]. Typically, the passive snubber has limited applicability for current-fed converters as it is a lossy and inefficient solution and compromises the efficiency, power density, and modularity of the converter.

B. Active Clamping Techniques

The active clamping technique is extensively utilized in current-fed converters due to their efficacy in clamping the switch voltage and achieving soft switching operation, thereby enhancing the efficiency [244]-[246]. Different current-fed topologies utilizing active clamp circuits are investigated. Several current-fed isolated boost-derived topologies are presented in the literature with higher gain capabilities [247]-[250]. The isolated boost converter has continuous input current with improvement in the voltage gain but the operation at higher gain is impacted by the asymmetric transformer currents and requires a small air gap to negate the core saturation while further introducing losses and efficiency degradation [251]. The isolated boost converter topology utilizing a buck-based active

clamp circuit is proposed which suppresses the voltage spike in switches due to leakage inductance of the HF transformer and recycles the energy back to the input [252]. However, the converter demonstrates moderate voltage gain and requires a higher number of passive and active components for realizing the buck-based clamp circuit with increased control complexity. The current-fed push-pull converter topologies are widely being adopted for fuel cell and RES applications, exhibiting high gain capability and low input current ripple [253]-[256]. The current-fed push-pull converter demonstrates high gain capability with low input current ripple and enhances efficiency by mitigating the switching losses using ZVS and ZCS operation for primary switches and secondary diodes respectively [235]. Conversely, the converter incorporates all high side switches which dramatically increases the complexity of gate drive design and further increases the EMI issues. To improve the range of ZVS operation in the current-fed push-pull converter, a parallel inductor is integrated with the transformer [257]. The major challenge in this converter is higher turn-off losses and increased count of complex isolated gate drives with greater sensitivity to the noise coupling due to all high side switches. The modified topology of the current-fed push-pull converter achieves full ZVS turn-off of secondary side switches and has short-circuit protection at the output [258]. Moreover, the converter eliminates the voltage spike on the switches by integrating clamping diodes with the resonant capacitors. However, the topological structure is highly complex with the addition of bidirectional switches and witnesses increased component count, involved converter design, gate drive complexity, and highly sophisticated control. Also, the voltage stress on the auxiliary switches is significantly higher. The above-mentioned topologies [253-258] are prone to introducing the DC bias in the HF transformer during asymmetric converter operation and suffer from magnetic core saturation, thereby potentially damaging the converter and severely

impacting the converter performance. This problem is mitigated in the modified current-fed push-pull topology by using a DC blocking capacitor in series with the primary winding of the HF transformer but sacrifices the voltage gain of the converter with higher circuit complexity [259]. The concept of the current-fed push-pull converter is extended to three-phase and four-phase topologies as reported in the literature [260]-[262]. This converter demonstrates higher power capacity with low input current ripple, increased voltage gain capability, and enhanced converter efficiency owing to the soft-switching operation. Nonetheless, the component count increases significantly with the higher number of high-side switches and complex gate drive circuits. The utilization of these topologies is suitable for high-power applications and their deployment for MLIC is highly expensive and not a viable solution for MLPS. The bridge-derived current-fed topologies exhibiting the ability to furnish high voltage gain are reported in the literature [263]-[266]. The current-fed bridge converters utilizing dual active bridge configuration facilitate bidirectional power flow, making them apposite for battery and EV applications [267]-[271]. However, higher device count with complex gate drive design and increased circulating currents while paralleling these converters leads to higher losses and reduced efficiency, making them unsuitable for MLIC. The current-fed half bridge achieves high efficiency with the ZCS operation of switches and mitigates the voltage spikes [272]. However, the operation at higher gain with wide input variations in high current applications demands larger voltage gain which increases the stress on the magnetics and switches. Furthermore, the resonant operation of the current-fed half-bridge converter utilizing the LC tank achieves the ZVS operation of switches and ZCS operation of diodes with the alleviation of the reverse recovery problem [273]. The key drawbacks of the converter that limit its utilization for MLIC are higher peak currents in the switches, increased losses in the auxiliary devices, and the narrow region of

operating voltage. The modified current-fed full-bridge converter with integration of the impedance source network eliminates the problem of start-up and voltage spike in the switches and incorporates integrated magnetics to reduce the board size [274]. The narrow operating region of the converter during boost operation and the higher risk of instability near the forbidden region impact its voltage gain capability and limit its suitability for MLIC. It is pertinent to observe that different converters utilizing active clamping techniques typically require high-side switches with complicated gate drive designs, and complex control strategies and observe a reduction in the voltage gain capability of converters.

C. Auxiliary Circuits

The auxiliary circuit-based technique is utilized as an alternative to the active clamping technique with its operation based on assisting the zero current commutation of semiconductor devices and alleviating the circulating currents. However, the major drawbacks of auxiliary circuits are the higher structural complexity and the increased component count. The current-fed topologies utilizing auxiliary-based circuits observe improvement in the boosting capabilities as compared to traditional clamping circuits but incur a substantial increase in the losses in the auxiliary circuits [275]-[276].

D. Snubberless / Natural Voltage Clamping Techniques

The snubberless and natural voltage clamping techniques for current-fed converters are gaining popularity and are extensively being investigated as they eliminate the requirement of snubber and clamping circuits. The snubberless techniques utilize modulation and resonant techniques for mitigating the voltage spike in switches. The current-fed topologies

achieving snubberless operation by employing a secondary-side modulation scheme are reported in the literature [277]-[280]. These topologies use secondary side modulation to clamp the switch voltage and prevent the voltage overshoot, thereby allowing natural voltage clamping and eliminating the requirement for additional snubber or clamp circuits. However, due to the secondary side active switches in the converter, the parallel operation of the converters increases the circulating currents, leading to an increase in conduction losses and efficiency degradation. Furthermore, the bidirectional power flow capability of such a converter is redundant for the PV system which needs unidirectional power flow. The above-mentioned problems discourage the utilization of these topologies for MLIC. The current-fed isolated boost topology achieves snubberless operation with reduced input current ripple, smaller rating of diodes and switches, and smaller turns ratio of HF transformer [281]. The primary limitation of the converter is its complex structure with the requirement of two HF transformers along with their separate voltage doubler rectifiers, thereby significantly increasing the count of passive and magnetic components. The resonant commutation technique applied on different current-fed topologies allows snubberless operation of the current-fed converters while achieving improved converter performance and higher efficiency with ZCS operation [282]-[284]. However, the utilization of variable frequency modulation increases the control complexity and necessitates the requirement of sophisticated controllers, posing a challenge in implementation for distributed power generation controllers, thereby discouraging their utilization for MLIC. Additionally, the topology discussed in [282] employing the impulse commutation technique suffers from high peak currents in the switches and resonant tank during the light loads due to higher circulating currents.

2.6.2. Survey of Topologies for MMIC

The increased PV penetration in the distribution system will see a huge surge in the demand for MLICs for integrating the PV panels with the DC microgrid and ultimately require substantially higher power conversion units and component count. This problem motivated extensive research on multi-input module interfacing converters (MMIC) for integrating PV modules with DC microgrids. The utilization of multi-input DC/DC converters is particularly suitable for PV applications where the energy storage system is needed to curb the PV intermittency and maintain the continuous power supply at the DC microgrid [285]-[286]. The multi-input converters offer several advantages compared to the single-input converters viz, reduction in the number of conversion units and component count, lower overall cost, smaller size, and higher power capacity and better power density due to the integration of multiple sources [287]-[288]. The ability of multi-input converters to integrate multiple PV panels while demonstrating higher modularity and operational flexibility further highlights the suitability of these converter topologies for MMIC.

Different topologies of multi-input DC/DC converters have been reported in the literature, with non-isolated topologies garnering notable attention due to their superior efficiency, higher power density, low cost, and compact design [289]-[297]. However, a major limitation in non-isolated topologies is the lack of galvanic isolation which increases the safety risk. Furthermore, similar to the MLICs, the multi-input converter topologies for MMIC are required to have galvanic isolation to ensure safe and reliable operation while integrating PV panels directly with the DC microgrid, thereby requiring isolated multi-input topologies. Several voltage-fed (VF) and current-fed (CF) isolated multi-input converter topologies have been investigated. Different topologies of the voltage-fed (VF) converter

are reported in the literature [298]-[300]. The voltage-fed topology integrates two sources with each module having an HF transformer whereas the three-leg converter is present at the secondary side [301]. The converter has lower intermodular circulating currents with a compact design. However, it exhibits a larger input current ripple with the need for a larger input filter capacitor, and the increased number of high-side switches with a greater number of isolated gate drivers and power supplies, thereby dramatically increasing the circuit complexity. The extension of the voltage-fed topology for telecom applications is given in the literature [302]. Another proposed topology incorporating different sources utilizes a dual-charge pump to furnish high voltage gain and recycle the leakage energy [303]. Moreover, the converter continues to operate even if one of the sources is interrupted and has a reduced component count. But the maximum duty cycle of the converter is 0.5 with the requirement of higher diode count, larger input current ripple, and the degradation of the voltage gain capability of the converter due to its leakage inductance, thereby limiting its applicability for MMIC. The utilization of a multi-input LLC converter for integrating PV panels exhibits enhanced efficiency by achieving ZVS operation for all switches over the entire range of source voltage with the voltage stress on switches not exceeding the input voltage [304]. The converter can continue to operate even if one of the PV panels fails. However, the converter has high side switches with demand for complex gate drive and does not have input inductors to smoothen out input current ripple and thus rely on the large input capacitors. Additionally, the inherent drawback of the converter is the need for phase shift modulation to balance the input power before the load regulation using frequency shift modulation. Also, MPPT operation is not guaranteed as the control solely relies on the input power.

The current-fed multi-input converter topologies are more suitable for MMIC as they inherently exhibit higher gain while utilizing input inductors to alleviate input current ripple and have natural short-circuit protection. The current-fed multi-input topology utilizing dual inputs for integrating low-voltage DC sources with the DC bus is presented in the literature [305]-[307]. The input inductors of the converter operate in discontinuous conduction mode (DCM) to avoid the saturation of the HF transformer even when different source voltages are applied. The converter achieves high efficiency by soft-switching operation using secondary side modulation [308]. However, the utilization of active switches on the secondary side increases the circulating currents during the paralleling of converters, which inflates the conduction losses and degrades its performance. Furthermore, the high turn-off voltage spike in the primary switches is observed which also degrades the converter performance. The DCM operation of input inductors increases the ripple current of the inductor where the higher peak current increases the stress on the inductors and requires a higher value of input capacitor. Also, the inability of the converter to operate during the failure of any source is observed. The extension of the current-fed topology utilizing an active voltage doubler on the secondary side is proposed in the literature [309]. The topology incorporates a DC blocking capacitor to mitigate the transformer saturation while the converter has a lower input current ripple with reduced input filter requirement. However, the bidirectional capability of the converter with secondary side active switches limits its application in MMIC. The multi-input converter reported in the literature exhibits a simple structure, soft-switching operation, and higher voltage gain [310]. However, the converter observes higher stress on the main switches and utilizes a complex control scheme for achieving load regulation. Additionally, during the interruption of a source, the converter operation is deeply impacted. The current fed dual-input microinverter topology

reported in the literature can be further extended for DC/DC conversion but secondary-side active devices limit its utility for MMIC [311]. The isolated dual-input SEPIC converter with a common active clamping leg for mitigating the additional switching losses and voltage stress on input legs is demonstrated [312]. However, the utilization of complex bidirectional switches with complicated gate drive designs increases the topological complexity and cost of the converter, thereby making it unsuitable for MMIC. The current-fed dual input topology achieves soft switching operation with highly efficient operation [313]. The major limitation of the converter is higher intermodular circulating currents, lack of decoupled operation, utilization of additional clamp circuit, and higher current stress on devices and components.

2.7. Identified Research Gaps

Based on the literature survey conducted in the previous sections, several research gaps have been identified, which are discussed below:

- The literature survey in the previous section discusses the increasing penetration of PV systems and the utilization of string PV systems (SPS) traditionally as the front-end section of the DC microgrid for evacuating the generated power and feeding it to the DC microgrid under different environmental conditions. To overcome the limitations of SPS, new configurations of the PV system have been studied. The module-level PV system (MLPS) studied in the literature offers major benefits and advantages compared to the SPS, highlighting its suitability for integration with the DC microgrid. However, further research is required to

understand the operational viability of MLPS when subjected to diverse conditions.

- The SPS is typically deployed in popular applications viz, off-grid / remote EV charging infrastructure, floating PV system, and transportation. Considering the merits of MLPS, its utilization, and adoptability in such applications need further investigation.
- It is observed from the literature that integration plays a critical role in the module-level PV system and necessitates MLIC which utilizes the DC/DC converter topologies with high gain capability. The major operational challenges in conventional boost converters propelled extensive research on the family of high-gain converters. The isolated topologies of high-gain converters are imperative as galvanic isolation is necessary while integrating low-voltage PV panels with high-voltage DC microgrids. The voltage-fed topologies of isolated DC/DC converters have limited application in MLIC due to their fundamental drawbacks of high input current ripple and larger turns ratio of HF transformer. Based on the observations from the literature review, it can be concluded that the current-fed topologies of isolated DC/DC converters are suitable for MLIC as the front-end interfacing converter due to their lower input current ripple, inherent boosting characteristics, and natural short-circuit protection. Moreover, several reported topologies of the current-fed isolated converter highlight the critical problem of high turn-off voltage spike in the switches and require different techniques to alleviate it. However, utilization of these techniques introduces additional issues in the converters which further need to be addressed. As a result, comprehensive

research is required to formulate suitable current-fed topologies of isolated converters.

- The isolated multi-input converters have gained widespread attention and are extensively documented in the literature for their capability of integrating a variety of DC sources such as batteries, fuel cells, and PV panels while minimizing the number of converter units and component count. It is pertinent to note that the PV panel and fuel cell are unidirectional power sources and require interfacing converters with unidirectional capability. Based on the findings of the literature review, it can be inferred that the current-fed topologies of multi-input isolated converters are suitable for MMIC. Furthermore, in addition to the intrinsic limitations of the current-fed topologies, these converters also face significant challenges like intermodular circulating currents, operational interference between the modules, the inability of the converter to operate during interruption of a source, the bottleneck in the power delivery, and the efficiency degradation at higher operating voltage gain. Comprehensive research is required for multi-input isolated current-fed topologies for MMIC alleviating the above-mentioned problems and seamlessly integrating two or more such PV panels with the DC microgrid.
- The increasing penetration of PV systems in the grid and their challenges are broadly discussed in the literature and are the driving force behind the recent trend of operating PV panels as a constant power source. The requirement of a flexible power point tracking (FPPT) algorithm arises due to the inability of the conventional MPPT algorithm to enable constant power generation from the PV panels. The FPPT algorithm facilitates both maximum power evacuation as well

as constant power generation from the PV panels. The operation and comparative performance of different FPPT algorithms are exhaustively investigated and reported in the literature. However, the implementations of these algorithms are primarily focused on the conventional string PV system, with the requirement of sophisticated and expensive controllers. Moreover, very limited literature is available on the implementation of FPPT algorithms for MLPS. As a result, extensive research is required on the implementation, operational performance, and viability of FPPT algorithms for MLPS.

- The shading of PV panels has been a significant challenge for the conventional string PV system and requires global MPPT algorithms for evacuating the maximum generated power from the panels. This problem becomes more severe during dynamic sub-panel shading of PV panels, which is prominent in applications where the panels are installed on the rooftops of moving locomotives such as trains and buses. The dynamic sub-panel shading of PV panels on moving locomotives experiences fast variations in the shading on panels and presents unique challenges which are relatively understudied. The slower scanning of GMPPT algorithms fails to detect such fast variations in the shade on panels and significantly impairs the overall performance with severe power fluctuations. The faster GMPPT algorithms documented in the literature improve the dynamic performance but require significantly complex implementation. The dynamic sub-panel shading of PV panels in MLPS achieves better performance than SPS owing to its superior power utilization from each PV panel but is still not satisfactory due to the failure of conventional MPPT algorithms to respond quickly during fast-shading changes with slow convergence and poor tracking accuracy, thus

diminishing the power generation. Additionally, the implementation of fast GMPPT techniques on the distributed controllers for MLPS offers diminishing returns while requiring resource-intensive controllers which is overkill and extremely expensive. Consequently, comprehensive research is required on the fast MPPT control algorithms having simpler implementation and faster convergence with superior tracking accuracy to cater to the fast-shading changes on PV panels during dynamic sub-panel shading.

2.8. Research Objectives

Based on the research gaps identified in the above section, the research objectives for the thesis are formulated below:

- Investigation of module-level PV system and its applications for the DC microgrid
- Study of flexible power point tracking control algorithm for module-level PV system under uniform insolation changes and its implementation on a low-cost controller.
- Study of fast-MPPT algorithm for module-level PV system under dynamic sub-panel shading on PV panels.
- Investigation of different interfacing converters for MLPS i.e., module-level interfacing converter (MLIC) and multi-input module interfacing converter (MMIC) for seamless integration of the low voltage PV panel with DC microgrid under different operating conditions.
- Analysis, design, simulation, and development of the interfacing converters for MLPS.

CHAPTER 3

FRONT-END CURRENT-FED HIGH-GAIN ISOLATED INTERFACING CONVERTER

3.1. General

The merits of current-fed isolated DC/DC converters and their viability in integrating the low-voltage PV panels with the DC microgrid have been established in the literature. In this chapter, a new current-fed isolated DC/DC converter topology is proposed. The topological modes of operation of the converter with its mathematical modeling, steady-state analysis, design, and loss distribution are also discussed in the chapter. Moreover, the comparative study of different state-of-the-art converter topologies to investigate the suitability of the proposed topology for module-level interfacing converter is also presented. The simulated performance of a 500W converter with 30V input and 380V output is extensively analyzed using the MATLAB Simulink environment. Furthermore, a scaled-down 125W hardware prototype of the proposed converter with 17V input and 170V output is developed and tested in the laboratory for experimentally validating the converter performance. The chapter is organized as follows: Section 3.2 discusses the proposed converter topology while section 3.3 presents the different topological operating modes of the converter. The mathematical modeling of the converter is presented in section 3.4 elucidating its static voltage gain and the mathematical expression for each operating mode. Section 3.5 provides the steady-state analysis of the converter while the design of the converter is explained in section 3.6. The theoretical loss distribution of the converter and

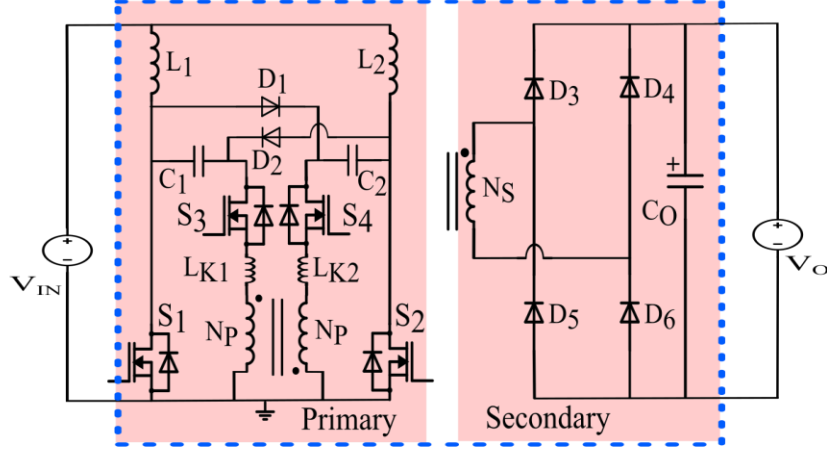


Fig.3.1. Topological structure of CF-HGIIC

the comparative study of different state-of-the-art topologies are discussed in sections 3.7 and 3.8 respectively, followed by the results and discussions of the converter performance in section 3.9.

3.2. Proposed Converter Topology

The topological structure of the proposed front-end current-fed high gain isolated interfacing converter (CF-HGIIC) is shown in Fig.3.1. The converter operates in the continuous conduction mode with its operating duty cycle ($d \geq 0.5$). The converter incorporates dual input inductors (L_1 , L_2) which facilitates continuous input current. Additionally, the primary side of the converter also has the coupling capacitors (C_1 , C_2), coupling diodes (D_1 , D_2), and four switches ($S_1 - S_4$). The full-bridge diode rectifier ($D_3 - D_6$) and the output capacitor (C_O) are present on the secondary side of the converter. The interlinking between the primary and secondary side of the converter is facilitated using a high frequency (HF) transformer having the leakage inductance (L_{K1} , L_{K2}) and magnetizing inductance (L_M) and utilizing the low turns ratio (1:1: n). The proposed converter integrates

a DC source at the input and feeds the power to the active load (DC sink). The notations of different converter parameters are provided in Table 3.1.

The proposed converter achieves enhanced voltage gain with a low turns ratio of the HF transformer. It also exhibits a unique distributed structure with parallel conduction paths, which help in minimizing the current stress and conduction losses in the input inductors, switches, coupling diodes and capacitors, and HF transformer. Moreover, the interleaved operation at the input of the converter significantly mitigates the input current ripple, easing the design constraints of the input filter and dramatically reducing its size. It also inherently mitigates the leakage current propagation at the output and the inter-converter circulating currents when multiple such units are operated in parallel. The converter demonstrates higher tolerance to the DC bias in the HF transformer during the asymmetric operation which prevents the saturation of the magnetic core, thereby improving the performance.

TABLE 3.1: Parametric notations of CF-HGIC		
Parameters	Voltage	Current
Input	V_{IN}	I_{IN}
Output	V_O	I_O
Input Inductor (L_1, L_2)	V_{L1}, V_{L2}	I_{L1}, I_{L2}
Coupling Capacitor (C_1, C_2)	V_{C1}, V_{C2}	I_{C1}, I_{C2}
Switches ($S_1 - S_4$)	Drain to Source: $V_{DS1} - V_{DS4}$	$I_{S1} - I_{S4}$
	Gate to Source: $V_{GS1} - V_{GS4}$	
Coupling Diodes (D_1, D_2)	Reverse Biased: V_{D1}, V_{D2}	I_{D1}, I_{D2}
	Forward Drop: V_{DF1}, V_{DF2}	
Rectifier Diodes ($D_3 - D_6$)	Reverse Biased: $V_{D3} - V_{D6}$	$I_{D3} - I_{D6}$
	Forward Drop: $V_{DF3} - V_{DF6}$	
<u>HF Transformer</u>		
Primary Winding	V_P	I_{LK1}, I_{LK2}
Secondary Winding	V_{SEC}	I_{SEC}
Magnetizing Inductance	V_{LM}	I_M

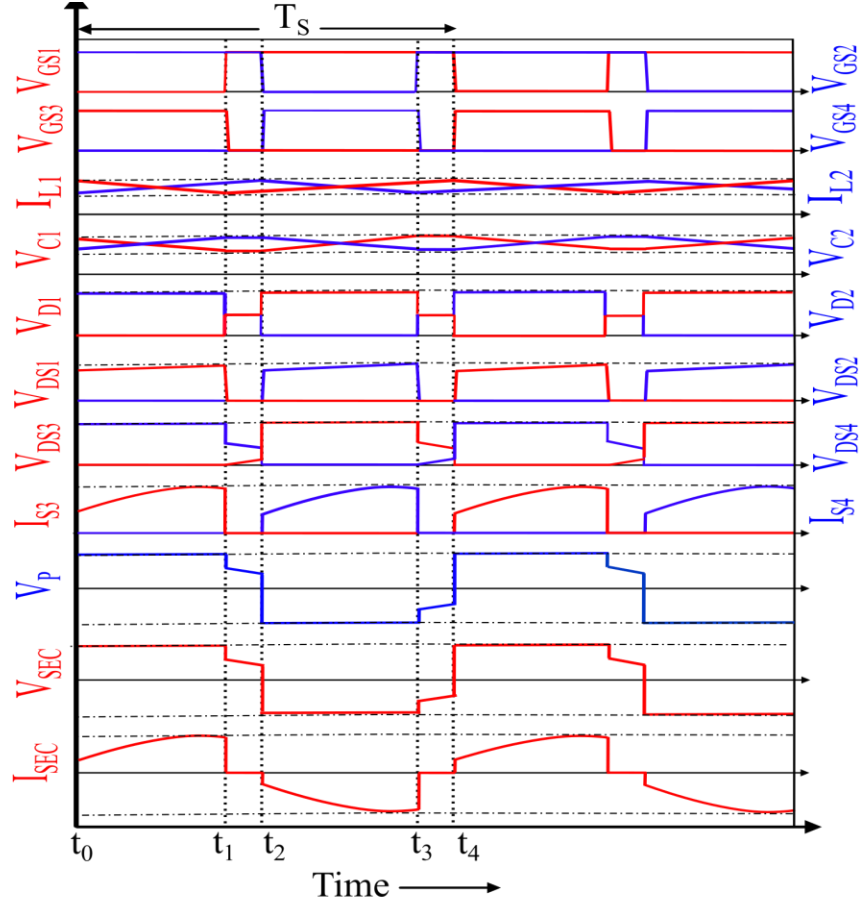
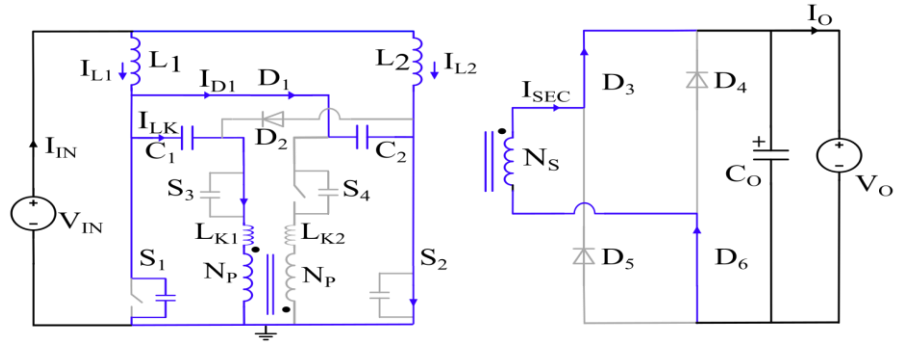


Fig.3.2. Analytical waveform of CF-HGIIC

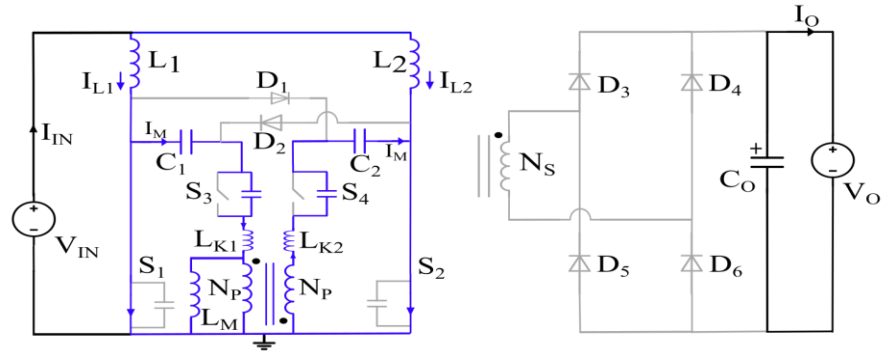
Meanwhile, CF-HGIIC also exhibits natural voltage clamping of switches S_1 and S_2 , thereby eliminating the requirement for an additional snubber or clamp circuit.

3.3. Topological Modes of Operation

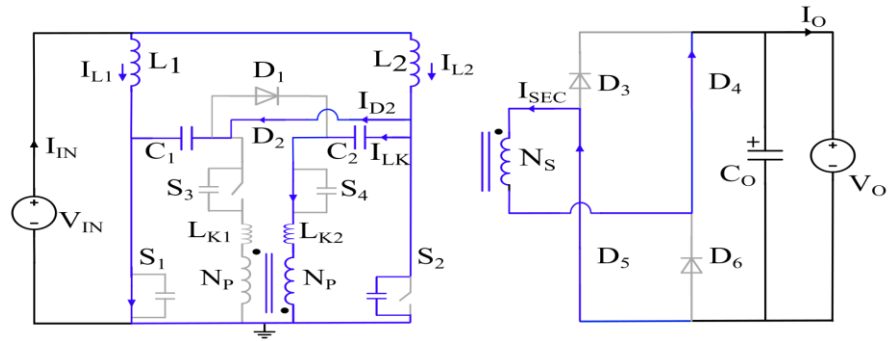
In this section, the topological operating modes of the converter are discussed. Fig.3.2 shows the steady-state analytical waveforms of the proposed converter with their operating duty cycle $d \geq 0.5$. The gating pulses of switches S_1 and S_2 are 180° phase shifted with their on-time greater than 50%. Additionally, the gating pulses of switches S_3 and S_4 are complements of S_1 and S_2 respectively. Various topological modes of the converter for



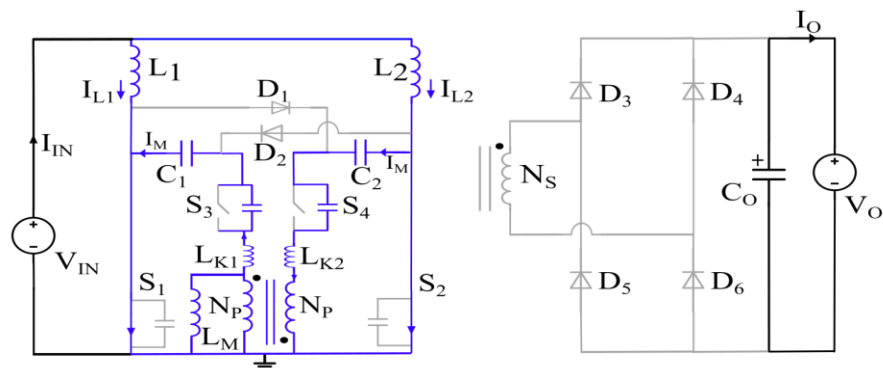
(a)



(b)



(c)



(d)

Fig.3.3. Topological operating modes of proposed converter (a) Mode 1 (b) Mode 2 (c) Mode 3 (d) Mode 4

different operating intervals are discussed below. Moreover, the equivalent circuits of the proposed converter for each operating interval are depicted in Fig.3.3.

3.3.1. Mode 1 ($t_0 - t_1$) : Power Transfer Mode – Fig.3.3(a)

At the beginning of this operating mode at the instant t_0 , switch S_1 turns off while S_2 is still conducting, which allows the inductor L_1 to start discharging while inductor L_2 continues to charge. Additionally, the coupling diode D_1 starts conducting whereas D_2 is still reverse biased. Consequently, the turn-on of switch S_3 at the instant t_0 facilitates the aggregation of the coupling capacitor (C_1, C_2) voltages which reflect across the primary winding of the HF transformer, while also exhibiting quasi-sinusoidal winding currents. Moreover, the power is transferred to the active load through the HF transformer and rectifier diodes D_3 and D_6 till the end of this operating mode.

3.3.2. Mode 2 ($t_1 - t_2$) : Overlapping Mode – Fig.3.3(b)

During this mode which begins at the instant t_1 , the switch S_1 turns on while S_2 is still conducting, which enables inductor L_1 to start charging while inductor L_2 continues to charge and further reverse biases the coupling diode D_1 . Furthermore, there is no power transfer to the active load in this mode as the switch S_3 turns off at the instant t_1 . Also, during this operating mode in the interval ($t_1 - t_2$), the output capacitor C_O feeds the load.

3.3.3. Mode 3 ($t_2 - t_3$) : Power Transfer Mode – Fig.3.3(c)

At the start of this mode at an instant t_2 , switch S_2 turn-off, causing the inductor L_2 to start discharging while inductor L_1 continues to charge. Also, the coupling diode D_2 becomes forward-biased. With the turn-on of switch S_4 at the instant t_2 , the voltage across each coupling capacitor (C_1, C_2) is aggregated and reflected across the primary winding of

the HF transformer, while also exhibiting quasi-sinusoidal winding currents. Moreover, the power is transferred to the active load through the HF transformer and rectifier diodes D_4 and D_5 till the end of this operating mode.

3.3.4. Mode 4 ($t_3 - t_4$) : Overlapping Mode – Fig.3.3(d)

The operation of this mode is principally similar to mode 2. At the start of this mode, the switch S_2 turns on at an instant t_3 while S_1 is still conducting, which enables inductor L_2 to start charging while inductor L_1 continues to charge and further reverse biases the coupling diode D_2 . Furthermore, no power is transferred to the active load in this mode as the switch S_4 turns off at instant t_3 . The output capacitor C_O feeds the load during this mode.

3.4. Mathematical Modeling of Converter

The mathematical modeling of the proposed converter is presented in this section. The converter operates in continuous conduction mode with $d \geq 0.5$. The basic assumptions for simplified converter modeling are outlined below:

- The input inductors are assumed to be sufficiently large to maintain stiff DC currents.
- The circuit components are assumed to be ideal with no PCB parasitic.
- The output voltage is assumed to be constant with a large output capacitor.
- It is assumed that the input inductors ($L_1=L_2=L$), coupling capacitors ($C_1=C_2=C$), and leakage inductances ($L_{K1}=L_{K2}=L_K$) referred to primary are identical.

3.4.1. Static Voltage Gain of Converter

For the viability of the proposed converter as the MLIC, it is required to furnish high voltage gain. The static voltage gain of the converter is analyzed in this subsection. The

operating duty cycle of the converter is d , while its input and output voltages are V_{IN} and V_O respectively. Moreover, the turns ratio of the HF transformer is $1:1:n$ while the operating switching period is T_s . The loop analysis is applied for each operating mode to synthesize the voltage gain.

During mode 2 to mode 4, the voltage across the inductor L_1 (V_{L1}) is calculated in (3.1). Moreover, during mode 1, the voltage across the inductor L_1 and coupling capacitor C_2 (V_{C2}) are computed in (3.2) and (3.3) respectively.

$$V_{L1} = V_{IN} \quad (3.1)$$

$$V_{L1} = V_{IN} - V_{C2} \quad (3.2)$$

$$V_{C2} = \frac{V_O}{2n} \quad (3.3)$$

Consequently, the voltage-second balance is applied to the inductor voltage which yields the expression (3.4). The substitution of (3.3) in (3.4) and further simplification provides the voltage gain expression (m) of the converter in (3.5).

$$(V_{IN} - V_{C2})(1 - d) + (V_{IN})(d) = 0 \quad (3.4)$$

$$m = \frac{V_O}{V_{IN}} = \frac{2n}{1-d} \quad (3.5)$$

The static voltage gain of the converter as a function of the duty cycle is shown in Fig.3.4. The converter exhibits significantly higher voltage gain with a smaller turns ratio of HF transformer, having a gain (m) of 10 for the operating duty cycle (d) of 0.6 and turns ratio (n) of 2. As a result, the higher voltage gain capability of the proposed converter

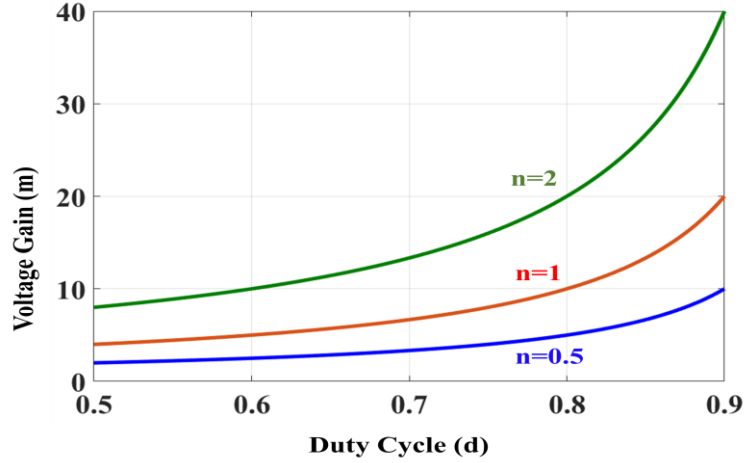


Fig.3.4. Static voltage gain of CF-HGIIC

utilizing a smaller turns ratio of HF transformer without operating at extreme duty cycle emphasizes its candidacy for MLICs.

3.4.2. Steady-State Operational Analysis

For optimal modeling of the proposed converter, the time-domain analysis with the derivation of mathematical equations for each operating mode is required. Moreover, the equations also assist the converter designing and device selection and further aid in understanding the operation of the converter. It is pertinent to note that the mathematical analysis for each operating mode is only discussed for half switching cycle, with the identical operation observed during the other half cycle owing to the circuit symmetry.

The current through the input inductor (3.6) is half of the input current.

$$i_{L1}(t) = i_{L2}(t) = \frac{I_{IN}}{2} \quad (3.6)$$

A. Mode 1:

During mode 1, the mathematical equations of the converter are discussed below:

$$i_{S1}(t) = i_{S4}(t) = i_{D2}(t) = 0 \quad (3.7)$$

$$i_{S3}(t) = i_{LK1}(t) = i_{C1}(t) = i_{C1}(t_0) + \frac{V_{eq}}{Z_0} \sin w_o(t - t_0) \quad (3.8)$$

$$i_{D1}(t) = i_{C2}(t) = i_{C2}(t_0) - \frac{V_{eq}}{Z_0} \sin w_o(t - t_0) \quad (3.9)$$

$$w_o = \frac{1}{\sqrt{0.5 L_K C}}, Z_0 = \sqrt{\frac{2L_K}{C}}, i_{C1}(t_0) = \frac{I_{IN}}{2} - \frac{C \Delta V_C}{(t_1 - t_0)}, i_{C2}(t_0) = \frac{C \Delta V_C}{(t_1 - t_0)} \quad (3.10)$$

$$V_{eq} = 2V_{C1}(t_0) - \frac{V_O}{n} - \Delta V_C, \quad \Delta V_C = (0.25 I_{IN}(1 - d)T_S)/C \quad (3.11)$$

$$i_{S2}(t) = \frac{I_{IN}}{2} + i_{C2}(t_0) - \frac{V_{eq}}{Z_0} \sin w_o(t - t_0) \quad (3.12)$$

$$V_{C1}(t) = \frac{-1}{C} \int_{t_0}^t i_{C1}(t) dt = V_{C1}(t_0) - \frac{i_{C1}(t_0)}{C} (t - t_0) - \frac{V_{eq}}{C w_o Z_0} (1 - \cos w_o(t - t_0)) \quad (3.13)$$

$$V_{C2}(t) = \frac{1}{C} \int_{t_0}^t i_{C2}(t) dt = V_{C2}(t_0) + \frac{i_{C2}(t_0)}{C} (t - t_0) - \frac{V_{eq}}{C w_o Z_0} (1 - \cos w_o(t - t_0)) \quad (3.14)$$

$$i_{SEC}(t) = \frac{i_{LK1}(t)}{n}, V_P = \frac{V_O}{n}, V_{DS1}(t) = V_{C2}(t), V_{DS4}(t) = V_P + V_{C2}(t), V_{SEC} = n V_P \quad (3.15)$$

$$T_{10} = (1 - d) T_S \quad (3.16)$$

B. Mode 2:

During mode 2, the mathematical equations of the converter are underlined below:

$$i_{S1}(t) = \frac{I_{IN}}{2} - I_M, i_{S2}(t) = \frac{I_{IN}}{2} + I_M \quad (3.17)$$

$$i_{D1}(t) = i_{D2}(t) = i_{D3-D6}(t) = 0 \quad (3.18)$$

$$V_{DS3}(t) = \frac{I_M}{C_{DS3}(V_{DS3})} (t - t_1) \quad (3.19)$$

$$V_{LM}(t) = V_P(t) = V_{C1}(t) - V_{DS3}(t), V_{DS4}(t) = V_P(t) + V_{C2}(t) \quad (3.20)$$

$$T_{21} = \frac{\left(\frac{V_O}{n} + V_{C1}(t)\right) C_{S3}(V_{DS3})}{I_M} \quad (3.21)$$

3.5. Steady-State Converter Analysis

In section 3.5, the steady-state analysis of the proposed converter is presented. The steady-state analysis investigates the input current ripple in the converter and the inherent mitigation of the leakage currents at the output of the converter.

3.5.1. Input Current Ripple Analysis

The proposed converter incorporates two-phase interleaving which facilitates a substantial reduction in the input current ripple. The input current of the converter is a cumulative aggregation of the inductor currents. The converter operates at duty cycle $d \geq 0.5$ with the switching frequency f_s , number of interleaved phases ‘P’, and parametric constant ‘k’ where $k < P$. The slope of inductor currents and changes in the input current during mode 1 are calculated in 3.22 and 3.23 respectively.

$$\frac{dI_{L1}}{dt} = \frac{V_{IN} - \frac{V_O}{2n}}{L_1}, \frac{dI_{L2}}{dt} = \frac{V_{IN}}{L_2} \quad (3.22)$$

$$\Delta I_{IN(1)} = \left(\frac{V_{IN} - \frac{V_O}{2n}}{L_1} + \frac{V_{IN}}{L_2} \right) \frac{(1-d)}{f_s} \quad (3.23)$$

Since the operating principles of mode 2 and mode 4 are similar, the slope of inductor currents and changes in the input current computed in 3.24 and 3.25 respectively are identical.

$$\frac{dI_{L1}}{dt} = \frac{V_{IN}}{L_1}, \frac{dI_{L2}}{dt} = \frac{V_{IN}}{L_2} \quad (3.24)$$

$$\Delta I_{IN(2)} = \Delta I_{IN(4)} = \left(\frac{V_{IN}}{L_1} + \frac{V_{IN}}{L_2} \right) \frac{(d-0.5)}{f_s} \quad (3.25)$$

The slope of inductor currents and changes in the input current during mode 3 are calculated in 3.26 and 3.27 respectively.

$$\frac{dI_{L1}}{dt} = \frac{V_{IN}}{L_1}, \frac{dI_{L2}}{dt} = \frac{V_{IN} - \frac{V_O}{2n}}{L_2} \quad (3.26)$$

$$\Delta I_{IN(3)} = \left(\frac{V_{IN}}{L_1} + \frac{V_{IN} - \frac{V_O}{2n}}{L_2} \right) \frac{(1-d)}{f_s} \quad (3.27)$$

Due to the two-phase interleaving (P=2) in the converter, the ripple frequency of the input current ripple is twice the switching frequency as calculated in (3.28), with the changes in the input current for mode 1 and mode 3 and similarly for mode 2 and mode 4 are equivalent ($\Delta I_{IN(1)} = \Delta I_{IN(3)}$), ($\Delta I_{IN(2)} = \Delta I_{IN(4)}$). For inductors $L_1=L_2=L$, the generalized expression of the input current ripple is formulated in (3.29).

$$f_{in,ripple} = P f_s \quad (3.28)$$

$$\Delta I_{IN,ripple} = \frac{P V_O}{2 n L f_s} \left(\frac{k+1}{P} - d \right) \left(d - \frac{k}{P} \right) \quad (3.29)$$

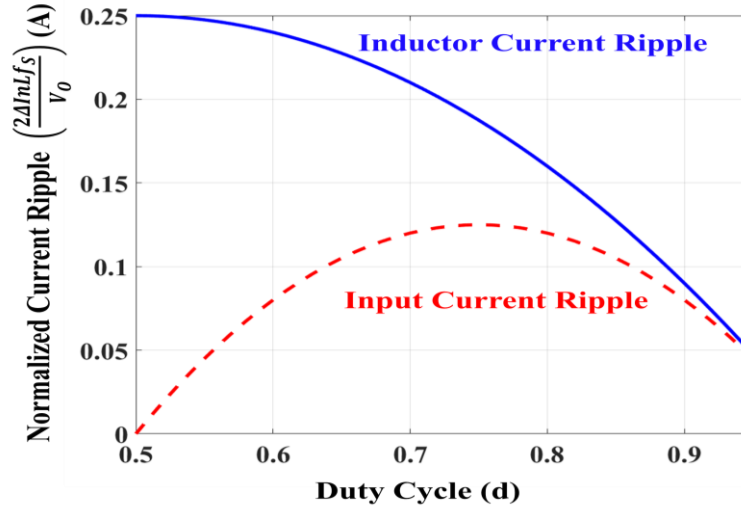


Fig.3.5. Normalized inductor and input current ripple vs duty cycle (d) for CF-HGIIC

It is noted that for a single input inductor, the input current ripple has a parametric value of $P=1$ and $k=0$. Meanwhile, during two-phase interleaving, the parametric values of input current ripple are $P=2$, $k=0$ for $d < 0.5$, and $P=2$, $k=1$ for $d \geq 0.5$. The variation of the normalized input current ripple and inductor current ripple with the duty cycle for the proposed converter is shown in Fig.3.5. It is observed that the input current ripple reduces notably around the duty cycle $d=0.6$, thereby alleviating the design constraint of the input filter with smaller filter size and improving the power density of the converter. Furthermore, the smaller input current ripple minimizes the steady-state power oscillation of the PV panel around the maximum power point (MPP), thereby encouraging the integration of the proposed converter with the PV panel and highlighting its viability as MLIC. Additionally, the smaller current ripple in the input capacitor reduces its losses and further enhances its operational life.

3.5.2. Leakage Current Modeling

In this subsection, the modeling of the leakage currents in the proposed converter generated from the switching circuit and their circulation at the output is investigated. The

leakage currents are critical for the MLICs, particularly during their deployment in the floating PV systems. The leakage model of the converter with their equivalent circuits for different operating modes is illustrated in Fig.3.6, where the input DC source is grounded while the output of the converter is grounded through the parasitic inductance (L_G) and capacitance (C_G). Moreover, the pulsating noise sources are incorporated in the leakage model and are induced by the dV/dt of semiconductor devices during the switching transitions such as drain-to-source voltage transitions ($V_{DS1}-V_{DS4}$) in the switches ($S_1 - S_4$). The leakage current model also includes the coupling capacitors ($C_1=C_2=C$), inter-winding capacitances (C_{SS}), and leakage inductance ($L_{K1}=L_{K2}=L_K$) of the HF transformer, current through the coupling diodes (I_{D1}, I_{D2}), capacitance of diodes ($C_{D1}-C_{D6}$) and switches ($C_{DS1} - C_{DS4}$). Also, the model considers current through the inductors as stiff current sources. The equivalent leakage model of the converter during mode 1 is demonstrated in Fig.3.6(a), with switch S_2 ON while the switches S_1, S_3 , and S_4 witness the switching transitions at the start and end of the mode, thereby generating high-frequency leakage currents. Similarly, Fig.3.6(b) shows the equivalent leakage model of the converter for mode 3 with the switch S_1 ON while the switches $S_2 - S_4$ experience the switching transitions during the starting and end of mode. The voltage transitions in switches during their switching operation generate high-frequency leakage currents. It is pertinent to observe that in both cases (mode 1 and mode 3), the HF transformer offers significantly lower impedance to the leakage currents in comparison to the secondary-side parasitic loop comprising C_{SS} , C_{D5} / C_{D6} , L_G , and C_G . As a result, the major component of the leakage current ($I_{G,ik}$) flows through the HF transformer whereas minimal leakage current ($I_{O,ik}$) circulates at the output of the converter. Furthermore, as the MLICs are required to operate in parallel to ensure optimal performance of MLPS, the inter-converter circulating currents become extremely

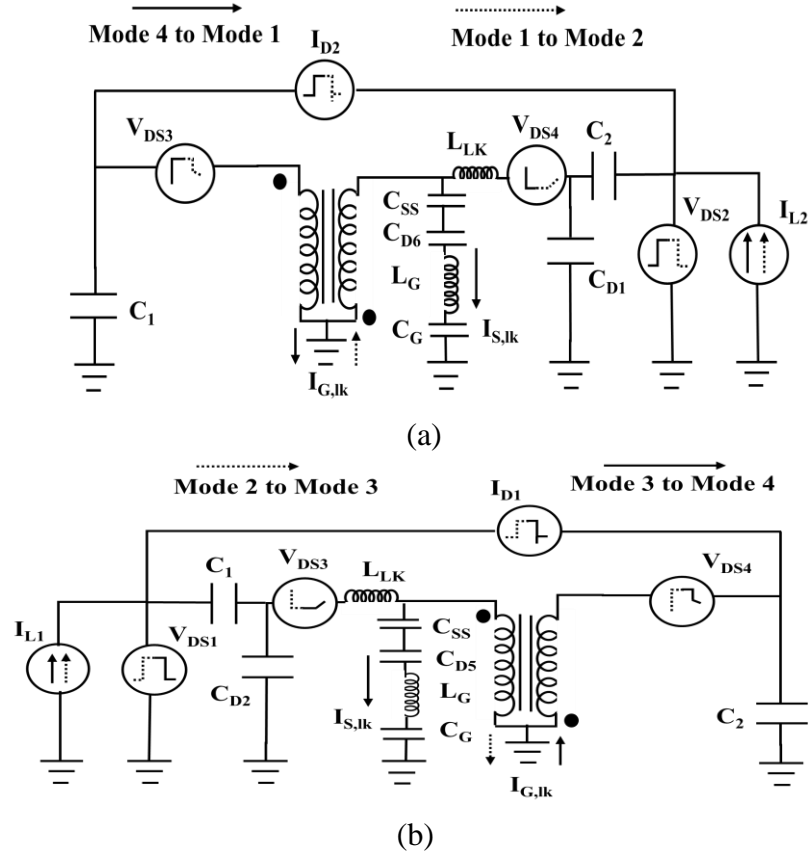


Fig.3.6. Leakage current model of CF-HGIC (a) mode 1 (b) mode 3

critical. It is necessary to mitigate these currents to ensure high performance. The proposed converter offers minimal circulating currents during their paralleling due to the presence of rectifier diodes which block these circulating currents, thereby underlining their suitability for MLIC.

3.5.3. Component Stress

The selection and designing of the suitable components for the converter are primarily dependent on their stress. The stress on different passive components such as inductors, capacitors, and transformer are critical for their optimal design and improvement in the converter performance. The converter employs interleaved operation which allows bifurcation of the input current, thereby alleviating the current stress on the input inductors

(3.30). Moreover, the voltage stress on the coupling and output capacitors shown in (3.31) and (3.32) is essential in deciding their voltage rating, which dictates their optimal selection and impacts other factors like safety, performance, and cost. The unique distributed structure of the proposed converter allows rms current through the primary winding of the HF transformer to be a fraction of the input current as demonstrated from (3.33), thereby significantly alleviating the current stress on the HF transformer and highlighting their merit and suitability for high current application.

$$I_{L1,AVG} = I_{L2,AVG} = \frac{I_{IN}}{2}, I_{L1,RMS} = I_{L2,RMS} = \sqrt{\frac{I_{IN}^2}{4} + \frac{\Delta I_L^2}{12}} \quad (3.30)$$

$$V_{C1} = V_{C2} = \frac{V_O}{2n} \quad (3.31)$$

$$V_{CO} = V_O \quad (3.32)$$

$$I_{LK1,RMS} = I_{LK2,RMS} = \frac{I_{IN}\sqrt{1-d}}{4} \quad (3.33)$$

The voltage and current stress on the coupling and rectifier diodes shown in (3.34) and (3.35) respectively help in selecting the appropriate ratings of the diodes for the converter which further enables improvements in the converter performance.

$$V_{D1} = V_{D2} = \frac{V_O}{n}, I_{D1} = I_{D2} = \frac{I_{IN}(1-d)}{4} \quad (3.34)$$

$$V_{D3-D6} = V_O, I_{D3-D6} = \frac{I_{IN}(1-d)}{4n} \quad (3.35)$$

The voltage and current stress on the switches S_1 / S_2 and S_3 / S_4 are shown in (3.36) and (3.37) respectively. The stress helps in selecting the appropriate device ratings while also assisting in optimized search from a diverse range of MOSFETs.

$$V_{DS1} = V_{DS2} = \frac{V_O}{2n}, \quad I_{S1,RMS} = I_{S2,RMS} = \frac{I_{IN}\sqrt{5-d}}{4} \quad (3.36)$$

$$V_{DS3} = V_{DS4} = \frac{3V_O}{2n}, \quad I_{S3,RMS} = I_{S4,RMS} = \frac{I_{IN}\sqrt{1-d}}{4} \quad (3.37)$$

3.6. Design Considerations of Converter

This section presents the comprehensive design of the proposed converter. The optimized design of the converter is necessary to ensure enhanced converter performance and minimal component stress. Furthermore, the design considerations of different components are discussed below.

3.6.1. Design of Input Inductors

For ensuring seamless power transfer and operation under CCM mode, the design of input inductors becomes vital. The inductor should be designed for the rated specifications while ensuring a smaller current ripple (ΔI_L) under all operating conditions using (3.38). Moreover, during hardware realization of the input inductors, the selection of a magnetic core is critical and requires extensive study of different magnetic properties. The powdered cores are typically used for inductors due to their property of distributed air gap which linearizes the B-H curve and further prevents saturation.

$$L_1 = L_2 = \left(\frac{d V_{IN}}{\Delta I_L f_S} \right) \quad (3.38)$$

3.6.2. Selection of HF Transformer Turns Ratio

The voltage gain of the proposed converter shown in the expression (3.5) is correlated with the turns ratio (n) of the HF transformer and the duty cycle (d) of the converter, with its graphical representation illustrated in Fig.3.7. It is vital to select the turns ratio of HF

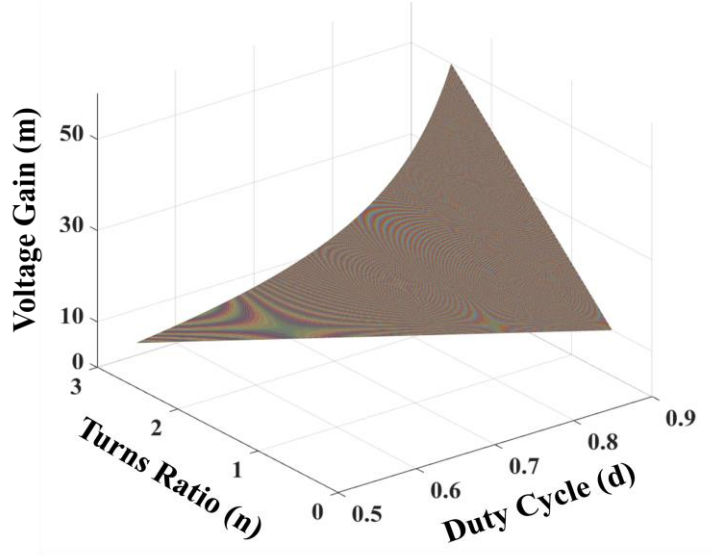


Fig.3.7. 3-D plot of voltage gain (m) vs duty cycle (d) vs turns ratio (n)

transformer appropriately for the desired converter voltage gain and optimized component selection. For calculating the maximum value of n (n_{MAX}), the boundary conditions of the operating converter are a minimum duty cycle (d_{MIN}) of 0.5 and a minimum desired voltage gain (m_{MAX}) of 10, which is $n_{MAX} = 2.5$. As the lower turns ratio of the HF transformer is utilized, the range of the operating duty cycle becomes smaller. Additionally, the voltage stress on the components increases dramatically which further increases their required voltage rating, thereby widening the cost vs performance trade-off while selecting the components. Conversely, a higher turns ratio reduces the voltage stress on components but impacts their current stress. As a result, after careful consideration of the above problem, the turns ratio of the HF transformer is selected as 1:1:2.

3.6.3. Design of Coupling Capacitors

The design of coupling capacitors is critical for the seamless converter operation and furnishing high voltage gain. The optimal selection of coupling capacitors is based on the expression in (3.39), allowing superior performance of the converter under different

operating conditions. The coupling capacitors appear across the switches S_1 and S_2 during mode 1 and mode 3 respectively, thereby enabling natural voltage clamping of the switches (S_1 and S_2). The voltage ripple of the coupling capacitor (ΔV_C) is affected by the input current and the operating duty cycle of the converter, and further impacts the converter performance. Fig.3.8(a) shows the variations in the voltage ripple in different coupling capacitors over a wide range of input currents. It is observed that voltage ripple (ΔV_C) in coupling capacitors varies linearly with the input current and has a smaller ripple at lower currents. The influence of duty cycle variation on the voltage ripple for several values of coupling capacitors is demonstrated in Fig.3.8(b). The voltage ripple for a specific value of coupling capacitor reduces at higher duty cycles, thereby enhancing the operation of the converter at higher voltage gain. Additionally, it is observed from both Fig.3.8 (a) and (b) that for a fixed value of input current and duty cycle, the smaller capacitor exhibits significantly higher voltage ripple. Also, for the wider operating range of input current and duty cycle of the converter, the coupling capacitor with smaller values demonstrates larger variations in their voltage ripples. It is quantified for the value of coupling capacitors ranging between $C=1\mu\text{F}$ and $C=4.7\mu\text{F}$, with $C=1\mu\text{F}$ and $C=4.7\mu\text{F}$ exhibiting voltage ripple variation of 15.22V and 3.24V respectively during the changes in duty cycle and 16.57V and 3.53V respectively during the input current variations. This clearly highlights that choosing smaller capacitors significantly increases the voltage ripple and its variations over the wider operating range of input current and duty cycle and further degrades its operational life and overall converter performance. Consequently, the selection of a coupling capacitor is closely tied to the performance improvements in the converter. The rms current in the coupling capacitor is calculated in (3.40). In the hardware implementation of the converter, the selection of the type of material is essential for the coupling capacitors.

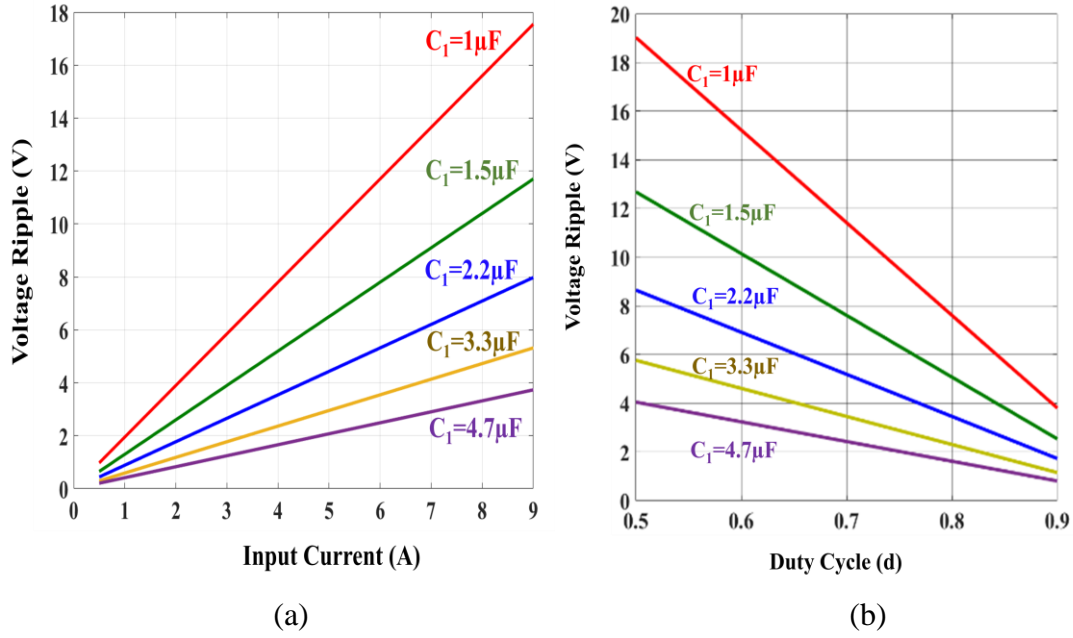


Fig.3.8. Voltage ripple (ΔV_C) of coupling capacitor vs (a) Input current (b) Duty cycle (d)

The coupling capacitors typically utilize film capacitors which offer superior reliability and lower ESR. Furthermore, as diverse materials of film capacitors are available, the polypropylene and PET-based film capacitor is highly suitable for coupling capacitors.

$$C_1 = C_2 = \frac{I_{IN} (1-d)}{4 \Delta V_C f_S} \quad (3.39)$$

$$I_{C1,RMS} = I_{C2,RMS} = \frac{I_{IN} \sqrt{(1-d)}}{2\sqrt{2}} \quad (3.40)$$

As the coupling capacitors are connected in series with the primary windings of the HF transformer, they naturally work as DC-blocking capacitors for alleviating the DC biasing of the transformer during the asymmetric converter operation, thereby enhancing the converter performance, and preventing the core saturation of the transformer. Moreover, the proposed converter does not require additional DC blocking capacitors or complex

control schemes to achieve mitigation of DC bias in the transformer, thereby reducing the cost and saving the board space.

3.6.4. Selection of Devices

The selection of devices is based on their ratings which in turn are dependent on their voltage and current stress. The ratings of switches S_1 and S_2 are dramatically reduced due to the natural clamping of their voltage by the coupling capacitors, thereby allowing the selection of high current- low voltage MOSFETs with low $R_{DS,ON}$. This also facilitates the reduction in the conduction losses of these switches. The calculated ratings of the switches (S_3 , S_4) are based on their voltage and current stress, which allows the selection of high voltage - low current MOSFETs. The selection of coupling and rectifier diodes is highly influenced by their stresses and requires a trade-off between reverse-recovery time and on-state voltage drop. The reverse-recovery time is an important factor when choosing the type of diode for both coupling and rectifier diodes.

3.6.5. Design of Output Capacitor

The design of the output capacitor is also important to ensure stable output voltage with a smaller voltage ripple. The value of the output capacitor depends on the input current, duty cycle, operating switching frequency of the converter, turns ratio of the HF transformer and output voltage ripple (ΔV_O) and is calculated using the expression in (3.41). The electrolytic capacitor is typically suited for the output capacitors owing to their bulk energy storage.

$$C_O \geq \left(\frac{I_{IN}}{2n\Delta V_O} \right) \frac{d(1-d)}{f_s} \quad (3.41)$$

TABLE 3.2: Loss equations of proposed converter	
Component	Loss Equation
Input Inductor	$P_{L1} = I_{L1,RMS}^2 R_{L1,DC}$
HF Transformer	$P_{TR} = 2 I_{LK1,RMS}^2 R_{W1} + P_C$
Coupling Capacitor	$P_{C1} = I_{C1,RMS}^2 R_{ESR}$
Coupling Diode	$P_{D1} = V_{DF1} I_{D1} + V_{D1} Q_{rr,D1} f_s$
Rectifier Diode	$P_{D3} = V_{DF3} I_{D3} + V_{D3} Q_{rr,D3} f_s$
<u>Switches</u>	
Conduction Loss	$P_{COND} = I_{S1,RMS}^2 R_{DS1} + I_{S3,RMS}^2 R_{DS3}$
Switching Loss	$P_{SW} = V_{DS1}^2 C_{DS1} f_s + 0.5 V_{DS3}^2 C_{DS3} f_s + 0.5 I_{LK1}^2 L_{LK1} f_s$
Gate Drive Loss	$P_{DR} = V_{GS1}^2 C_{IS1} f_s + V_{GS3}^2 C_{IS3} f_s$

3.7. Theoretical Loss Distribution of Converter

In this section, the loss distribution of different components in the proposed converter is evaluated which assists the estimation of converter efficiency. The losses in various components of the proposed converter are calculated from the mathematical expression provided in Table 3.2. Furthermore, it is observed that the loss distribution in the components is dependent on various converter parameters. The losses in the input inductors are computed from Table 3.2, where the conduction loss depends on the rms inductor current and DC resistance of copper wire ($R_{L1,DC}$). Losses in the coupling and output capacitors of the converter are dominated by ESR losses. The losses in the HF transformer are further classified into conduction and core loss (P_C), where conduction losses are primarily governed by the rms currents through the windings and the winding resistances (R_{W1}). The losses in coupling and rectifier diodes are computed from the mathematical equations in Table 3.2, with the conduction losses being the primary contributor while reverse recovery turn-off loss also impacts the overall performance of the converter. It is observed from the loss distribution in Table 3.2 that MOSFET loss is further classified into switching loss and conduction loss. The rms currents and on-state resistance ($R_{DS,ON}$) of

MOSFET influence its conduction loss while the switching loss of MOSFET depends on its output capacitance and its drain-to-source voltage as well as the operating switching frequency of the converter. Moreover, loss distribution also includes the gate drive losses.

$$\eta = 1 - \frac{(2P_{L1}+P_{TR}+2P_{C1}+2P_{D1}+4P_{D3}+2P_{COND}+2P_{SW}+2P_{DR})}{P_{IN}} \quad (3.42)$$

The efficiency of the proposed converter is computed from (3.42) after cumulatively aggregating the component losses. The optimal selection of components is required to maximize the converter efficiency while minimizing the losses. Additionally, it is desired to select MOSFETs with their specific ratings having low $R_{DS,ON}$. The ferrite cores should be used for the HF transformer to mitigate their core loss. Further improvements in the efficiency and performance of the converter can be attained by optimizing the gate drive circuitry developed in the laboratory, having separate turn-on and turn-off gate resistors. It is pertinent to note that the converter efficiency can be maximized by optimal designing of the converter and the selection of superior components corresponding to their ratings, but it also increases the cost of the converter.

3.8. Comparative Study of the State-of-the-art Topologies

In this section, different state-of-the-art converter topologies are comparatively studied, and the merits of the proposed converter are evaluated. The limitations of the conventional boost converter have been well documented in the literature, with their inability to practically achieve high voltage gain being a major drawback. The proposed converter,

TABLE 3.3: Comparative study of state-of-the-art topologies										
Parameters	No. of Switches / Diodes	No. of Inductors / Capacitors	Voltage Gain	Input Current Ripple	Control Complexity	Inter-Converter Circulating Currents	Operating Range	DC Blocking Capacitor	Modularity	External Snubber / Clamp Circuit
[216]	2 / 3	1 / 4	$\frac{n_1 + n_2}{(1 - d)}$	High	Medium	No	$0.2 \leq d \leq 0.8$	No	No	Yes
[229]	4 / 4	1 / 2	Gain*	High	High	No	Low	Yes	No	No
[234]	8 / 0	2 / 4	$M_F = \frac{V_H}{2N V_{CC}}$ $M_B = \frac{2N V_{CC}}{V_H}$	Low	Medium	Yes	$0 \leq D_F \leq 0.15$ $0 \leq D_B \leq 0.5$	No	No	Yes
[235]	3 / 2	1 / 4	$\frac{n}{(1 - d)}$	Medium	Low	No	$0.5 \leq d < 1$	No	No	Yes
[260]	16 / 0	5 / 2	$\frac{n}{d}$	Very Low	High	Yes	$0.25 < d < 0.75$	No	No	Yes
[274]	4 / 5	2 / 3	$\frac{n}{2(1 - d)}$	Medium	Medium	No	$0.5 \leq d < 0.75$	No	No	No
[277]	6 / 0	1 / 1	$\frac{n}{2(1 - d)}$	Medium	High	Yes	$0.5 \leq d < 1$	No	No	No
Proposed Converter	4 / 6	2 / 3	$\frac{2n}{(1 - d)}$	Low	Low	No	$0.5 \leq d < 1$	Yes	Yes	No
Gain*: $\frac{1}{\sqrt{(1 + \lambda - \lambda A^2)^2 + Q^2 \left(\frac{1}{A} - A\right)^2}}$, where $A = \frac{f_r}{f_{sw}}$										

being a high gain converter with a turns ratio of 2 has four times higher theoretical voltage gain capability as compared to the CBC.

Based on the comparative study of different high-gain DC/DC converter topologies in Table 3.3, the following observations are underlined below.

- The voltage gain of various topologies is listed in Table 3.3. The voltage gain of resonant topology is highly complex and requires a higher number of variables. Moreover, the gain is notably impacted by the selection of resonant tank components. Some high gain isolated topologies solely rely on a large turns ratio of HF transformer for achieving high voltage gain. The proposed converter has the highest voltage gain capabilities among the studied topologies in Table 3.3 and is not solely reliant on the HF transformer to meet the gain demand. Moreover, its voltage gain only depends on the duty cycle and turns ratio of the transformer.
- The control complexity is another attribute of converter topology that needs to be investigated, particularly for deployment in MLIC. The control and modulation scheme becomes highly complex for a few topologies, especially for the resonant topologies requiring frequency modulation control and four phase isolated converter topology requiring phase-shift modulation control, thereby necessitating expensive controllers with substantially higher computation power. Conversely, the proposed topology utilizes a simpler control scheme and needs low-cost controllers, enabling its utilization in the distributed system where multiple such units are required.

- For the integration of converter topology with the PV panel, input current ripple is a critical parameter. The input current ripple impacts the performance of the PV panel and further degrades its operating life. Some topologies listed in Table 3.3 experiences higher input current ripple and are prone to severe degradation in the performance and operational life of PV panel. Moreover, they require significantly higher input filters with stringent design constraints. The topologies utilizing single input inductor observe comparatively smaller ripples but still are dependent on the ripple current of the inductor for achieving low input current ripple. As a result, selecting a notably higher input inductor dramatically degrades the converter response. The interleaved operation of CF-HGIIC enables significantly smaller input current ripple for smaller input inductors, thereby improving the performance and operational life of the PV panel. Additionally, the converter also minimizes the requirement of an input filter and eases its design constraints.
- The operation of converter topologies during wide input variations is a cardinal requirement for their employment in MLPS. LLC topology has a narrow range of operations and is highly susceptible to large input variations. The current-fed impedance source full bridge converter is also observed to have a limited operating range during boost mode with its operating duty cycle restricted below 75%. The proposed converter can seamlessly operate over wide variations in the input voltage and current owing to its distributed structure.
- The current-fed converters are severely impacted by the turn-off voltage spike in the switches. Few topologies employ active clamp circuits to alleviate this spike

but increases the circuit complexity. Moreover, the snubberless operation of the current-fed topology eliminates the external snubber/clamp circuit, but its bidirectional operation is redundant for PV applications. Also, the presence of secondary side switches increases the circulating and leakage currents during the parallel operation of the converter, which further inflates the losses and degrades the overall efficiency. The proposed converter facilitates unidirectional power flow and has minimal circulating and leakage currents, which allows seamless integration of multiple such units.

- The proposed converter demonstrates high modularity and scalability. Also, it enables plug-and-play operation which allows integration of multiple such units in the system to dynamically increase the overall power capacity without impacting the operation of the existing converters.

The salient features and merits of the CF-HGIIC highlight its suitability for MLIC and make it a viable topological solution for MLPS.

3.9. Results and Discussions

In this section, the simulated and experimental performance of the proposed converter is analyzed, and their results are presented to validate the theoretical analysis and design of the converter.

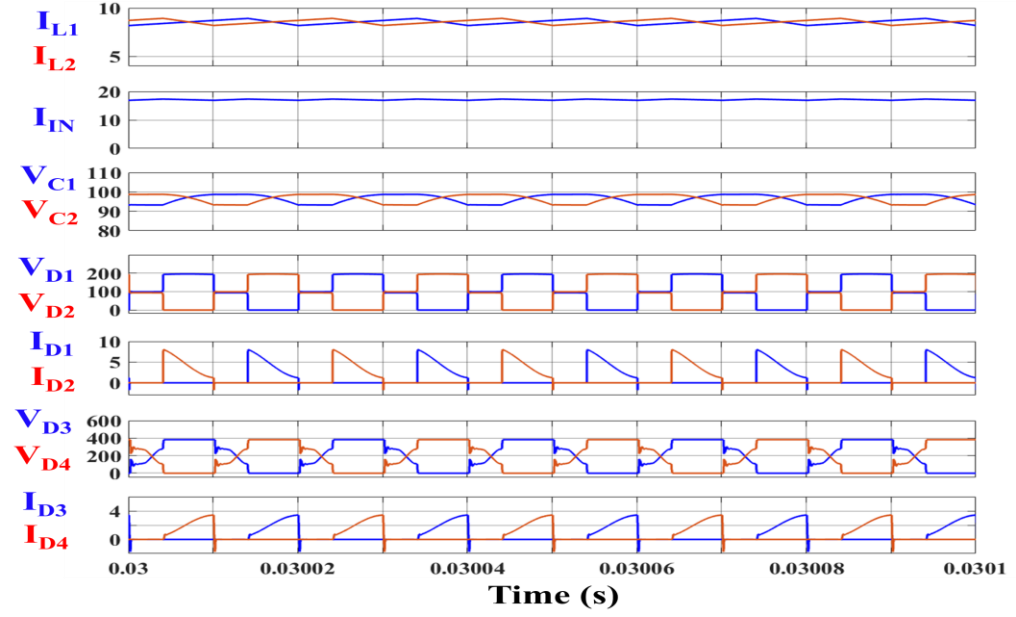
3.9.1. Simulation Results

The simulated performance of the proposed converter is evaluated in this subsection, with the objective of validating the mathematical analysis of the converter using the simulation results. The steady-state operation of a 500W converter is simulated in

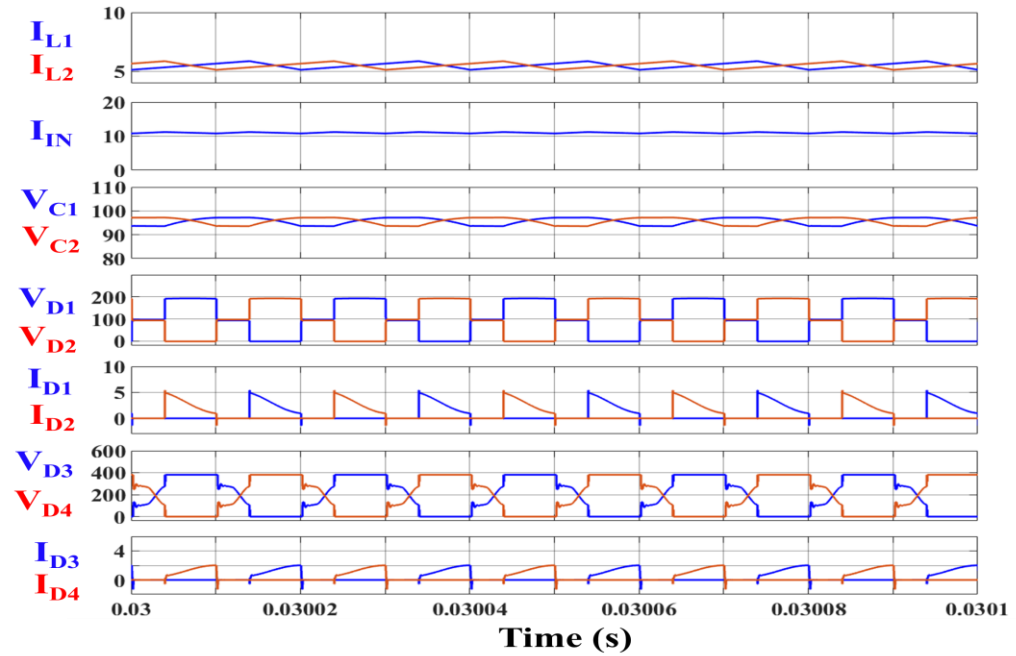
TABLE 3.4: Simulated converter specifications	
Parameter	Value
Input Voltage	30V
Output Voltage	380V
Rated Input Power	500W
Switching Frequency	50kHz

TABLE 3.5: Simulated converter design parameters	
Parameter	Value
Input Inductor (L_1, L_2)	560 μ H
Coupling Capacitor (C_1, C_2)	4.7 μ F
<u>HF Transformer</u>	
Leakage Inductance (L_{K1}, L_{K2})	2.4 μ H
Magnetizing Inductance (L_M)	3.5 mH
Turns Ratio (1:1: n)	1:1:2
Output Capacitor (C_O)	100 μ F

MATLAB Simulink environment for the converter specification listed in Table 3.4. Moreover, the converter design parameters are specified in Table 3.5. The simulated model of the proposed converter operates at a switching frequency of 50kHz and integrates a DC source of 30V with the 380V active load using the HF transformer with a turns ratio of 2. Moreover, the steady-state performance of the simulated converter model is evaluated for different input powers. Fig.3.9 demonstrates the steady-state converter waveforms of input current, inductor currents, coupling capacitor voltages, and current in the coupling diodes and rectifier diodes for input power conditions, i.e., 500W (rated input power $P_{IN, RATED}$) and 325W. The impact of interleaving is evident from the waveforms as 180° phase-shifted inductor currents having a current ripple of 8.7% result in a significantly smaller input current ripple of 2.41% for rated input power. The results corroborate with the theoretical analysis of the input interleaving operation of the proposed converter and highlight the bifurcation of input current with each inductor receiving half



(a)



(b)

Fig.3.9. Simulated waveform of inductor currents I_{L1} , I_{L2} (A), input current I_{IN} (A), voltage across coupling capacitors V_{C1} , V_{C2} (V), coupling diode voltages V_{D1} , V_{D2} (V) and currents I_{D1} , I_{D2} (A), rectifier diode voltages V_{D3} (V_{D6}), V_{D4} (V_{D5}) (V) and currents I_{D3} (I_{D6}), I_{D4} (I_{D5}) (A) (a) Input power of 500W (b) Input power of 325W.

the input current, thereby alleviating the conduction loss in inductors. The voltage across coupling capacitors for both input power conditions are shown in Fig. 3.9(a) and (b)

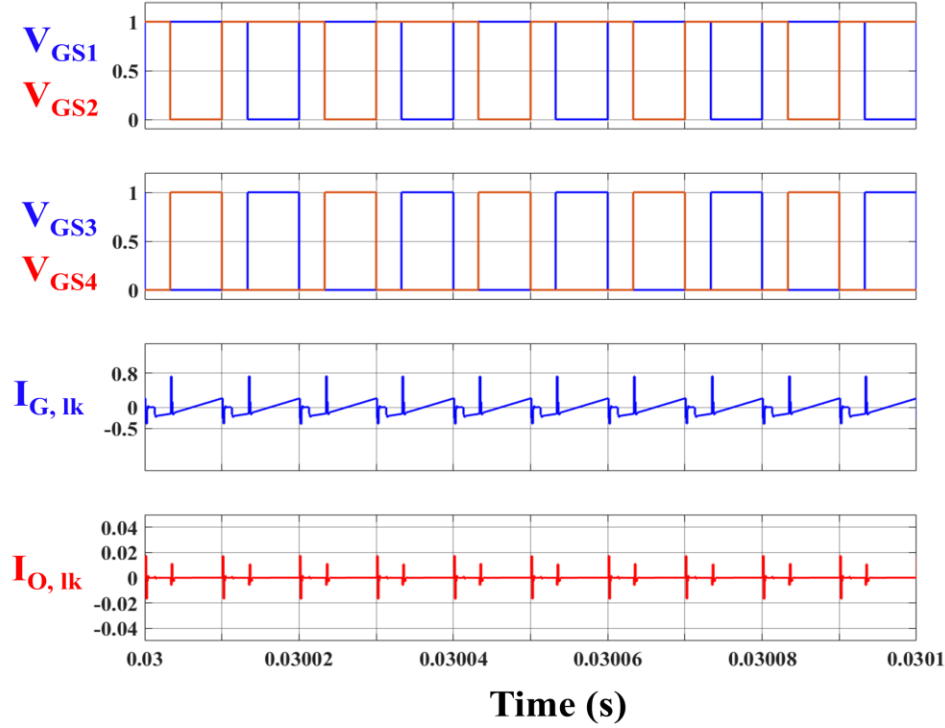


Fig.3.10. Simulated waveform of gating signals of switches, leakage current through HF transformer into ground ($I_{G, lk}$) and leakage current at output ($I_{O, lk}$)

respectively, with the steady-state voltage ripple of capacitors for $P_{IN, RATED}$ is 5.68%. Furthermore, the conduction of the coupling diodes (D_1 / D_2) and rectifier diodes ($D_3 - D_6$) and their reverse biased voltages are observed from the simulated results and conform to the topological operating modes of the converter. The leakage currents in the converter for rated input power during the switching transitions are shown in Fig.3.10. The high-frequency leakage current passing through the center-tapped HF transformer to the ground ($I_{G, lk}$) observes large peaks of 740mA and -410mA during the switching transitions while the leakage currents at the converter output ($I_{O, lk}$) have significantly smaller peaks of 17.2mA and -16.8mA, thereby validating the leakage model and further proving that the HF transformer filters major component of the leakage currents and minimizes its propagation at the output. The performance of the HF transformer during input power conditions with its primary and secondary winding voltages and their corresponding

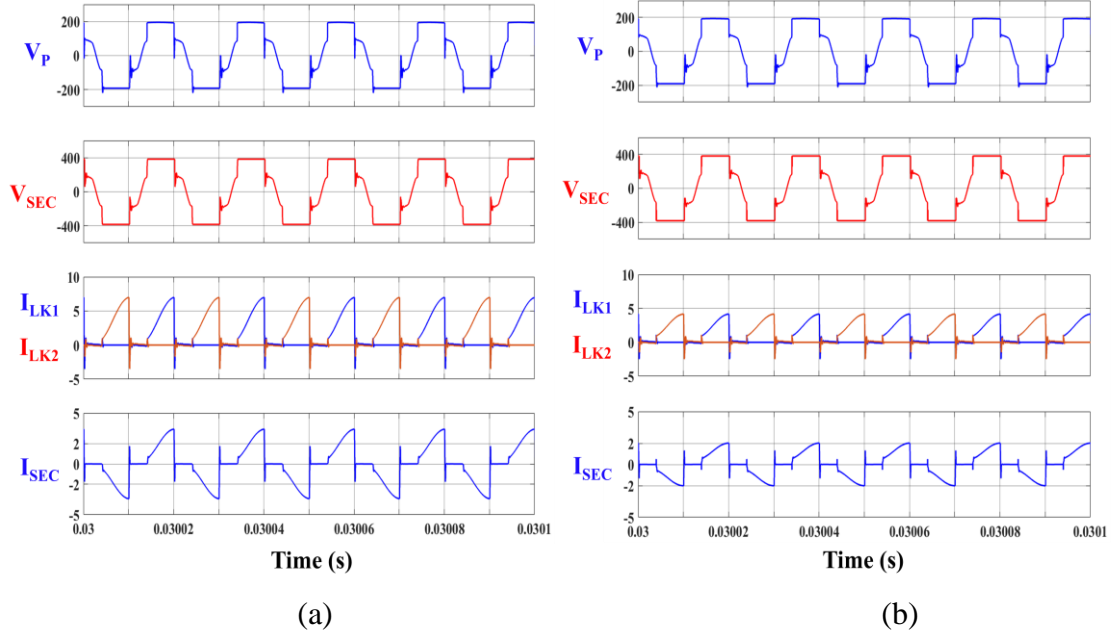
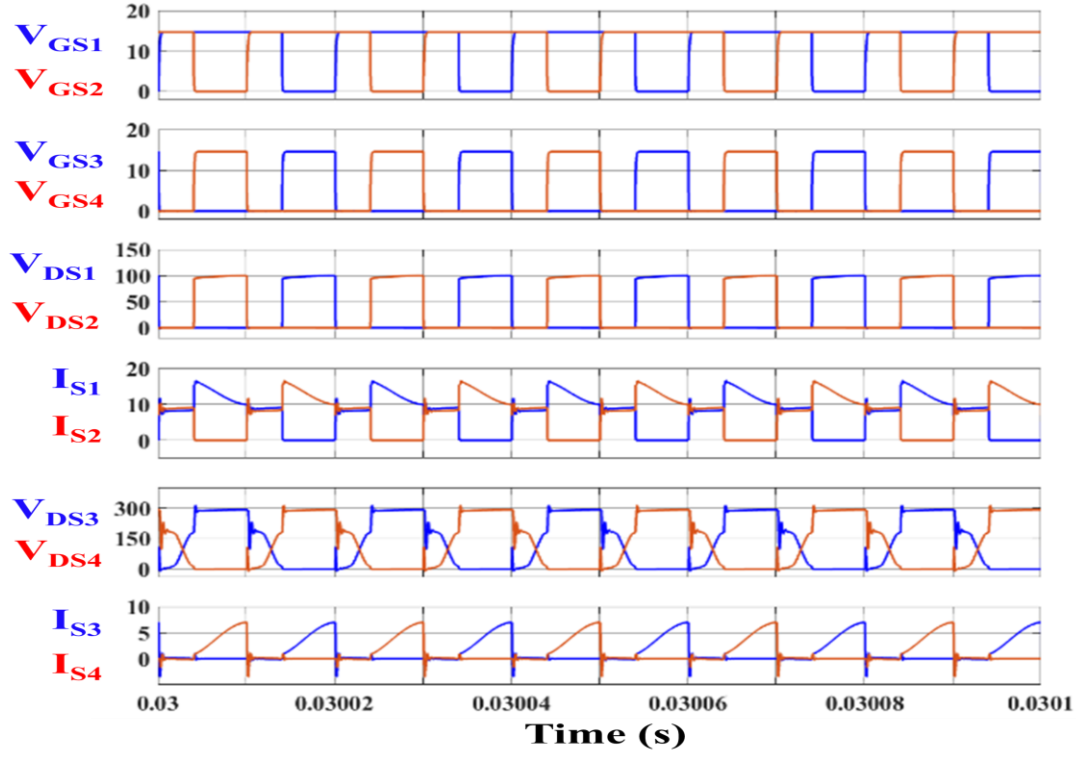
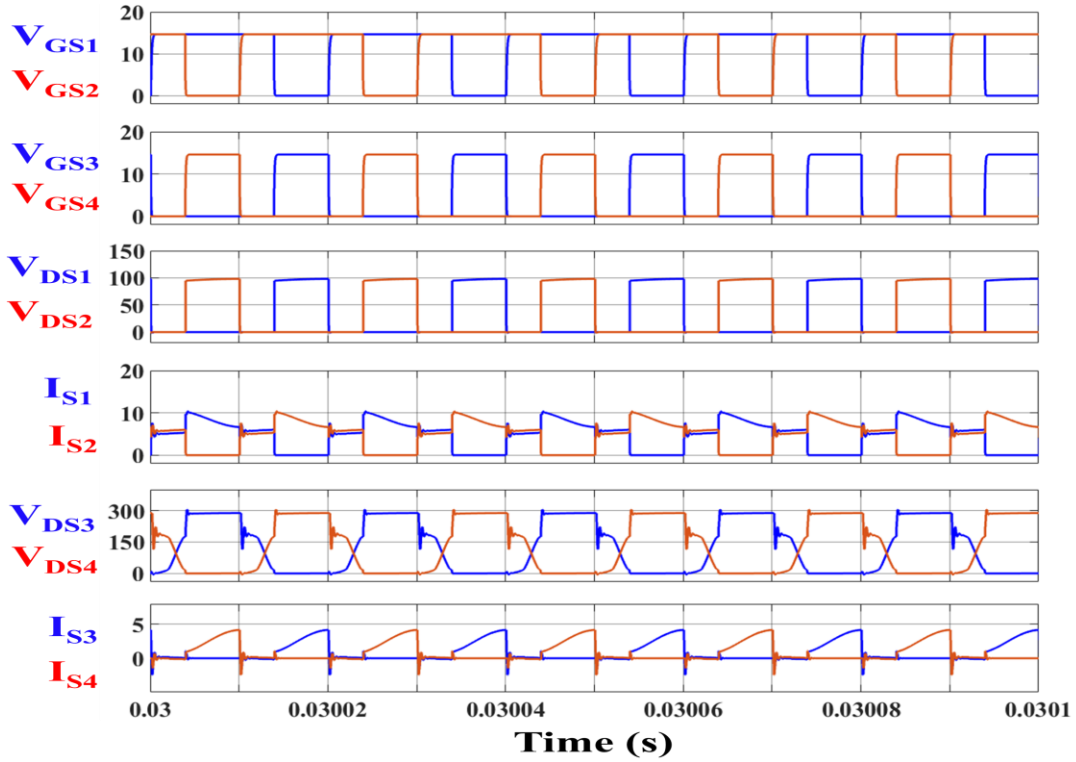


Fig.3.11. Simulated waveform of voltages and currents of primary winding V_P (V) and I_{LK1} , I_{LK2} (A) and secondary winding V_{SEC} (V) and I_{SEC} (A) of HF transformer (a) Input power of 500W (b) Input power of 325W

currents are presented in Fig.3.11. The voltage across the primary and secondary windings of the HF transformer quantifies its turns ratio of 2. Moreover, the quasi-sinusoidal waveform of the winding currents is also demonstrated from the results, thereby supporting the mathematical analysis. The switching performance of the proposed converter for input power conditions with the gating signal, voltage, and current of each switch is shown in Fig.3.12. The minimal turn-off voltage spike in switches S_1 and S_2 shown in Fig.3.12(a) and (b) is attributed to the natural voltage clamping by the coupling capacitors. The variations in the input power influence the operating switch currents as observed from the results. Moreover, the results also demonstrate that voltage across the switches S_3 and S_4 gradually rises or falls during the overlapping period (S_1 and S_2 are on) because the drain-to-source capacitance of switches gets slowly charged or discharged by the small magnetizing current. The steady-state input-output profile of the converter for both input



(a)



(b)

Fig.3.12. Simulated waveform of gating signals of switches V_{GS1} - V_{GS4} (V), voltages: V_{DS1} , V_{DS2} (V) and currents: I_{S1} , I_{S2} (A) in S_1 and S_2 and voltages: V_{DS3} , V_{DS4} (V) and currents: I_{S3} , I_{S4} (A) in S_3 and S_4 (a) Input power of 500W (b) Input power of 325W

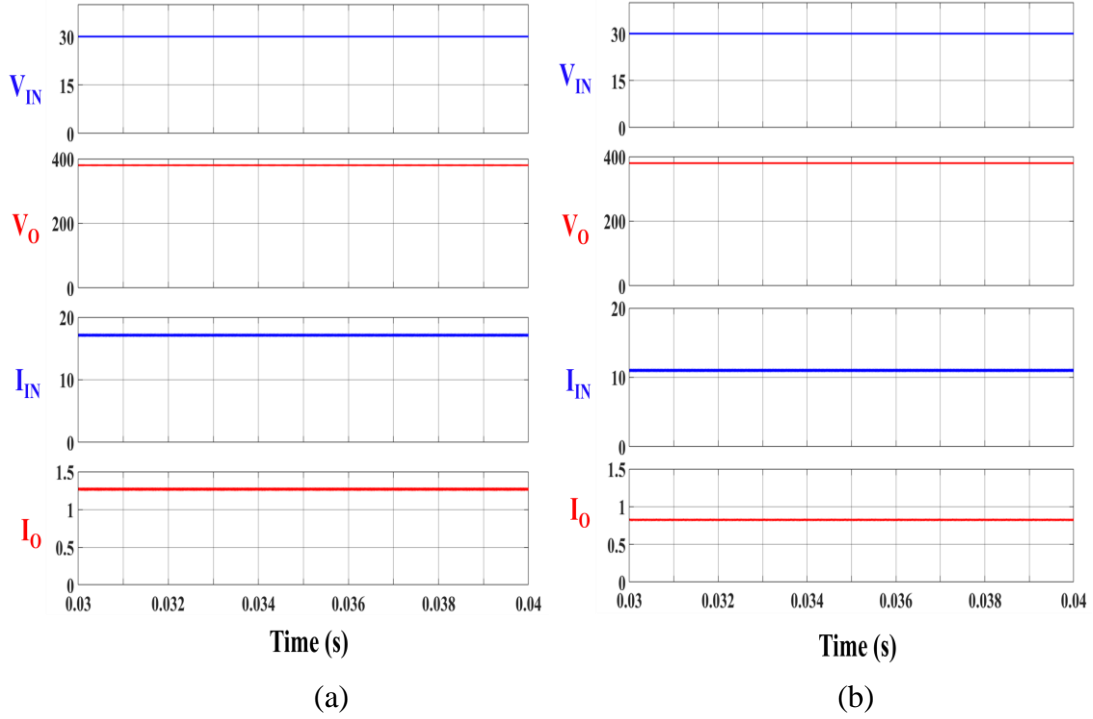


Fig.3.13. Simulated waveform of voltages of input V_{IN} (V) and output V_O (V) and currents of input I_{IN} (A) and output I_O (A) (a) Input power of 500W (b) Input power of 325W

powers of 500W and 325W is shown in Fig.3.13(a) and (b) respectively. The converter observes a reduction in its input and output current from 16.67A and 1.26A respectively during operation at 500W to 10.83A and 0.823A during the input power of 325W.

Consequently, the steady state simulation results and the simulated performance of the proposed converter validate the theoretical analysis, modeling, and operation of the converter and highlight its salient features and efficient design.

3.9.2. Experimental Results

In this subsection, the experimental performance of the proposed converter is comprehensively analyzed. The scaled-down 125W hardware prototype of the converter operating at 50kHz is shown in Fig.3.14 and is designed and developed in the laboratory in accordance with the converter specifications and design parameters listed in Table 3.6 and

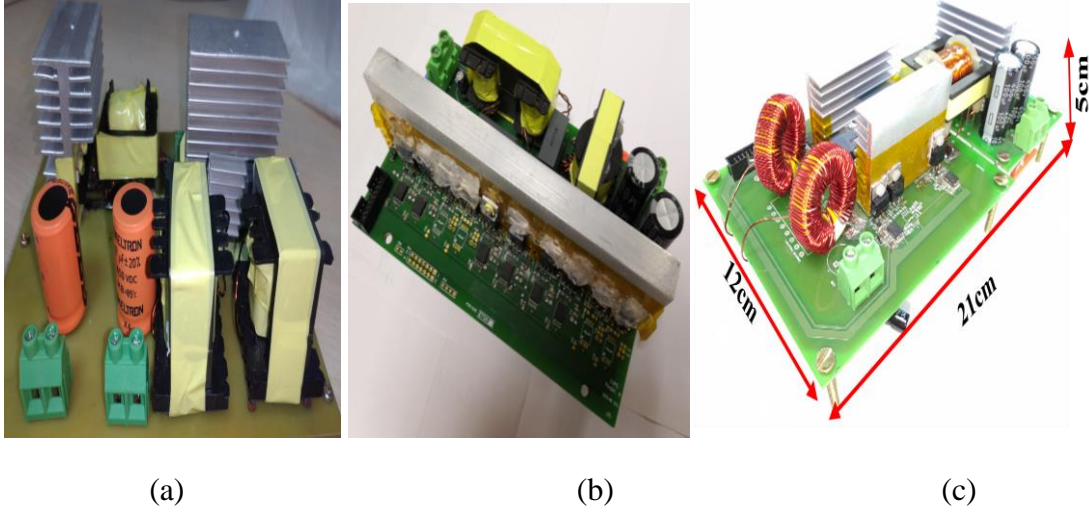
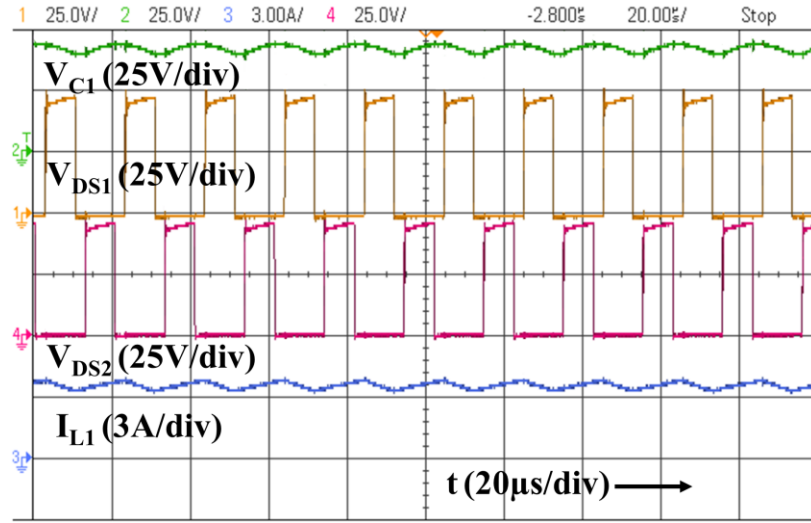


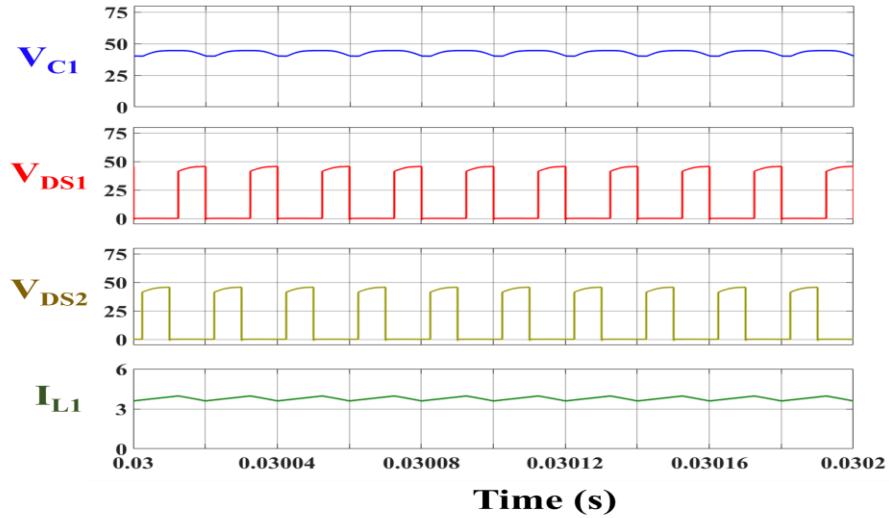
Fig.3.14. Hardware prototype of CF-HGIIC (a) Gen 1 (b) Gen 2 (c) Gen 3 (latest)

TABLE 3.6: Experimental converter specifications	
Parameter	Value
Input Voltage	17V
Output Voltage	170V
Rated Input Power	125W
Switching Frequency	50kHz

TABLE 3.7: Experimental converter design parameters	
Parameter	Value
Input Inductor (L_1, L_2)	MultiComp Pro -MCAP series (Torroidal): 560 μ H
Coupling Capacitor (C_1, C_2)	Kemet- R60 series (Metalized PET):3.3 μ F, 250V
HF Transformer	ETD Ferrite Core (Ferroxcube 3C90), Primary Turns- 30, 30, Secondary Turns- 60, Turns ratio- 1:1:2, L_{K1} =2.1 μ H, L_{K1} =2.16 μ H
Output Capacitor (C_O)	Electrolytic Capacitor:2 x100 μ F, 450V (in series)
Switches (S_1, S_2)	SQP90142E_GE3; 200V, 12.7m Ω
Switches (S_3, S_4)	IPP60R125CFD7XKSA1: 600V, 104m Ω
Coupling Diodes (D_1, D_2)	MUR860: 8A, 600V
Rectifier Diodes ($D_3 - D_6$)	
Gate Driver	ADUM4121



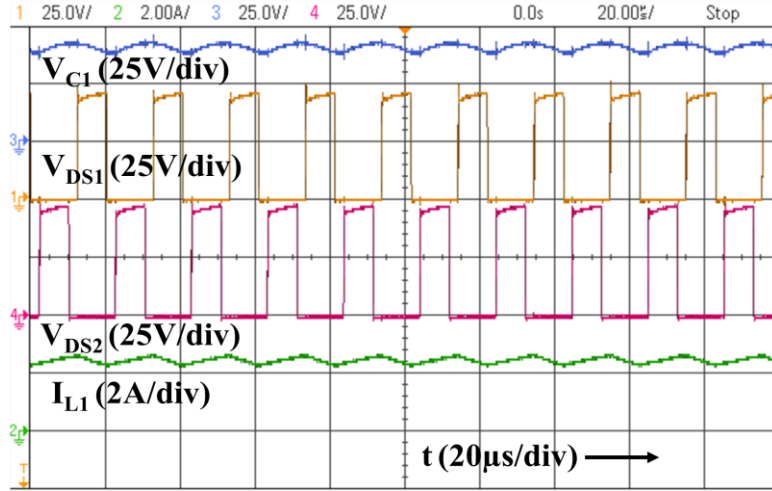
(a)



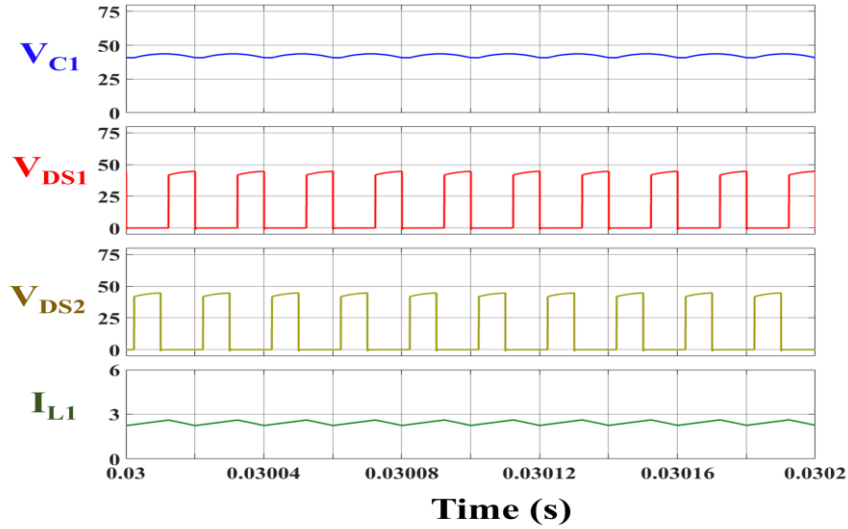
(b)

Fig.3.15. Waveform of coupling capacitor voltage V_{C1} (V), drain to source voltage of switch S_1 : V_{DS1} (V) and S_2 : V_{DS2} (V) and inductor current I_{L1} (A) for input power of 125W (a) Experimental result (b) Simulated result

Table 3.7 respectively. Furthermore, the hardware converter prototype is experimentally tested in the laboratory for the input powers of 125W (rated) and 85W while having the input voltage of 17V and feeding the power to the 170V active load. Additionally, for the seamless understanding of the experimental results and keeping the uniformity between the experimental results with scaled-down converter ratings and the simulation results having



(a)



(b)

Fig.3.16. Waveform of coupling capacitor voltage V_{C1} (V), drain to source voltage of switch S_1 : V_{DS1} (V) and S_2 : V_{DS2} (V) and inductor current I_{L1} (A) for input power of 85W (a) Experimental result (b) Simulated result

higher converter ratings, the simulated performance of the converter operating at the mentioned scaled-down ratings is also presented. This also allows a simpler and more comprehensive understanding with consistency in comparative analysis between the experimental and simulated results. The steady-state performance of a 125W converter with its experimental and simulated waveforms of inductor currents, coupling capacitor voltage,

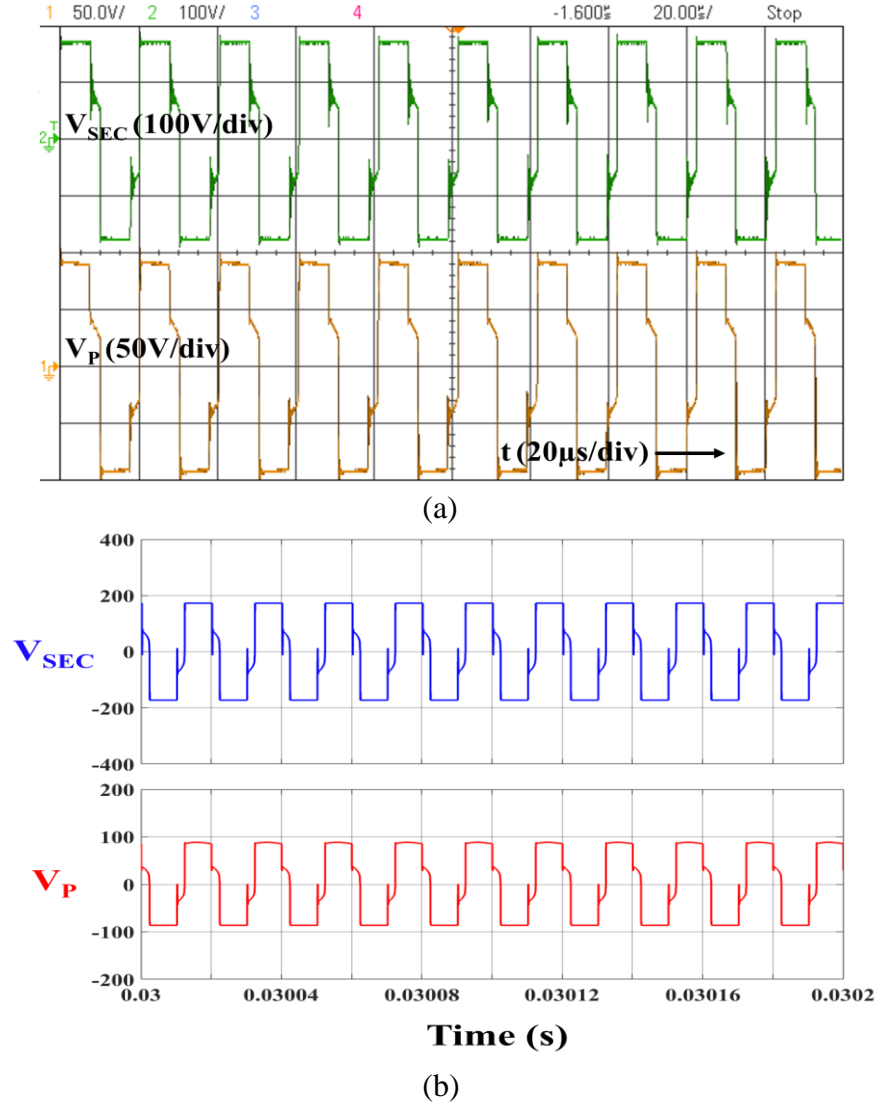
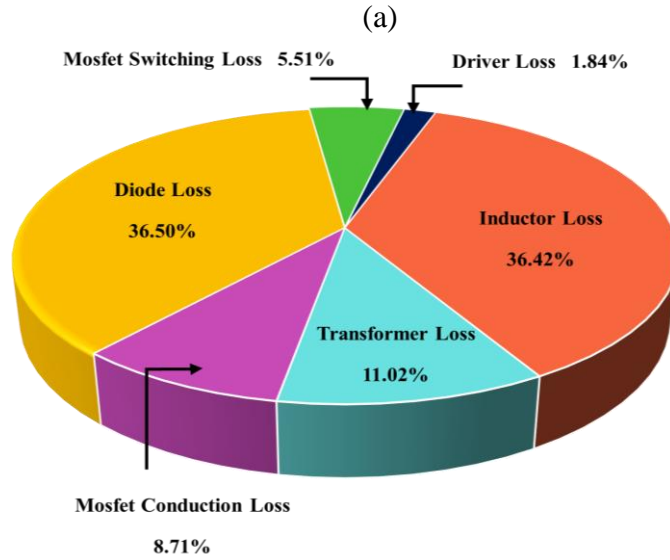
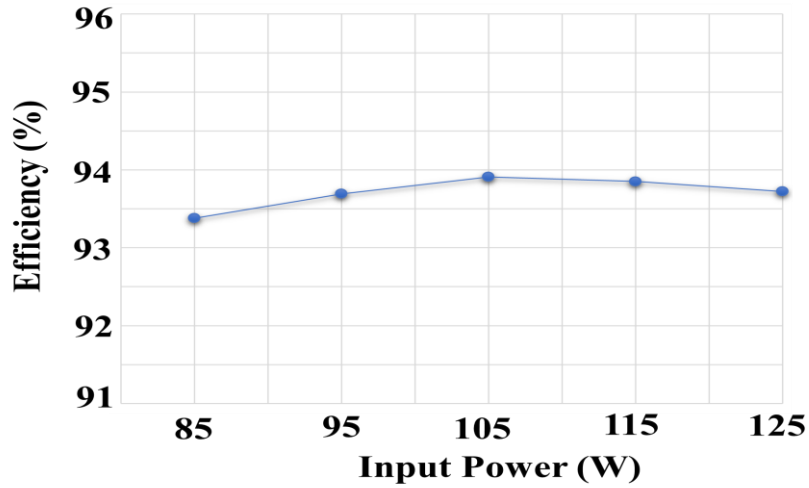


Fig.3.17. Waveform of voltage across primary winding V_P (V) and secondary winding V_{SEC} (V) for input power of 125W (a) Experimental result (b) Simulated result

and the drain-to-source voltage of switch S_1 for input powers of 125W and 85W is shown in Fig.3.15 and 3.16. The interleaved operation of the converter is demonstrated from the experimental waveform where the drain-to-source voltage of switches S_1 and S_2 are 180° phase shifted while the current through the inductor L_1 is one-half of the calculated input current, thereby further conforming to the theoretical analysis. Also, the experimental and simulated waveforms of the converter shown in Fig.3.15 and 3.16 are closely matched. Furthermore, it is noted from the result in Fig.3.15(a) that the experimental steady state



(b)

Fig.3.18. Experimental performance (a) Efficiency of CF-HGIIC for variation in input power (b) Loss analysis of converter for input power of 125W

voltage ripple in the coupling capacitor for the rated input power is 9.4% which is similar to the observed ripple in the simulated result in Fig.3.15(b). The experimental waveform of the proposed converter also highlights a minimal turn-off voltage spike in the drain-to-source voltage across the switches S_1 and S_2 , thereby indicating the natural voltage clamping of the switches by the coupling capacitor and further validating the mathematical converter analysis. Fig.3.17 shows the experimental and simulated waveforms of the

winding voltages of the HF transformer. The experimental waveform of primary and secondary winding voltages of the HF transformer in Fig.3.17(a) demonstrates that the ETD ferrite core-based transformer has a practical turns ratio of 2. Also, the experimental waveform of the transformer conforms with the theoretical analysis and the simulated waveform shown in Fig.3.17(b). The experimental efficiency of the proposed converter for variations in the input power is shown in Fig.3.18(a). The efficiency of the proposed converter at the rated input power of 125W is 93.72% while the peak efficiency of 93.91% is observed at 105W. Moreover, the loss analysis of the converter operating at the rated input power is shown in Fig.3.18(b). It is noticed from the loss analysis that the major contributors to the overall converter loss are the inductor and diode losses whereas the loss components of the switches and HF transformer are much smaller. The efficiency of the converter can be further improved by selecting superior and high-performance components with better PCB design. The experimental performance of the proposed converter highlights its ability to practically operate at a voltage gain of 10 using a transformer turns ratio of 2 with high efficiency, making it a suitable topology for MLIC.

3.10. Conclusion

In this chapter, a new topology of the current-fed isolated converter has been proposed. The salient features of the proposed converter have been studied and comparatively analyzed with different state-of-the-art high-gain converter topologies. The operating modes of the converter are provided in this chapter with a detailed mathematical analysis of each mode. Moreover, comprehensive modeling of the converter with the static voltage gain analysis and the in-depth steady state analysis of the converter has also been studied.

The extensive designing of different parameters of the converter has been presented in this chapter while considering the practical limitations of the components. The theoretical loss distribution of the proposed converter has been analyzed to get a better understanding of losses in individual components and pinpoint the specific component responsible for the overall converter loss.

The simulated performance of the converter has been evaluated by developing the converter model on MATLAB Simulink environment. Based on the simulated converter specification and its corresponding calculated design parameters, the simulated converter performance highlighted the merits of the proposed converter and validated the theoretical analysis. Moreover, the converter demonstrated the operation at high gain with a lower turns ratio of the HF transformer. The simulated results underlined a significantly smaller input current ripple in the converter with mitigation of leakage current at the output. Additionally, the minimal turn-off voltage spike in switches S_1 and S_2 is observed from the results, highlighting the natural voltage clamping of the switch voltage by the coupling capacitor.

The hardware prototype of the proposed converter developed in the laboratory using the calculated design parameters has been experimentally tested. The experimental results further highlighted the natural voltage clamping of switches in S_1 and S_2 while also indicating the superior performance of the HF transformer. The experimental efficiency of the proposed converter prototype and its loss analysis have been studied and demonstrated higher converter efficiency. The ability of the converter prototype to operate experimentally at a high voltage gain of 10 is indicated by the experimental results. Moreover, the experimental performance of the converter prototype further validated the simulated performance and corroborated with the theoretical analysis and converter design. The

merits of the proposed converter and its superior performance emphasized the suitability of the converter topology for MLIC.

CHAPTER 4

TOPOLOGICAL MODIFICATIONS AND PERFORMANCE ENHANCEMENTS

4.1. General

The merits and operational performance of the current-fed high gain isolated interfacing converter (CF-HGIIC) have been discussed in Chapter 3 and their viability for module-level interfacing converter has been explored. However, the topological structure of the converter requires some improvements to enhance the converter's performance. In this chapter, topological modifications in the converter and their performance improvements have been studied. The operating topological modes of the modified converter with its mathematical modeling are also discussed in the chapter. The modified converter topology with its rated input power of 500W while having 30V input and 380V output has been simulated on the MATLAB Simulink environment and its performance under input voltage variations has been extensively analyzed. Moreover, for validating the performance of the converter experimentally during input voltage variations, a scaled-down 190W hardware prototype of the converter with its rated input voltage of 26V and 270V output has been developed and tested in the laboratory. The chapter is organized as follows: Section 4.2 discusses the improvements required in the existing converter topology (CF-HGIIC) while section 4.3 presents the modified converter topology. The topological operating modes of the converter are discussed in section 4.4 followed by its mathematical modeling in section 4.5 while the discussions on the performance of the modified converter are presented in section 4.6.

4.2. Improvements in the Existing Topology

The key scope of improvements in the CF-HGIIC to enhance its operational performance is discussed below.

- The converter natively incorporates high-side switches (S_3 , S_4) which increases the cost and complexity of the gate drive design and drive circuitry while also necessitating a higher count of isolated power supplies.
- CF-HGIIC with its high-side switches is susceptible to the false triggering operation which can degrade the overall performance while also making the converter more prone to EMI issues.
- Furthermore, the converter observes a higher voltage spike in these switches during turn-off which induces higher losses.

As a result, the topological modifications in CF-HGIIC are imperative for improving the converter operation and its performance while also reducing the cost.

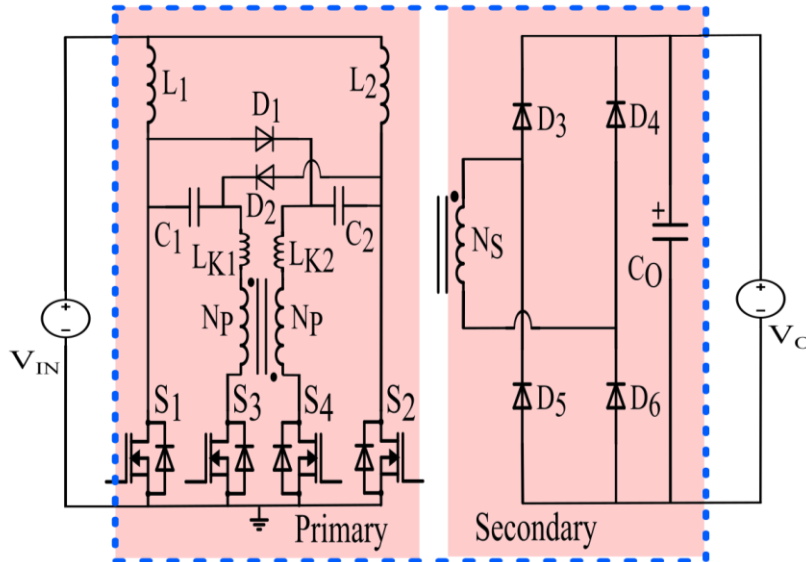


Fig.4.1. Topological structure of MCF-HGIIC

4.3. Proposed Converter Topology

The modified current-fed high gain isolated interfacing converter (MCF-HGIIC) has been proposed in this chapter and offers key improvements over the conventional CF-HGIIC. The proposed converter retains all the inherent topological merits and salient features of the conventional converter. The topological structure of the proposed modified current-fed high gain isolated interfacing converter (MCF-HGIIC) is shown in Fig.4.1. The proposed converter operates in the continuous conduction mode with its operating duty cycle ($d \geq 0.5$). The primary side of the converter utilizes dual input inductors (L_1, L_2) for facilitating continuous input current. Furthermore, the converter has coupling diodes (D_1, D_2), coupling capacitors (C_1, C_2), and all four low-side switches ($S_1 - S_4$). The secondary side of the converter incorporates a full-bridge diode rectifier ($D_3 - D_6$) and the output capacitor (C_o). The primary and secondary side of the converter is interlinked using a high

TABLE 4.1: Parametric notations of MCF-HGIIC

Parameters	Voltage	Current
Input	V_{IN}	I_{IN}
Output	V_O	I_O
Input Inductor (L_1, L_2)	V_{L1}, V_{L2}	I_{L1}, I_{L2}
Coupling Capacitor (C_1, C_2)	V_{C1}, V_{C2}	I_{C1}, I_{C2}
Switches ($S_1 - S_4$)	Drain to Source: $V_{DS1} - V_{DS4}$	$I_{S1} - I_{S4}$
	Gate to Source: $V_{GS1} - V_{GS4}$	
Coupling Diodes (D_1, D_2)	Reverse Biased: V_{D1}, V_{D2}	I_{D1}, I_{D2}
	Forward Drop: V_{DF1}, V_{DF2}	
Rectifier Diodes ($D_3 - D_6$)	Reverse Biased: $V_{D3} - V_{D6}$	$I_{D3} - I_{D6}$
	Forward Drop: $V_{DF3} - V_{DF6}$	
<u>HF Transformer</u>		
Primary Winding	V_P	I_{LK1}, I_{LK2}
Secondary Winding	V_{SEC}	I_{SEC}
Magnetizing Inductance	V_{LM}	I_M

frequency (HF) transformer having the leakage inductance (L_{K1} , L_{K2}) and magnetizing inductance (L_M) and utilizing the low turns ratio (1:1: n). The proposed converter interfaces a DC source at the input and feeds the power to the active load (DC sink). The notations of different converter parameters of MCF-HGIIC are similar to the CF-HGIIC and are listed in Table 4.1.

The proposed MCF-HGIIC retains the salient features of the conventional CF-HGIIC like the high voltage gain while utilizing the low turns ratio of the HF transformer and exhibiting a unique distributed structure with parallel conduction paths to minimize the stress and losses in the components. Furthermore, the converter significantly reduces input current ripple using interleaved operation and has a higher tolerance to the DC bias in the HF transformer during the asymmetric operation. Meanwhile, MCF-HGIIC also exhibits natural voltage clamping of the switches S_1 and S_2 , thereby eliminating the requirement for an additional snubber or clamp circuit. In addition, the proposed converter offers some improvements over the conventional CF-HGIIC. The utilization of low-side switches in MCF-HGIIC encourages the use of low cost gate drivers with simplified gate drive design and driver complexity and eliminates the requirement for a higher count of isolated power supplies. Furthermore, the converter topology improves the immunity to false triggering and EMI issues by incorporating low-side switches. Additionally, the proposed converter utilizes a new modulation scheme to achieve quasi-zero current switching (quasi-ZCS) during the turn-off transition in the switches S_3 and S_4 , which mitigates the turn-off voltage spike and losses, thereby improving the converter performance.

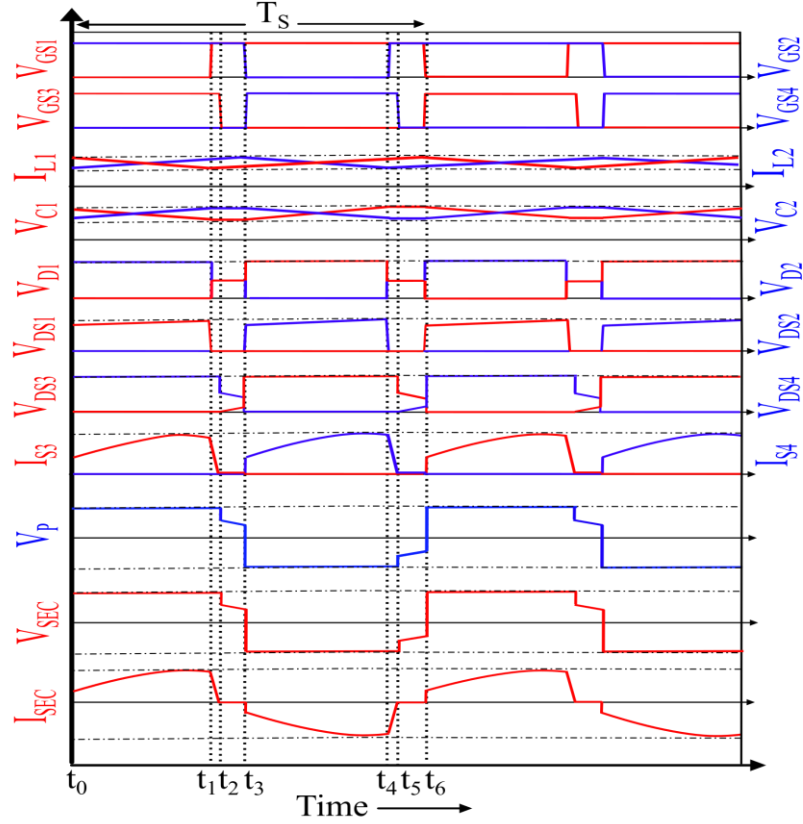


Fig.4.2. Analytical waveforms of MCF-HGIC

4.4. Topological Modes of Operation

The topological operating modes of the proposed converter are discussed in this section. Fig.4.2 demonstrates the steady-state analytical waveforms of the MCF-HGIC with its operating duty cycle $d \geq 0.5$. The gating pulses of switches S_1 and S_2 are 180° phase shifted with their on-time greater than 50%, while the gating pulses of switches S_3 and S_4 operate for less than 50%. Additionally, the gating pulses of switch S_3 and S_4 have some overlap with the S_1 and S_2 respectively, thereby assisting in the quasi-ZCS operation of S_3 and S_4 . The topological modes of the proposed converter for different operating intervals are examined below. Additionally, the equivalent circuits of the MCF-HGIC for each operating interval are depicted in Fig.4. 3.

4.4.1. Mode 1 ($t_0 - t_1$) : Power Transfer Mode – Fig.4.3(a)

At the start of this operating mode, switch S_2 is assumed to be conducting while the turn-off of switch S_1 at the instant t_0 forward biases the coupling diode D_1 . The voltage across the coupling capacitors (C_1, C_2) appears across the primary winding of the HF transformer as the switch S_3 turn-on with quasi-sinusoidal winding currents. Moreover, during this operating mode, the power is transferred to the active load through the HF transformer and rectifier diodes D_3 and D_6 .

4.4.2. Mode 2 ($t_1 - t_2$) : Transition Mode – Fig.4.3(b)

At the instant t_1 , switch S_1 turn-on, which starts increasing the switch current (I_{S1}) linearly and further reverse biases the diode D_1 . Concurrently, the energy stored in leakage inductance (L_{K1}) of the HF transformer is transferred to the load as it starts discharging. Moreover, current through the leakage inductance of the transformer decreases linearly to the small magnetizing current (I_M) at the instant t_2 . This linear decrease in the current assists in the natural commutation of the switch S_3 current (I_{S3}) to a small magnetizing current before the removal of its gating signal (V_{GS3}). At the end of this mode, the rectifier diodes D_3 , and D_6 get reverse biased.

4.4.3. Mode 3 ($t_2 - t_3$) : quasi-ZCS Mode – Fig.4.3(c)

At the instant t_2 during the beginning of this mode, the gating signal (V_{GS3}) of switch S_3 is removed and the switch turn-off with a small magnetizing current (I_M) while having zero switch voltage (V_{DS3}), thus demonstrating quasi-ZCS operation. The switch capacitance (C_{DS3}) is a non-linear function of switch voltage (V_{DS3}) and is charged by the magnetizing current, observing gradual increases in the switch voltage with small dV/dt . Simultaneously, the output capacitor of switch S_4 discharges to counterbalance the increase

in V_{DS3} . During this operating mode, no power is transferred to the load. At the end of this mode at the instant t_3 , S_3 reaches its steady state voltage while S_2 and S_4 turn-off and on respectively.

4.4.4. Mode 4 ($t_3 - t_4$) : Power Transfer Mode – Fig.4.3(d)

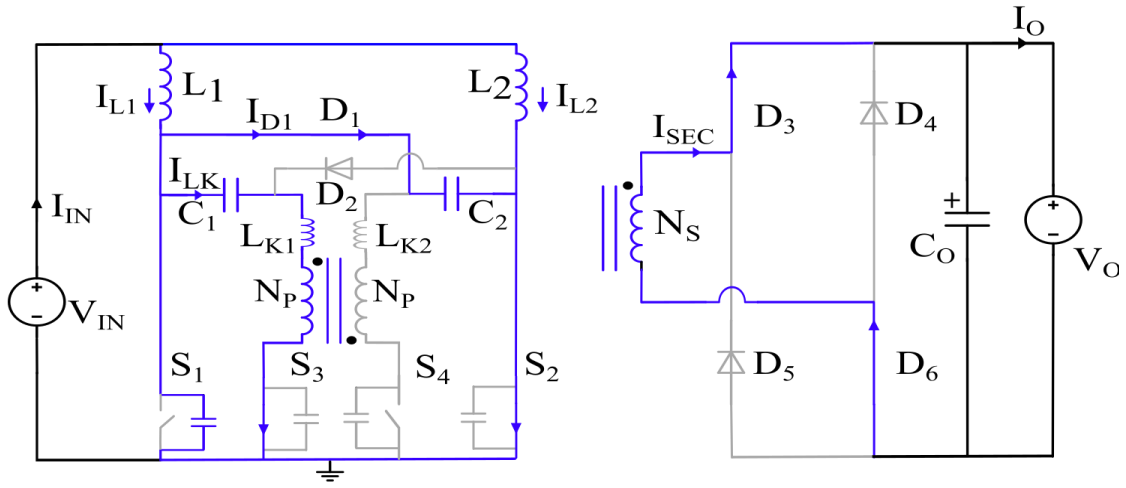
The switch S_1 is conducting while the switch S_2 turn-off at the beginning of this mode at the instant t_3 , which forward biases the coupling diode D_2 . The turn-on of switch S_4 at the instant t_3 allows the voltage across the coupling capacitors (C_1, C_2) to appear across the primary winding of the HF transformer while exhibiting quasi-sinusoidal winding currents. Additionally, during this operating mode, the power is transferred to the active load through the HF transformer and rectifier diodes D_4 and D_5 .

4.4.5. Mode 5 ($t_4 - t_5$) : Transition Mode – Fig.4.3(e)

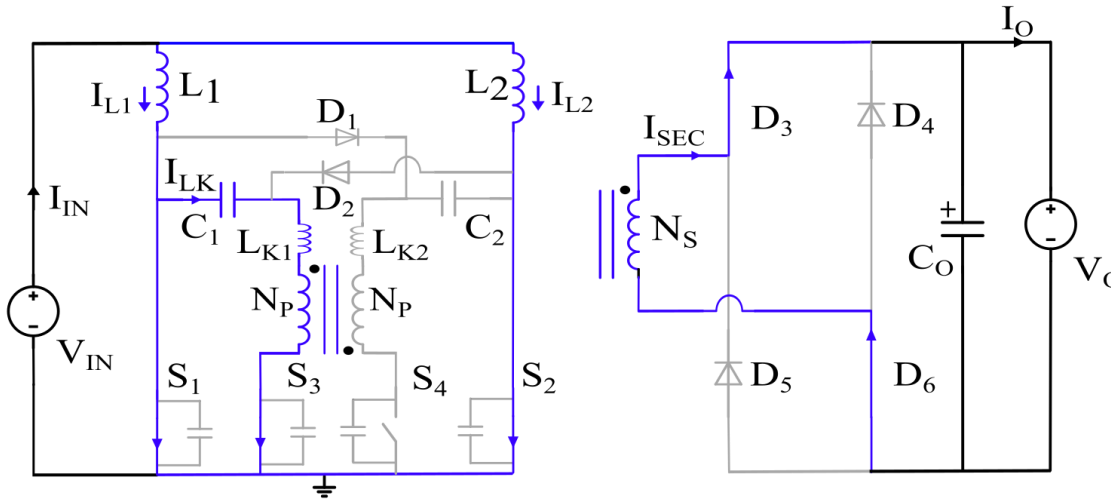
The switch S_2 turn-on at the instant t_4 , which starts increasing the switch current (I_{S2}) linearly and reverse biases the coupling diode D_2 . Simultaneously, the leakage inductance (L_{K2}) of the HF transformer starts discharging and transfers its energy to the load. Additionally, the current through the leakage inductance of the transformer decreases linearly to a small magnetizing current (I_M) at the instant t_5 . This linear decrease in the current facilitates the natural commutation of the switch S_4 current (I_{S4}) to a small magnetizing current before the removal of its gating signal (V_{GS4}). At the end of this mode, the rectifier diodes D_4 , and D_5 get reverse biased.

4.4.6. Mode 6 ($t_5 - t_6$) : quasi-ZCS Mode – Fig.4.3(f)

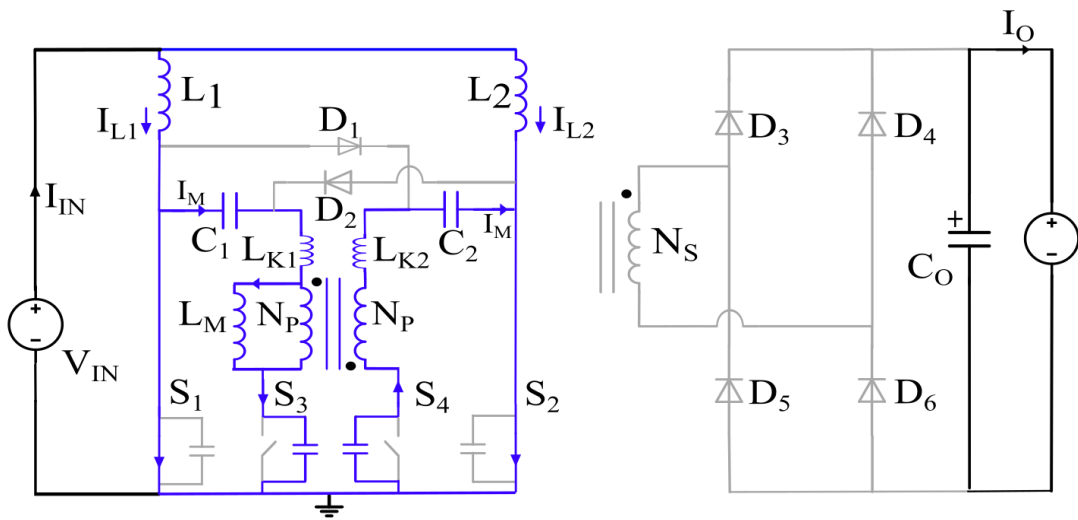
During the start of this mode at the instant t_5 , the switch S_4 turn-off with a small magnetizing current (I_M) while having zero switch voltage (V_{DS4}) as the gating signal (V_{GS4})



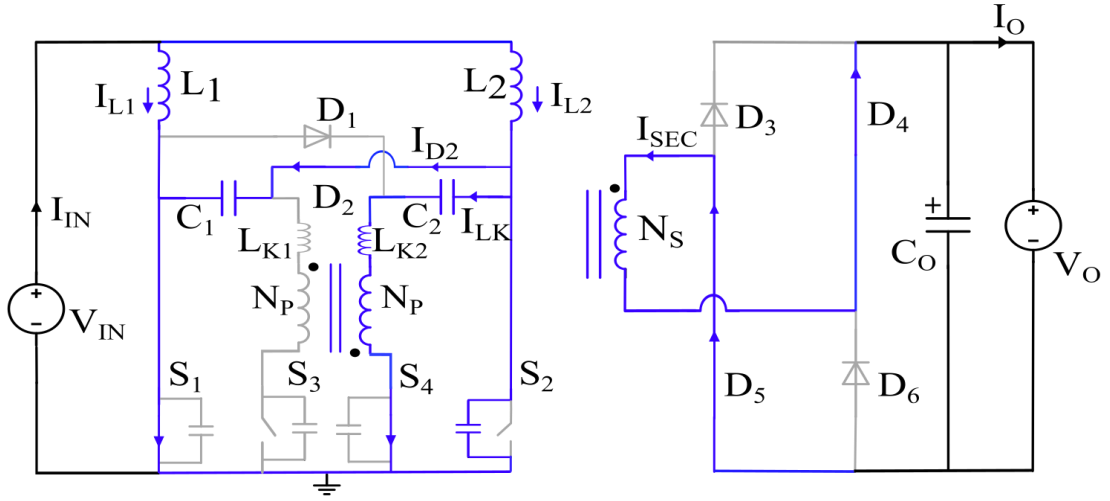
(a)



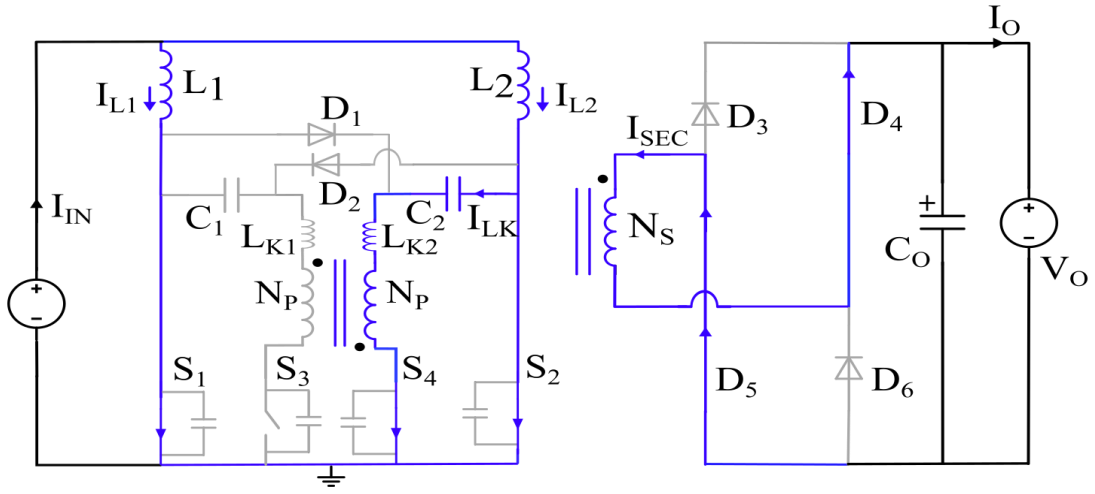
(b)



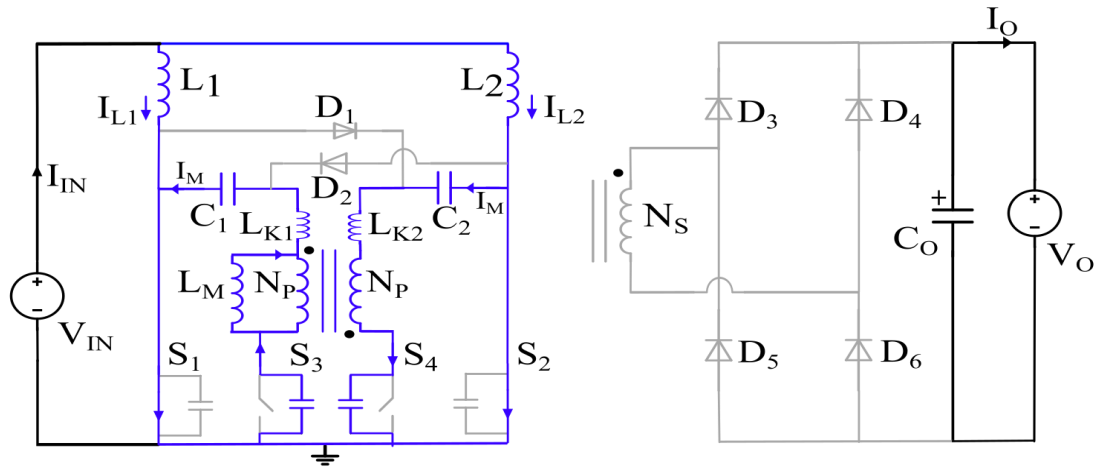
(c)



(d)



(e)



(f)

Fig.4.3. Topological operating modes of proposed converter (a) Mode 1 (b) Mode 2 (c) Mode 3 (d) Mode 4 (e) Mode 5 (f) Mode 6

of S_4 is removed, thereby highlighting quasi-ZCS operation. The non-linear switch capacitance (C_{DS4}) as a function of switch voltage (V_{DS4}) is charged by the magnetizing current and observes gradual increases in the switch voltage with small dV/dt . Instantaneously, the switch S_3 capacitance discharges to counterbalance the increase in V_{DS4} . No power is transferred to the load during this mode. The switch S_4 reaches its steady state voltage while S_1 and S_3 turn-off and on respectively at the end of this mode at the instant t_6 .

4.5. Mathematical Modeling of Converter

In this section, the mathematical modeling of the proposed converter is presented. The converter operates in the continuous conduction mode with $d \geq 0.5$. The fundamental assumptions for the simplified converter modeling are outlined below:

- The input inductors are assumed to be sufficiently large to maintain stiff DC currents.
- The circuit components are assumed to be ideal with no PCB parasitic.
- The output voltage is assumed to be constant with a large output capacitor.
- It is assumed that the input inductors ($L_1=L_2=L$), coupling capacitors ($C_1=C_2=C$), and leakage inductances ($L_{K1}=L_{K2}=L_K$) referred to primary are identical.

4.5.1. Steady-State Operational Analysis

Time-domain analysis with the derivation of mathematical equations for each operating mode of MCF-HGIIC is necessary to optimally model the converter. Additionally, these equations facilitate the converter designing and device selection while assisting in a comprehensive understanding of the converter operation. As the identical operation of the

converter is observed during the other half cycle of the switching cycle owing to the circuit symmetry, the mathematical analysis for each operating mode of the converter is only discussed for one-half of the switching cycle.

The current through the input inductor (4.1) is half of the input current.

$$i_{L1}(t) = i_{L2}(t) = \frac{I_{IN}}{2} \quad (4.1)$$

A. Mode 1($t_0 - t_1$):

During mode 1, the mathematical equations of the converter are discussed below:

$$i_{S1}(t) = i_{S4}(t) = i_{D2}(t) = 0 \quad (4.2)$$

$$i_{S3}(t) = i_{LK1}(t) = i_{C1}(t) = i_{C1}(t_0) + \frac{V_{eq}}{Z_o} \sin w_o(t - t_0) \quad (4.3)$$

$$i_{D1}(t) = i_{C2}(t) = i_{C2}(t_0) - \frac{V_{eq}}{Z_o} \sin w_o(t - t_0) \quad (4.4)$$

$$w_o = \frac{1}{\sqrt{0.5 L_K C}}, Z_o = \sqrt{\frac{2L_K}{C}}, i_{C1}(t_0) = \frac{I_{PV}}{2} - \frac{C \Delta V_C}{(t_1 - t_0)}, i_{C2}(t_0) = \frac{C \Delta V_C}{(t_1 - t_0)} \quad (4.5)$$

$$V_{eq} = 2V_{C1}(t_0) - \frac{V_o}{n} - \Delta V_C, \quad \Delta V_C = (0.25 I_{IN}(1 - d)T_S)/C \quad (4.6)$$

$$i_{S2}(t) = \frac{I_{IN}}{2} + i_{C2}(t_0) - \frac{V_{eq}}{Z_o} \sin w_o(t - t_0) \quad (4.7)$$

$$V_{C1}(t) = \frac{-1}{C} \int_{t_0}^t i_{C1}(t) dt = V_{C1}(t_0) - \frac{i_{C1}(t_0)}{C} (t - t_0) - \frac{V_{eq}}{C w_o Z_o} (1 - \cos w_o(t - t_0)) \quad (4.8)$$

$$V_{C2}(t) = \frac{1}{C} \int_{t_0}^t i_{C2}(t) dt = V_{C2}(t_0) + \frac{i_{C2}(t_0)}{C} (t - t_0) - \frac{V_{eq}}{C w_o Z_o} (1 - \cos w_o (t - t_0)) \quad (4.9)$$

$$i_{SEC}(t) = \frac{i_{LK1}(t)}{n}, V_P = \frac{V_O}{n}, V_{DS1}(t) = V_{C2}(t), V_{DS4}(t) = V_P + V_{C2}(t), V_{SEC} = n V_P \quad (4.10)$$

$$T_{10} = (1 - d) T_S \quad (4.11)$$

B. Mode 2 ($t_1 - t_2$):

During mode 2, the mathematical equations of the converter are underlined below:

$$i_{S2}(t) = \frac{I_{IN}}{2}, i_{S4}(t) = 0 \quad (4.12)$$

$$i_{D1}(t) = i_{D2}(t) = i_{C2}(t) = 0 \quad (4.13)$$

$$i_{S3}(t) = i_{LK1}(t) = i_{LK1}(t_1) - \frac{\left(\frac{V_O}{n} - V_{C1}(t)\right)}{L_{K1}} (t - t_1) \quad (4.14)$$

$$i_{S1}(t) = \frac{I_{IN}}{2} - i_{LK1}(t), i_{SEC}(t) = \frac{i_{LK1}(t)}{n}, V_P = \frac{V_O}{n} \quad (4.15)$$

$$V_{DS4}(t) = V_{DS4}(t_1), V_{C1}(t) = V_{C1}(t_1), V_{C2}(t) = V_{C2}(t_1) \quad (4.16)$$

$$T_{21} = \frac{(i_{LK1}(t_1) - I_M) L_{K1}}{\frac{V_O}{n} - V_{C1}(t_1)} \quad (4.17)$$

C. Mode 3 ($t_2 - t_3$):

During mode 3, the mathematical equations of the converter are underlined below:

$$i_{S1}(t) = \frac{I_{IN}}{2} - I_M, i_{S2}(t) = \frac{I_{IN}}{2} + I_M \quad (4.18)$$

$$i_{D1}(t) = i_{D2}(t) = i_{D3-D6}(t) = 0 \quad (4.19)$$

$$V_{DS3}(t) = \frac{I_M}{C_{DS3}(V_{DS3})}(t - t_2) \quad (4.20)$$

$$V_{LM}(t) = V_P(t) = V_{C1}(t) - V_{DS3}(t), \quad V_{DS4}(t) = V_P(t) + V_{C2}(t) \quad (4.21)$$

$$T_{32} = \frac{\left(\frac{V_O}{n} + V_{C1}(t)\right)C_{S3}(V_{DS3})}{I_M} \quad (4.22)$$

4.6. Results and Discussions

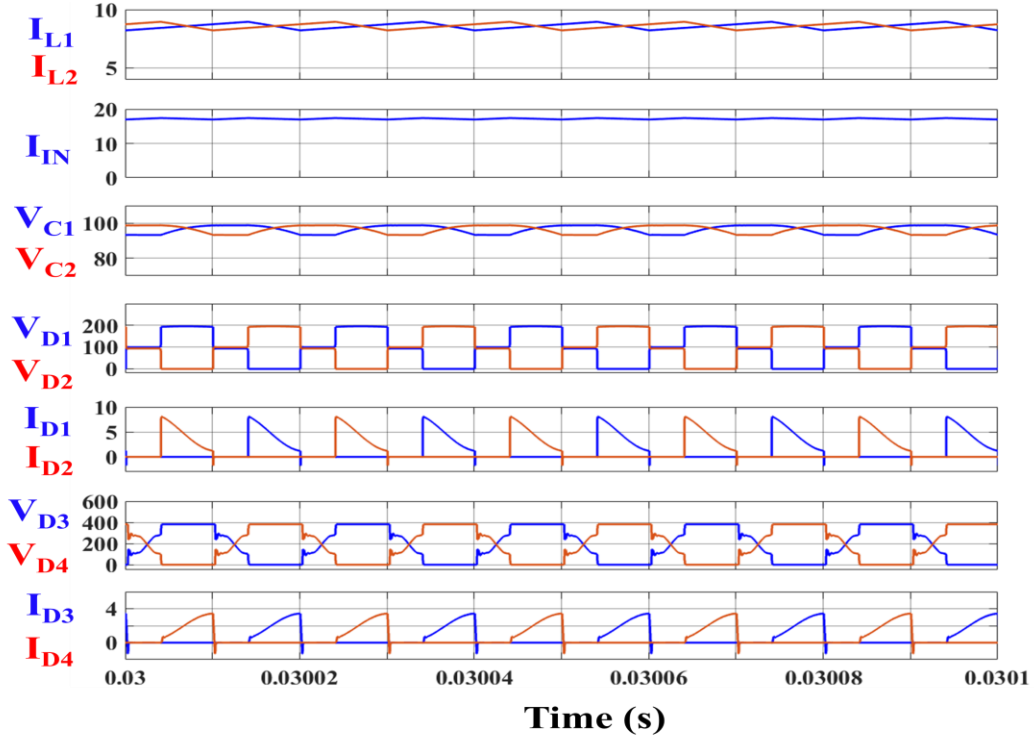
The simulated and experimental performance of the proposed converter is analyzed in this section, and their results are presented to validate their theoretical analysis.

TABLE 4.2: Simulated converter specifications	
Parameter	Value
Input Voltage	20V - 30V(rated)
Output Voltage	380V
Rated Input Power	500W
Switching Frequency	50kHz

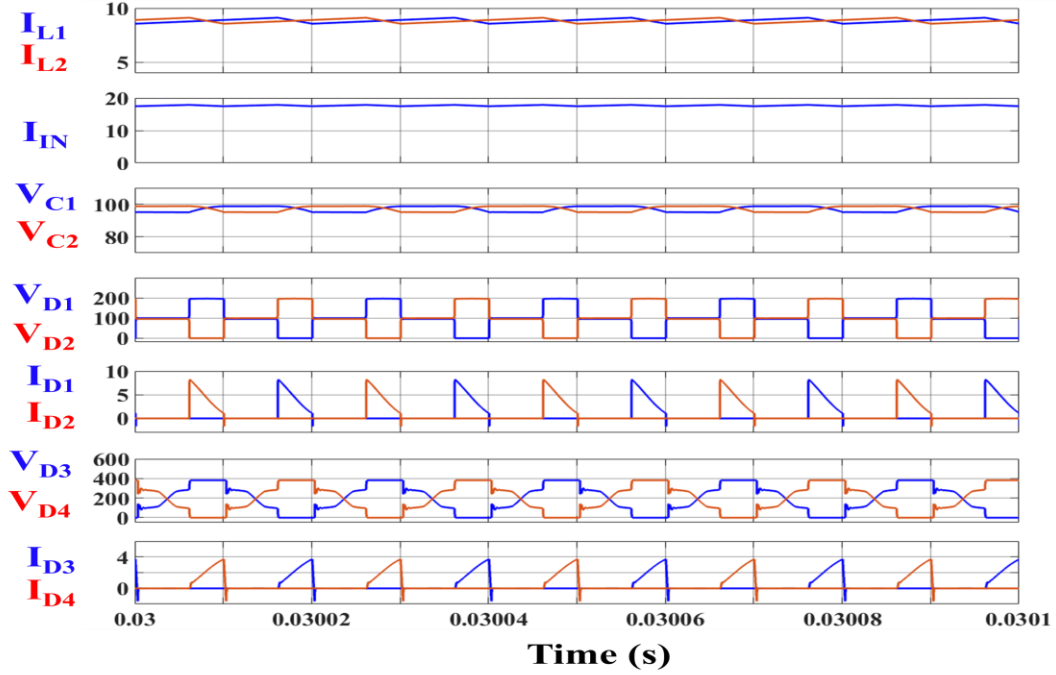
TABLE 4.3: Simulated converter design parameters	
Parameter	Value
Input Inductor (L_1, L_2)	560 μ H
Coupling Capacitor (C_1, C_2)	4.7 μ F
<u>HF Transformer</u>	
Leakage Inductance (L_{K1}, L_{K2})	2.4 μ H
Magnetizing Inductance (L_M)	3.5 mH
Turns Ratio (1:1: n)	1:1:2
Output Capacitor (C_O)	100 μ F

4.6.1. Simulation Results

In this subsection, the simulated performance of the proposed converter is studied and the corroboration between the results and the theoretical analysis is also evaluated. The

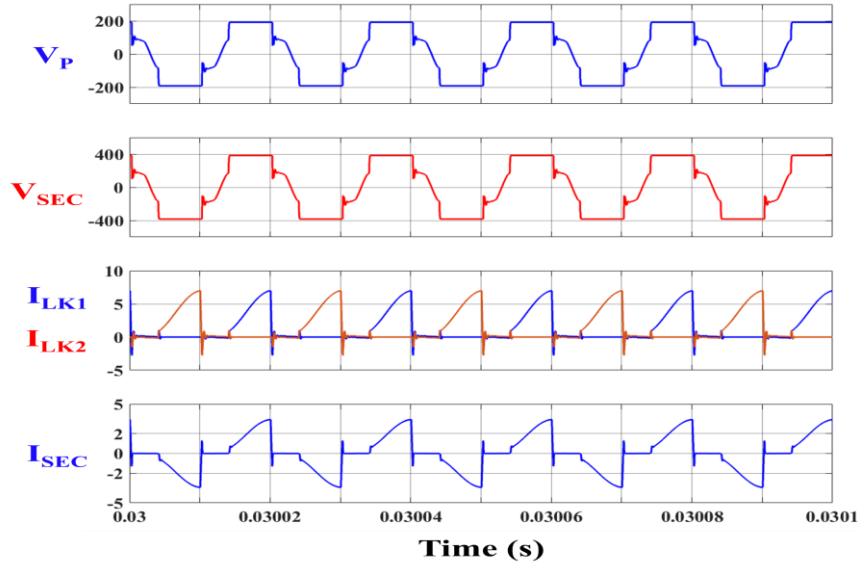


(a)

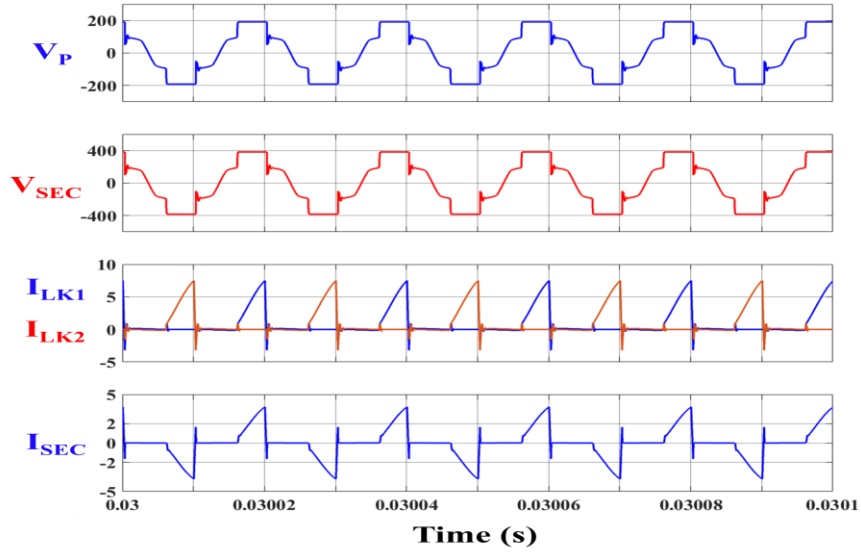


(b)

Fig.4.4. Simulated waveform of inductor currents I_{L1} , I_{L2} (A), input current I_{IN} (A), voltage across coupling capacitors V_{C1} , V_{C2} (V), coupling diode voltages V_{D1} , V_{D2} (V) and currents I_{D1} , I_{D2} (A), rectifier diode voltages V_{D3} (V_{D6}), V_{D4} (V_{D5}) (V) and currents I_{D3} (I_{D6}), I_{D4} (I_{D5}) (A) (a) Input voltage of 30V (b) Input voltage of 20V.



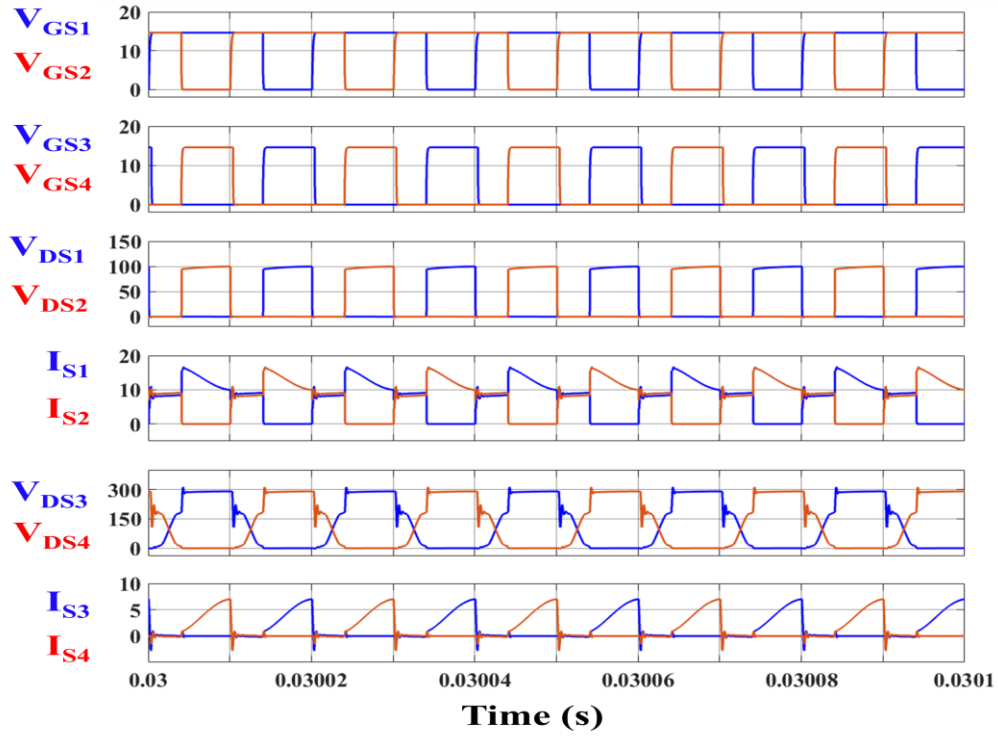
(a)



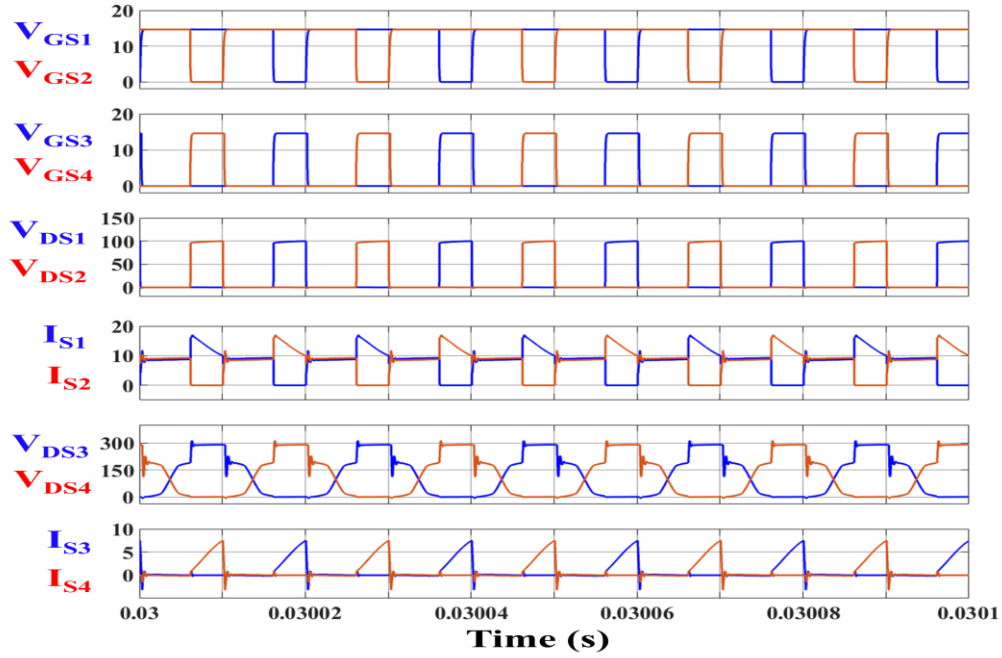
(b)

Fig.4.5. Simulated waveform of voltages and currents of primary winding V_P (V) and I_{LK1} , I_{LK2} (A) and secondary winding V_{SEC} (V) and I_{SEC} (A) of HF transformer (a) Input voltage of 30V (b) Input voltage of 20V

500W converter is simulated in the MATLAB Simulink environment using the converter specifications and design parameters listed in Table 4.2 and 4.3 respectively. The steady-state operation of the simulated converter is evaluated for wide variations in the input voltage ranging from 20V to 30V while the 380V active load is integrated at the output.



(a)



(b)

Fig.4.6. Simulated waveform of gating signals of switches V_{GS1} - V_{GS4} (V), voltages: V_{DS1} , V_{DS2} (V) and currents: I_{S1} , I_{S2} (A) in S_1 and S_2 and voltages: V_{DS3} , V_{DS4} (V) and currents: I_{S3} , I_{S4} (A) in S_3 and S_4 (a) Input voltage of 30V (b) Input voltage of 20V

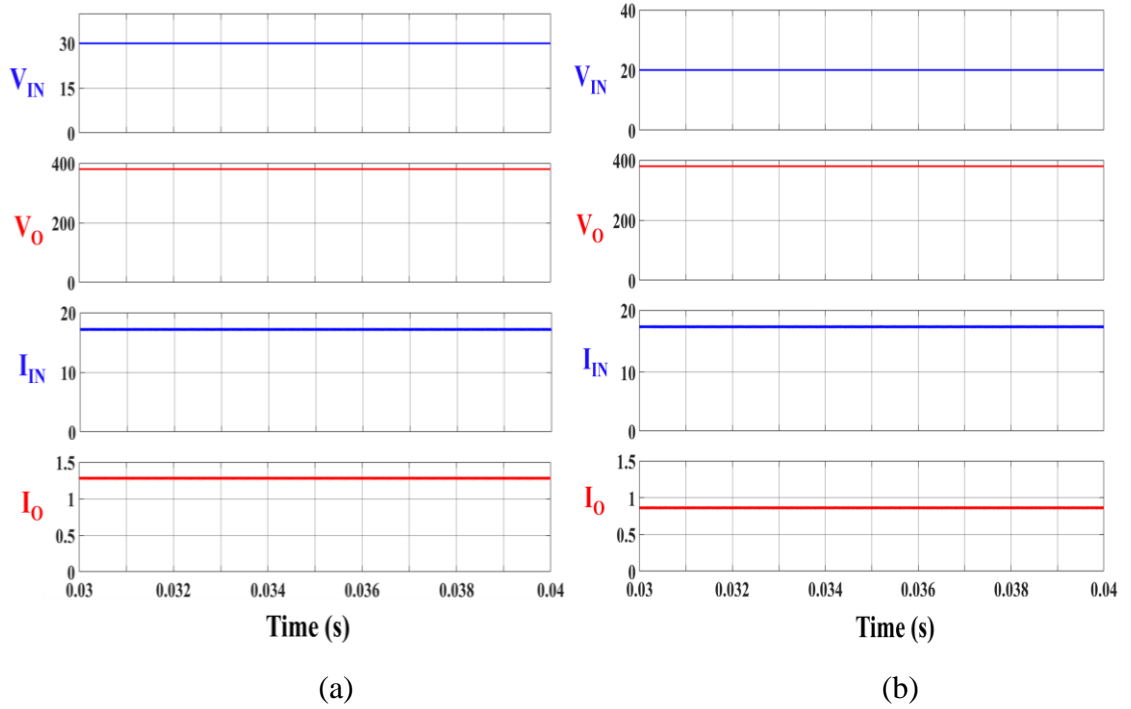


Fig.4.7. Simulated waveform of voltages of input V_{IN} (V) and output V_O (V) and currents of input I_{IN} (A) and output I_O (A) (a) Input voltage of 30V (b) Input voltage of 20V

Furthermore, the converter utilizes the HF transformer with a turns ratio of 2 and operates at a switching frequency of 50kHz.

The steady-state waveforms of input current, inductor currents, coupling capacitor voltages, current, and voltage across the coupling diodes and rectifier diodes is shown in Fig.4.4 for different input voltages, i.e., V_{IN} of 20V and 30V. The result demonstrates the interleaved operation of inductor currents having 180° phase shifted waveform, with their current ripple varying from 8.7% to 6.63% for the changes in input voltage from 30V to 20V. Also, the inductor currents observe prolonged charging during the operation at an input voltage of 20V due to an increase in the duty cycle of the converter. Moreover, the input current ripple observes a significant reduction to the tune of 2.41% for the input voltage of 30V. The voltage across the coupling capacitors for both input voltages is

demonstrated in Fig.4.4(a) and (b) and observes a reduction in the voltage ripple from 5.68% to 3.85% for the variation in the input voltage from 30V to 20V respectively. This affirms the theoretical analysis of the impact on voltage ripple of coupling capacitors due to the duty cycle variations. The voltage and current of the coupling and rectifier diodes are shown in Fig.4.4, with the variation in their conduction time observed as the input voltage changes. The voltage and current through the primary and secondary windings of the HF transformer for different input voltages are presented in Fig.4.5. The voltage waveforms of primary and secondary windings of the HF transformer indicate the turns ratio of 2 while the quasi-sinusoidal waveform of the winding currents is also observed from the results. The switching performance of the proposed converter for different input voltages is demonstrated in Fig.4.6. The results show the switching sequence of the converter with a slight overlap between the gating pulses of S_1 (S_2) and S_3 (S_4), with the decrease in input voltage from 30V to 20V increases the on-time of the gating pulses of S_1 and S_2 . Moreover, the waveforms exhibit minimal turn-off voltage spike in the switches S_1 and S_2 , thereby highlighting the natural voltage clamping by the coupling capacitors. The quasi-ZCS operation in the switches S_3 and S_4 with the small magnetizing current in the switches and zero switch voltage during their turn-off is observed from the results. Furthermore, the quasi-ZCS operation in the switches is independent of the input voltage variations in the converter and mitigates the switching losses during their turn-off transition. Also, during the turn-on transition in switches S_3 and S_4 , minimal switching losses are observed. The voltage spike during the turn-off of S_3 and S_4 is also mitigated due to the energy transfer of the leakage energy to the output. The slow charging and discharging of the switch capacitance of S_3 and S_4 is due to a small magnetizing current as evident from the results in Fig.4.6 and highlights the gradual rise and fall of the switch voltage during the overlapping

period when both S_1 and S_2 conducts. The decrease in the input voltage from 30V to 20V witnessed an increase in the operating duty cycle of the converter and the duration of the overlapping period, leading to a prolonged duration of charging and discharging of the switch (S_3 , S_4) capacitance. Fig.4.7 shows the steady state input-output profile of the converter for different input voltages. The variation in the input voltage from 30V to 20V observes a reduction in the output current of the converter from 1.273A to 0.84A while the input current and output voltage are maintained at 16.67A and 380V respectively.

The steady-state simulation results of the MCF-HGIIC validate the theoretical analysis and modeling of the converter and further highlight the improvements over the conventional CF-HGIIC.

4.6.2. Experimental Results

The experimental performance of the proposed converter is extensively investigated in this subsection. The scaled-down hardware prototype of a 190W proposed converter shown in Fig.4.8 operating at a switching frequency of 50kHz is developed in the laboratory in

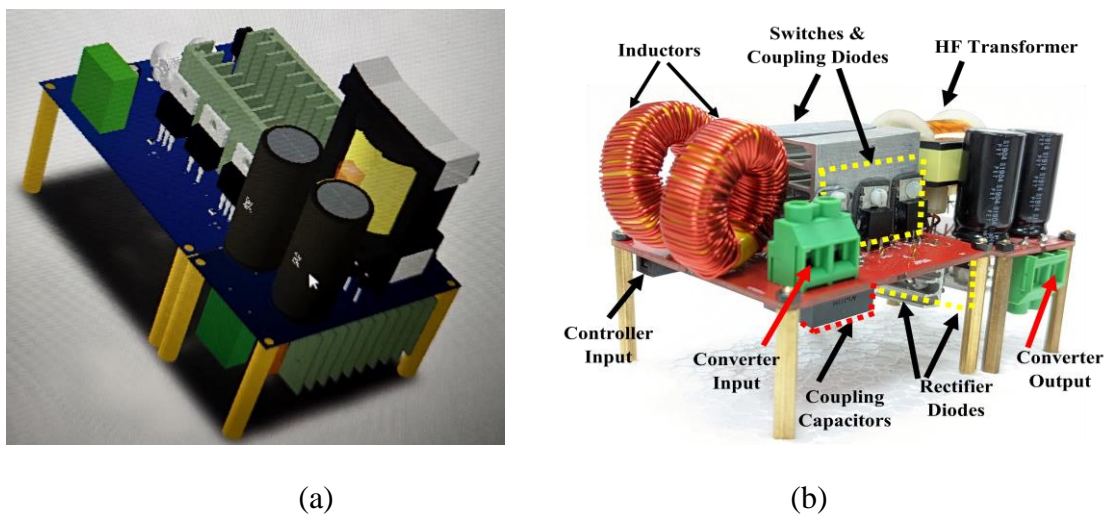


Fig.4.8. MCF-HGIIC (a) 3-D PCB design (b) Hardware Prototype

TABLE 4.4: Experimental converter specifications	
Parameter	Value
Input Voltage	18V - 26V(rated)
Output Voltage	270V
Rated Input Power	190W
Switching Frequency	50kHz

TABLE 4.5: Experimental converter design parameters	
Parameter	Value
Input Inductor (L_1, L_2)	MultiComp Pro -MCAP series (Torroidal): 560 μ H
Coupling Capacitor (C_1, C_2)	Kemet- R75 series (Polypropylene):3.3 μ F, 250V
HF Transformer	ETD Ferrite Core (Ferroxcube 3C90), Primary Turns- 32, 32, Secondary Turns- 64, Turns ratio- 1:1:2, $L_{K1}=2.71\mu$ H, $L_{K1}=2.79\mu$ H
Output Capacitor (C_O)	Electrolytic Capacitor:2 x100 μ F, 450V (in series)
Switches (S_1, S_2)	SQP90142E_GE3; 200V, 12.7m Ω
Switches (S_3, S_4)	IPP60R070CFD7; 600V, 70m Ω
Coupling Diodes (D_1, D_2)	VS-C06ET07T-M3; 650V,6A
Rectifier Diodes ($D_3 - D_6$)	VS-C04ET07T-M3; 650V,4A
Gate Driver	TC4420VOA

accordance with the converter specifications and design parameters in Tables 4.4 and 4.5. The hardware prototype of MCF-HGIIC is experimentally tested for different input voltages i.e., V_{IN} of 26V and 18V while feeding the power to the 270V active load. Furthermore, to maintain consistency and uniformity between the experimental and simulated performance of the proposed converter, the simulated results for the above-mentioned scaled-down ratings are also presented.

The steady-state experimental and simulated waveform of the inductor currents (I_{L1}, I_{L2}), coupling capacitor voltage (V_{C1}), and the drain to source voltage across the switch S_1 (V_{DS1})

for the input voltages of 26V and 18V is demonstrated in Fig.4.9 and 4.10 respectively. Fig.4.9 and 4.10 shows the 180° phase shifted inductor currents which underlines the interleaved operation while further observing longer charging period of inductors while operating at lower input voltage of 18V. Moreover, the experimental results also highlight the reduction in the steady state voltage ripple of the coupling capacitor from 5V to 3.8V as the input voltage dips from 26V to 18V. The experimental results corroborate the theoretical analysis of the coupling capacitor and the influence of duty cycle variation on their voltage ripple. Fig.4.11 and 4.12 demonstrate the experimental and simulated waveforms of the primary and secondary winding voltage of the HF transformer and the quasi-sinusoidal secondary winding current for different input voltages. The practical turns ratio of 2 of ETD ferrite core-based HF transformer is evident from the winding voltages in experimental waveforms in Fig.4.11 (a) and 4.12(a). Additionally, the waveshape of winding voltages and quasi-sinusoidal secondary winding current for different input voltages in the experimental results closely match the simulated waveforms. Fig.4.13 and 4.14 display experimental and simulated waveforms of voltage across the coupling diodes (D_1 , D_2) for input voltages of 26V and 18V. It is observed from the experimental results in Fig.4.13(a) and 4.14(a) that a reduction in the input voltage of the converter from 26V to 18V reduces the conduction period of the diodes, which is attributed to the increase in the duty cycle. The quasi-ZCS operation of switch S_3 during its turn-off is demonstrated in Fig.4.15 and 4.16, where the waveforms of gating signals of S_1 (V_{GS1}) and S_3 (V_{GS3}), and the current (I_{S3}) and voltage (V_{DS3}) across S_3 is shown for the input voltage of 26V and 18V. It is observed from the results that during slight overlap between V_{GS1} and V_{GS3} , the switch current naturally decays to a small magnetizing current. The switch S_3 turn-off with a small magnetizing current and mitigates the turn-off switching losses. As a result, the

experimental waveforms in Fig.4.15(a) and 4.16(a) highlight the quasi-ZCS operation of S_3 which is independent of the input voltage variations. It is pertinent to observe from the experimental result in Fig.4.16(a) that the turn-on switching loss for the switch S_3 is reduced during the converter operation at an input voltage of 18V. Additionally, a small turn-off voltage spike is observed in the switch S_3 . The experimental waveform in Fig.4.15(a) and 4.16(a) also exhibits slow dV/dt of switch voltage (V_{DS3}) during its turn-off which conforms to the mathematical analysis and the simulated results. The experimental efficiency of the proposed converter for variations in the input power while operating at the input voltages of 26V and 18V is shown in Fig.4.17. In Fig.4.17(a), the converter operating at an input voltage of 26V achieves an efficiency of 94.1% at the rated input power of 190W. Moreover, while operating at an input voltage of 18V, the proposed converter attains the efficiency of 93.1% at 131W as shown in Fig.4.17(b). The loss analysis of the proposed converter for a rated input power of 190W and input voltage of 26V is shown in Fig.4.18. The loss analysis indicates that inductor and diode losses are primary contributors to converter loss while the losses in the switches and HF transformer are relatively nominal. Further efficiency improvements in the converter can be achieved by better PCB design and more optimized component selection.

It is observed that the experimental results of the converter corroborate with the simulated results and further validate the theoretical analysis of the converter. Additionally, the results also highlight the salient features of the proposed converter. The experimental performance of the MCF-HGIIC also demonstrates its ability to practically operate under wide variations in the input voltage and duty cycle, while also highlighting its capability to experimentally operate at significantly higher voltage gain of nearly 16 with high

efficiency, thereby affirming its suitability for MLIC.

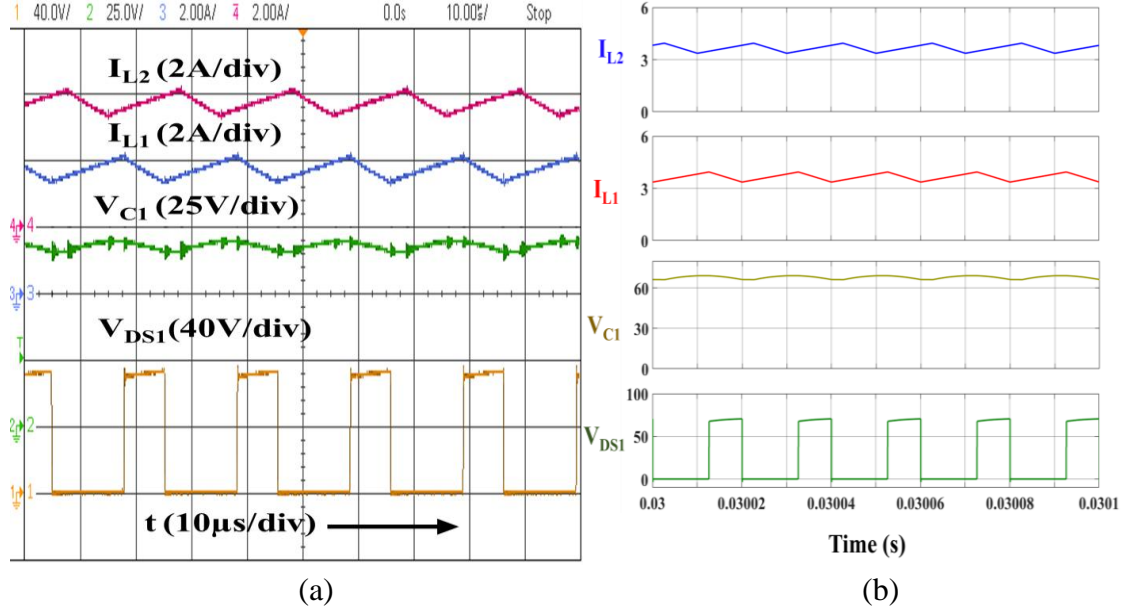


Fig.4.9. Waveform of inductor currents I_{L1} , I_{L2} (A) coupling capacitor voltage V_{C1} (V), drain to source voltage of switch S_1 : V_{DS1} (V) for input voltage of 26V (a) Experimental result (b) Simulated result

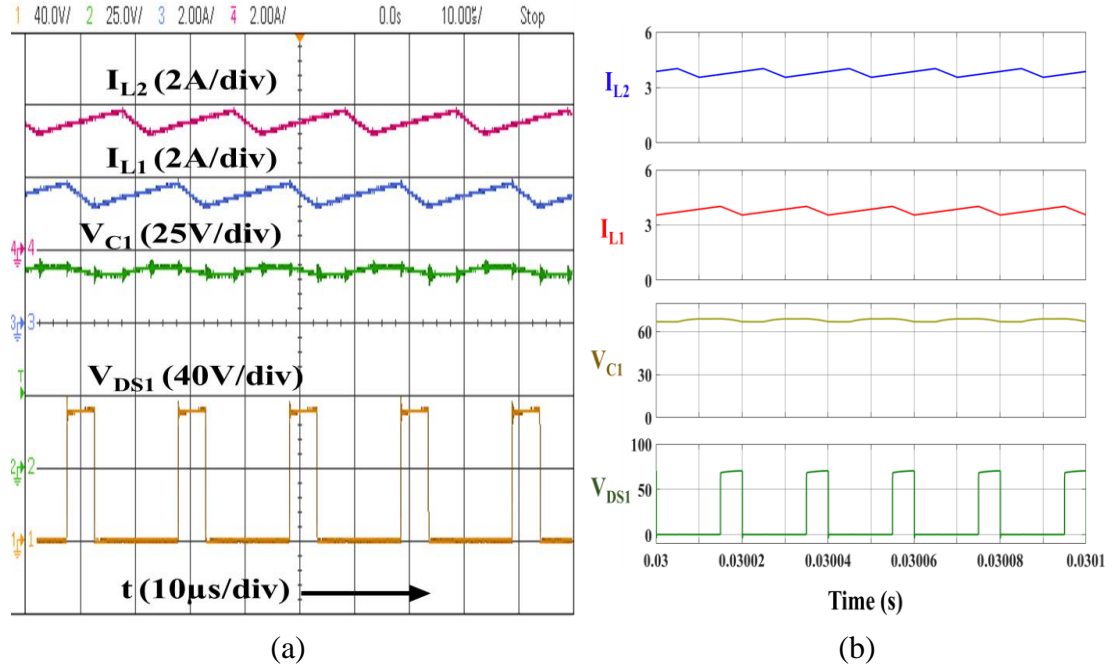
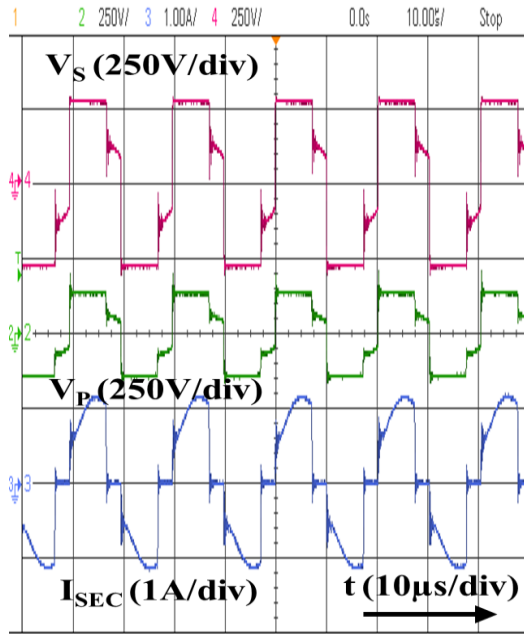
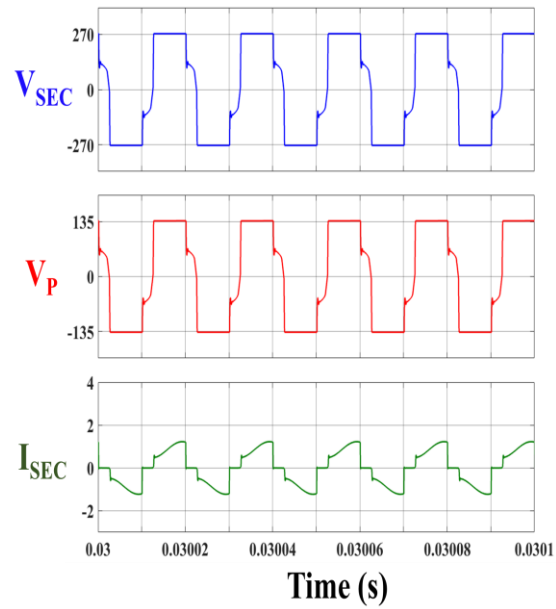


Fig.4.10. Waveform of inductor currents I_{L1} , I_{L2} (A) coupling capacitor voltage V_{C1} (V), drain to source voltage of switch S_1 : V_{DS1} (V) for input voltage of 18V (a) Experimental result (b) Simulated result

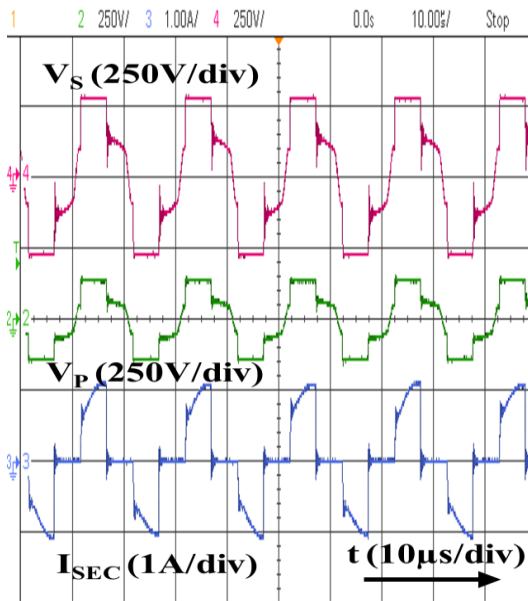


(a)

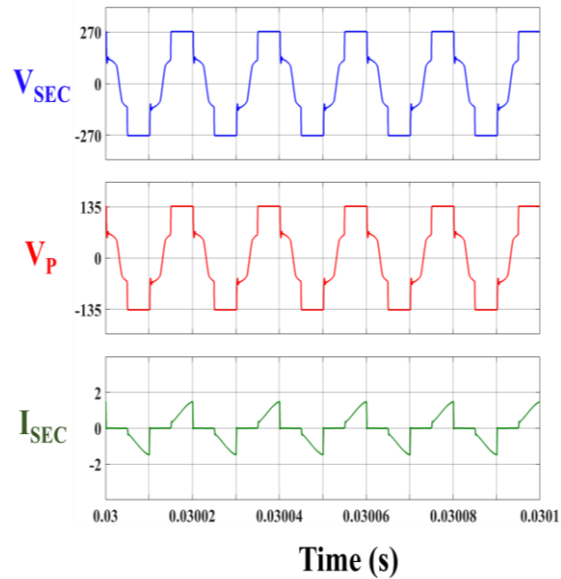


(b)

Fig.4.11. Waveform of voltage V_{SEC} (V) and current in secondary winding I_{SEC} (A) and voltage across primary winding V_P (V) for input voltage of 26V (a) Experimental result (b) Simulated result

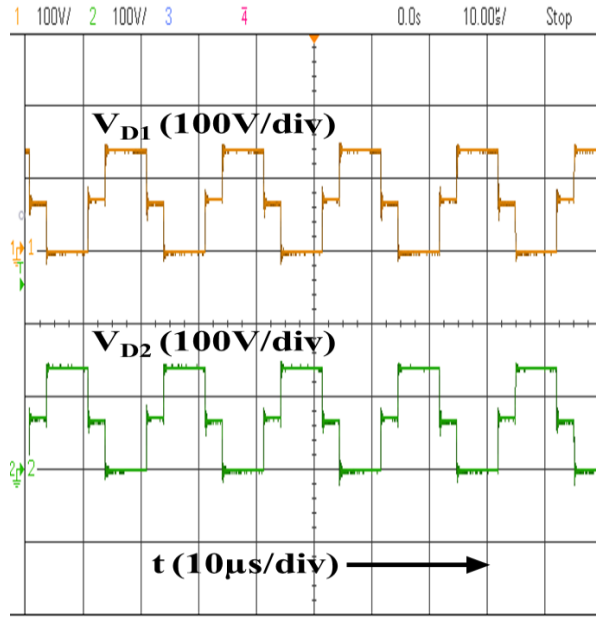


(a)

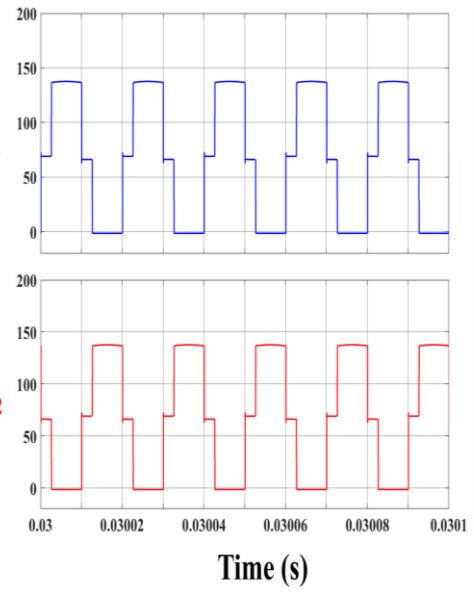


(b)

Fig.4.12. Waveform of voltage V_{SEC} (V) and current in secondary winding I_{SEC} (A) and voltage across primary winding V_P (V) for input voltage of 18V (a) Experimental result (b) Simulated result

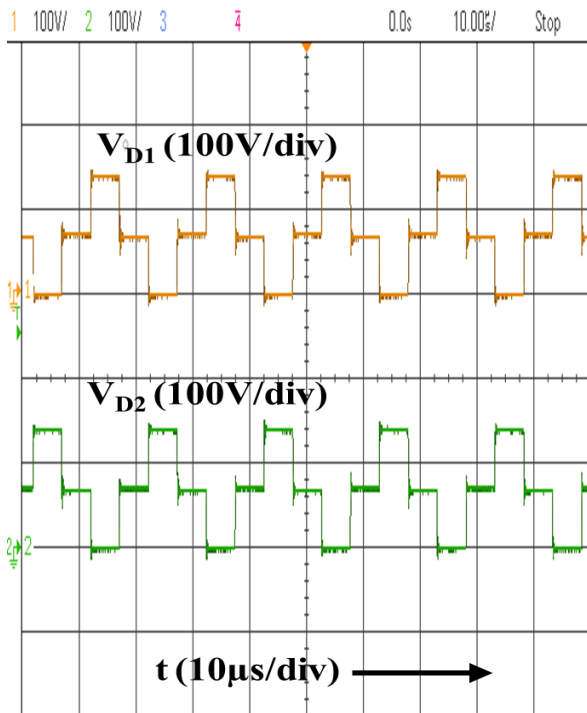


(a)

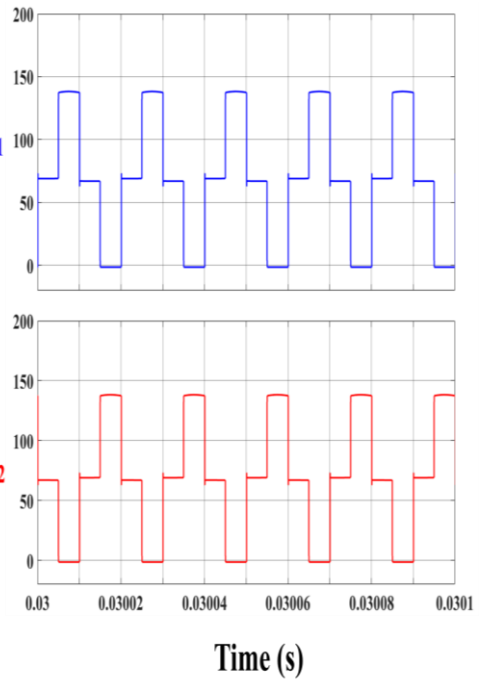


(b)

Fig.4.13. Waveform of voltage across coupling diodes V_{D1} , V_{D2} (V) for input voltage of 26V (a) Experimental result (b) Simulated result

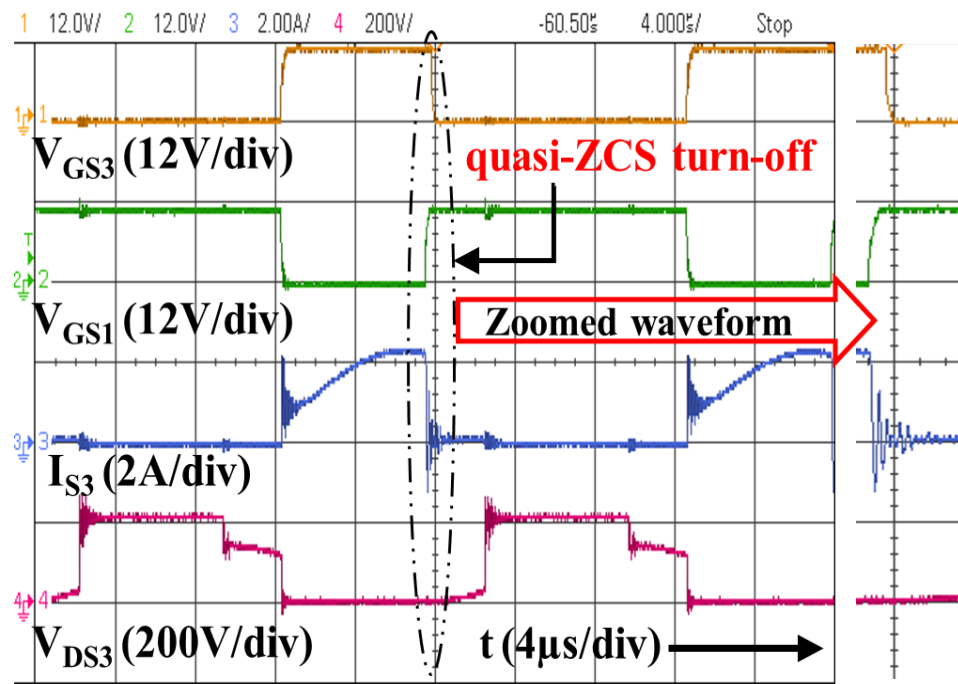


(a)

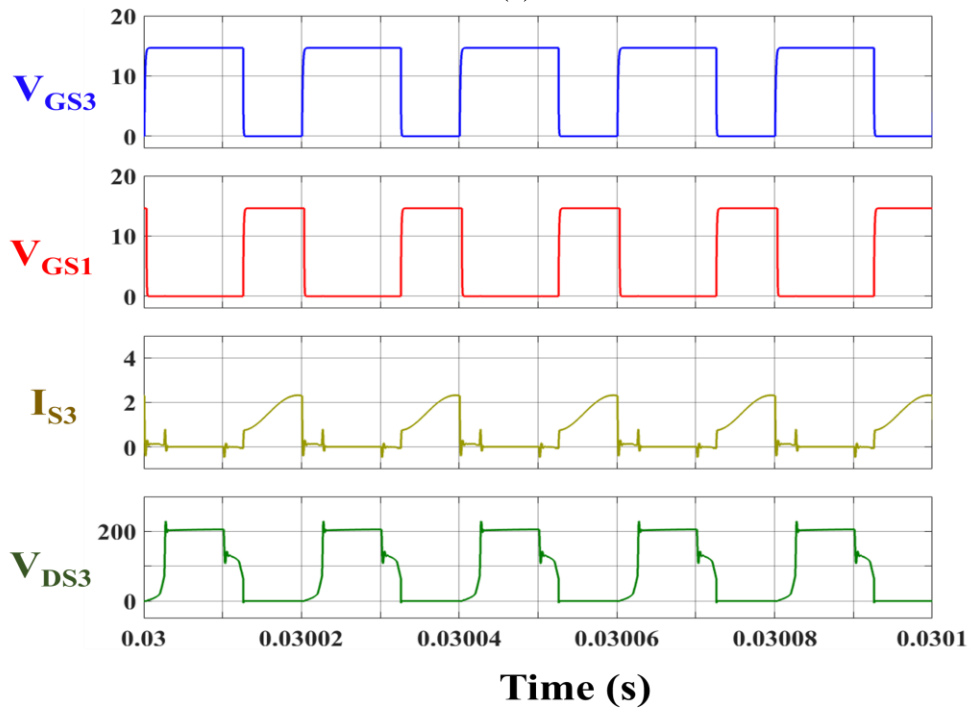


(b)

Fig.4.14. Waveform of voltage across coupling diodes V_{D1} , V_{D2} (V) for input voltage of 18V (a) Experimental result (b) Simulated result

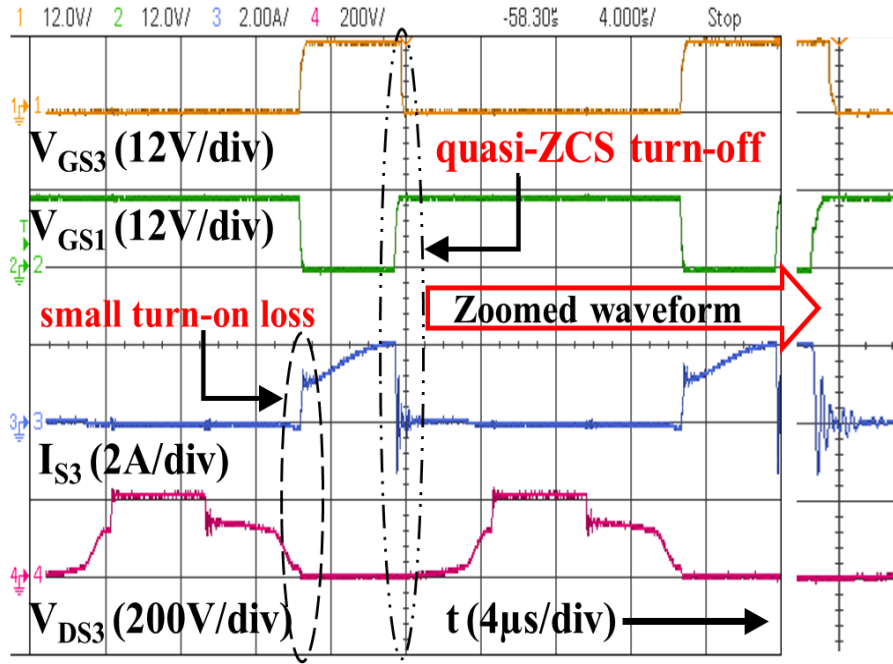


(a)

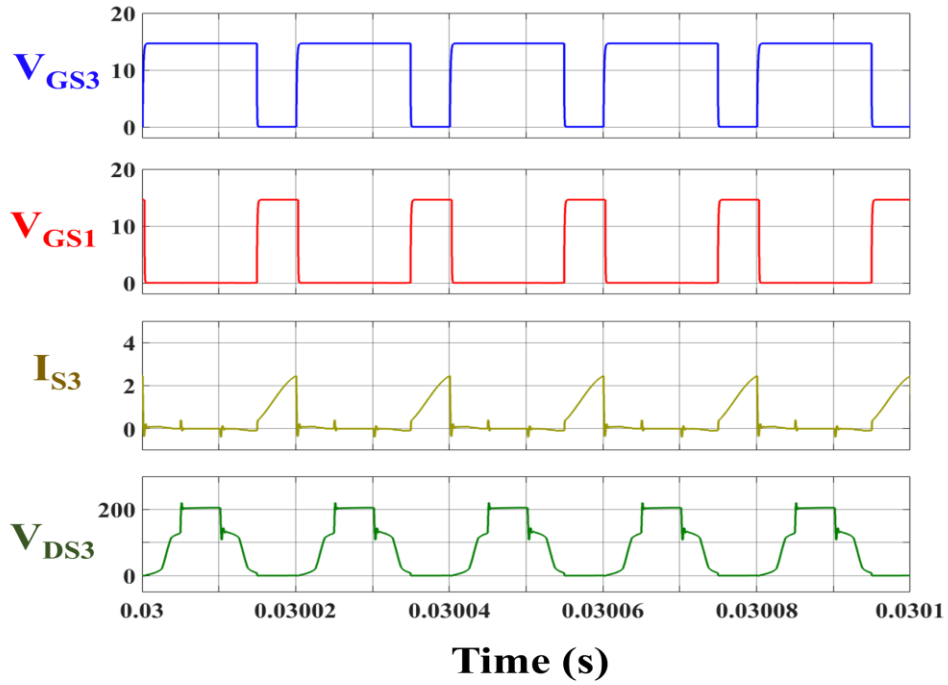


(b)

Fig.4.15. Waveform of gating signals of S_3 : V_{GS3} (V) and S_1 : V_{GS1} (V), switch S_3 voltage V_{DS3} (V) and current I_{S3} (A) for input voltage of 26V (a) Experimental result (b) Simulated result



(a)



(b)

Fig.4.16. Waveform of gating signals of S_3 : V_{GS3} (V) and S_1 : V_{GS1} (V), switch S_3 voltage V_{DS3} (V) and current I_{S3} (A) for input voltage of 18V (a) Experimental result (b) Simulated result

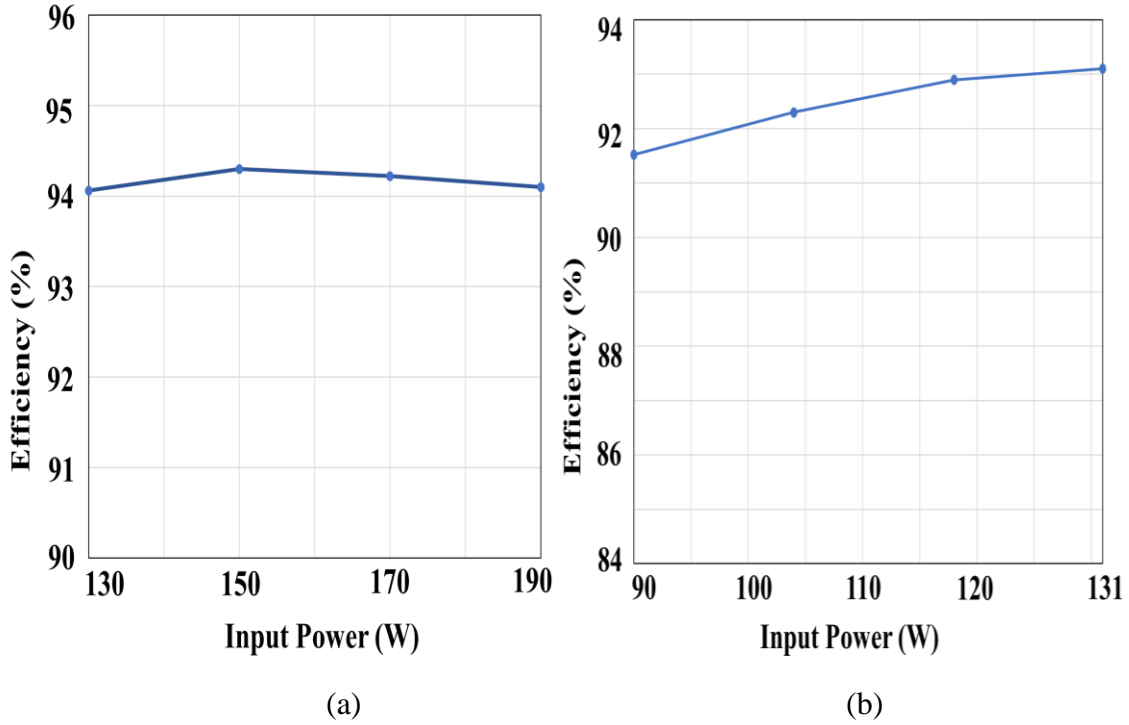


Fig.4.17. Experimental efficiency of MCF-HGIC for variation in input power at (a) Input voltage of 26V (b) Input voltage of 18V

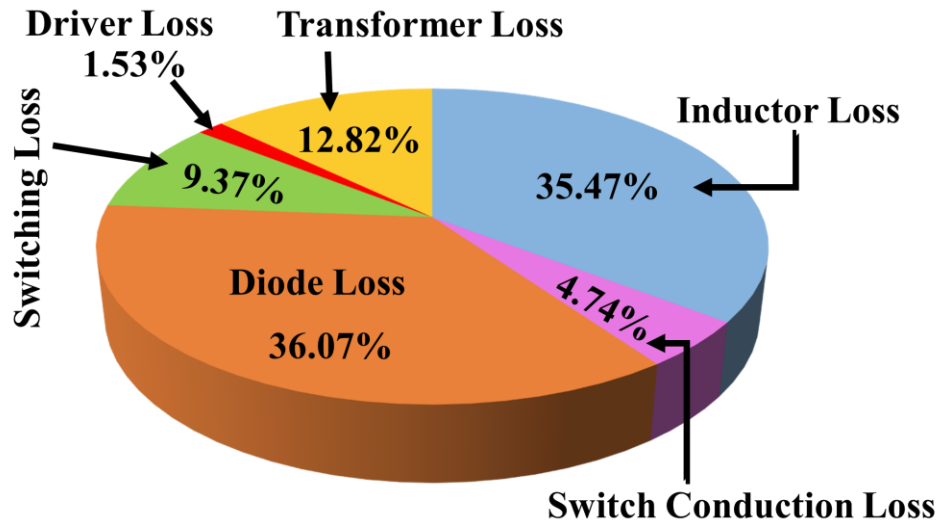


Fig.4.18. Loss analysis of MCF-HGIC for rated power of 190W and input voltage of 26V

4.7. Conclusion

This chapter presented the improvements and modifications in the conventional CF-HGIIC topology. Modifications in the conventional CF-HGIIC allowed utilization of all low side switches which simplified the gate drive design while eliminating the requirement of additional isolated power supplies and low EMI issues. Moreover, the MCF-HGIIC topology achieved quasi-ZCS operation during turn-off in switches S_3 and S_4 using the modulation scheme and mitigated their turn-off switching losses. The results also indicated that switches S_3 and S_4 exhibited minimal turn-on switching losses while operating at higher duty cycle. It is observed that the existing merits of conventional CF-HGIIC are inherited by the MCF-HGIIC. The topological operating modes of the MCF-HGIIC with the detailed mathematical analysis of each operating mode of the converter are discussed in this chapter.

The simulated performance of the proposed converter has been analyzed in MATLAB Simulink environment by implementing the model of MCF-HGIIC based on the simulated converter specification and its corresponding calculated design parameters. The simulated performance of the proposed converter underlined the merits of the converter and validated the theoretical analysis. The wide operating range of the converter is demonstrated by its ability to seamlessly operate at different input voltages. Additionally, the converter exhibited wide gain variations and highlighted its ability to achieve higher voltage gain during the operation at lower input voltage while using a smaller turns ratio of the HF transformer. The simulated results further highlighted significantly smaller input current ripple in the MCF-HGIIC and natural voltage clamping of switches S_1 and S_2 .

The hardware prototype of the MCF-HGIIC developed in the laboratory using the computed design parameters has been experimentally tested. The experimental results

demonstrated the operation of the converter for different input voltages and highlighted the input interleaving and natural voltage clamping of switches in S_1 and S_2 . Additionally, the results also indicated the superior performance of the HF transformer. The switching performance of the switch S_3 while operating the converter at different input voltages and exhibiting quasi-ZCS operation during turn-off has been observed from the results. The experimental efficiency of the hardware prototype of MCF-HGIIC and its loss analysis has been analyzed and showed higher converter efficiency while operating at different input voltages. The operation of the converter prototype to experimentally deliver a significantly higher voltage gain of nearly 16 is indicated by the experimental results. Furthermore, the performance of the hardware prototype of MCF-HGIIC further experimentally validated the simulated performance and conformed to the theoretical analysis and converter design. The merits of the proposed converter and its superior performance while operating under wide input voltage variations stressed the candidacy of the converter topology for MLIC.

CHAPTER 5

MULTI-INPUT CONFIGURATION OF CURRENT-FED HIGH-GAIN ISOLATED INTERFACING CONVERTER

5.1. General

Chapters 3 and 4 have principally focussed on the current-fed high gain isolated interfacing converter (CF-HGIIC) and evaluated its merits, topological improvements, and performance under different operating conditions. Fundamentally, the topological structure of CF-HGIIC is based on the single-input configuration where a single DC source has been integrated with the converter. In this chapter, the multi-input configuration of CF-HGIIC has been introduced and explored. The topological structure of the proposed multi-input current-fed high gain isolated interfacing converter (MI-CF-HGIIC) and its operating modes have been studied and mathematically analyzed. Moreover, the modulation scheme of the proposed converter and its design are also discussed. The proposed converter topology operating at its rated input power of 1kW while integrating two 30V DC sources at its input and further feeding the 380V active load (DC sink) has been simulated on the MATLAB Simulink environment. The simulated performance of the proposed converter has been comprehensively evaluated for the symmetric and asymmetric operating conditions to validate its merits and study its candidacy for a multi-input module interfacing converter (MMIC). The chapter is organized as follows: Section 5.2 discusses the topological structure of MI-CF-HGIIC and its modulation scheme while the topological operating modes of converter are provided in section 5.3. Section 5.4 presents the

mathematical modeling of the converter while its design is briefly discussed in section 5.5. The simulated performance of the MI-CF-HGIIC is presented in section 5.6.

5.2. Proposed Converter Topology and Modulation Scheme

The topological structure and the modulation scheme of the proposed converter have been discussed in this section.

5.2.1. Proposed Converter Topology

The multi-input current-fed high gain isolated interfacing converter (MI-CF-HGIIC) has been proposed in this chapter and retains all the inherent topological merits and salient features of the conventional CF-HGIIC. Fig.5.1 shows the topological structure of the proposed MI-CF-HGIIC operating in the continuous conduction mode with its operating duty cycle ($d \geq 0.5$). The topological structure of the converter is further divided into power modules which are present on the primary side of the converter. Each power module utilizes

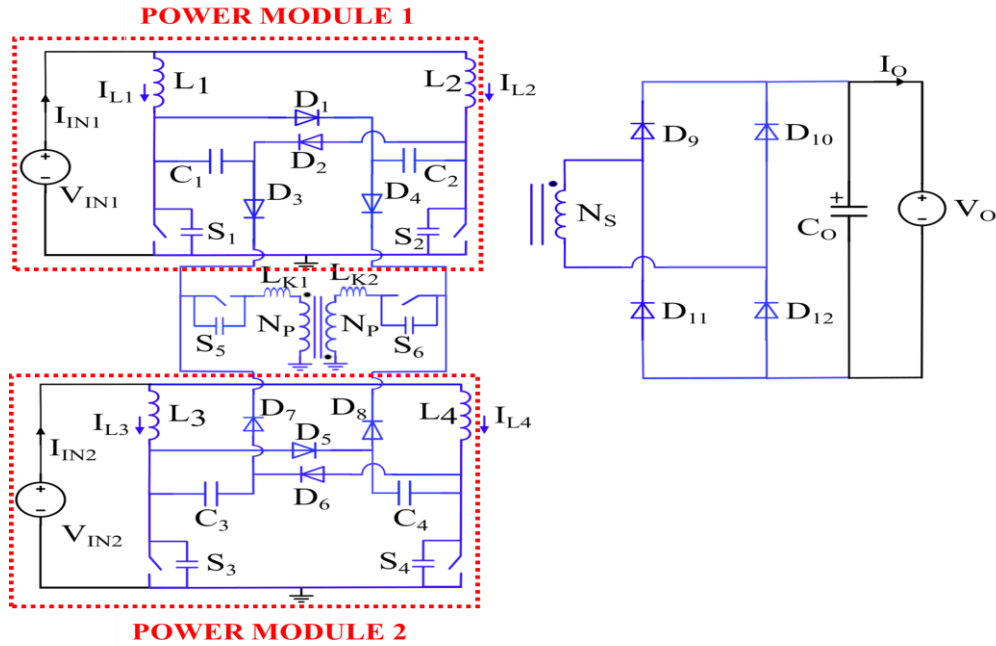


Fig.5.1. Topological structure of MI-CF-HGIIC

TABLE 5.1: Parametric notations of MI-CF-HGHC			
Parameters		Voltage	Current
Input		V_{IN1}, V_{IN2}	I_{IN1}, I_{IN2}
Output		V_O	I_O
Input Inductor	Module 1: L_1, L_2	V_{L1}, V_{L2}	I_{L1}, I_{L2}
	Module 2: L_3, L_4	V_{L3}, V_{L4}	I_{L3}, I_{L4}
Coupling Capacitor	Module 1: C_1, C_2	V_{C1}, V_{C2}	I_{C1}, I_{C2}
	Module 2: C_3, C_4	V_{C3}, V_{C4}	I_{C3}, I_{C4}
Switches	Module 1: S_1, S_2	Drain to Source: V_{DS1}, V_{DS2} Gate to Source: V_{GS1}, V_{GS2}	I_{S1}, I_{S2}
	Module 2: S_3, S_4	Drain-Source Voltage: V_{DS3}, V_{DS4} Gate-Source Voltage: V_{GS3}, V_{GS4}	I_{S3}, I_{S4}
	S_5, S_6	Drain-Source Voltage: V_{DS5}, V_{DS6} Gate-Source Voltage: V_{GS5}, V_{GS6}	I_{S5}, I_{S6}
Coupling Diodes	Module 1: D_1, D_2	Reverse Biased: V_{D1}, V_{D2} Forward Drop: V_{DF1}, V_{DF2}	I_{D1}, I_{D2}
	Module 2: D_5, D_6	Reverse Biased: V_{D5}, V_{D6} Forward Drop: V_{DF5}, V_{DF6}	I_{D5}, I_{D6}
Blocking Diodes	Module 1: D_3, D_4	Reverse Biased: V_{D3}, V_{D4} Forward Drop: V_{DF3}, V_{DF4}	I_{D3}, I_{D4}
	Module 2: D_7, D_8	Reverse Biased: V_{D7}, V_{D8} Forward Drop: V_{DF7}, V_{DF8}	I_{D7}, I_{D8}
Rectifier Diodes	$D_9 - D_{12}$	Reverse Biased: $V_{D9} - V_{D12}$ Forward Drop: $V_{DF9} - V_{DF12}$	$I_{D9} - I_{D12}$
<u>HF Transformer</u>			
Primary Winding		V_P	I_{LK1}, I_{LK2}
Secondary Winding		V_{SEC}	I_{SEC}
Magnetizing Inductance		V_{LM}	I_M

dual input inductors L_1, L_2 (L_3, L_4) for facilitating continuous input current while incorporating coupling diodes D_1, D_2 (D_5, D_6), coupling capacitors C_1, C_2 (C_3, C_4), and blocking diodes D_3, D_4 (D_7, D_8). The power modules are integrated with the primary windings of high frequency (HF) transformer using switches S_5 and S_6 . The secondary side of the converter incorporates a full-bridge diode rectifier ($D_9 - D_{12}$) and the output capacitor (C_O). Moreover, the HF transformer interlinks the primary and secondary sides of the converter while having leakage inductance (L_{K1}, L_{K2}) and magnetizing inductance (L_M) and utilizing the low turns ratio (1:1:n). The proposed MI-CF-HGIIC having dual inputs integrates two DC sources and feeds the power to the active load (DC sink). The notations of different converter parameters of MI-CF-HGIIC are listed in Table 5.1.

The proposed MI-CF-HGIIC utilizes a low turns ratio of HF transformer to achieve high voltage gain and exhibits a unique distributed structure with parallel conduction paths to minimize the current stress and losses in the components. Moreover, the converter experiences a significant reduction in the input current ripple by employing interleaved operation and observes higher tolerance to the DC bias in the HF transformer during the asymmetric operation. Another salient feature of the proposed converter is the natural voltage clamping of the switches S_1, S_2, S_3 and S_4 , eliminating the requirement for an additional snubber or clamp circuit. MI-CF-HGIIC demonstrates minimal inter-converter circulating currents when multiple such converter units are operated in parallel. Additionally, the converter also achieves minimal inter-modular circulating currents between its power modules, thereby preventing severe conduction losses in the converter. The decoupled operation of the power modules of the converter with minimal interference

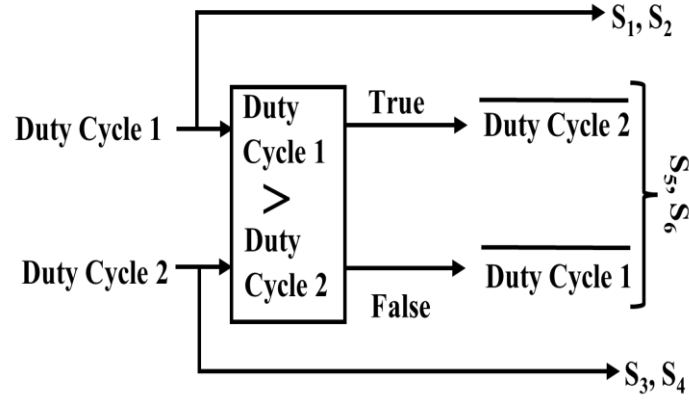


Fig.5.2. Modulation scheme of MI-CF-HGIIC

between them allows each source to independently feed the power to the load. This enables the converter to seamlessly operate under asymmetric operating conditions.

5.2.2. Modulation Scheme

The modulation scheme of the proposed converter is shown in Fig.5.2. The gating signals of the low side switches of each power module have an on-time greater than 50%. Moreover, the gating pulses of the switches S_1 (S_3) and S_2 (S_4) are 180° phase shifted. The switches S_5 and S_6 interlink both the power modules with the HF transformer and their operation is critical for the power transfer to the active load. The gating signals of S_5 and S_6 shown in Fig.5.2 depend on the operating duty cycle of both power modules and the complement of the smaller of the two duty cycles. This facilitates seamless operation of the converter and power flow during the asymmetric operation.

5.3. Topological Modes of Operation of Converter

In this section, the topological operating modes of the proposed converter for different operating intervals are examined. The analytical waveform of the converter is shown in

Fig.5.3. Additionally, the equivalent circuits of the MI-CF-HGIIC for each operating interval are depicted in Fig.5.4.

5.3.1. Mode 1 ($t_0 - t_1$) : Power Transfer Mode – Fig.5.4(a)

At the start of this operating mode at the instant t_0 , switches S_2 (S_4) are still conducting while the switches S_1 (S_3) turn off, which allows the inductors L_1 (L_3) to start discharging while inductors L_2 (L_4) continue to charge. Subsequently, the coupling diodes D_1 (D_5) start conducting whereas D_2 (D_6) is still reverse biased. At the instant t_0 , the switch S_5 turn-on, facilitating the aggregation of voltage across coupling capacitors C_1 (C_3) and C_2 (C_4) in each module which reflects across the primary winding of the HF transformer and forward biases the blocking diodes of each module D_3 (D_7). Moreover, the power is transferred to the active load through the HF transformer and rectifier diodes D_9 and D_{12} till the end of this operating mode.

5.3.2. Mode 2 ($t_1 - t_2$) : Overlapping Mode – Fig.5.4(b)

At the beginning of this mode at the instant t_1 , the switches S_1 (S_3) turn on while switches S_2 (S_4) are still conducting, thereby enabling the inductors L_1 (L_3) to start charging while inductors L_2 (L_4) continues to charge. The coupling diodes D_1 (D_5) and blocking diodes D_3 (D_7) are reverse-biased during this operating mode. Furthermore, there is no power transfer to the active load in this mode as the switch S_5 turn-off at the instant t_1 . Also, during this operating mode in the interval ($t_1 - t_2$), the output capacitor C_O feeds the load.

5.3.3. Mode 3 ($t_2 - t_3$) : Power Transfer Mode – Fig.5.4(c)

At the beginning of this mode at an instant t_2 , the switches S_2 (S_4) turn off, causing the inductors L_2 (L_4) to start discharging while inductors L_1 (L_3) continue to charge.

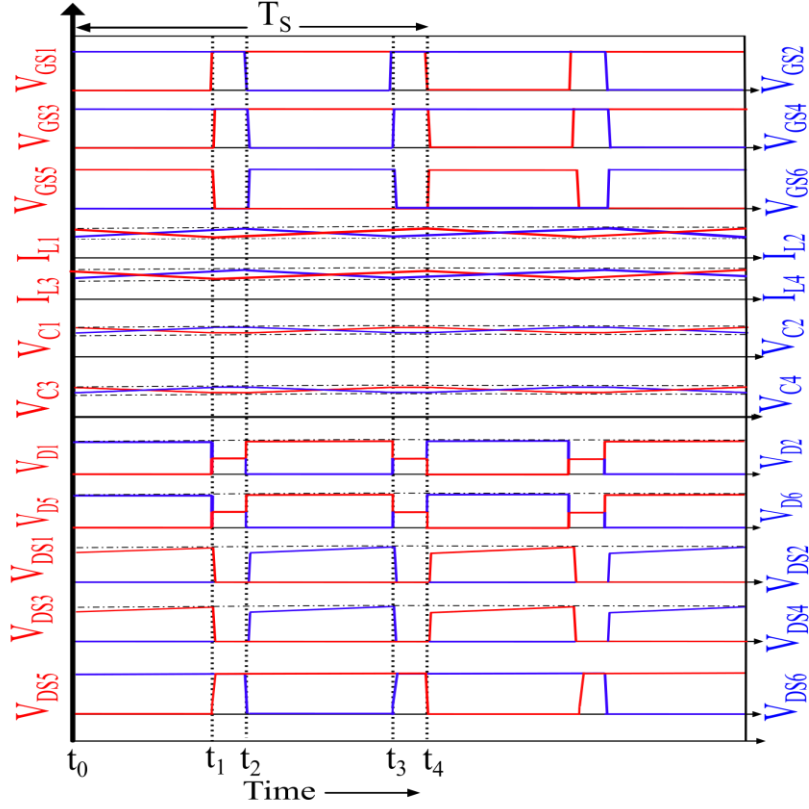
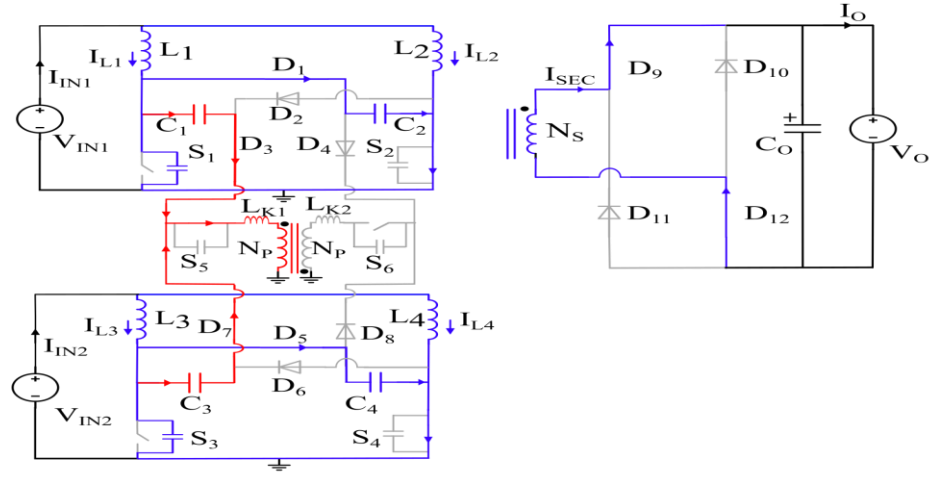


Fig.5.3. Analytical waveforms of MI-CF-HGIIC

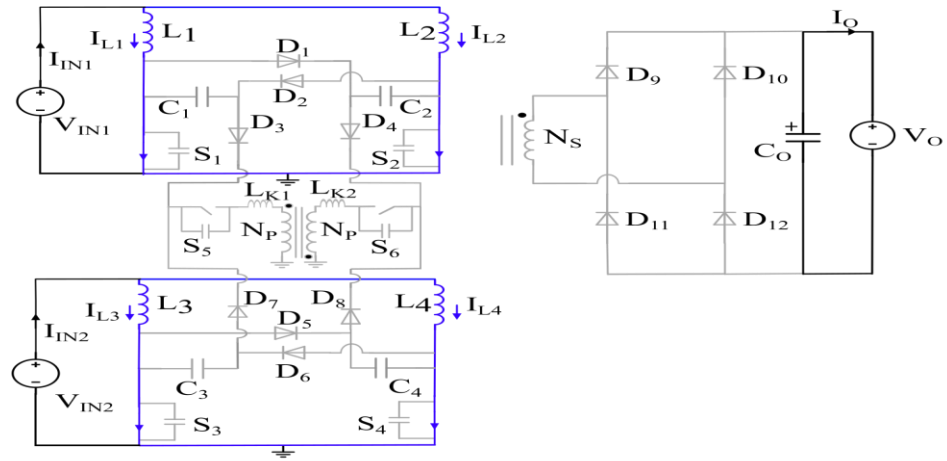
Moreover, the coupling diodes D_2 (D_6) become forward-biased. The turn-on of switch S_6 at the instant t_2 allows the aggregation of voltage across each coupling capacitors C_1 (C_3) and C_2 (C_4) in each module which is reflected across the primary winding of the HF transformer, while also forward biasing the blocking diodes D_4 (D_8). Additionally, the power is transferred to the active load through the HF transformer and rectifier diodes D_{10} and D_{11} till the end of this operating mode.

5.3.4. Mode 4 ($t_3 - t_4$) : Overlapping Mode – Fig.5.4(b)

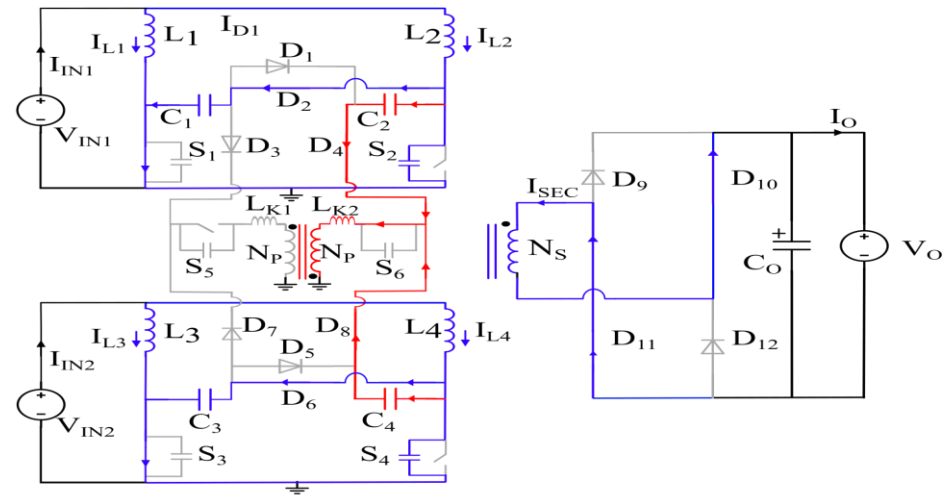
The operation of this mode is fundamentally identical to mode 2. At the start of this mode, the switches S_2 (S_4) turn-on at an instant t_3 while switches S_1 (S_3) are still conducting, enabling inductors L_2 (L_4) to start charging while inductors L_1 (L_3) continue



(a)



(b)



(c)

Fig.5.4. Topological operating modes of proposed converter (a) Mode 1 (b) Mode 2 and Mode 4 (c) Mode 3

to charge. Furthermore, the coupling diodes D_2 (D_6) and blocking diodes D_4 (D_8) are reverse-biased during this mode. Also, there is no power transfer to the active load in this mode as the switch S_6 turns off at the instant t_3 and the output capacitor C_O feeds the load.

5.4. Mathematical Modeling of Converter

The mathematical modeling of the proposed converter is presented in this section. The converter operates in the continuous conduction mode with $d \geq 0.5$. The fundamental assumptions for the simplified converter modeling are outlined below:

- The power modules of the converter are assumed to be symmetric with identical components. Additionally, the symmetric converter operation with identical input sources is also assumed.
- The input inductors are assumed to be sufficiently large to maintain stiff DC currents.
- The circuit components are assumed to be ideal with no PCB parasitic.
- The output voltage is assumed to be constant with a large output capacitor.
- It is assumed that the input inductors ($L_1=L_2=L_3=L_4=L$), coupling capacitors ($C_1=C_2=C_3=C_4=C$), and leakage inductances ($L_{K1}=L_{K2}=L_K$) referred to the primary side are identical.

5.4.1. Steady-State Operational Analysis

The mathematical derivation with the time-domain analysis for each operating mode of MI-CF-HGIIC is imperative for optimal converter modeling. These equations assist the converter designing and device selection while allowing an extensive understanding of the converter operation. Due to the identical operation of the converter during the other half

cycle of the switching cycle because of the circuit symmetry, the mathematical analysis for each operating mode of the converter is only discussed for one-half of the switching cycle.

The symmetric operation of the converter allows identical input currents of each source as shown in (5.1). The current through the input inductors in each module (5.2) is half of the input current.

$$I_{IN1} = I_{IN2} = I_{IN} \quad (5.1)$$

$$i_{L1}(t) = i_{L2}(t) = \frac{I_{IN}}{2}, i_{L3}(t) = i_{L4}(t) = \frac{I_{IN}}{2} \quad (5.2)$$

A. Mode 1($t_0 - t_1$):

The mathematical equations of the converter during mode 1 are discussed below:

$$i_{S1}(t) = i_{S3}(t) = i_{S6}(t) = i_{D2}(t) = i_{D4}(t) = i_{D6}(t) = i_{D8}(t) = 0 \quad (5.3)$$

$$i_{S5}(t) = i_{LK1}(t) = i_{C1}(t) + i_{C3}(t) = 2i_{C1}(t_0) + \frac{2V_{eq}}{Z_0} \sin w_0(t - t_0) \quad (5.4)$$

$$i_{D3}(t) = i_{D7}(t) = i_{C1}(t) = i_{C3}(t) = i_{C1}(t_0) + \frac{V_{eq}}{Z_0} \sin w_0(t - t_0) \quad (5.5)$$

$$i_{D1}(t) = i_{D5}(t) = i_{C2}(t) = i_{C4}(t) = i_{C2}(t_0) - \frac{V_{eq}}{Z_0} \sin w_0(t - t_0) \quad (5.6)$$

$$w_0 = \frac{1}{\sqrt{L_K C}}, Z_0 = \sqrt{\frac{L_K}{C}}, i_{C1}(t_0) = \frac{I_{IN}}{2} - \frac{C \Delta V_C}{(t_1 - t_0)}, i_{C2}(t_0) = \frac{C \Delta V_C}{(t_1 - t_0)} \quad (5.7)$$

$$V_{eq} = 2V_{C1}(t_0) - \frac{V_O}{n} - \Delta V_C, \quad \Delta V_C = (0.25 I_{IN}(1 - d)T_S)/C \quad (5.8)$$

$$i_{S2}(t) = i_{S4}(t) = \frac{I_{IN}}{2} + i_{C2}(t_0) - \frac{V_{eq}}{Z_0} \sin w_0(t - t_0) \quad (5.9)$$

$$V_{C1}(t) = V_{C3}(t) = \frac{-1}{C} \int_{t_0}^t i_{C1}(t) dt = V_{C1}(t_0) - \frac{i_{C1}(t_0)}{C} (t - t_0) - \frac{V_{eq}}{C w_o Z_o} (1 - \cos w_o (t - t_0)) \quad (5.10)$$

$$V_{C2}(t) = V_{C4}(t) = \frac{1}{C} \int_{t_0}^t i_{C2}(t) dt = V_{C2}(t_0) + \frac{i_{C2}(t_0)}{C} (t - t_0) - \frac{V_{eq}}{C w_o Z_o} (1 - \cos w_o (t - t_0)) \quad (5.11)$$

$$i_{SEC}(t) = \frac{i_{LK1}(t)}{n}, V_P = \frac{V_O}{n}, V_{DS1}(t) = V_{C2}(t), V_{DS3}(t) = V_{C4}(t), V_{DS6}(t) = V_P + V_{C2}(t), V_{SEC} = n V_P \quad (5.12)$$

$$T_{10} = (1 - d) T_S \quad (5.13)$$

B. Mode 2 (t_1 - t_2):

During mode 2, the mathematical equations of the converter are underlined below:

$$i_{S1}(t) = i_{S3}(t) = \frac{I_{IN}}{2}, i_{S2}(t) = i_{S4}(t) = \frac{I_{IN}}{2} \quad (5.14)$$

$$i_{D1-D12}(t) = 0 \quad (5.15)$$

$$V_{DS5}(t) = \frac{V_O}{n} + V_{C1}(t) \quad (5.16)$$

$$T_{21} = (d - 0.5) T_S \quad (5.17)$$

5.5. Design Considerations of Converter

The stress on the components and the design of MI-CF-HGIIC is similar to the conventional CF-HGIIC as discussed in chapter 3. However, the stress and design of blocking diodes in the proposed converter need careful consideration.

The maximum voltage across the blocking diode and the average current in the diode is provided in (5.18) and (5.19) respectively

$$V_{D3}(t) = V_{D4}(t) = V_{D7}(t) = V_{D8}(t) = V_O \quad (5.18)$$

$$I_{D3}(t) = I_{D4}(t) = I_{D7}(t) = I_{D8}(t) = \frac{I_{IN}(1-d)}{4} \quad (5.19)$$

The blocking diodes are critical for the proposed converter as they assist in mitigating the intermodular circulating currents, thereby necessitating their proper selection.

5.6. Results and Discussions

The simulated performance of the proposed MI-CF-HGIIC has been studied in this section and evaluates the degree of validation of the operating modes of the converter and its theoretical analysis. The proposed converter rated at 1kW is simulated in the MATLAB Simulink environment using the converter specifications and design parameters listed in Table 5.2 and 5.3 respectively. The simulated converter model integrates dual 30V DC sources at the inputs of the converter and feeds the 380V active load at the output. Furthermore, the converter utilizes the HF transformer with a turns ratio of 2 and operates at a switching frequency of 50kHz. The steady-state operation of the proposed converter is studied for symmetric and asymmetric operating conditions.

During the symmetric operation, the converter operates at its rated specification with each power module of the converter powered by 30V input while feeding 500W power to the load. The input–output profile of the converter presented in Fig.5.5 highlights the constant input voltage and current of each module at 30V and 16.67A respectively while its output current is 2.56A. The steady-state waveform of input current, inductor currents,

coupling capacitor voltages, current, and voltage across the coupling diodes and blocking diodes for both power modules is shown in Fig.5.6. The interleaved operation of the inductor currents of each module is evident from the 180° phase shifted waveform with their current ripple to the tune of 8.7%. Moreover, the impact of the interleaved operation on input current ripple is demonstrated from the results with a significantly smaller input current ripple of 2.41% in each module is observed. The voltage across the coupling capacitors in each module has a ripple of 5.68%. The results show the voltage and current waveforms of coupling and blocking diodes for each module and highlight minimal intermodular circulating currents. The switching performance of the converter with the gating signals, voltage, and current in each switch is demonstrated in Fig.5.7. The minimal turn-off voltage spike in the switches $S_1 - S_4$ observed from the results indicates the natural voltage clamping of these switches by the coupling capacitors. Additionally, these switches

TABLE 5.2: Simulated converter specifications	
Parameter	Value
Input Voltages	Module 1: 30V (rated)
	Module 2: 20V - 30V (rated)
Output Voltage	380V
Rated Input Power	Rated Power of converter :1kW (Module 1: 500W, Module 2: 500W)
Switching Frequency	50kHz

TABLE 5.3: Simulated converter design parameters	
Parameter	Value
Input Inductor ($L_1 - L_4$)	560 μ H
Coupling Capacitor ($C_1 - C_4$)	4.7 μ F
<u>HF Transformer</u>	
Leakage Inductance (L_{K1}, L_{K2})	2.4 μ H
Magnetizing Inductance (L_M)	3.5 mH
Turns Ratio (1:1: n)	1:1:2
Output Capacitor (C_O)	100 μ F

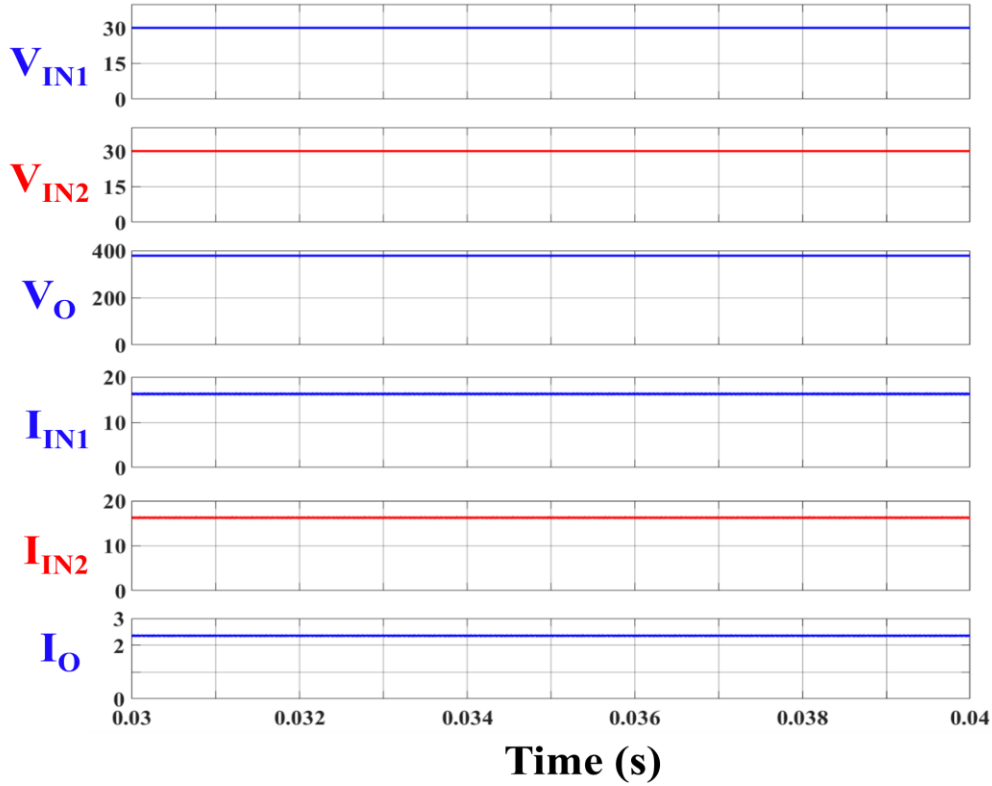


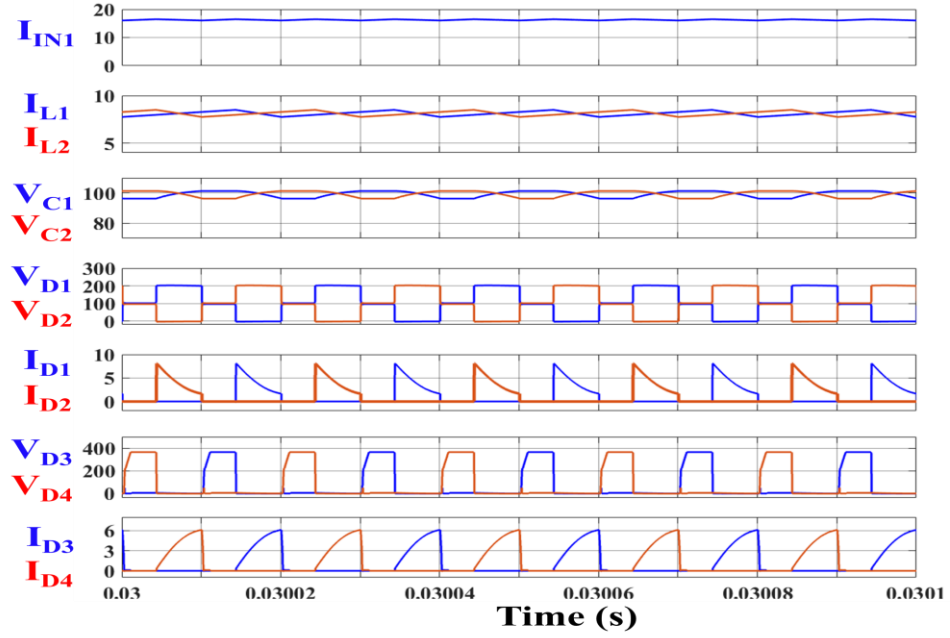
Fig.5.5. Simulated waveform of input voltages of each module (V), output voltage (V), input currents of each module (A), output current (A)

exhibit minimal turn-on switching losses as their current increases linearly. The quasi-sinusoidal switch currents in S_5 and S_6 observed from the simulated waveforms have minimal current during turn-on transition and naturally decay to a small value during turn-off transition, thereby exhibiting smaller switching losses. Moreover, the voltage across these switches increases gradually and conforms to the theoretical analysis and analytical waveform. The voltage and current in the primary and secondary windings of the HF transformer are shown in Fig.5.8 and highlight the quasi-sinusoidal waveshape of the winding currents. Additionally, the voltages of primary and secondary windings indicate a turn ratio of 2. The simulated result of rectifier diodes shown in Fig.5.9 presents the reverse-biased voltages and forward-biased currents of the diodes.

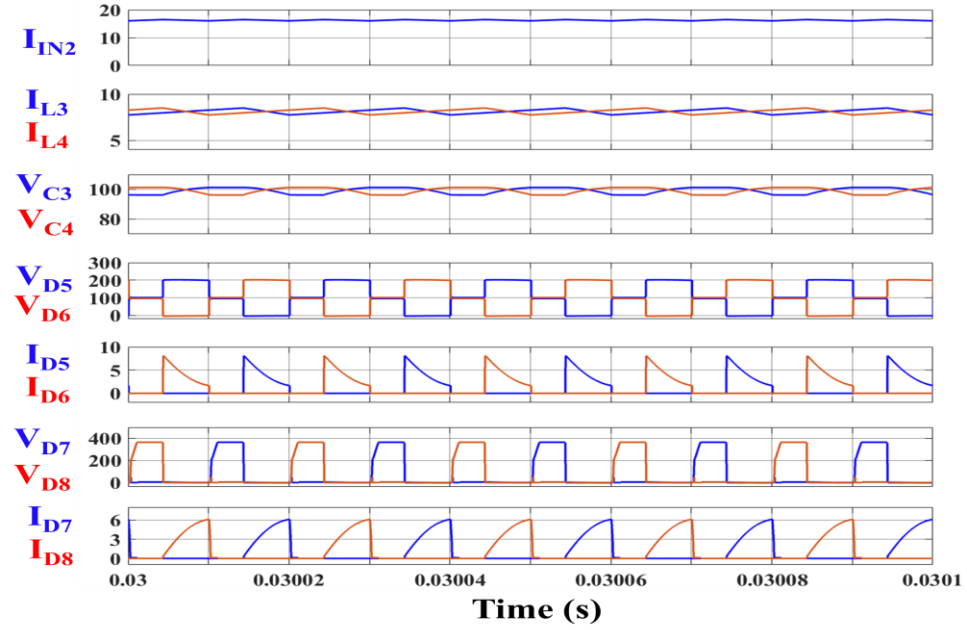
During the asymmetric operation of the converter, the power modules of the converter operate at different ratings. The current-based asymmetric operation of the converter shows the module to have identical input voltages of 30V but different operating input currents, while the voltage-based asymmetric operation of the converter observes different input voltages of 30V and 20V. The input-output profile of the converter shown in Fig.5.10 demonstrates the asymmetric operation of the converter. Fig.5.10(a) shows the current-based asymmetric operation where the input voltages of the converter are regulated at 30V each but different input currents flow through each module with their value of 16.67A and 10.83A. Moreover, the results show the output current of 2.1A. The voltage-based asymmetric operation is shown in Fig.5.10(b) where the identical module currents are observed to the tune of 16.67A while the input voltage of each module is different with the value of 30V and 20V. Moreover, the output current is observed to be 2.1A. The simulated waveforms of input current, inductor currents, coupling capacitor voltages, voltage, and current in the coupling and blocking diodes for asymmetric converter operation are shown in Fig 5.11 and 5.12. The current-based asymmetry shown in Fig.5.11 shows the difference in the values of input currents and the inductor currents of each module. Additionally, the voltage across coupling capacitors, coupling diodes, and blocking diodes are observed from the results. The variation in the currents of the coupling and blocking diodes of each module is evident from the simulated results and indicates the current-based asymmetry. Fig.5.12 shows the voltage-based asymmetry where the charging time of inductor currents of both modules are different, emphasizing the difference in their operating duty cycles and further indicating the interfacing of different voltage sources at the inputs. Additionally, the inductor current ripples in module 2 are observed to be 6.63%, which are comparatively smaller than their module 1 counterpart because of their higher operating duty cycle. The

results also indicate voltage ripple to the tune of 3.85% in the coupling capacitors of module 2 which is smaller compared to module 1 which has 5.68% while also highlighting the seamless counterbalancing of the voltage-based asymmetry in the converter. The difference in the conduction and reverse biased period for the coupling and blocking diodes of modules due to variation in the duty cycle in response to the voltage-based asymmetry is evident from Fig.5.12. Moreover, the results also highlight minimal intermodular circulating currents even during the asymmetric operation of the converter. The switching performance of the converter during asymmetric operation is shown in Fig.5.13. The proposed converter observes variation in the operating duty cycle for each power module during voltage-based asymmetric operation which is evident from the result in Fig.5.13(b). Moreover, the waveforms in Fig.5.13 also highlight the natural voltage clamping of switches $S_1 - S_4$ during asymmetric operation and observe minimal turn-off voltage spike. Additionally, the switches S_5 and S_6 experience smaller turn-on and turn-off losses as the voltage increases linearly during turn-off while the current increases gradually during turn-on transition. The voltage and current through the windings of the HF transformer during both types of asymmetries are demonstrated in Fig.5.14. Furthermore, the simulated waveform of rectifier diodes operating under asymmetric conditions is shown in Fig.5.15.

The simulated performance of the proposed converter under both symmetric and asymmetric conditions underlines its seamless operation without any intermodular circulating currents. Moreover, the results also highlight a higher degree of operational independence of individual modules with each module having decoupled operation and not impacting the performance of other modules. The proposed converter demonstrates high efficacy in furnishing higher voltage gain, achieving a significantly higher voltage gain of



(a)



(b)

Fig.5.6. Simulated waveform of input current (A), inductor currents (A), voltage across coupling capacitors (V), coupling diode voltages (V) and currents (A), blocking diode voltages (V) and currents (A) during symmetric converter operation (a) Module 1 (b) Module 2.

nearly 20 while utilizing a low turns ratio of 2. Also, the capability of the proposed converter in integrating the sources with different voltages is established from the results, highlighting

its wide operating range and high degree of operational flexibility. The salient features of the MI-CF-HGIIC emphasize its viability for the MMIC.

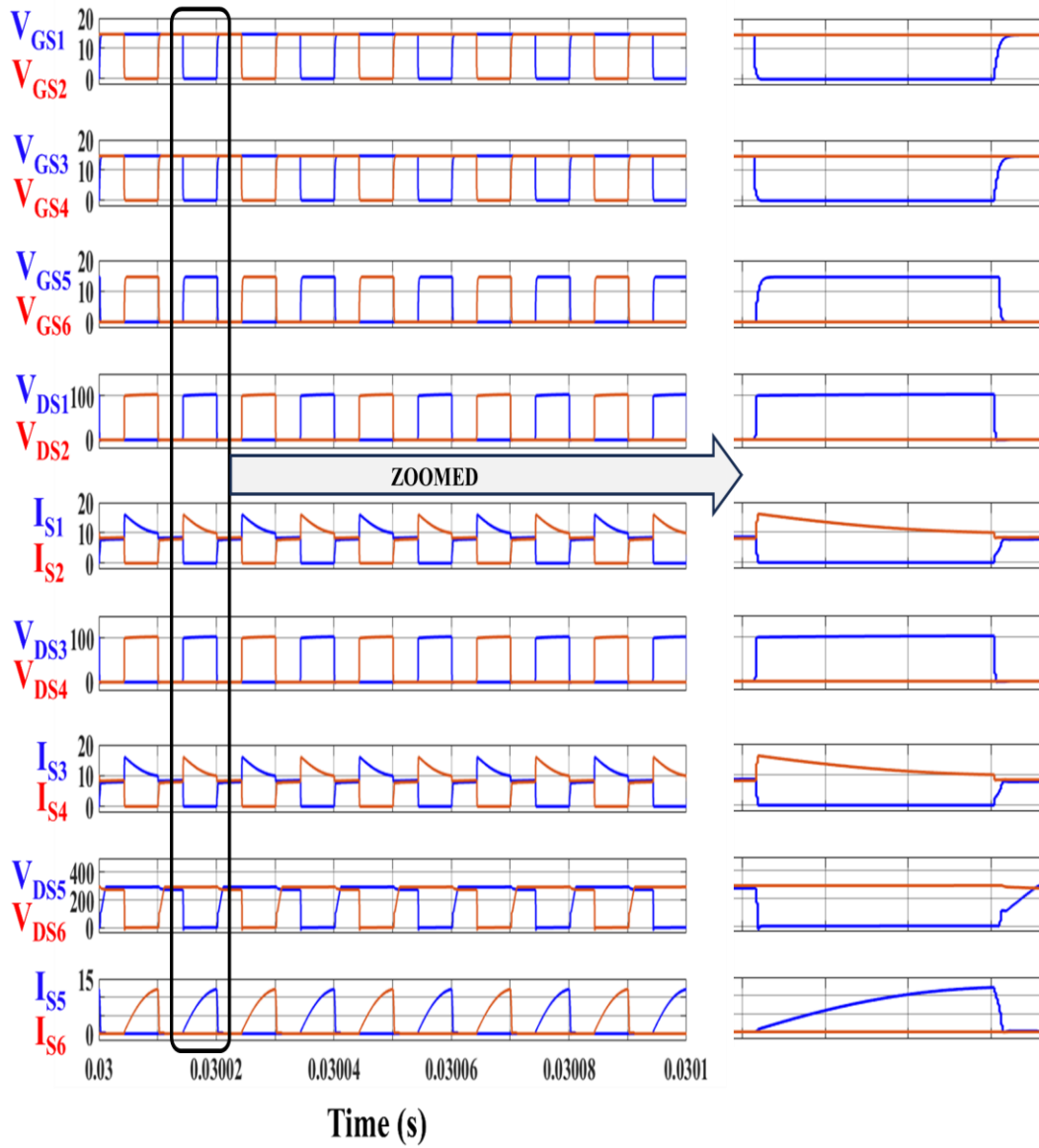


Fig.5.7. Simulated waveform of gating signals $V_{GS1} - V_{GS6}$ (V) of switches $S_1 - S_6$ (A), voltage V_{DS1}, V_{DS2} (V) and current I_{S1}, I_{S2} (A) in switches S_1, S_2 , voltage V_{DS3}, V_{DS4} (V) and current I_{S3}, I_{S4} (A) in switches S_3, S_4 , voltage V_{DS5}, V_{DS6} (V) and current I_{S5}, I_{S6} (A) in switches S_5, S_6 during symmetric operation

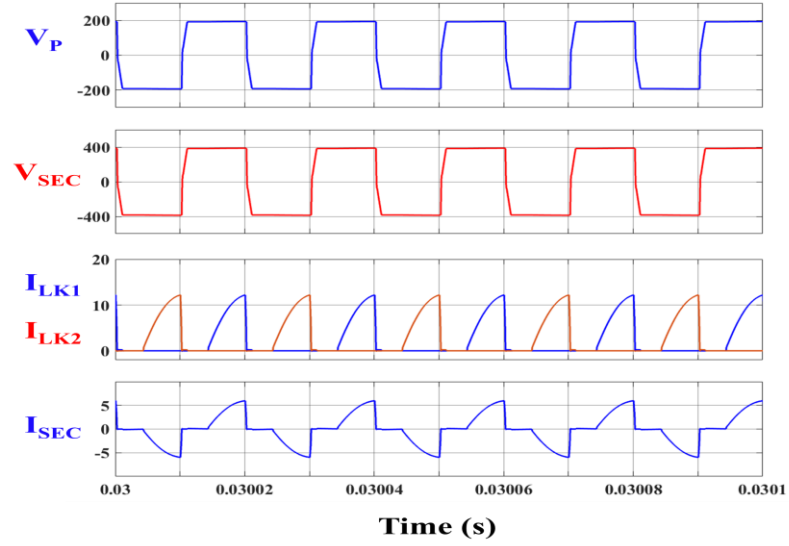


Fig.5.8. Simulated waveform of primary V_P (V) and secondary V_{SEC} (V) winding voltages of HF transformer and primary I_{LK1} , I_{LK2} (A) and secondary winding I_{SEC} (A) currents during symmetric operation

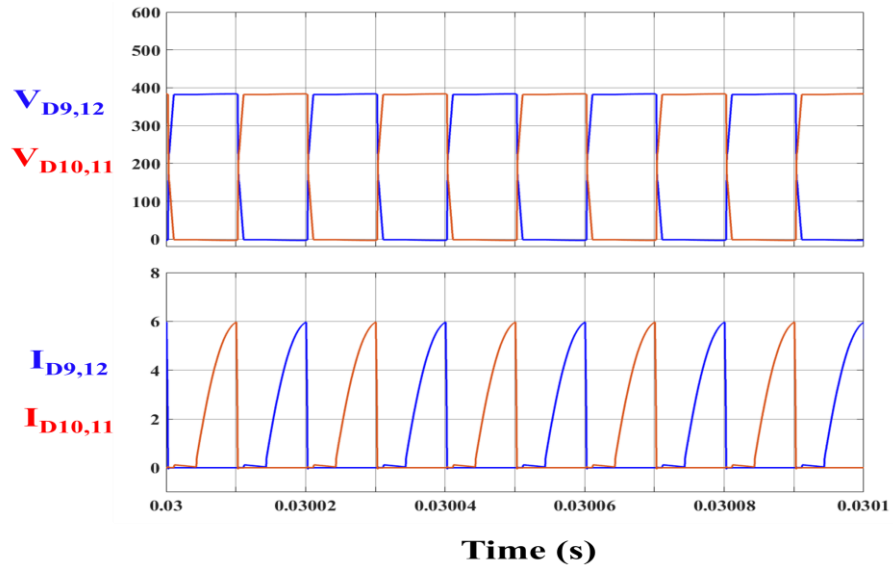
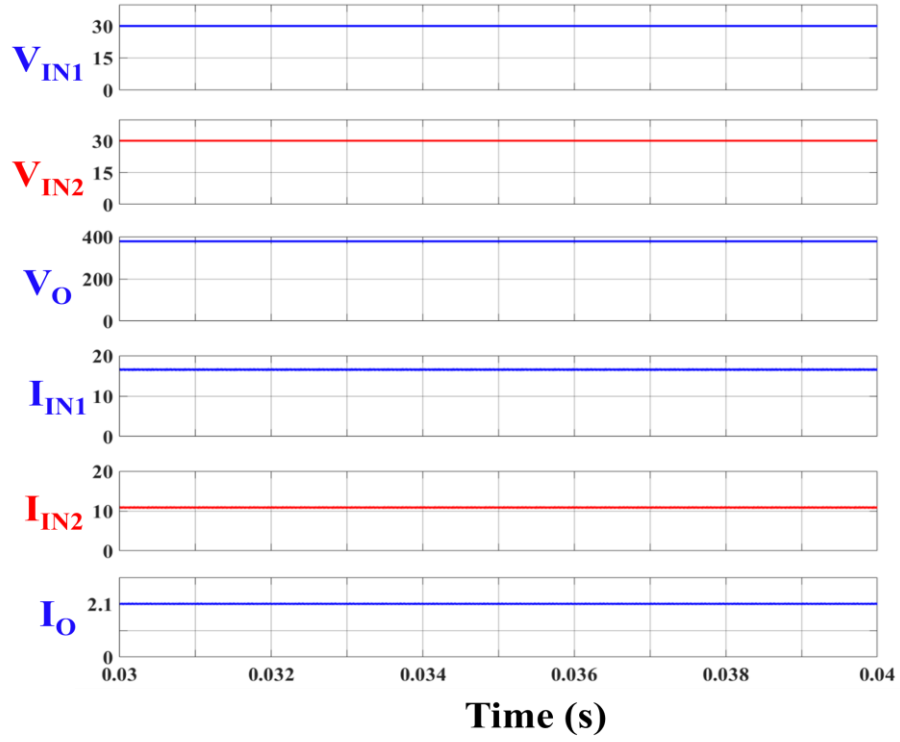
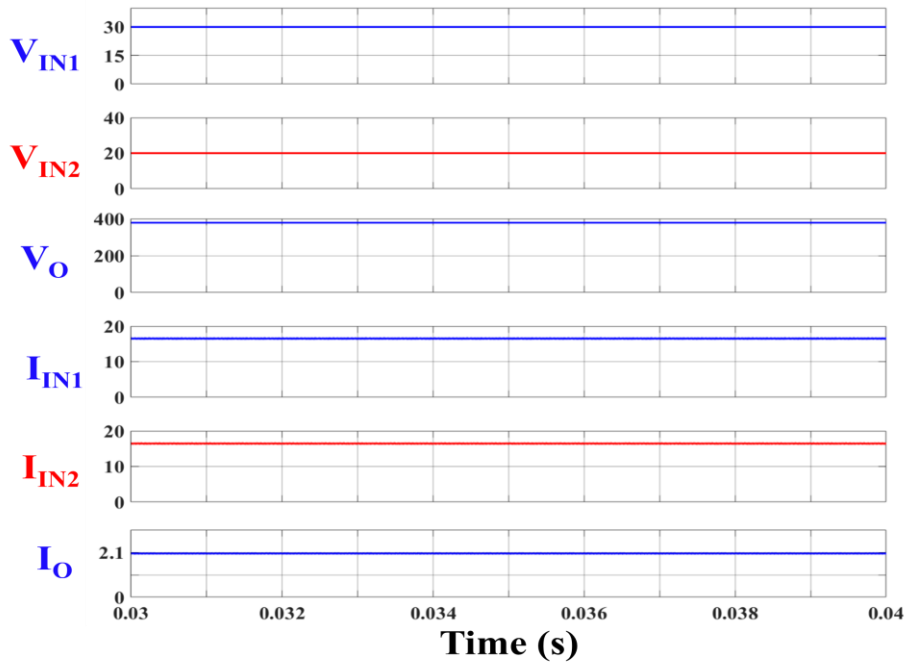


Fig.5.9. Simulated waveform of rectifier diode voltages V_{D9-D12} (V) and currents I_{D9-D12} (A) during symmetric operation

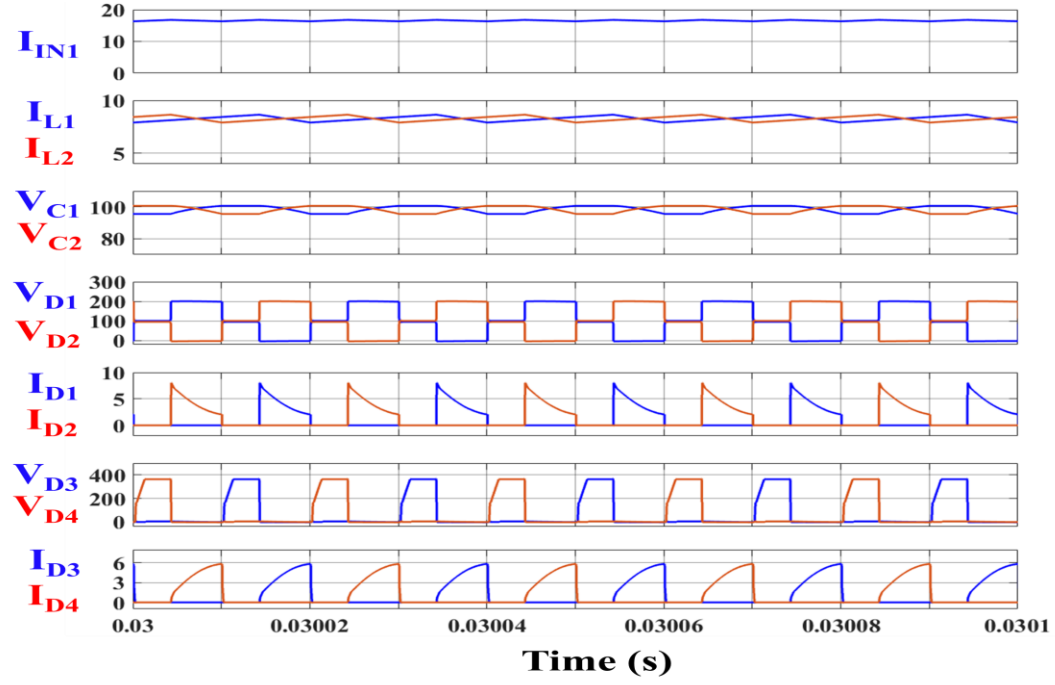


(a)

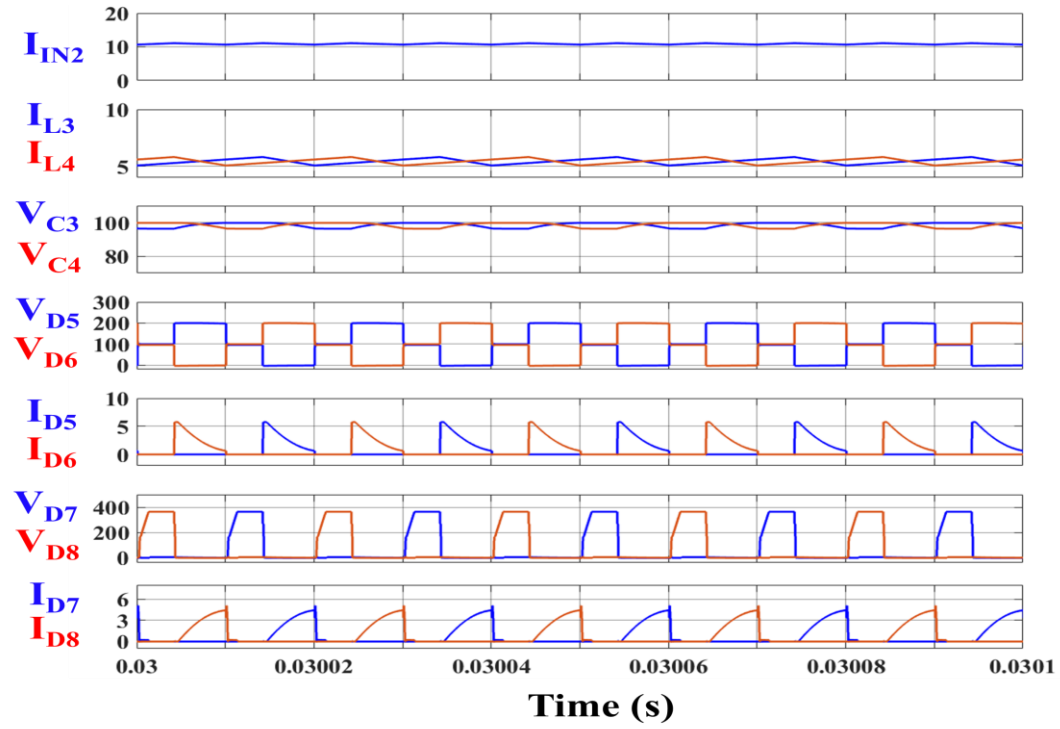


(b)

Fig.5.10. Simulated Waveform of input voltages of each module (V), output voltage (V), input currents of each module (A), output current (A) (a) Current based asymmetric converter operation (b) Voltage based asymmetric converter operation

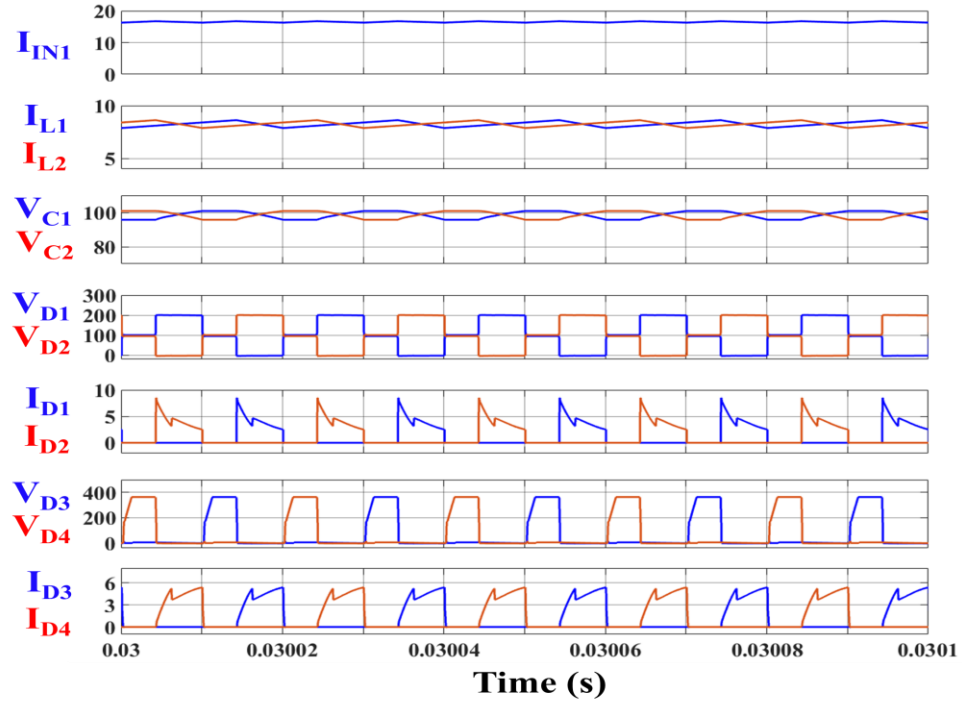


(a)

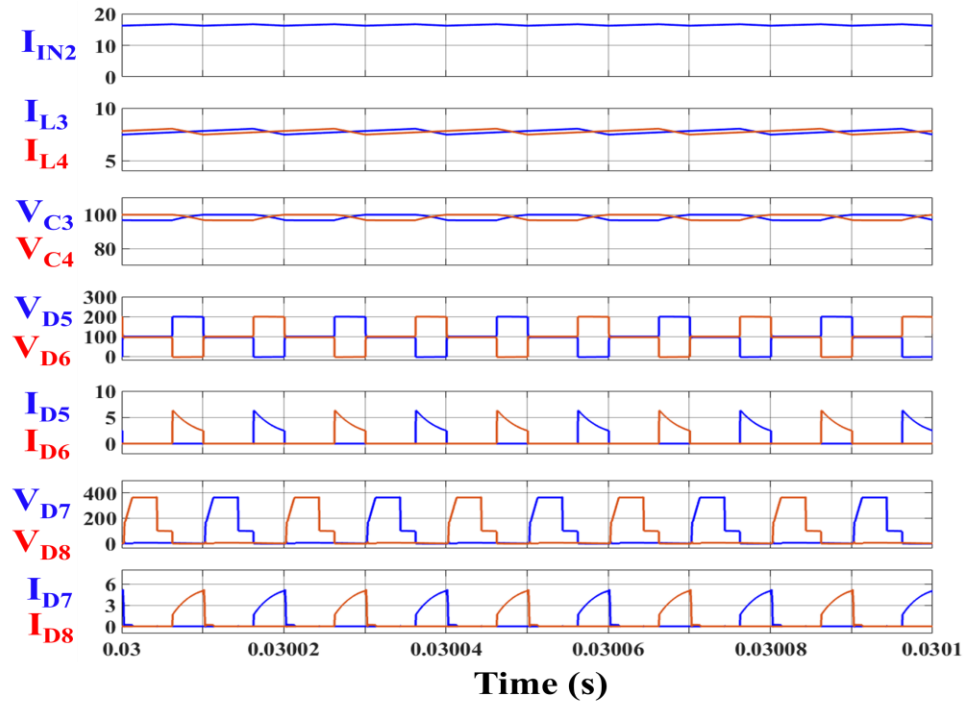


(b)

Fig.5.11. Simulated waveform of input current (A), inductor currents (A), voltage across coupling capacitors (V), coupling diode voltages (V) and currents (A), blocking diode voltages (V) and currents (A) during current based asymmetric converter operation (a) Module 1 (b) Module 2.

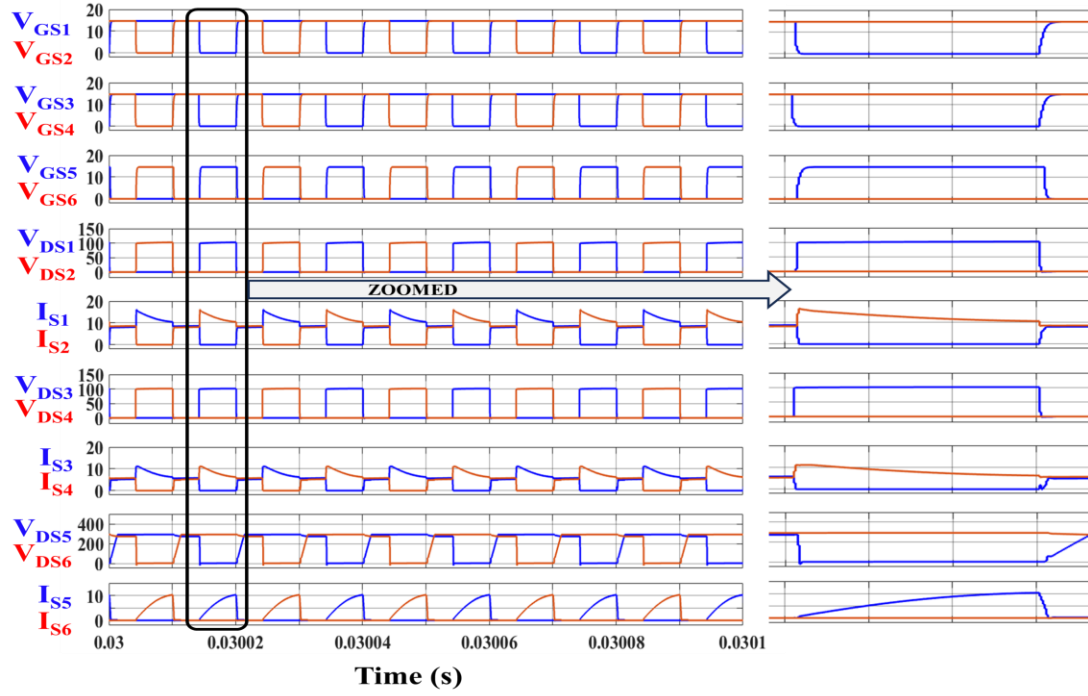


(a)

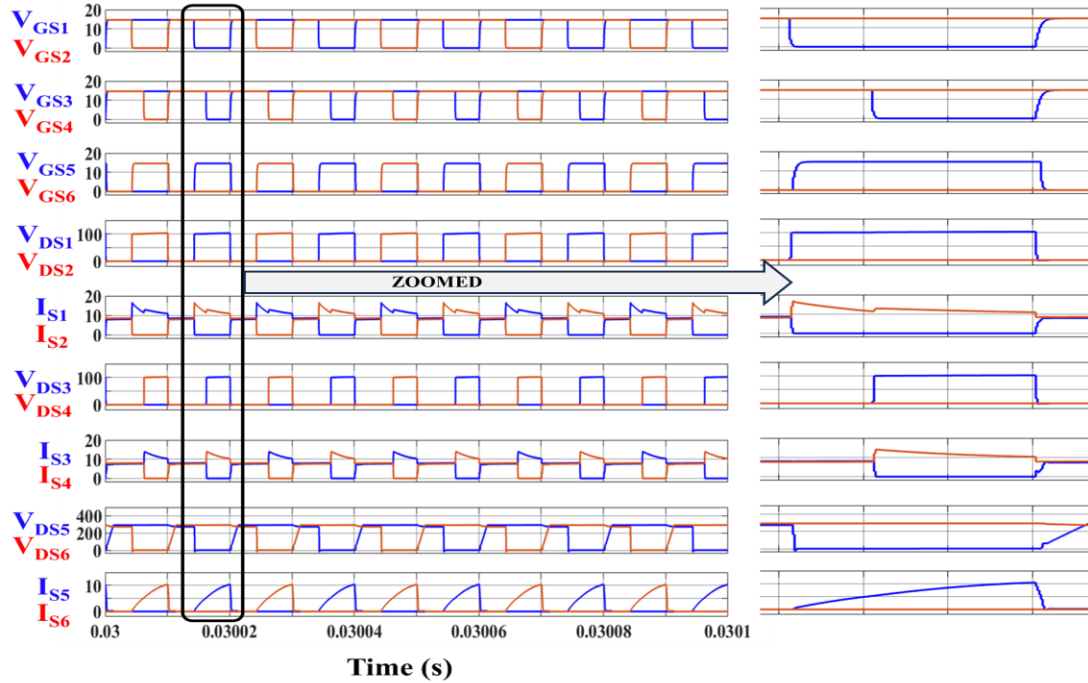


(b)

Fig.5.12. Simulated waveform of input current (A), inductor currents (A), voltage across coupling capacitors (V), coupling diode voltages (V) and currents (A), blocking diode voltages (V) and currents (A) during voltage based asymmetric converter operation (a) Module 1 (b) Module 2.

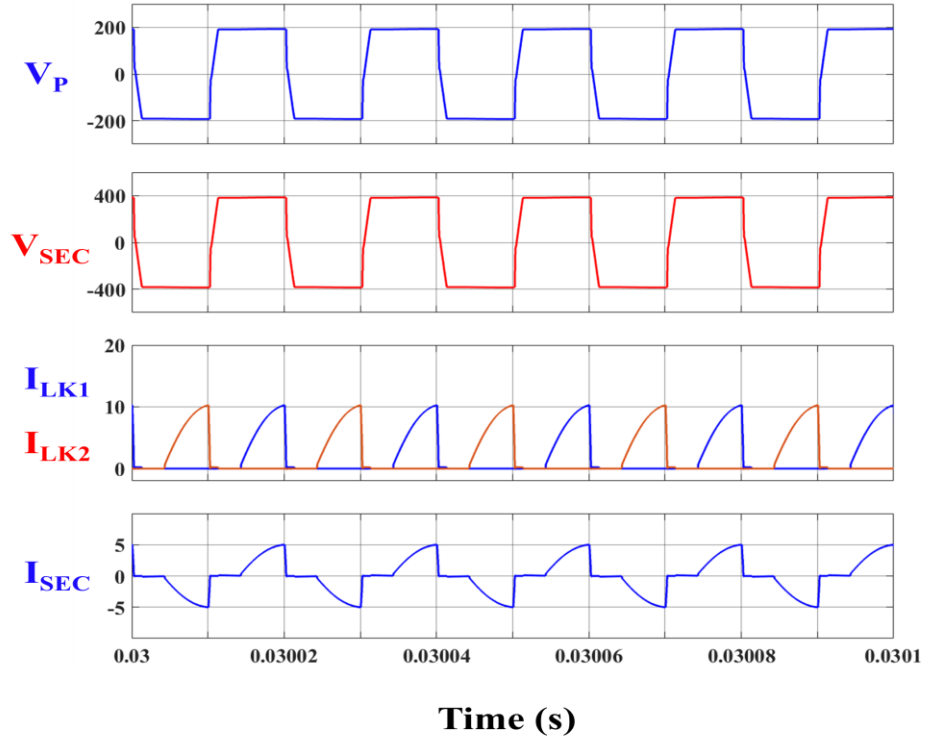


(a)

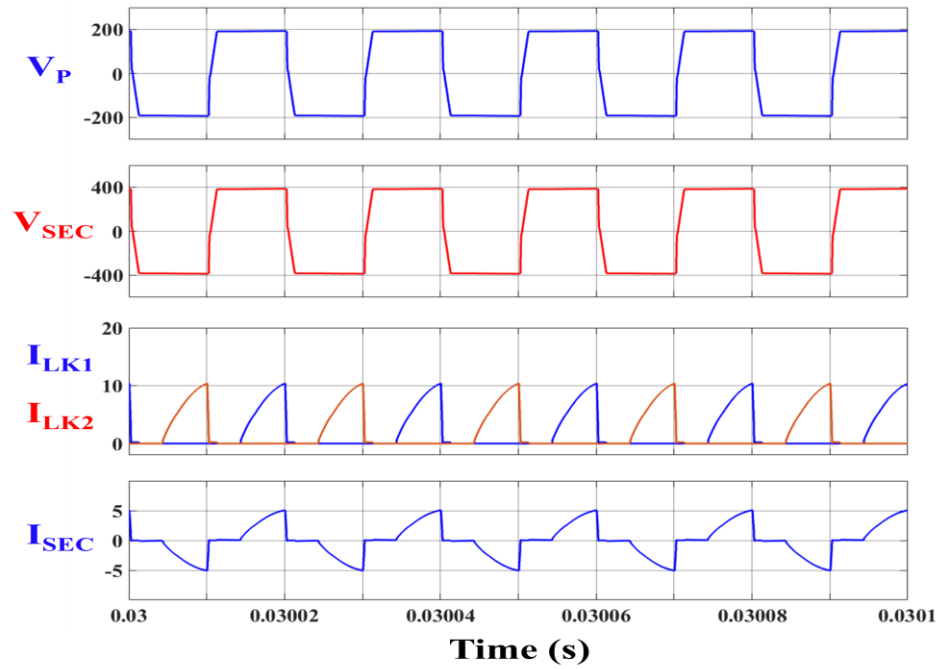


(b)

Fig.5.13. Simulated waveform of gating signals $V_{GS1} - V_{GS6}$ (V) of switches $S_1 - S_6$ (A), voltage V_{DS1}, V_{DS2} (V) and current I_{S1}, I_{S2} (A) in switches S_1, S_2 , voltage V_{DS3}, V_{DS4} (V) and current I_{S3}, I_{S4} (A) in switches S_3, S_4 , voltage V_{DS5}, V_{DS6} (V) and current I_{S5}, I_{S6} (A) in switches S_5, S_6 during (a) Current based asymmetric converter operation (b) Voltage based asymmetric converter operation

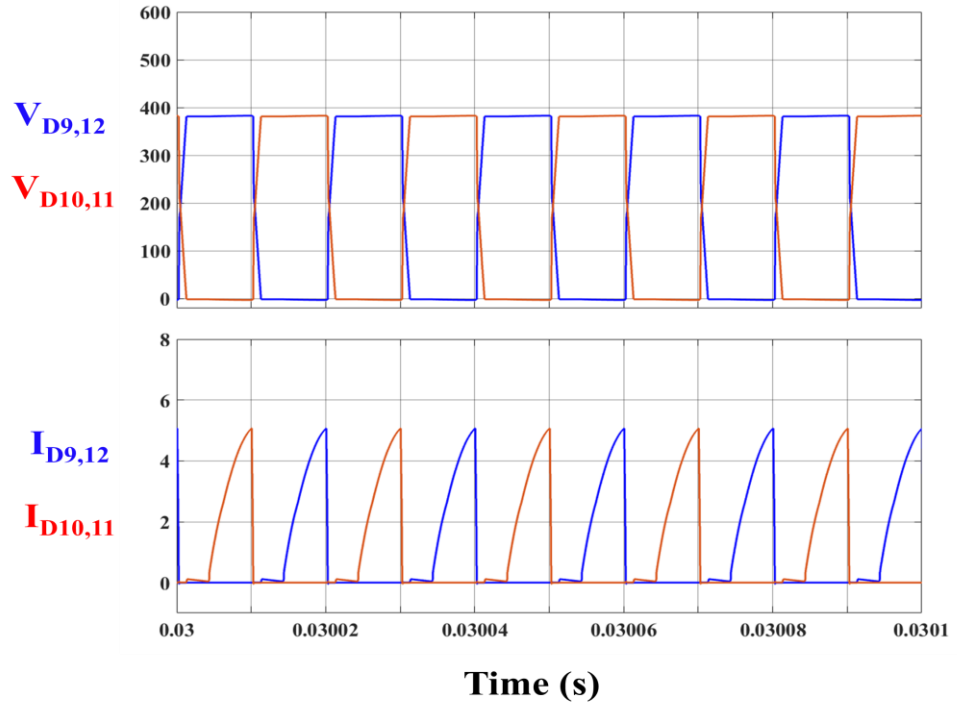


(a)

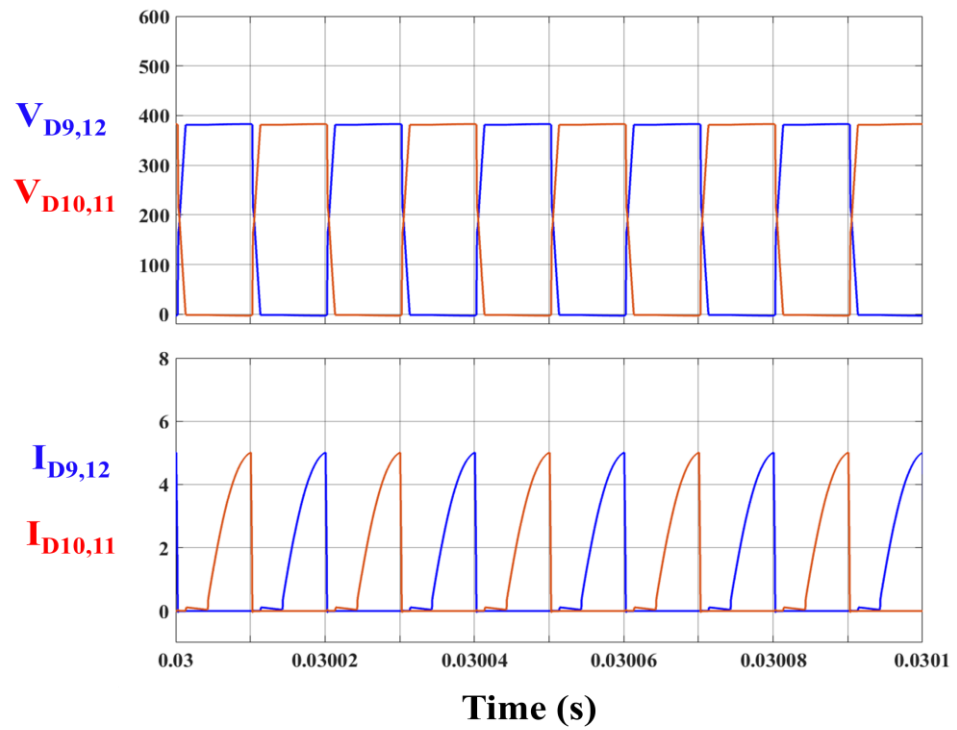


(b)

Fig.5.14. Simulated waveform of primary V_P (V) and secondary V_{SEC} (V) winding voltages of HF transformer and primary I_{LK1} , I_{LK2} (A) and secondary winding I_{SEC} (A) currents during (a) Current based asymmetric converter operation (b) Voltage based asymmetric converter operation



(a)



(b)

Fig.5.15. Simulated waveform of rectifier diode voltages V_{D9-D12} (V) and currents I_{D9-D12} (A) during (a) Current based asymmetric converter operation (b) Voltage based asymmetric converter operation

5.7. Conclusion

The proposed converter based on the multi-input approach of the conventional CF-HGIIC topology has been presented in this chapter. The topological structure of the proposed MI-CF-HGIIC and its modulation scheme has been discussed. In this chapter, the operating modes of the converter and comprehensive mathematical analysis for each mode were provided and further highlighted the theoretical operation of the converter.

The model of MI-CF-HGIIC using simulated converter specification and its corresponding calculated design parameters has been implemented on MATLAB Simulink environment to evaluate the simulated performance under symmetric and asymmetric operating conditions. The proposed converter inherited the salient features of conventional CF-HGIIC. The simulated results demonstrated the high gain capability of the converter while utilizing a smaller turn ratio of the HF transformer. The results showed the natural voltage clamping of switches ($S_1 - S_4$) with smaller switching loss in the converter. The simulated results further indicated minimal intermodular circulating currents. Moreover, the converter also exhibited seamless operation under asymmetric operation without impacting the performance of any module. The decoupled operation of each module under any condition has been highlighted from the simulated results and further displayed modular operational independence. Additionally, the converter exhibited a higher degree of operational flexibility and wide operating range. The proposed converter also demonstrated modular and scalable architecture while its ability to continue operation despite interruptions in one of the sources is evident from the decoupled operation of the power modules of the converter. Moreover, the plug-and-play operation has been facilitated in the converter owing to its merits like minimal inter-converter and intermodular circulating

currents. The simulated results of MI-CF-HGIC validated the topological operating modes and theoretical analysis of the converter and its merits further affirmed its viability and topological candidacy for MMIC.

CHAPTER 6

SYSTEM INTEGRATION AND PERFORMANCE UNDER VARIABLE INSOLATION AND SHADING CONDITIONS

6.1. General

The module-level PV system discussed in the literature is widely gaining popularity and offers considerable advantages as compared to the conventional string PV system. In this chapter, the integration of the module-level PV system (MLPS) with the DC microgrid as the front-end section and its performance under different operating conditions is presented. The chapter discusses the system architecture where multiple PV panels are independently interfaced with the DC microgrid using a module-level interfacing converter (MLIC) and multi-input module interfacing converter (MMIC). Furthermore, MLIC and MMIC employ high-gain isolated current-fed topologies proposed in chapters 3– 5. The chapter provides a comprehensive study of various applications of the system architecture based on MLPS while also delineating the concept of dynamic sub-panel shading conditions and their consequences in detail. The power generation control algorithms for flexible power point tracking and fast MPP tracking are proposed, with extensive investigation of their concept and operation. The performance of system architecture under different environmental conditions like insolation variations and shading conditions, and other system-level operational conditions like PV panel outage and the insertion of new PV panel in the existing system is simulated on MATLAB Simulink environment. Furthermore, the

experimental performance of the scaled-down system under different environmental operating conditions is also presented in the chapter to validate the simulated performance and theoretical concepts. Additionally, the system-level simulated and experimental results evaluate the performance of proposed converter topologies operating as MLIC and MMIC and highlight their merits. Moreover, the performance of the proposed power generation control algorithms is comprehensively analyzed under different operating conditions. The chapter is organized as follows: Section 6.2 discusses the merits of module-level PV systems and presents the MLPS-based system architecture. The different applications of the MLPS-based system architecture are discussed in section 6.3 while the concept of dynamic sub-panel shading is presented in section 6.4. Different power generation control algorithms are proposed in section 6.5. Section 6.6 extensively investigates the simulated and experimental performance of the system.

6.2. System Architecture

In this section, the merits of MLPS and the backbone structure of the MLPS-based front-end section of the DC microgrid are discussed.

6.2.1. Merits of MLPS

MLPS is widely being adopted and researched as an alternative to the conventional string PV system. The widespread adoption of MLPS is attributed to the key advantages underlined below:

- MLPS achieves superior power utilization from each PV panel due to their independent integration with the DC microgrid and deployment of individual

distributed power generation controllers, thereby allowing a greater degree of power generation control from each panel.

- MLPS is more tolerant to shading conditions.
- MLPS achieves better reliability, robustness, and operational flexibility while enabling seamless operation under system outage, and maintenance of a section or PV panel.
- Higher modularity and scalability are observed in MLPS with ease in reparability and low cost maintenance.
- MLPS also supports plug-and-play operation where the power capacity of the system can be increased dynamically by integrating new power units without compromising the performance of the existing system.

Consequently, the merits of MLPS make it a viable solution for integration with the DC microgrid as the front-end section. The performance of the DC microgrid is further enhanced by incorporating MLPS and provides better modularity, flexibility, reliability, and distributed power generation.

6.2.2. MLPS based System Architecture

This section presents the MLPS based system architecture. The system architecture broadly focuses on the front-end section of the DC microgrid where MLPS is interfaced with the DC microgrid. The closer examination of the system architecture in Fig.6.1 demonstrates the direct integration of low-voltage PV panels with the high-voltage DC microgrid using MLIC and MMIC topologies. The MLIC employs the proposed CF-HGIIC and MCF-HGIIC topologies which integrates a single low-voltage PV panel with the DC microgrid, while the proposed MI-CF-HGIIC is utilized for MMIC to interface dual PV

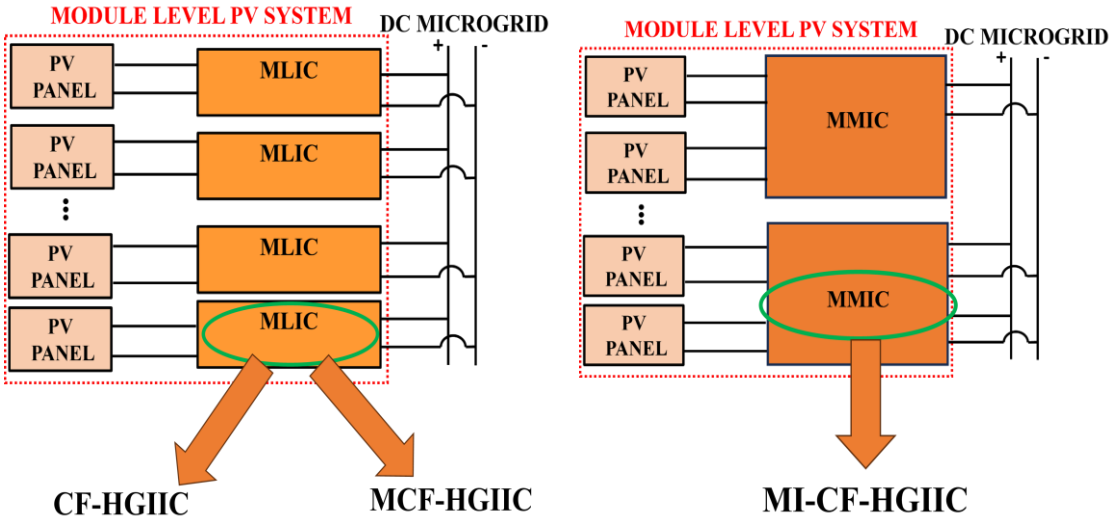


Fig.6.1. MLPS system architecture

panels with the microgrid. Additionally, the MLPS is required to operate in the slave configuration while integrating with the DC microgrid whereas the voltage sources viz,

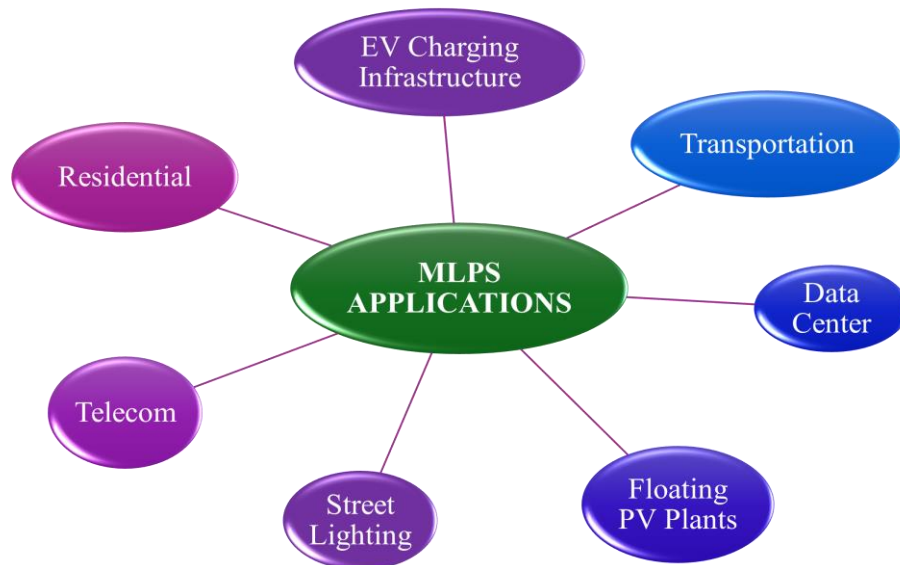


Fig.6.2. Applications of MLPS

BSS operate as a master. As a result, it is imperative for PV-fed MLICs and MMICs to operate as a current source and facilitate the seamless integration of multiple such units with the DC microgrid.

MLPS typically encompasses the PV panel, MLIC / MMIC, and power generation control. The power generation control (PGC) employs different algorithms for achieving maximum power generation and constant power generation from the PV panels under different operating conditions. PGC inputs the sensed PV parameters and provides a duty cycle as the output which drives the MLIC / MMIC topologies. The operation of the PV panel, interfacing converter, and power generation control in synergy becomes essential for the optimal performance of the MLPS as well as the overall system infrastructure.

6.3. Applications of MLPS

Different applications of PV systems utilizing MLPS are shown in Fig.6.2 while their benefits are highlighted in this section. Primarily, three applications of PV systems viz, Off-Grid EV charging infrastructure, floating PV system, and rooftop PV system on the train are delineated extensively. Conventionally, the string PV system has been adopted for these applications but suffers from poor performance due to their inherent drawbacks, thereby limiting their viability for these applications.

6.3.1. Off-Grid EV Charging Infrastructure

EV charging infrastructure is critical for the adoption of electric vehicles and requires suitable charging facilities. Typically, in urban regions where the AC grid is prevalent, the EV charging infrastructure is seamless. However, in remote areas where the AC grid is not present, they are primarily dependent on PV-based generation [314]-[316]. Additionally, the installation of charging infrastructure is a challenge in remote areas and requires PV systems for electricity generation. The conventional string PV systems are predominantly used for Off-Grid EV charging infrastructure owing to their simpler architecture. However,

the operational performance of string PV-based charging infrastructure is significantly impacted by environmental conditions such as shading. Furthermore, the single-point failure of string PV systems severely affects the operational performance of charging infrastructure and leads to substantial loss of electricity generation and frequent disruption in their services. As a result, the string-based EV charging infrastructure has poor reliability, and complex repairability and requires frequent maintenance which further inflates their maintenance cost and limits their viability.

The MLPS-based Off-Grid EV charging infrastructure offers multiple advantages and superior performance. Fig.6.3 shows the architecture of MLPS-based Off-Grid EV charging infrastructure with MLPS being the front-end section of the infrastructure and facilitating the integration of individual PV panels with the 380V DC bus using MLICs while operating

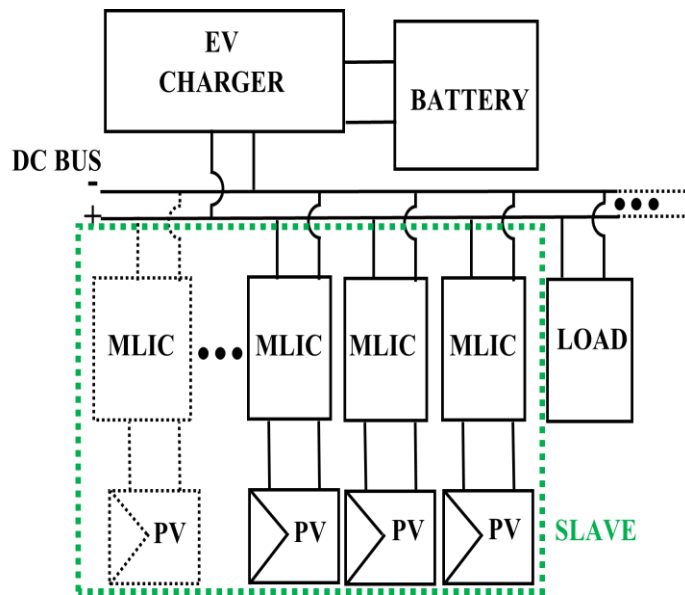


Fig.6.3. MLPS based off-grid EV charging infrastructure

as slaves. Moreover, the DC bus further acts as an intermediate storage and caters to the demand for EV chargers for e-bikes and e-rickshaws while also powering non-critical loads

during lean load conditions. This Off-Grid EV charging infrastructure achieves superior performance under different operating conditions while demonstrating enhanced robustness. Furthermore, they don't suffer from single-point failure and continue to operate even during an outage of a PV panel or component, thereby exhibiting decentralized architecture and higher reliability. This architecture enables superior operational flexibility and easy repairability while significantly reducing service disruptions. As a result, the maintenance of this charging infrastructure becomes seamless and dramatically cheaper, particularly considering their operation in remote areas with minimal resource accessibility. The MLPS-based Off-Grid EV charging infrastructure also achieves better modularity and scalability while supporting the plug-and-play operation, allowing a seamless increase in the power capacity in the future by augmenting additional units without compromising the performance of the existing system.

6.3.2. Floating PV System

The Floating PV (FPV) systems are widely gaining popularity due to the limitations of terrestrial PV systems as the land prices are increasing steeply with the scarcity of large areas of land suitable for installation of the PV panels [317]-[319]. Furthermore, the floating PV system offers better power generation due to cooler ambient temperatures, minimizes the soiling of panels, prevents algae proliferation in the water, and assists in water conservation. Presently, the FPV system is primarily based on the string PV system. The major bottlenecks in the current FPV system are steep installation cost, recurring maintenance with higher expense, and complex repairability. The installation procedure of FPV systems is complex as they are located remotely and are not easily accessible. Furthermore, string PV systems are inherently prone to frequent disruption due to their

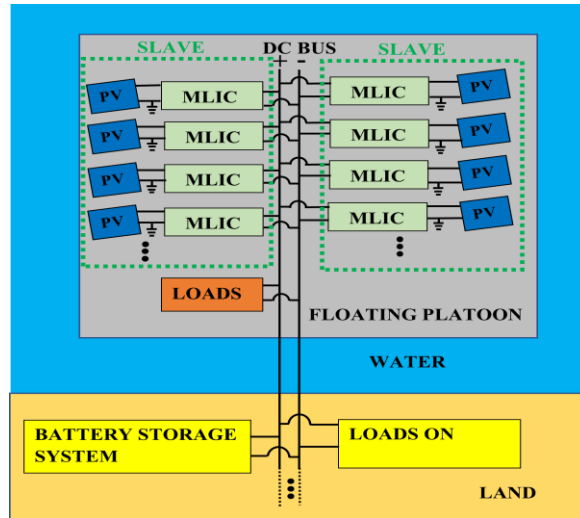


Fig.6.4. MLPS based floating PV system

single-point failure and require recurring maintenance and dedicated manpower. Additionally, the string-based FPV system has complex repairability with the need for replacement of the entire unit in case of any failure. As a result, the conventional FPV system has exponentially expensive maintenance with a lower adoption rate.

The MLPS-based FPV system shown in Fig.6.4 offers notable merits and enhanced

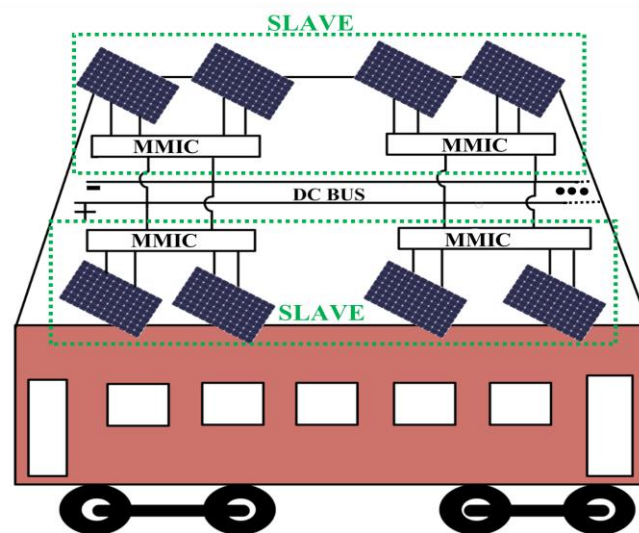


Fig.6.5. Rooftop MLPS on train

performance. Multiple PV panels buoyed on the floating platoon are independently integrated with the 380V DC bus while operating as slaves. Additionally, the DC bus further interfaces the battery storage system on land as well as different water and land-based loads. The MLPS-based FPV system achieves superior power generation under different operating conditions and offers higher reliability and robustness while eliminating single-point failure. This allows the system to operate autonomously without any disruption during any outage or failure. Additionally, the ease of repairability in the system allows the replacement of a single module instead of an entire unit in case of any fault. Consequently, this dramatically improves the performance of the system with cheaper and reduced frequency of maintenance. The MLPS-based FPV system also offers modular architecture with higher scalability and supports plug-and-play operation, thereby enabling a dynamic increase in the power capacity of the system to meet future requirements without impacting the existing system performance.

6.3.3. Rooftop MLPS on Train

The installation of PV systems on trains is a novel concept that is increasingly being researched [320]-[322]. The traditional string-based PV system is employed with a series connected PV panels installed on the roof of the train. The demerits of string PV system limits the performance of the entire system and minimizes electricity generation. Fig.6.5 shows the rooftop MLPS for the train where multiple PV panels are integrated with the 380V DC bus using MMICs and further operate as slaves. Moreover, the DC bus further integrates the light, fan, and electronic loads like mobile phone and laptop charging. MLPS-based architecture for train achieves higher reliability, robustness, and superior performance under different operating conditions. Moreover, it demonstrates lower

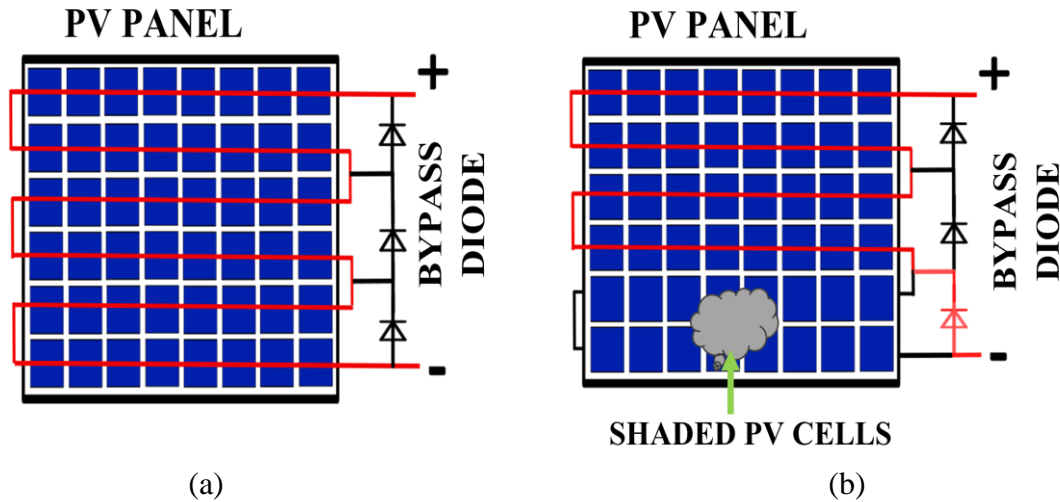
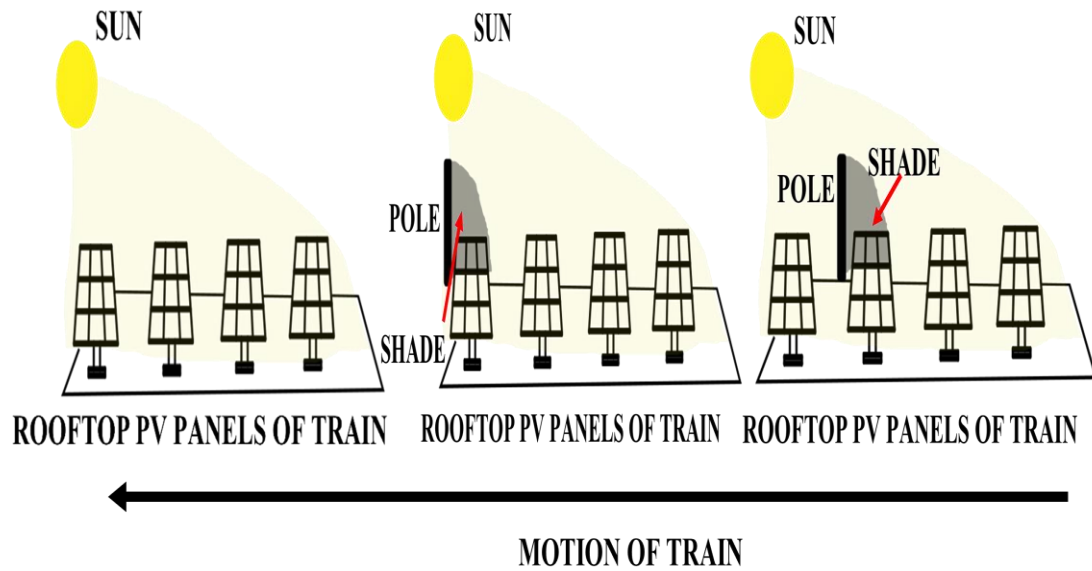


Fig.6.6. PV Panel with bypass diode operation (a) Unshaded PV cells (b) Shaded PV cells

maintenance costs with easy repairability and further exhibits sustained operation during an outage or failure. Also, the system achieves higher modularity and scalability and allows plug-and-play operation.

6.4. Concept of Dynamic Sub-Panel Shading

The installation of rooftop PV panels of the moving locomotive-like train presents a unique challenge which is discussed in this section. The concept of sub-panel shading for stationary PV panels is discussed in detail and is further extended to dynamic shading. The sub-panel shading is a class of shading conditions where each PV panel experiences localized shading due to the objects. The typical configuration of a PV panel utilizes the bypass diodes in parallel with a few PV cells, with a total of 3 bypass diodes installed in a PV panel. The diode bypasses the section of shaded PV cells and primarily prevents the hotspot generation in the panels during shading conditions, thereby improving the



(a) (b) (c)
 Fig.6.7. Concept of dynamic sub-panel shading as train is moving (a) No panel is shaded (b) Stationary pole shades some section of PV Panel 1 as it crosses the pole (c) Stationary pole then shades some section of PV panel 2 as it crosses the pole

operational life of the PV panel. This is visually represented in Fig.6.6. However, bypassing the shaded section of the panel induces power fluctuations with the reduction in the overall power and voltage of the PV panel. As a result, sub-panel shading is a critical challenge for PV system and require suitable MPPT control algorithms to track the maximum power. The MLPS is more tolerant to sub-panel shading as compared to string PV systems owing to its distributed MPPT controller and better control over the power generation of individual panels.

The dynamic sub-panel shading is a novel challenge for PV systems which stems from the installation of PV panels on the moving locomotive like trains and trams. This introduces an additional variable in the sub-panel shading conditions, i.e., relative motion. As the PV panel is moving relative to stationary objects like a tree, pole, or building and

moving objects, the fast changes in the shade on the PV panel are experienced. The concept of dynamic sub-panel shading is illustrated in Fig.6.7, where the changes in the shade on the PV panel due to the relative motion of the panel installed on the moving train with respect to the object is demonstrated. The dynamic sub-panel shading conditions are more challenging than stationary sub-panel shading conditions due to fast variations in the shade on the PV panel. The operation of string PV systems with slow conventional GMPPT controllers during dynamic sub-panel shading conditions fails to detect such fast-shading variations and experiences poor performance. Typically, MLPS utilizing a conventional MPPT algorithm is more tolerant to shading, but during dynamic shading conditions, they also fail to detect the fast-shading variations and exhibit sub-optimal performance. Furthermore, the inability of conventional MPPT algorithms to track the maximum power point during dynamic sub-panel shading conditions is evident from its drawbacks such as slower convergence speed and poor tracking accuracy.

Consequently, it is imperative to study the performance of the proposed MLPS-based system architecture under dynamic sub-panel shading conditions.

6.5. Power Generation Control Algorithms

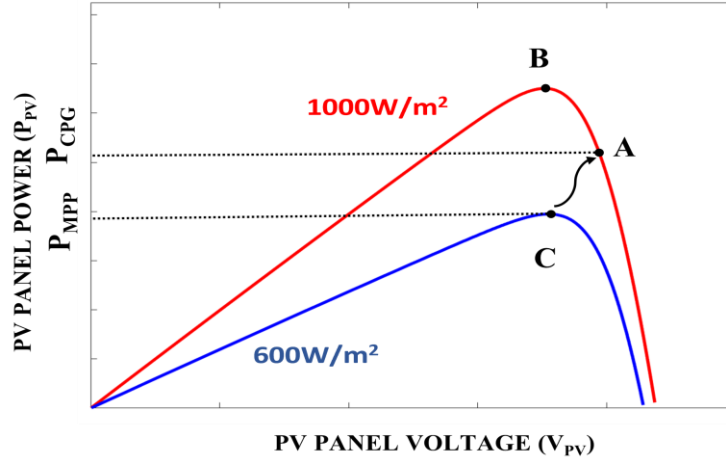
Different power generation control algorithms for flexible power generation and tracking the MPP under dynamic sub-panel shading conditions are discussed in this section.

6.5.1. CPG-InC Flexible Power Point Tracking Algorithm

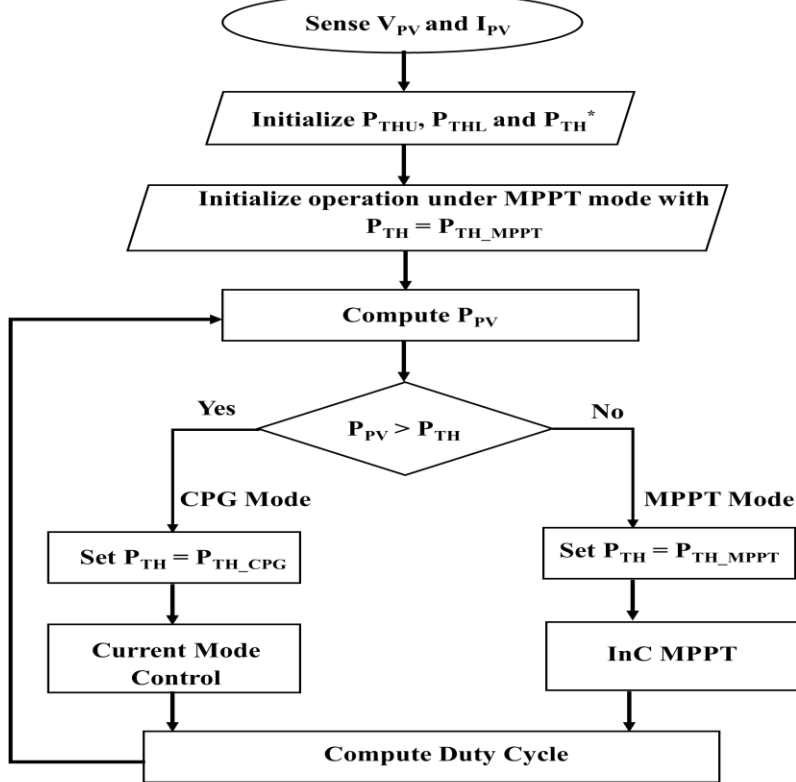
In this subsection, the concept and operation of the CPG-InC flexible power point tracking algorithm are discussed. The proposed algorithm facilitates dual operating mode i.e., constant power generation (CPG) and maximum power generation (MPG) from the PV

panel. The algorithm achieves flexible power generation during insolation variation and adequately selects the requisite operating mode. The fundamental concept and operation of flexible power generation is illustrated in Fig.6.8(a) where the PV panel operates at different operating points on the P-V curve depending on the insolation level. Initially, the PV panel is operating at a lower insolation with its operating point C on the P-V curve, with the selection of the MPPT mode facilitating the maximum power evacuation from the PV panel as the operating power is lesser than the threshold power ($P_{PV} \leq P_{TH}$). The increase in the insolation causes the operating PV power to cross the threshold power ($P_{PV} > P_{TH}$) and subsequently trigger the movement of the operating point in the P-V curve from point C corresponding to the MPPT mode to point A corresponding to the CPG mode. Moreover, the operation of the PV panel in CPG mode at higher insolation becomes evident as it moves to the constant power point (CPP) at A instead of the maximum power point (MPP) at B, thereby allowing constant power generation from the panel. The flowchart of the proposed CPG-InC FPPT algorithm is demonstrated in Fig.6.8(b) and operates under uniform insolation variations, with operating modes selected based on (6.1). Initially, the algorithm operates under MPPT mode with the Incremental Conductance (InC) tracking the maximum power point and facilitating maximum power evacuation from the PV panel. During MPPT mode, the threshold power is set to P_{TH_MPPT} ($P_{TH} = P_{TH_MPPT}$) with its value equal to the absolute threshold power (P_{TH}^*) as shown in (6.2). Moreover, the absolute threshold power is set to 80% of the rated PV power corresponding to the insolation of $1000W/m^2$. The operating power P_{PV} increases as the solar insolation increases, which facilitates the operation under MPPT mode as long as $P_{PV} \leq P_{TH}$. It is pertinent to note that as soon as P_{PV} exceeds the P_{TH} (P_{TH_MPPT}), the FPPT algorithm seamlessly transits to CPG mode and maintains the operating PV power at the threshold power corresponding to CPG ($P_{TH} =$

P_{TH_CPG}). The operating limits of P_{TH_CPG} during CPG operation are defined in (6.3) and show the value of the tolerance band (Δp) of 2.5% of P_{TH}^* while the value of P_{TH_CPG} is set to the lower operating limit (P_{THL}). Moreover, the extreme limits of the power band are P_{THL}



(a)



(b)

Fig.6.8. Flexible power generation (a) Basic concept (b) Flowchart of flexible power point tracking algorithm

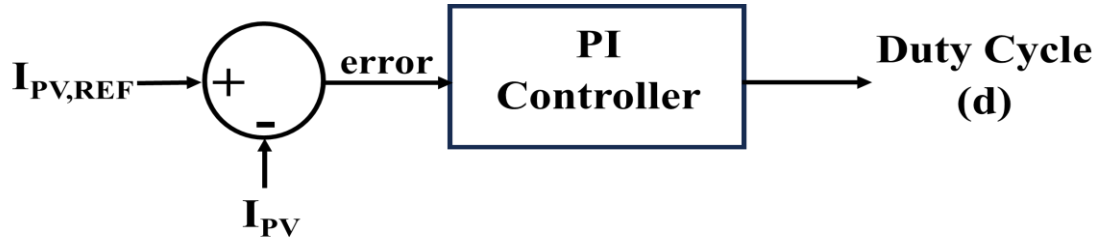


Fig.6.9. Block diagram of current control

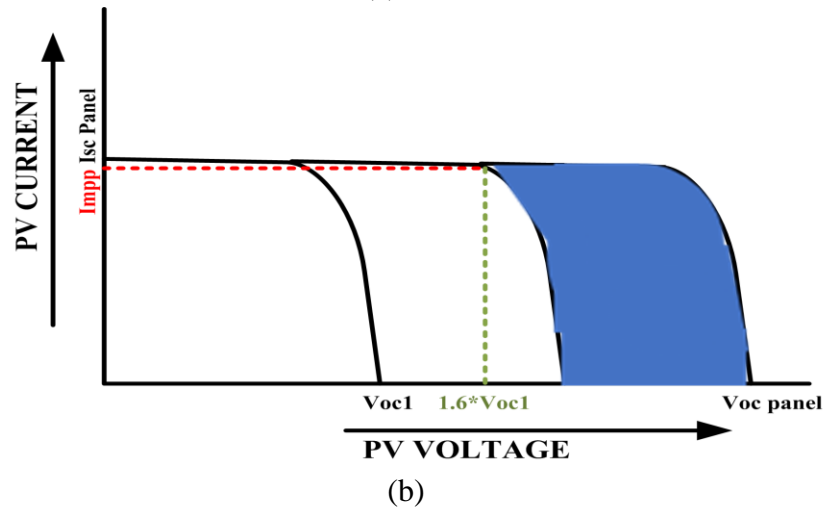
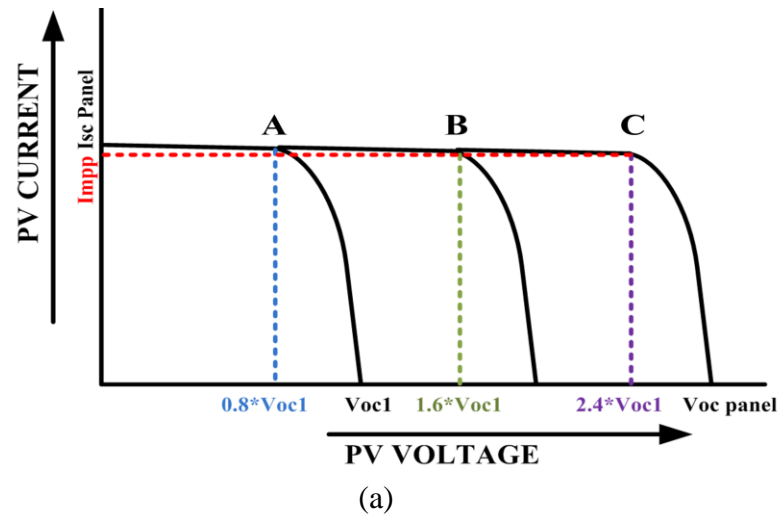


Fig.6.10. Operation of PV panel under sub-panel shading with I-V curve having (a) No shading (b) One-third shading

and P_{THU} . It is observed that a further increase in the insolation maintains the operation in CPG mode while ensuring regulated PV power. Additionally, a similar operating principle

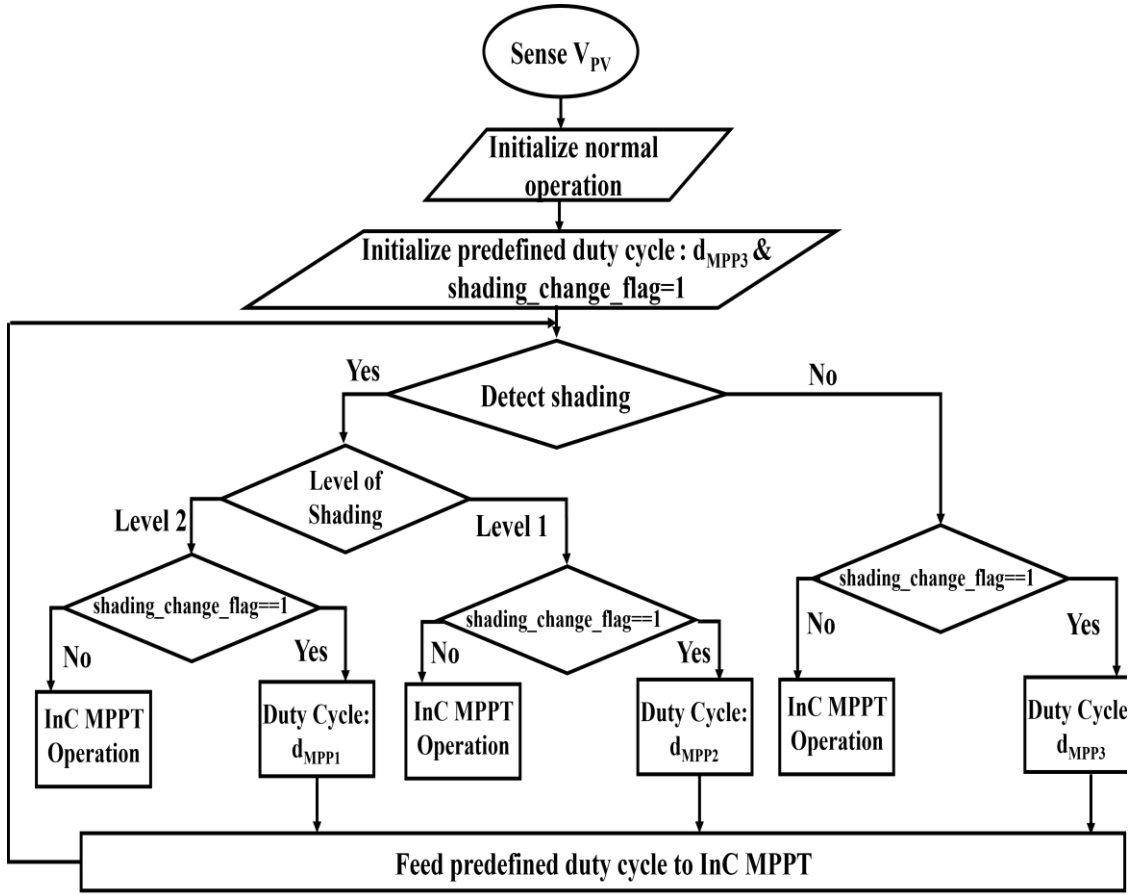


Fig.6.11. Flowchart of fast MPPT algorithm

of the proposed algorithm during the mode transition from CPG to MPPT mode is observed during uniform insolation variation.

$$Mode = \begin{cases} CPG & \text{for } P_{PV} > P_{TH} \text{ } (P_{TH} = P_{TH_CPG}) \\ MPPT & \text{for } P_{PV} \leq P_{TH} \text{ } (P_{TH} = P_{TH_MPPT}) \end{cases} \quad (6.1)$$

$$P_{TH_MPPT} = P_{TH}^* \quad (6.2)$$

$$P_{THU} = P_{TH}^* + \Delta p, P_{THL} = P_{TH}^* - \Delta p, P_{TH_CPG} = P_{THL} \quad (6.3)$$

The regulation of P_{PV} during CPG operating mode is achieved by implementing the current mode control where the reference PV current (I_{PV_REF}) is set to the current

corresponding to the upper limit of threshold power (P_{THU}) at the insolation of 1000W/m^2 . The block diagram of current mode control is shown in Fig.6.9 where the error between the operating PV current and reference current is fed to the PI controller with its objective to minimize the error and further generate the duty cycle. As a result, the regulation of PV current at reference current allows the power regulation of PV panels within the power band for different insolations. The MPPT operation is achieved by employing the InC MPPT algorithm which tracks the maximum power point for particular insolation and evacuates the maximum available power from the panel. The experimental implementation of the proposed algorithm on low-cost DSP controllers is feasible due to its low computational complexity. Furthermore, the algorithm implementation of the DSP controller observes inherent filtering of high-frequency power oscillations due to significantly slower ADC sampling and does not intervene with the operation of the algorithm. Additionally, the CPG-InC FPPT algorithm supports the battery storage system in mitigating intermittency.

6.5.2. Fast MPPT Algorithm

The operation of PV panels during dynamic sub-panel shading conditions highlights the drawbacks of conventional MPPT algorithms such as slow convergence and poor tracking accuracy. It is imperative to develop the MPPT algorithm tailor-made for operation under dynamic sub-panel shading conditions and facilitate the evacuation of maximum power during fast shading variations. The fast MPPT algorithm is proposed in this sub-section with the objective of faster response to the shading variations during dynamic shading. The fundamental operating principle of the proposed algorithm is demonstrated in Fig.6.10, where the algorithm operates in InC MPPT mode during normal operating conditions or insolation variations and tracks the corresponding maximum power point, but the shading

conditions trigger the fast shade subroutine. In the fast shading subroutine, the algorithm detects the degree of shade and only needs to operate at one of the three operating points (A, B, and C) during fast shading transitions by selecting one of the three predefined reference duty cycles. This significantly reduces the transit time between the operating points during the shading and allows a dramatically faster response to shade variations, which is not possible for conventional MPPT algorithms. Once the suitable operating point depending on the degree of shade has been selected, the algorithm forces the InC MPPT subroutine to operate in the vicinity of that particular operating point and predefined duty cycle. Fig.6.10(a) shows the operation of an unshaded PV panel at point C with the operating voltage of $2.4V_{OC1}$ (V_{OC1} is one-third of the open circuit voltage of the PV panel) and the corresponding duty cycle of d_{MPPT3} . Moreover, the operation of one-third shaded PV panel shown in Fig.6.10(b) is at point B with a corresponding operating panel voltage of $1.6V_{OC1}$ and duty cycle of d_{MPPT2} . Fig.6.11 shows the flowchart of the proposed fast MPPT algorithm. The algorithm is initialized for normal unshaded operation with the operating initial duty cycle of d_{MPPT3} and the shading_change_flag is set. The status of shading_change_flag being 1 indicates the change in the shading. Furthermore, the degree of shade is denoted by Level 1 (one-third shading of the panel) and Level 2 (two-thirds shading of the panel). The algorithm first detects the shade and then checks whether shading_change_flag is set. The unshaded PV panel with shading_change_flag being reset indicates that there is no change in shading and the algorithm continues the InC MPPT operation while shading_change_flag being set indicates that a change in the shading has been observed and subsequently forces InC MPPT to operate in the vicinity of the predefined duty cycle d_{MPPT3} and further reset the shading_change_flag. Conversely, for shaded PV panel, the level of shading is further detected, and based on the level of shading

and shading_change_flag being set, the operating duty cycle of d_{MPPT1} (Level 2) or d_{MPPT2} (Level 1) is forced on the InC MPPT with the subsequent resetting of the flag whereas if the shading_change_flag is already reset, the algorithm observes no shading change and continues the InC MPPT operation. The proposed converter demonstrates faster convergence to MPP during dynamic shading as it seamlessly transits between the three operating points. The ability of the proposed algorithm to quickly detect the fast-shading variations and decide the operating duty cycle depending on the degree of shading highlights the fast response of the proposed algorithm operating during dynamic sub-panel shading. Moreover, the proposed fast MPPT algorithm is suitable for low-cost controllers as it is computationally inexpensive.

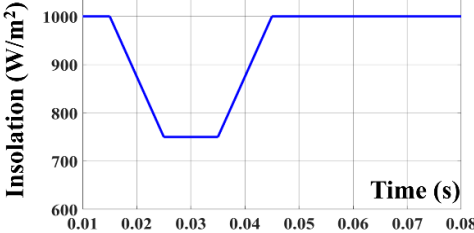
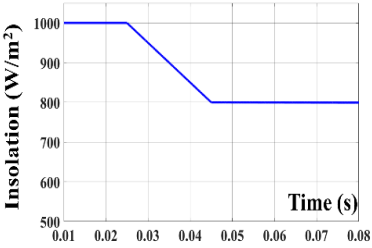
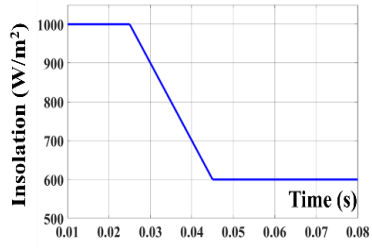
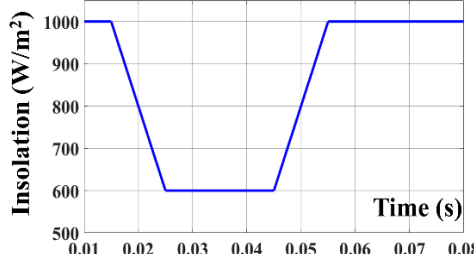
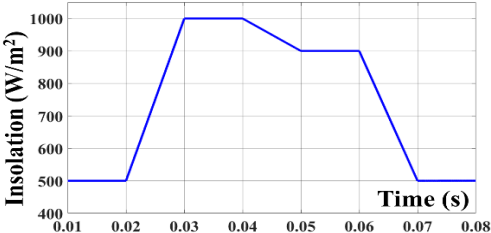
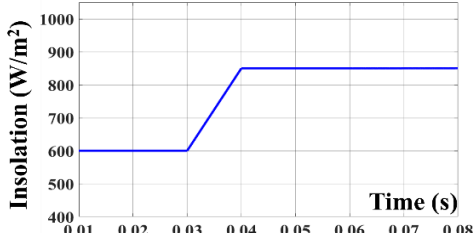
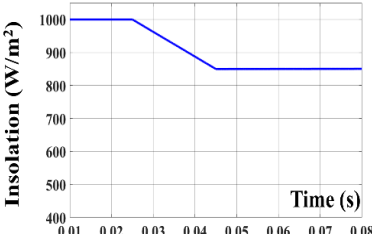
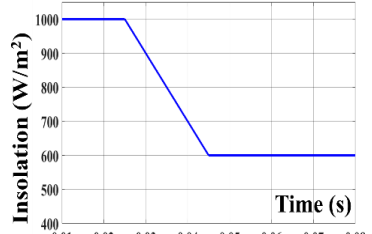
6.6. Results and Discussions

The simulated and experimental performance of the proposed MLPS system architecture employing MLIC and MMIC is investigated under different operating conditions in this section.

6.6.1. Simulation Results

TABLE 6.1: Simulated system parameters	
Parameter	Value
PV Panel Kyocera KD250GX- LFB	Rated Power (P_{MPP}) – 250W (1000W/m ²)
	Rated Voltage (V_{MPP}) – 29.8V (1000W/m ²)
	Rated Current (I_{MPP}) – 8.39A (1000W/m ²)
Nominal Voltage of DC Microgrid	380V
Number of PV panel units	2
MLIC	Refer to Table 3.5 for simulated parameters of MLIC
MMIC	Refer to Table 5.3 for simulated parameters of MMIC

TABLE 6.2: Simulated operating conditions for MLIC

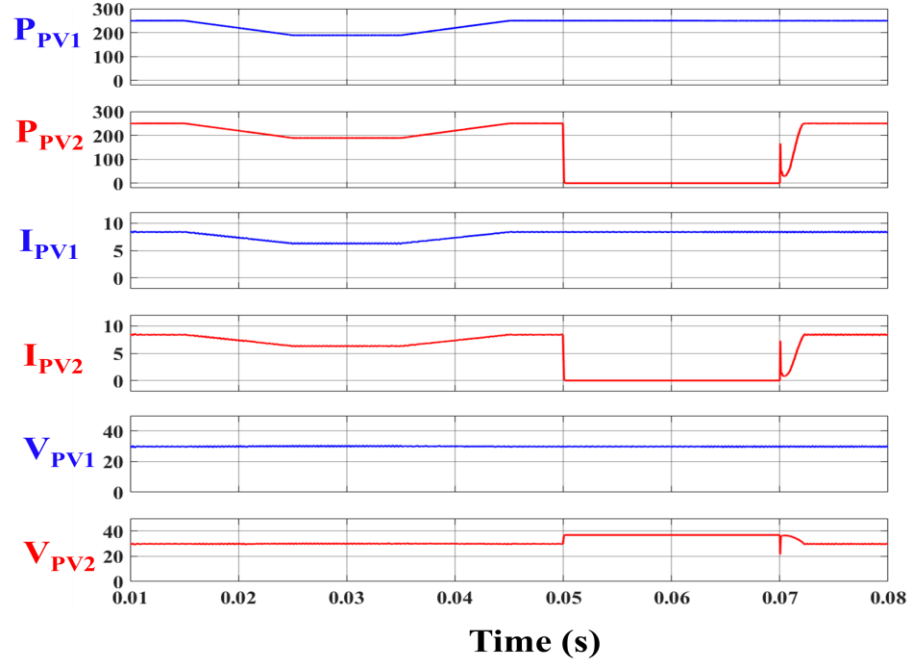
Case	PV Panel 1	PV Panel 2	Other
Case 1			Outage of PV Panel 2 at $t=0.05s$ and its reinsertion at $t=0.07s$
Case 2			
Case 3			Addition of a new PV panel (PV3) at $t=0.03s$
Case 4	Sub-panel shading at $t=0.02s$ and removal at $t=0.05s$	Sub-panel shading at $t=0.03s$ and removal at $t=0.06s$	
Case 5			
Case 6			Outage of PV Panel 2 at $t=0.06s$
Case 7			

This subsection delineates the simulated performance of MLPS-based system architecture under different operating conditions. The simulated model of the proposed MLPS system architecture is implemented on the MATLAB Simulink environment using simulated system parameters provided in Table 6.1. The simulated system model incorporates two PV panels based on Kyocera KD250GX-LFB which are independently integrated with a 380V DC microgrid using independent MLIC as well as a single MMIC. The simulated performance of the system investigates the steady-state and dynamical operation under different environmental operating conditions such as insolation variations and shading conditions as well as operational conditions such as the outage of a panel and the addition of a new panel in the system. For coherent understanding and comprehensive study of the simulated MLPS system, it is subdivided into MLIC interfaced MLPS system and MMIC interfaced MLPS system. The simulated performance of both these subsystems under different operating conditions are presented as cases in this subsection.

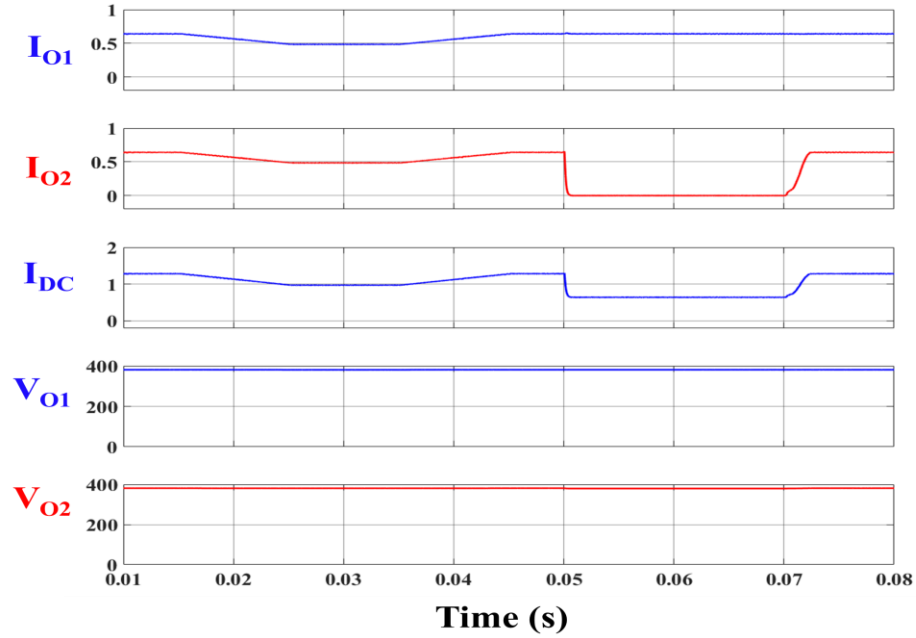
A. MLIC interfaced MLPS System Architecture

The MLIC interfaced MLPS system architecture incorporates two PV panels which are independently interfaced with the 380V DC microgrid using individual MLICs. The simulated operating conditions for MLIC based MLPS are shown in Table 6.2. For cases 1 to 4, the MLIC utilizes the conventional InC MPPT algorithm while the CPG-InC FPPT algorithm is employed for cases 5 – 7

Case – 1: Operation of the system under uniform insolation variation with the outage of a PV panel and its subsequent reinsertion



(a)

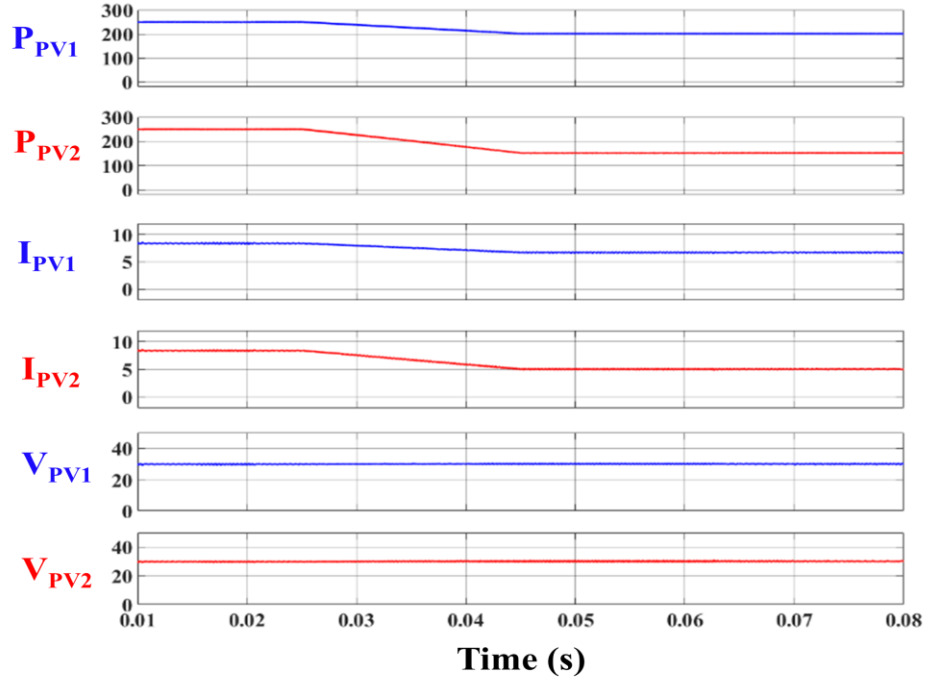


(b)

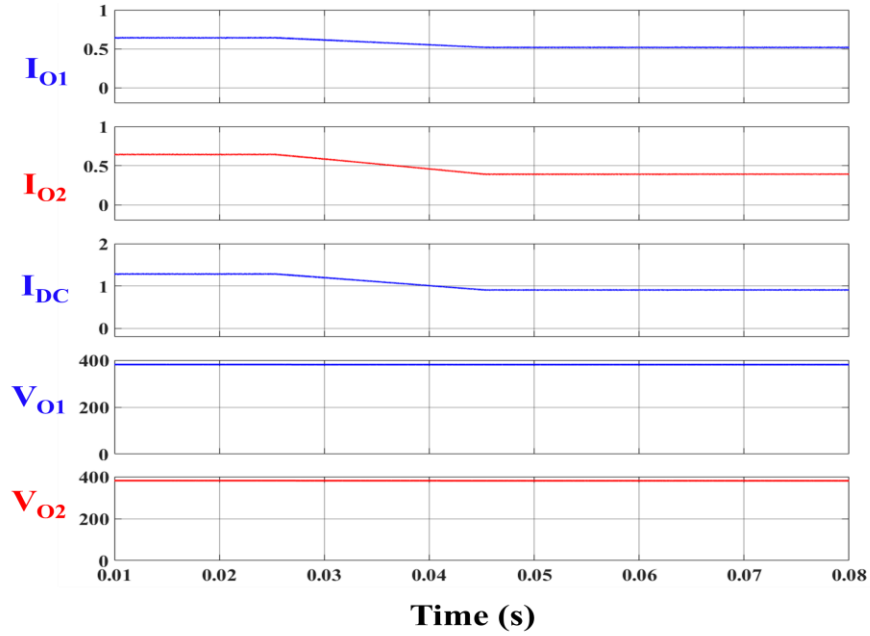
Fig.6.12. Case 1: Simulated operation of MLIC system under uniform insolation variation from 1000W/m^2 to 750W/m^2 from $t=0.015$ s till $t=0.025$ s and vice versa from $t=0.035$ s till $t=0.045$ s and further outage of PV panel 2 at $t=0.05$ s and its reinsertion at $t=0.07$ s (a) Profile of PV panels with their powers P_{PV1} and P_{PV2} (W), PV current I_{PV1} and I_{PV2} (A) and PV voltage V_{PV1} and V_{PV2} (V) (b) Output profile with current of MLICs I_{O1} and I_{O2} (A), current in the DC microgrid I_{DC} (A) and output voltages of MLICs V_{O1} and V_{O2} (V)

The PV panels operate under uniform insolation variations from 1000W/m^2 to 750W/m^2 and vice versa from $t=0.015\text{s}$ to $t=0.045\text{s}$. The profile of PV panels is observed in Fig.6.12(a) where the PV power reduces from 250W at $t=0.015\text{s}$ to 189.3W at $t=0.025\text{s}$ and vice versa till $t=0.045\text{s}$. Moreover, the outage of PV panel 2 at $t=0.05\text{s}$ and its subsequent reinsertion at $t=0.07\text{s}$ is demonstrated from the results. It is pertinent to observe that the outage of PV panel 2 has minimal impact on the performance of PV panel 1 which continues to operate at 250W . Also, the result shows a seamless outage and reinsertion of PV panel 2 without creating large fluctuations. The operating current of both PV panels experienced the transition from 8.39A to 6.305A and vice versa during uniform insolation variation and further observed seamless transition in the current of PV panel 2 during an outage and reinsertion without affecting the current of PV panel 1. The voltage profile of both PV panels is shown with the outage of PV panel 2 causing its voltage to increase to its open circuit voltage (V_{OC}) of 36.9V and subsequently back to the original value of 29.8V (V_{MPP} - voltage corresponding to MPP). The output profile is shown in Fig.6.12(b) where the output currents of both MLICs witness a transition from 0.642A to 0.487A and vice versa. Moreover, the outage of PV panel 2 observes the output current of MLIC 2 (I_{O2}) to reach zero before returning to its original value upon reinsertion of PV panel 2, while the output current of MLIC 1 (I_{O1}) remains unaffected, thereby further highlighting minimal inter converter circulating currents. The result also highlights the waveform of current (I_{DC}) flowing through the DC microgrid which is the aggregation of both I_{O1} and I_{O2} . Moreover, the terminal voltage across each converter is also observed from the result in Fig.6.12(b).

Case – 2: Operation of the system under partial shading conditions



(a)



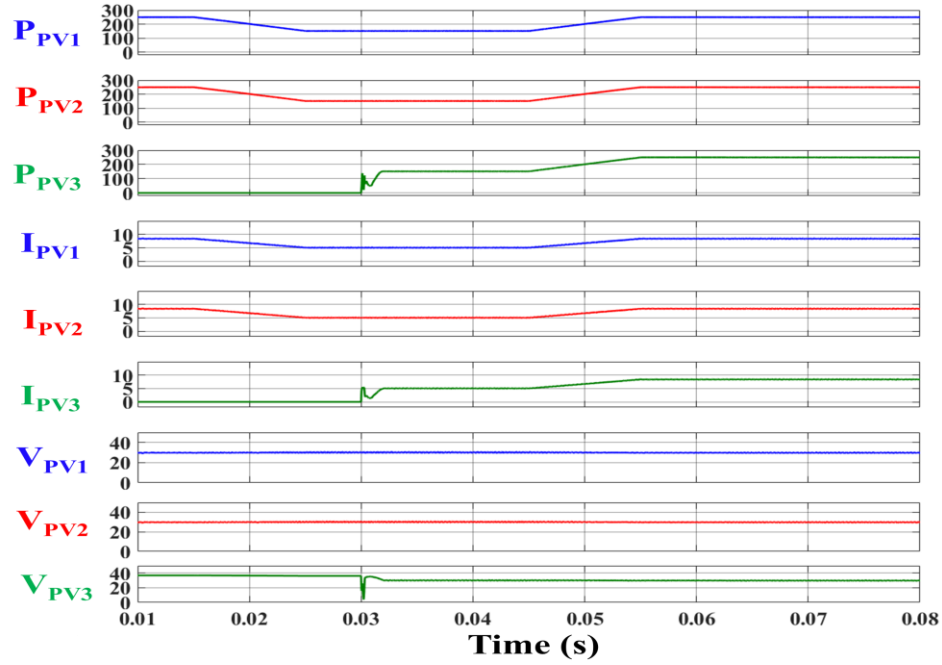
(b)

Fig.6.13. Case 2: Simulated operation of MLIC system under partial shading with insolation variation from 1000W/m^2 to 800W/m^2 in panel 1 and 600W/m^2 in panel 2 from $t=0.025\text{s}$ till $t=0.045\text{s}$ (a) Profile of PV panels with their powers P_{PV1} and P_{PV2} (W), PV current I_{PV1} and I_{PV2} (A) and PV voltage V_{PV1} and V_{PV2} (V) (b) Output profile with current of MLICs I_{O1} and I_{O2} (A), current in the DC microgrid I_{DC} (A) and output voltages of MLICs V_{O1} and V_{O2} (V)

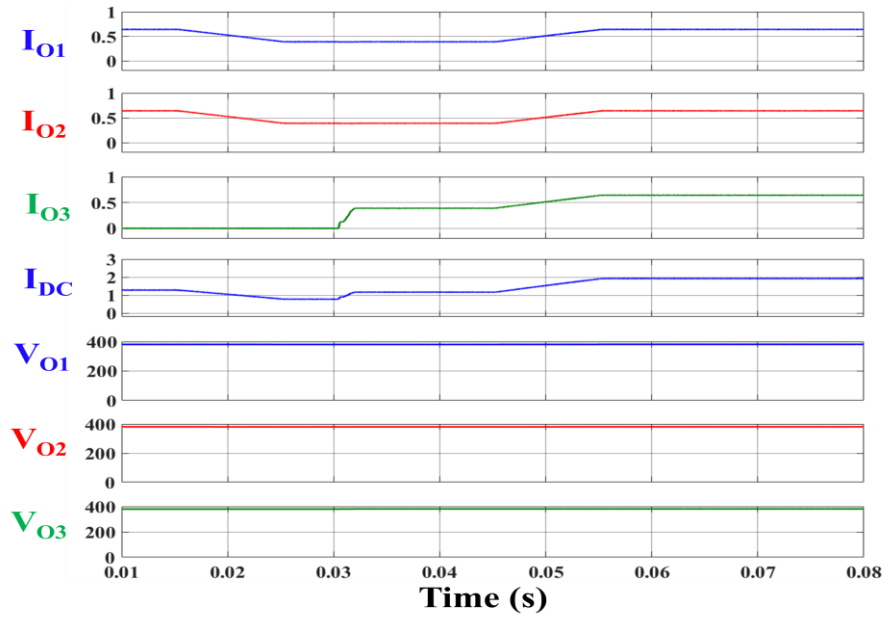
In this case, both PV panels operate at 1000W/m^2 and experience a different rate of insolation change from $t=0.025\text{s}$ till $t=0.045\text{s}$ with their final insolation of 800W/m^2 and 600W/m^2 respectively, thereby exhibiting partial shading conditions. Fig.6.13(a) displays the profile of the PV panel where both PV panels operating at 250W till $t=0.025\text{s}$ witness different rates of change of insolation and finally evacuate the maximum power of 201W and 152W respectively. Furthermore, the current of both PV panels operating at 8.39A reduces to 6.72A and 5.05A respectively, which corresponds to the insolation of 800W/m^2 and 600W/m^2 respectively. The result highlights the superior performance of the system under partial shading conditions where each PV panel receiving different insolation operates seamlessly at its corresponding maximum power point and evacuates the maximum available power. This also affirms the merits of MLPS where it exhibits superior power utilization from each panel and is more shade tolerant. The output profile of the system is demonstrated in Fig.6.13(b) where the output currents of both MLICs operating at 0.641A reduce to 0.517A and 0.389A respectively. Furthermore, the profile also shows the current in the DC microgrid (I_{DC}) and the terminal voltage across each converter.

Case – 3: Plug and Play operation: Addition of a new PV panel

The PV panels observe uniform insolation variation from 1000W/m^2 to 600W/m^2 and vice versa from $t=0.015\text{s}$ to $t=0.055\text{s}$ in this case. The profile of PV panels is shown in Fig.6.14(a) where the powers of PV panels 1 and 2 observe the transition from 250W at $t=0.015\text{s}$ to 152W at $t=0.025\text{s}$ and vice versa from $t=0.045\text{s}$ till $t=0.055\text{s}$. Moreover, a new PV panel (panel 3) has been added to the system at $t=0.03\text{s}$ to increase the overall power capacity of the system. It is observed from the result that the new PV panel seamlessly evacuates the maximum power of 152W during insolation of 600W/m^2 and effectively



(a)



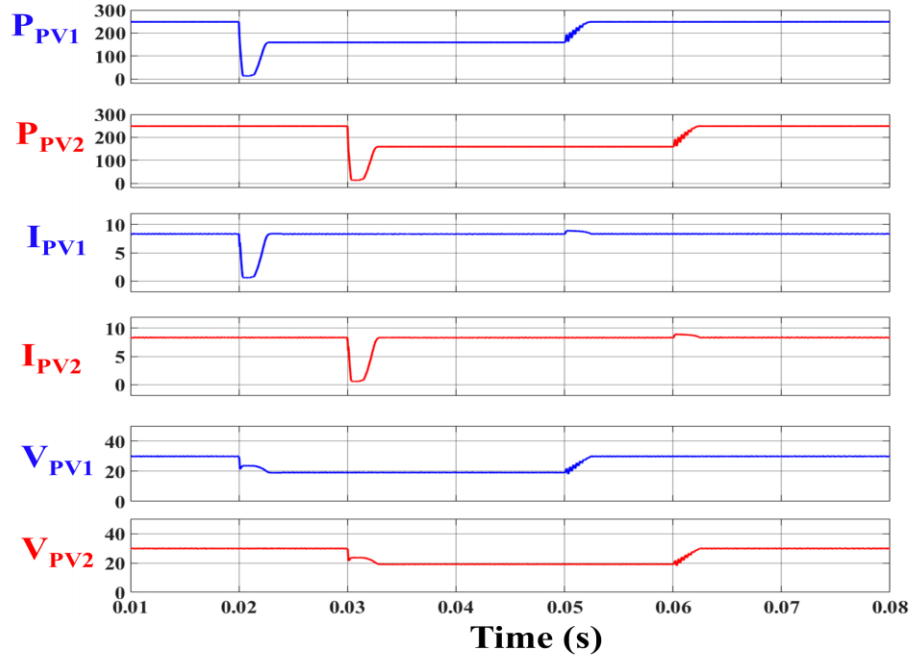
(b)

Fig.6.14. Case 3: Simulated operation of MLIC system under uniform insolation variation from 1000W/m^2 to 600W/m^2 from $t=0.015\text{s}$ till $t=0.025\text{s}$ and vice versa from $t=0.045\text{s}$ to $t=0.055\text{s}$ and addition of new panel (PV3) at $t=0.03\text{s}$ (a) Profile of PV panels with their powers P_{PV1} , P_{PV2} and P_{PV3} (W), PV current I_{PV1} , I_{PV2} and I_{PV3} (A) and PV voltage V_{PV1} , V_{PV2} and V_{PV3} (V) (b) Output profile with current of MLICs I_{O1} , I_{O2} and I_{O3} (A), current in the DC microgrid I_{DC} (A) and output voltages of MLICs V_{O1} , V_{O2} and V_{O3} (V)

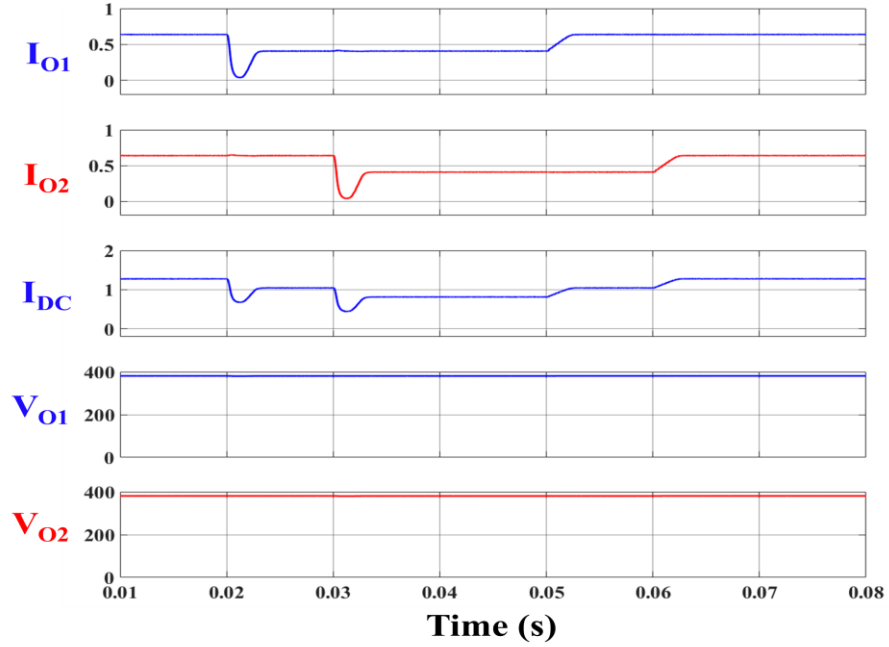
tracks the maximum power point during insolation increase to 1000W/m^2 at $t=0.055\text{s}$. The operating current of the PV panels experiences the transition from 8.39A to 5.05A and vice versa during uniform insolation variation. Moreover, the integration of the new PV panel in the system is evident from the result where the operating current increases from zero to 5.05A corresponding to the insolation of 600W/m^2 , and further increases to 8.39A @ 1000W/m^2 . The voltage profile of the PV panels is also shown in the results with the voltage of the new PV panel falling from its V_{OC} of 36.9V to its V_{MPP} of 30.07V at the insolation of 600W/m^2 at $t=0.03\text{s}$. The results highlight the dynamical increase in the power capacity of the system with minimal impact on the performance of the other PV panels due to the addition of a new PV panel, thereby emphasizing the plug-and-play operation of the proposed MLPS system architecture. Fig.6.14(b) shows the output profile of the system where the output currents of both MLICs witness a transition from 0.641A to 0.389A and vice versa. Furthermore, the addition of a new PV panel observes an increase in the output current of MLIC3 to 0.389A @ 600W/m^2 and further to 0.641A @ 1000W/m^2 . It is observed from the result that the addition of a new PV panel exhibits minimal fluctuations in the output current (I_{O3}) without compromising the performance of other MLICs and has no inter converter circulating currents. The result also highlights the waveform of I_{DC} and the terminal voltage across each converter.

Case – 4: Operation of the system under sub-panel shading condition

The profile of PV panels is shown in Fig.6.15(a), where both PV panels are operating at 1000W/m^2 initially with a maximum power evacuation of 250W . The sub-panel shading on PV panel 1 at $t=0.02\text{s}$ observes one-third shading of PV panel 1 with the dip in the operating PV power and finally settling at 160W while the removal of shade on panel 1 at



(a)



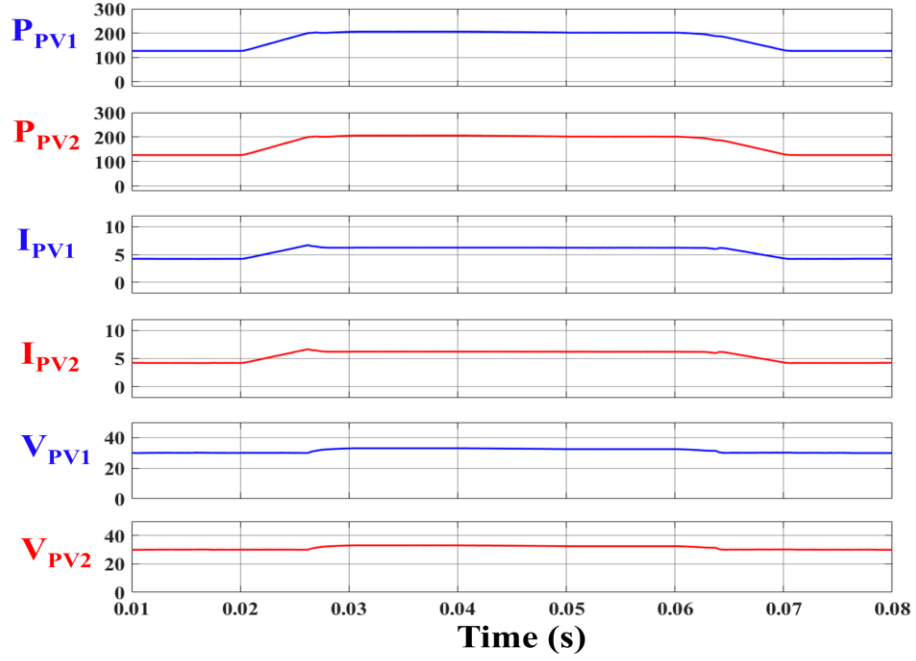
(b)

Fig.6.15. Case 4: Simulated operation of MLIC system under sub-panel shading in panel 1 at $t=0.02s$ and panel 2 at $t=0.03s$ and removal of shade in panel 1 at $t=0.05s$ and panel 2 at $t=0.06s$ (a) Profile of PV panels with their powers P_{PV1} and P_{PV2} (W), PV current I_{PV1} and I_{PV2} (A) and PV voltage V_{PV1} and V_{PV2} (V) (b) Output profile with current of MLICs I_{O1} and I_{O2} (A), current in the DC microgrid I_{DC} (A) and output voltages of MLICs V_{O1} and V_{O2} (V)

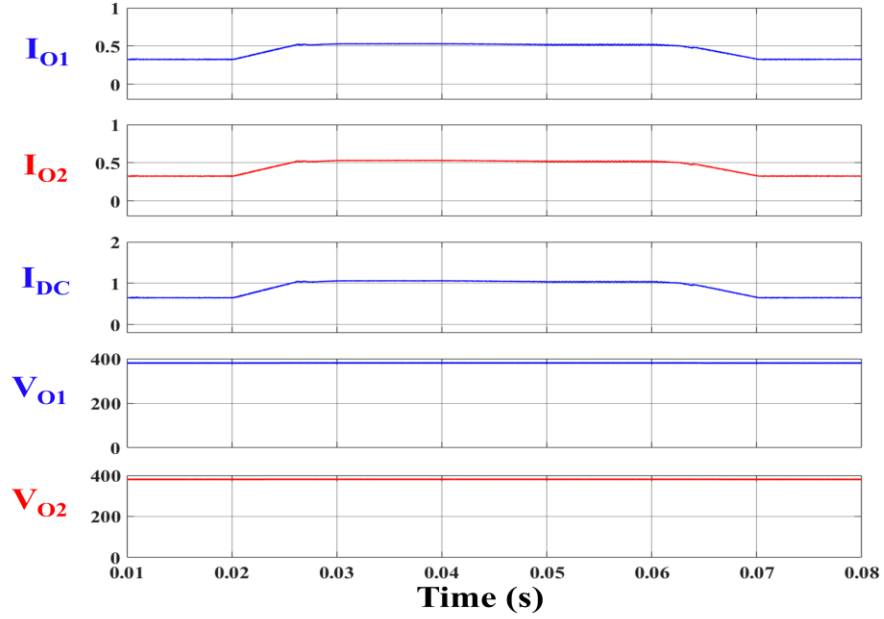
$t=0.05s$ causes the operating PV power to return to 250W. The result observes a similar operation during sub-panel shading on PV panel 2 at $t=0.03s$ and the removal of shade on panel 2 at $t=0.06s$. The current profile of PV panels under sub-panel shading and subsequent removal of shade observes a dip in the PV currents before settling back to their original value of 8.39A, thereby highlighting the functioning of the bypass diode. The voltage profile of PV panels demonstrated from the result highlights the dip in their operating voltages during sub-panel shading and subsequent return to their operating voltage corresponding to V_{MPP} of 29.8V @1000W/m². The output profile of the system is highlighted in Fig.6.15(b) where the output currents of MLICs observe a reduction from 0.641A to 0.405A during sub-panel shading of their corresponding PV panels while reverting to their original value of 0.641A after removal of their shades. The result also shows the I_{DC} and terminal voltages of MLICs. The simulated results show that dynamic transitions in the performance of one PV panel during shading or removal of shade have no impact on the performance of the other PV panel. Furthermore, the high gain capability of the proposed MLIC is highlighted during sub-panel shading conditions when the operating PV panel voltage reduces and the MLIC seamlessly increases its operating voltage gain to a notably high value of nearly 20 in order to meet the gain demand.

Case – 5: Flexible power generation during insolation variation

During case 5, both PV panels initially operate at 500W/m² and experience an increase to 1000W/m² from $t=0.02s$ to $t=0.03s$. Furthermore, the insolation linearly drops to 900W/m² at $t=0.05s$ and further reduces back to 500W/m² at $t=0.07s$. Fig.6.16(a) shows the profile of PV panels where they evacuate a maximum power of 126.7W till $t=0.02s$. The maximum available power evacuated from the PV panels starts increasing as the insolation



(a)

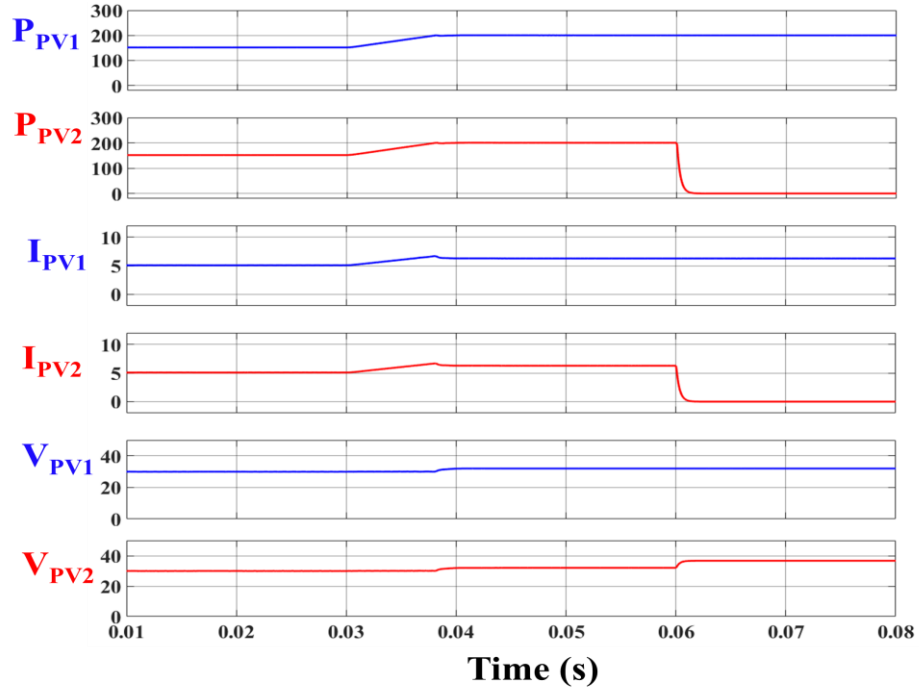


(b)

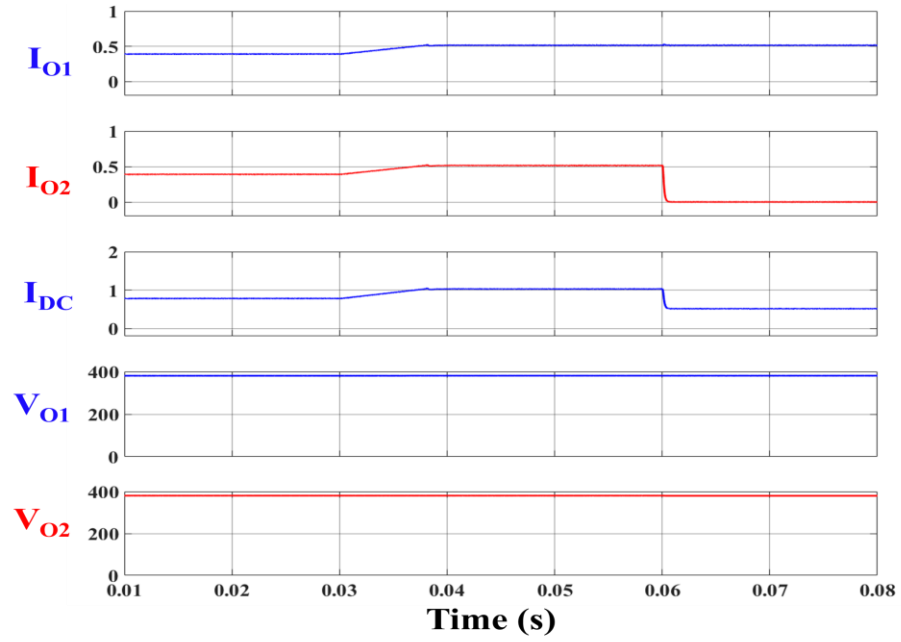
Fig.6.16. Case 5: Simulated flexible power operation of MLIC system under insolation variation from 500W/m^2 to 1000W/m^2 from $t=0.02\text{s}$ to $t=0.03\text{s}$, then from 1000W/m^2 to 900W/m^2 from $t=0.04\text{s}$ to $t=0.05\text{s}$ and finally from 900W/m^2 back to 500W/m^2 from $t=0.06\text{s}$ to $t=0.07\text{s}$ (a) Profile of PV panels with their powers P_{PV1} and P_{PV2} (W), PV current I_{PV1} and I_{PV2} (A) and PV voltage V_{PV1} and V_{PV2} (V) (b) Output profile with current of MLICs I_{O1} and I_{O2} (A), current in the DC microgrid I_{DC} (A) and output voltages of MLICs V_{O1} and V_{O2} (V)

rises and further experiences a transition from the MPPT mode to CPG mode at $t=0.026s$, after which the PV power is regulated within the power band during variations in the insolation till $t=0.063s$. After $t=0.063s$, the operation reverts to MPPT mode with maximum available power being evacuated during insolation drop to $500W/m^2$ and its sustained operation till $t=0.08s$. The current of both PV panels observes operation at I_{MPP} of $4.217A$ corresponding to the insolation of $500W/m^2$ and further increases to $6.675A$ at $t=0.026s$, after which it is regulated at the reference current of $6.235A$ till $t=0.063s$. Moreover, the operating current further observes reduction from $t=0.063s$ and tracks the I_{MPP} according to the insolation changes and finally settles back to $4.217A$ corresponding to $500W/m^2$. The voltage profile also observes significant changes in the operating panel voltage during the mode transitions from MPPT to CPG at $t=0.026s$ and further CPG to MPPT at $t=0.063s$. The output profile of the system is demonstrated in Fig.6.16(b) where variations in the output currents of MLIC and DC microgrid currents are observed. The results highlight the seamless transitions between MPPT and CPG modes and also underline the efficacy of constant power generation from the PV panels during insolation variations. The results quantify the effectiveness of CPG operation as the ratio of variation in the regulated input power to the variation in power corresponding to insolation change during CPG operation is significantly small value of 18.1%. Moreover, results also highlight the efficacy of the proposed FPPT algorithm in seamlessly facilitating the mode transition between MPPT and CPG and effectively regulating the operating power of PV panels in CPG mode during the operation at higher insolations.

Case – 6: Flexible power generation with panel outage



(a)



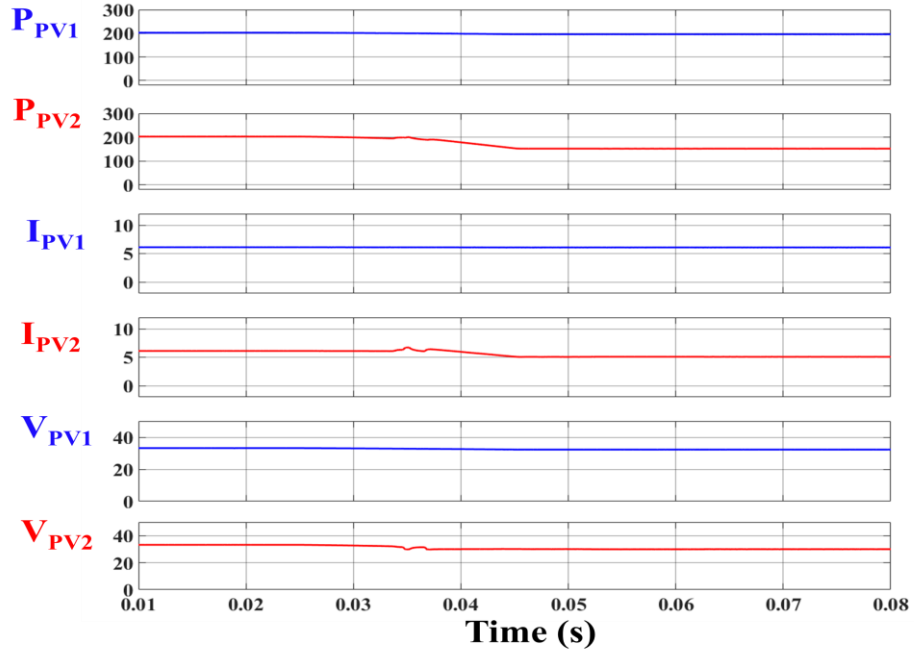
(b)

Fig.6.17. Case 6: Simulated flexible power operation of MLIC system under insolation variation from 600W/m^2 to 850W/m^2 from $t=0.03\text{s}$ till $t=0.04\text{s}$ and the outage of PV panel 2 at $t=0.06\text{s}$ (a) Profile of PV panels with their powers P_{PV1} and P_{PV2} (W), PV current I_{PV1} and I_{PV2} (A) and PV voltage V_{PV1} and V_{PV2} (V) (b) Output profile with current of MLICs I_{O1} and I_{O2} (A), current in the DC microgrid I_{DC} (A) and output voltages of MLICs V_{O1} and V_{O2} (V)

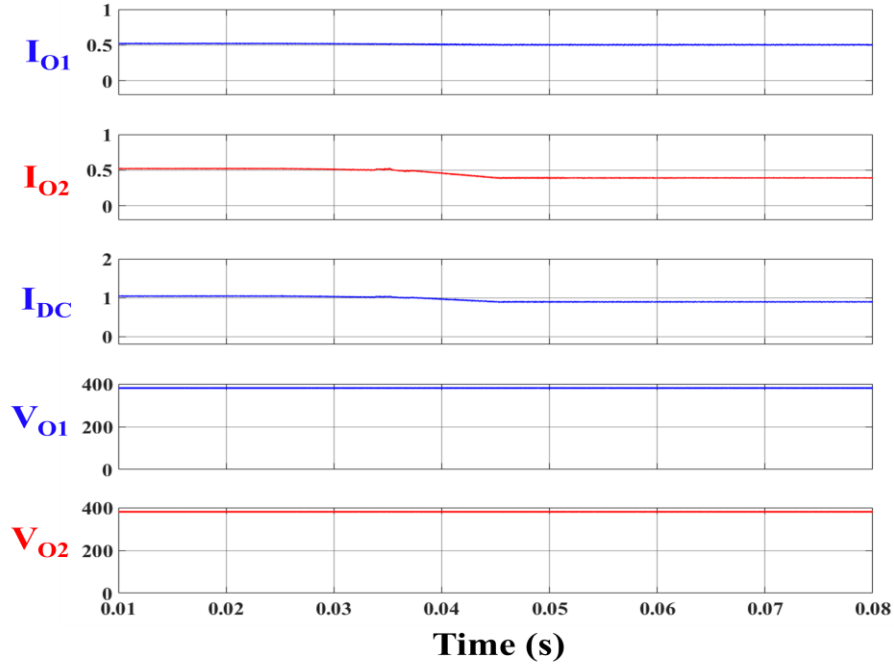
The system is tested for an increase in the insolation from 600W/m^2 to 850W/m^2 from $t=0.03\text{s}$ till $t=0.04\text{s}$ and the subsequent outage of PV panel 2 at $t=0.06\text{s}$. The profile of PV observed in Fig.6.17(a) shows that both PV panels evacuate a maximum power of 152W for the insolation of 600W/m^2 . The increase in the insolation observes the operation in MPPT mode operation which transits to the CPG mode at $t=0.0377\text{s}$ where the PV power regulates within the power band despite the increase in the insolation to 850W/m^2 till $t=0.04\text{s}$. Additionally, it is observed that the outage of PV panel 2 at $t=0.06\text{s}$ has no impact on the performance of PV panel 1 which continues to operate in CPG mode with regulated PV power. The operating current of PV panels observes the value of 5.05A at 600W/m^2 and further experiences an increase due to the rising insolation. The PV panel currents start following the reference current of 6.235A at $t=0.0377\text{s}$ during mode transition to CPG and further remain regulated despite of insolation increase till $t=0.04\text{s}$. Also, the voltage profile of PV panels shows the increase in the panel voltage during mode transition at $t=0.0377\text{s}$ and further observes an increase in the voltage of PV panel 2 to 36.9V (V_{oc}) during its outage. The output profile is shown in Fig.6.17(b) where the output currents of MLICs and DC microgrid observe an increase in the current between $t=0.03\text{s}$ and $t=0.0377\text{s}$ and then remains regulated due to operation in CPG mode. Moreover, the outage of PV panel 2 at $t=0.06\text{s}$ witnesses the drop of the output current of MLIC 2 to zero while the operation of other MLIC remains unaffected with constant output current.

Case – 7: Flexible power generation under partial shading conditions

The PV panels operating at 1000W/m^2 experience different rates of insolation change from $t=0.025\text{s}$ till $t=0.045\text{s}$ with their final insolation of 850W/m^2 and 600W/m^2 respectively, thereby exhibiting partial shading conditions. The profile of the PV panel is

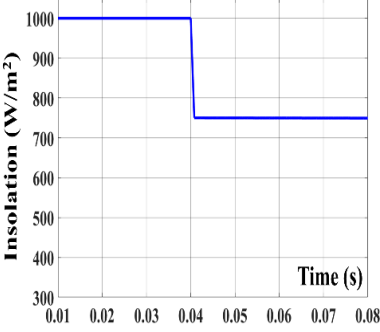
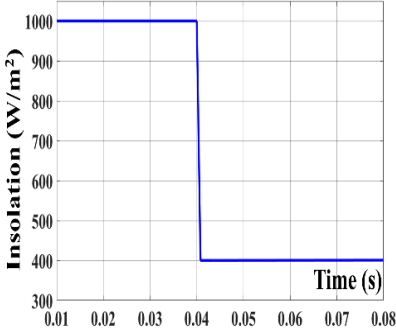
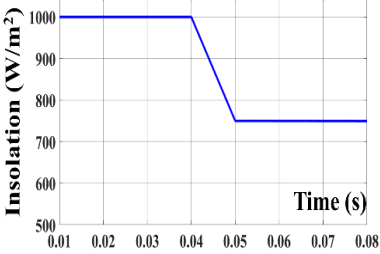


(a)



(b)

Fig.6.18. Case 7: Simulated flexible power operation of MLIC system under partial shading with insolation variation from 1000W/m^2 to 850W/m^2 in panel 1 and 600W/m^2 in panel 2 from $t=0.025$ s till $t=0.045$ s (a) Profile of PV panels with their powers P_{PV1} and P_{PV2} (W), PV current I_{PV1} and I_{PV2} (A) and PV voltage V_{PV1} and V_{PV2} (V) (b) Output profile with current of MLICs I_{O1} and I_{O2} (A), current in the DC microgrid I_{DC} (A) and output voltages of MLICs V_{O1} and V_{O2} (V)

TABLE 6.3: Simulated operating conditions for MMIC			
Case	PV Panel 1	PV Panel 2	Other
Case 1			
Case 2		Constant Insolation at 1000W/m ²	Outage of PV panel 2 at t=0.03s and its reinsertion at t=0.05s
Case 3	Constant Insolation at 1000W/m ²	Sub-panel shading at t=0.03s and removal at t=0.05s	
Case 4	Sub-panel shading at t=0.03s, 0.04s, 0.045s, 0.055s and their subsequent removal at t=0.035s, 0.042s, 0.05s	Sub-panel shading at t=0.032s, 0.042s, 0.05s, 0.06s and their subsequent removal at t=0.037s, 0.045s, 0.057s	

demonstrated in Fig.6.18(a) where both PV panels operating under CPG mode with regulated power of 202.6W till t=0.025s witness different rates of change of insolation. It is observed that PV panel 1 continues to regulate the PV power within the power band as the insolation drops to 850W/m² whereas PV panel 2 transits to MPPT mode at t=0.036s and starts tracking maximum power point as the insolation continues to drop till 600W/m² with its steady state power of 152W. Furthermore, the current of PV panels regulated at the reference current of 6.235A begins observing deviations between them from t=0.036s where the current of PV panel 2 starts operating at I_{MPP} . The voltage profile of PV panels is also demonstrated from the results with PV panel 2 observing a reduction in the operating

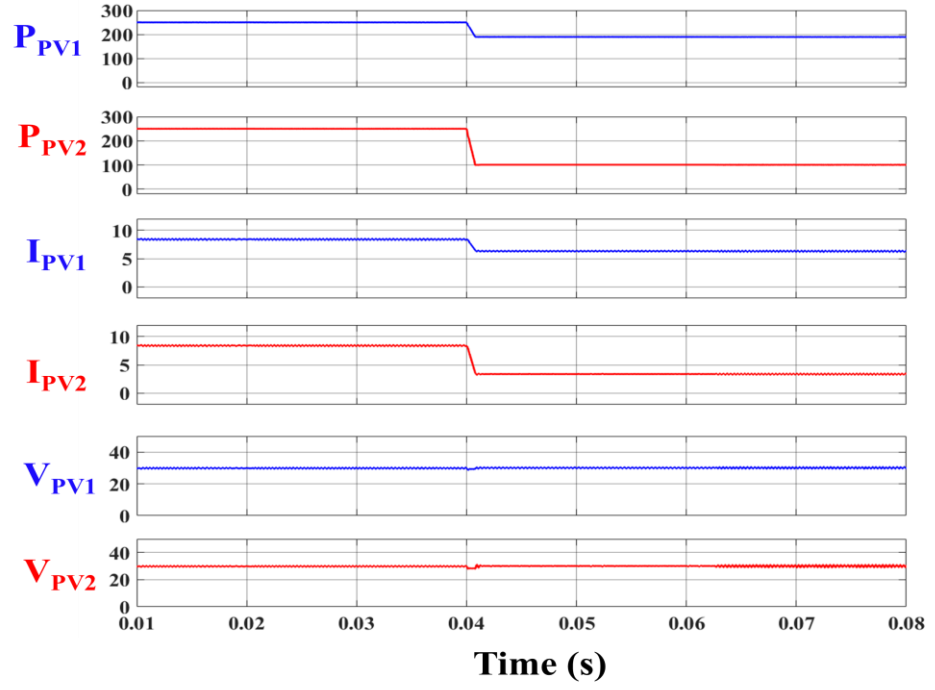
voltage to 29.8V at $t=0.036s$. Fig.6.18(b) demonstrates the output profile of the system where the output current of MLICs operating at 0.52A observes variation between them from $t=0.036s$ with I_{O1} constantly maintained while I_{O2} reduces to 0.39A. The current (I_{DC}) in the DC microgrid observes a variation from 1.042A to 0.91A as it is a summation of both I_{O1} and I_{O2} . The terminal voltage across each converter is also shown in the results. The result also highlights the ability of the proposed system to mitigate the effects of partial shading to a certain extent and continue to operate at constant power, thereby supporting in reducing the intermittency. This is attributed to the superior performance of the FPPT algorithm and its effectiveness in facilitating constant power generation and seamless mode transitions during partial shading conditions.

B. MMIC interfaced MLPS system architecture:

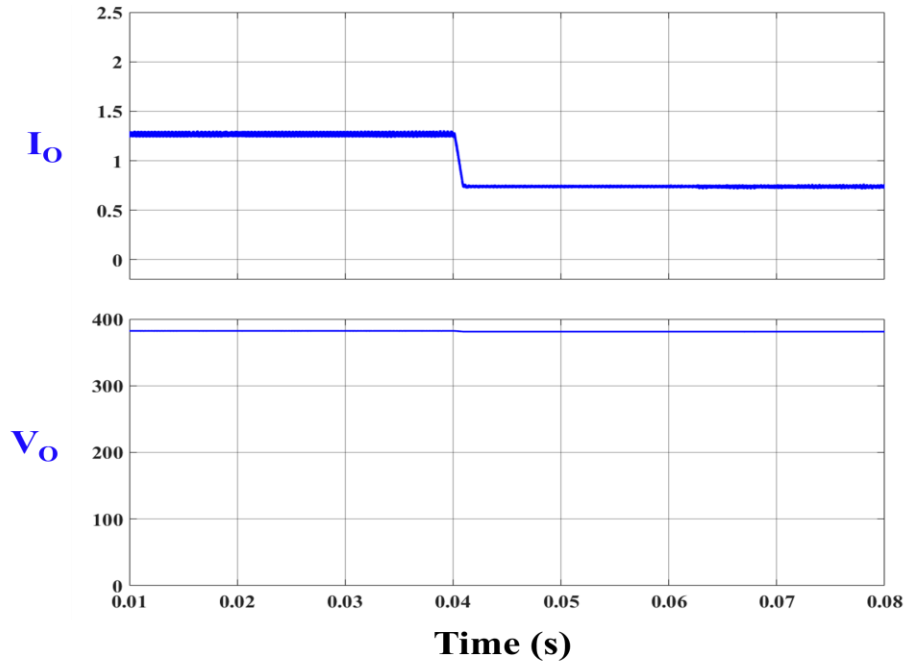
The MMIC interfaced MLPS system architecture incorporates two PV panels which are interfaced with the 380V DC microgrid using a single dual input MMIC. The simulated operating conditions for MMIC based MLPS are shown in Table 6.3. Furthermore, the MMIC incorporates the Fast MPPT algorithm for evacuating maximum power during all operating conditions.

Case – 1: Operation of the system under partial shading condition

Fig.6.19(a) demonstrates the profile of PV panels where both PV panels operate at $1000W/m^2$ till $t=0.04s$ and further observe deviation in the insolation rate with final insolutions of $750W/m^2$ and $400W/m^2$. The PV panels initially operating at an insolation of $1000W/m^2$ have a power of 250W while the deviation in their insolation rate after $t=0.04s$ observes steady state power of PV panels of 189.3W and 101.3W respectively.



(a)



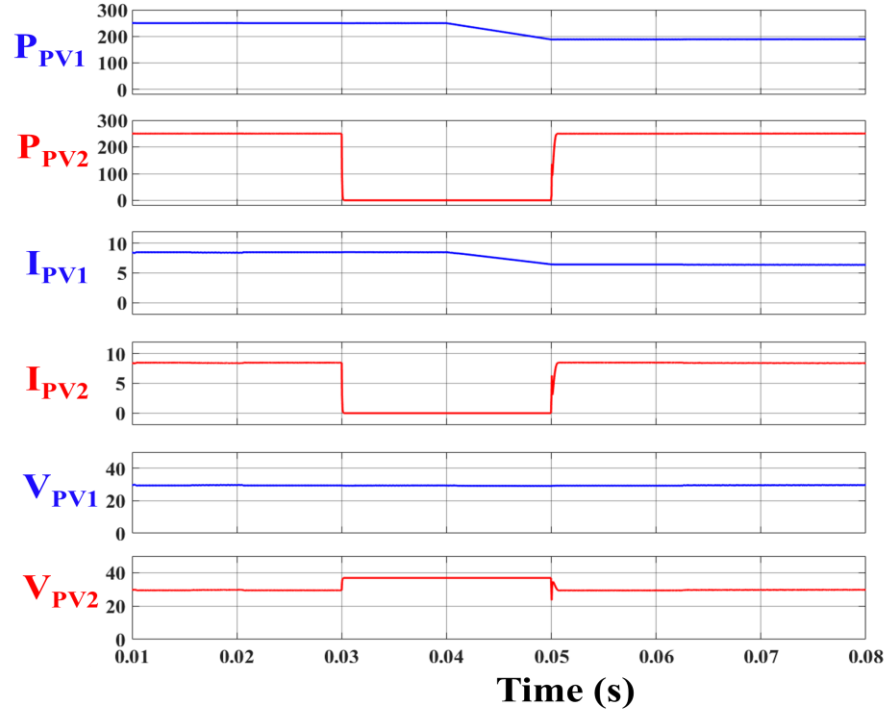
(b)

Fig.6.19. Case 1: Simulated operation of MMIC system under partial shading with insolation variation from 1000W/m^2 to 750W/m^2 in panel 1 and 400W/m^2 in panel 2 from $t=0.04\text{s}$ till $t=0.0408\text{s}$ (a) Profile of PV panels with their powers P_{PV1} and P_{PV2} (W), PV current I_{PV1} and I_{PV2} (A) and PV voltage V_{PV1} and V_{PV2} (V) (b) Output current I_O (A) and output voltage V_O (V) of MMIC

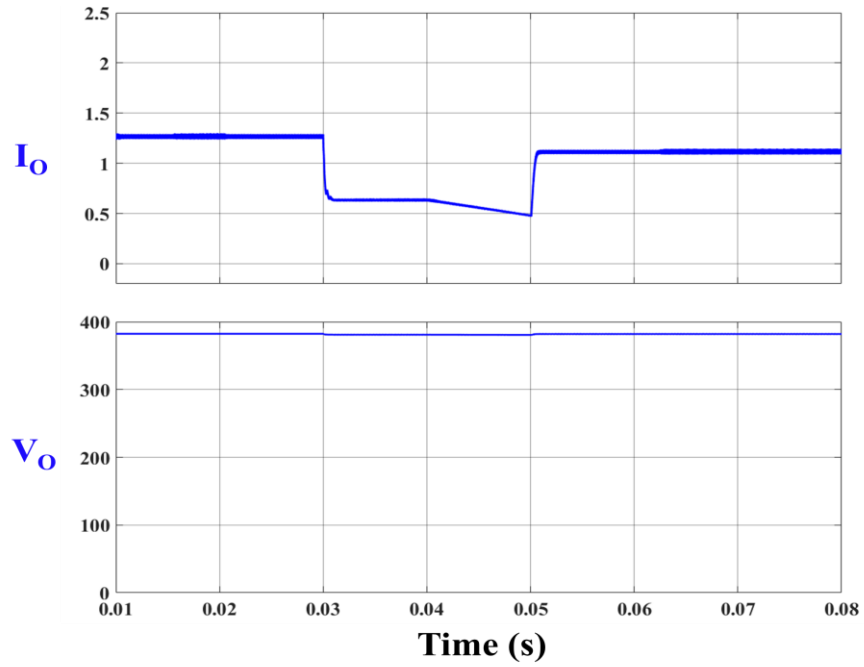
Additionally, the currents of each PV panel operating at 8.39A @1000W/m² observe variation in their steady-state value of 6.305A and 3.37A respectively after t=0.04s. The result demonstrates seamless operation under partial shading conditions where each PV panel receives different insolation and displays the maximum power evacuation from each panel during partial shading. Moreover, the operational independence of each power module of MMIC and its seamless operation during current-based asymmetry is effectively highlighted from the results where no interference between the modules operating at different power is observed. Fig.6.19(b) shows the variation in the output current of MMIC due to partial shading condition and its terminal voltage.

Case – 2: Operation of the system under insolation variation and outage and subsequent reinsertion of a PV panel

The profile of PV panels is shown in Fig.6.20(a) with both PV panels operating at 250W corresponding to the insolation of 1000W/m². The outage of PV panel 2 at t=0.03s causes its power to drop to zero while PV panel 1 continues its unperturbed operation at 250W. Furthermore, the insolation reduces from 1000W/m² to 750W/m² from t=0.04s to t=0.05s where the operating power of PV panel 1 reduces to 189.3W. The reinsertion of PV panel 2 in the system at t=0.05s shows the increase in its operating power to 250W without affecting the operation of PV panel 1. The current in PV panel 1 observes variation from 8.39A to 6.305A during the insolation change while the PV panel 2 current drops to zero during the outage of the panel and further increases to 8.39A upon reinsertion in the system. The voltage profile of PV panels is also observed from the results and indicates the variation of PV panel 2 from V_{MPP} of 29.8V to V_{OC} of 36.9V and vice versa during an outage of the panel and its subsequent reinsertion into the system. The output current and the terminal



(a)



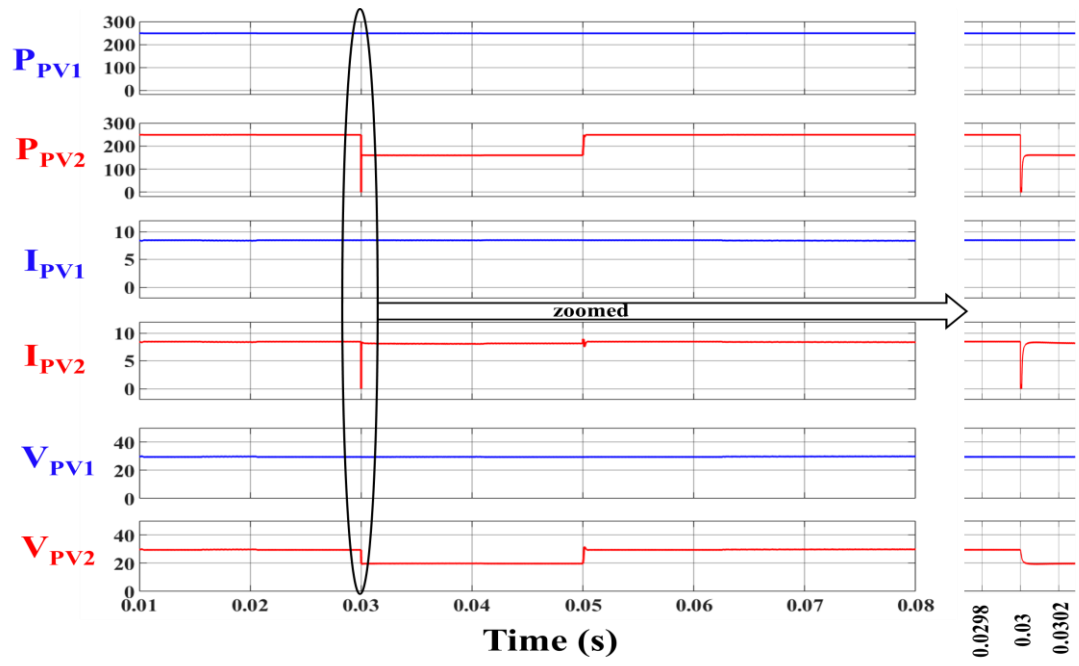
(b)

Fig.6.20. Case 2: Simulated operation of MMIC system under insolation change in PV panel 1 from 1000W/m^2 to 750W/m^2 from $t=0.04\text{s}$ till $t=0.05\text{s}$ and outage of PV panel 2 at $t=0.03\text{s}$ and its reinsertion at $t=0.05\text{s}$ (a) Profile of PV panels with their powers P_{PV1} and P_{PV2} (W), PV current I_{PV1} and I_{PV2} (A) and PV voltage V_{PV1} and V_{PV2} (V) (b) Output current I_O (A) and output voltage V_O (V) of MMIC

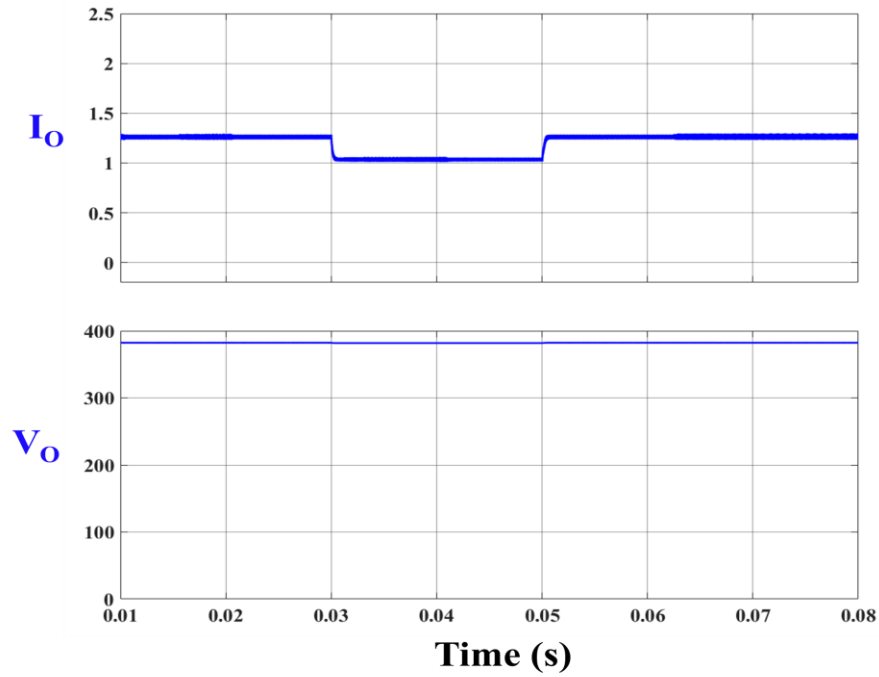
voltage of MMIC is shown in Fig.6.20(b) and highlights variation in current because of insolation variations and the outage and reinsertion of the PV panel. The results show the independence in operation of each power module of MMIC with the variations in the one module does not impact the performance of the other module. Moreover, no intermodular circulating current is observed which is affirmed from the waveforms of the PV panels during the outage of panel 2.

Case – 3: Operation of the system under sub-panel shading of one PV panel

Fig.6.21(a) shows the power, current, and voltage waveforms of the PV panels where the PV panel continues its operation at 250W at the insolation of 1000W/m^2 . Meanwhile, PV panel 2 experiences sub-panel shading with one-third section of the panel getting shaded, which observes a dip in the maximum power at $t=0.03\text{s}$ with the reduction in the steady state maximum evacuated power from 250W to 160W. The removal of shade at $t=0.05\text{s}$ experiences the transition of operating power of PV panel 2 back to 250W. The current waveforms of PV panels observe that panel 1 current remains constant while panel 2 undergoes dips and settles back at 8.39A when it is subjected to sub-panel shading and its subsequent removal. Moreover, the voltage of PV panels is also observed from the results where PV panel 1 maintains its operation at 29.8V whereas the voltage of PV panel 2 experiences variations from 29.8V to 19.86V during sub-panel shading and vice versa during the removal of shade. The profile of the output current and the terminal voltage of MMIC is shown in Fig.6.21(b) and highlights variation in the output current of MMIC from 1.264A to 1.04A during sub-panel shading and vice versa when the shade is removed. The results demonstrate the operational independence of each power module of MMIC with the optimal performance under sub-panel shading conditions while also highlighting the



(a)



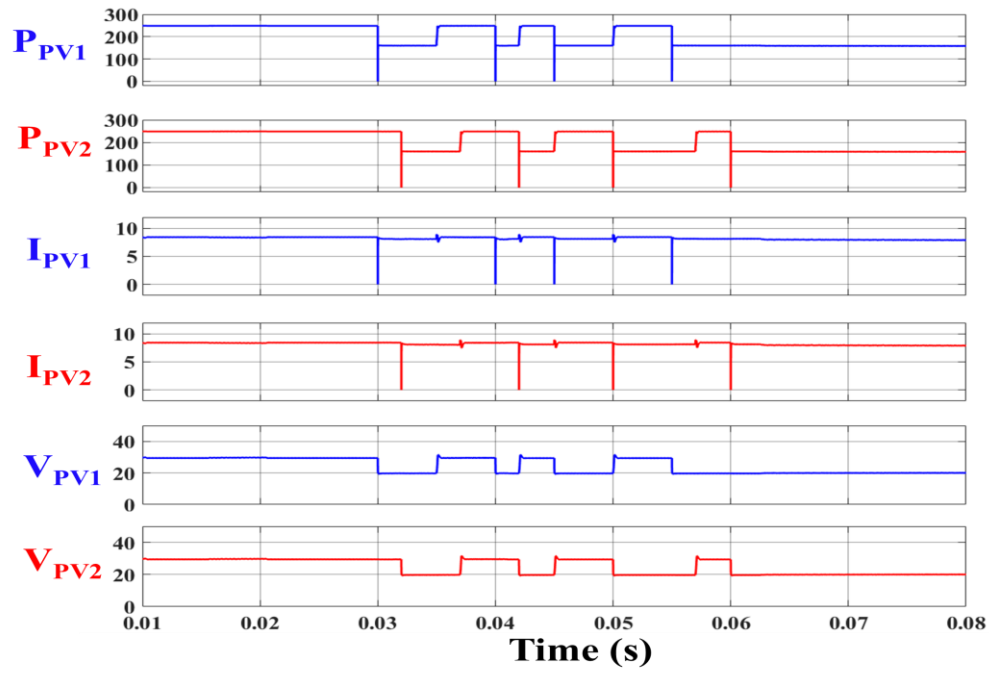
(b)

Fig.6.21. Case 3: Simulated operation of MMIC system with PV panel 1 operation at 1000W/m^2 while sub panel shading of PV panel 2 at $t=0.03$ and removal of shade at $t=0.05$ s (a) Profile of PV panels with their powers P_{PV1} and P_{PV2} (W), PV current I_{PV1} and I_{PV2} (A) and PV voltage V_{PV1} and V_{PV2} (V) (b) Output current I_O (A) and output voltage V_O (V) of MMIC

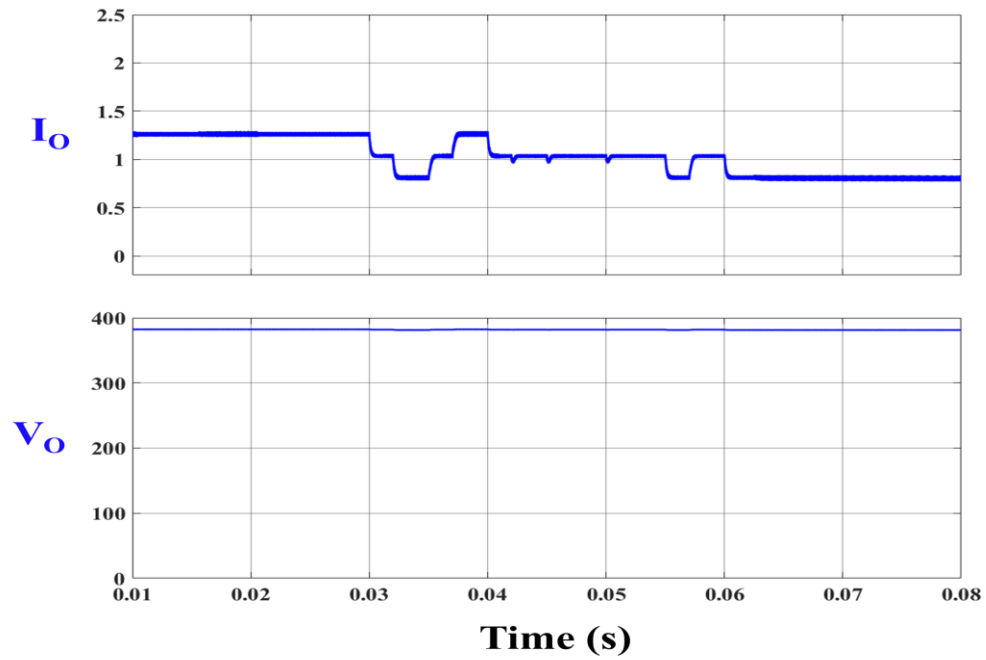
seamless operation of MMIC during voltage-based asymmetry where the power modules of MMIC have different operating duty cycles. Furthermore, it is observed from the results that MMIC achieves a substantially higher operating gain of nearly 20 during sub-panel shading.

Case – 4: Operation of the system under dynamic sub-panel shading with fast shading variations

In this case, the dynamic sub-panel shading with fast shading variations on the PV panels is observed. The PV panel 1 observes dynamic sub-panel shading at $t=0.03s$, $t=0.04s$, $t=0.045s$, and $t=0.055s$ with its corresponding removal of shade at $t=0.035s$, $t=0.042s$ and $t=0.05s$. Similarly, the dynamic sub-panel shading is observed for PV panel 2 at $t=0.032s$, $t=0.042s$, $t=0.05s$, and $t=0.06s$ while its corresponding removal of shade is observed at $t=0.037s$, $t=0.045s$, and $t=0.057s$. Fig.6.22(a) demonstrates the variations in the operating power, current, and voltage of both PV panels during these fast variations in shading and removal of shade and highlights the maximum power evacuation under these conditions. Furthermore, the results also display the fast convergence of the proposed Fast MPPT algorithm which quickly responds to the variation in shade and ensures seamless tracking of maximum power point. Additionally, the decoupled operation of each power module of MMIC is evident as the operation of one module under such fast-shading variations does not impact the performance of another module which remains consistent. Fig.6.22(b) shows the profile of the output current and the terminal voltage of MMIC where variations in the output current of MMIC are attributed to the dynamic sub-panel shading conditions. The results also validate the wide operating range and fast dynamics of the proposed converter and highlight its ability to furnish such a high voltage gain of nearly 20 during such fast-



(a)



(b)

Fig.6.22. Case 4: Simulated operation of MMIC system with dynamic sub panel shading in PV panel 1 and panel 2 (a) Profile of PV panels with their powers P_{PV1} and P_{PV2} (W), PV current I_{PV1} and I_{PV2} (A) and PV voltage V_{PV1} and V_{PV2} (V) (b) Output current I_O (A) and output voltage V_O (V) of MMIC

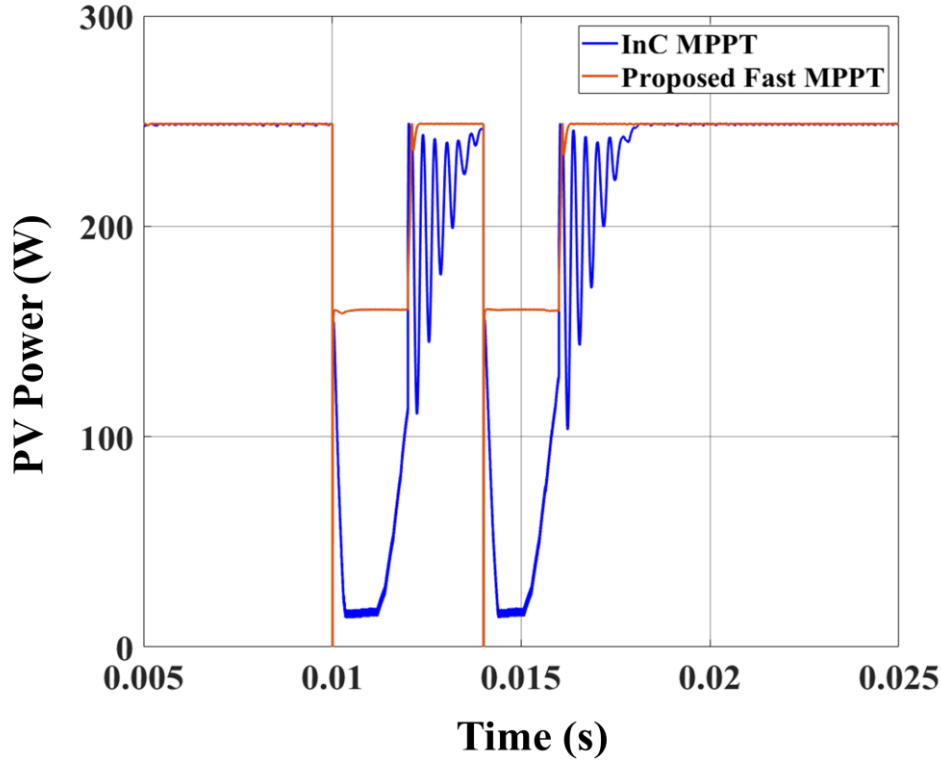


Fig.6.23. Comparative performance of conventional InC MPPT algorithm and fast MPPT algorithm under dynamic sub-panel shading

shading variations. Moreover, the seamless operation of MMIC under voltage-based asymmetry with each power module operation at different duty cycles is also highlighted in the results.

The comparative performance of InC and the proposed Fast MPPT algorithm under dynamic sub-panel shading conditions is shown in Fig.6.23. The results indicate that during sub-panel shading of the PV panel at $t=0.01s$, the Fast MPPT algorithm quickly converges to the MPP corresponding to the one-third shade on the panel and exhibits the maximum power evacuation of 160W. Meanwhile, the InC MPPT algorithm is unable to respond to such fast shading variation and dips to 15W for a considerable time and then starts converging toward the MPP @ one-third shade. However, before reaching the MPP, the shade is removed at $t=0.012s$ which induces significant power fluctuations. The proposed

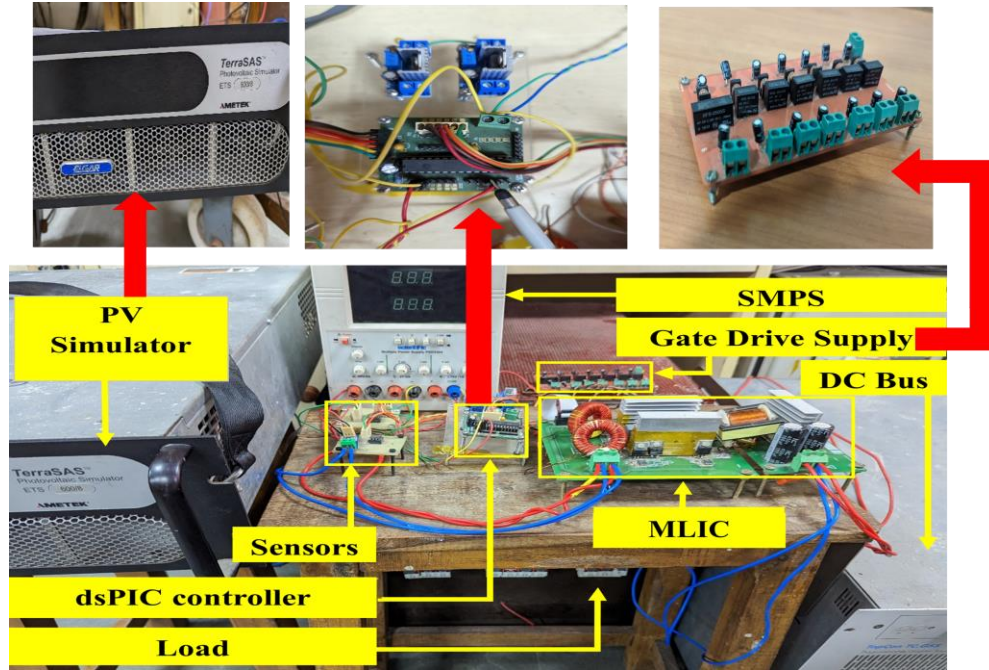


Fig.6.24. Experimental hardware setup of MLIC based MLPS system architecture interfacing the PV simulator with the section of DC microgrid

Fast MPPT algorithm quickly tracks the MPP @1000W/m² upon removal of shade at t=0.012s without any power oscillations. Both algorithms remain consistent in their respective responses during another cycle of shading variations. It is pertinent to observe that upon removal of shade at t=0.016s, the proposed Fast MPPT algorithm quickly evacuates maximum power of 250W corresponding to 1000W/m² and tracks the MPP in 330μs whereas the conventional InC MPPT algorithm exhibits severe power oscillations before settling at 250W @ 1000W/m² in 2.2ms, which is considerably slower than the Fast MPPT algorithm. The result highlights the superior performance of the Fast MPPT algorithm and validates its substantially faster convergence without any power oscillations during the fast-shading variations while also demonstrating the inability of the conventional MPPT algorithm to operate under dynamic sub-panel shading.

6.6.2. Experimental Results

The experimental steady-state and dynamic performance of the proposed MLPS system architecture under different operating conditions is extensively investigated in this subsection. The scaled-down experimental setup of the proposed system integrating a single PV panel with a section of DC microgrid is demonstrated in Fig.6.24. The algorithms are implemented on the low cost 16-bit dsPIC33FJ16GS502 controller. The experimental performance of the proposed system architecture has been tested using different topologies of MLIC which have been proposed in chapters 3 and 4.

A. CF-HGIIC based MLIC for MLPS system architecture

The hardware setup of the proposed system operating at 212W is developed in the laboratory based on the system parameters in Table 6.4. The proposed 130W CF-HGIIC is utilized as MLIC and interfaces the AMETEK TerraSaS 600/8 PV simulator with the section of the DC microgrid. The characteristics of Kyocera KC130GT have been emulated on the PV simulator with a maximum power of 130W at an insolation of 1000W/m².

TABLE 6.4: Experimental parameters of CF-HGIIC based MLIC for MLPS system architecture	
Parameter	Value
PV Panel Kyocera KC130GT	Rated Power (P_{MPP}) – 130W (1000W/m ²)
	Rated Voltage (V_{MPP}) – 17.6V (1000W/m ²)
	Rated Current (I_{MPP}) – 7.39A (1000W/m ²)
PV Simulator	AMETEK TerraSaS 600/8
Nominal Voltage of DC Bus	170V
Load	212W
Number of PV panel units	1
Sampling of MPPT	1kHz
CF-HGIIC	Refer to Table 3.7 for experimental parameters

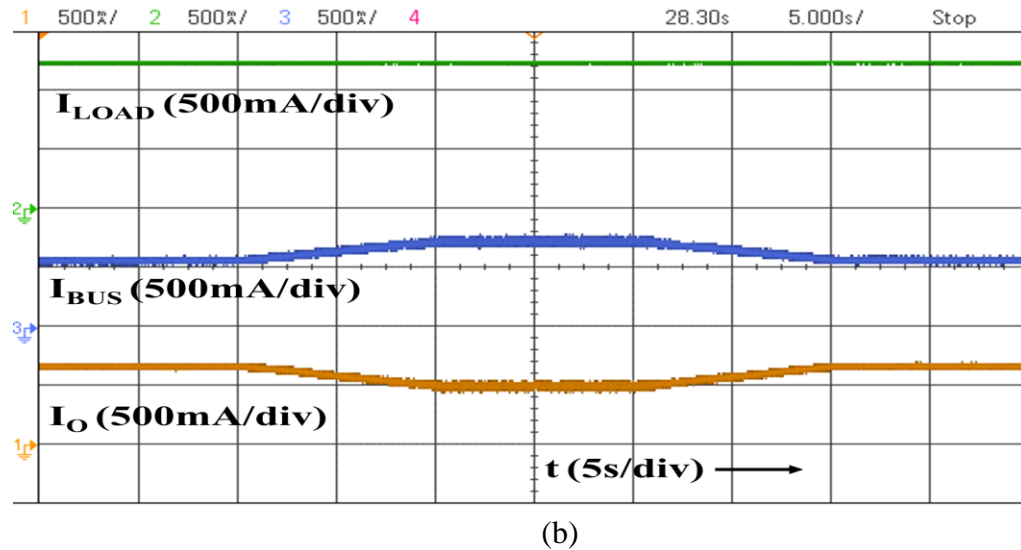
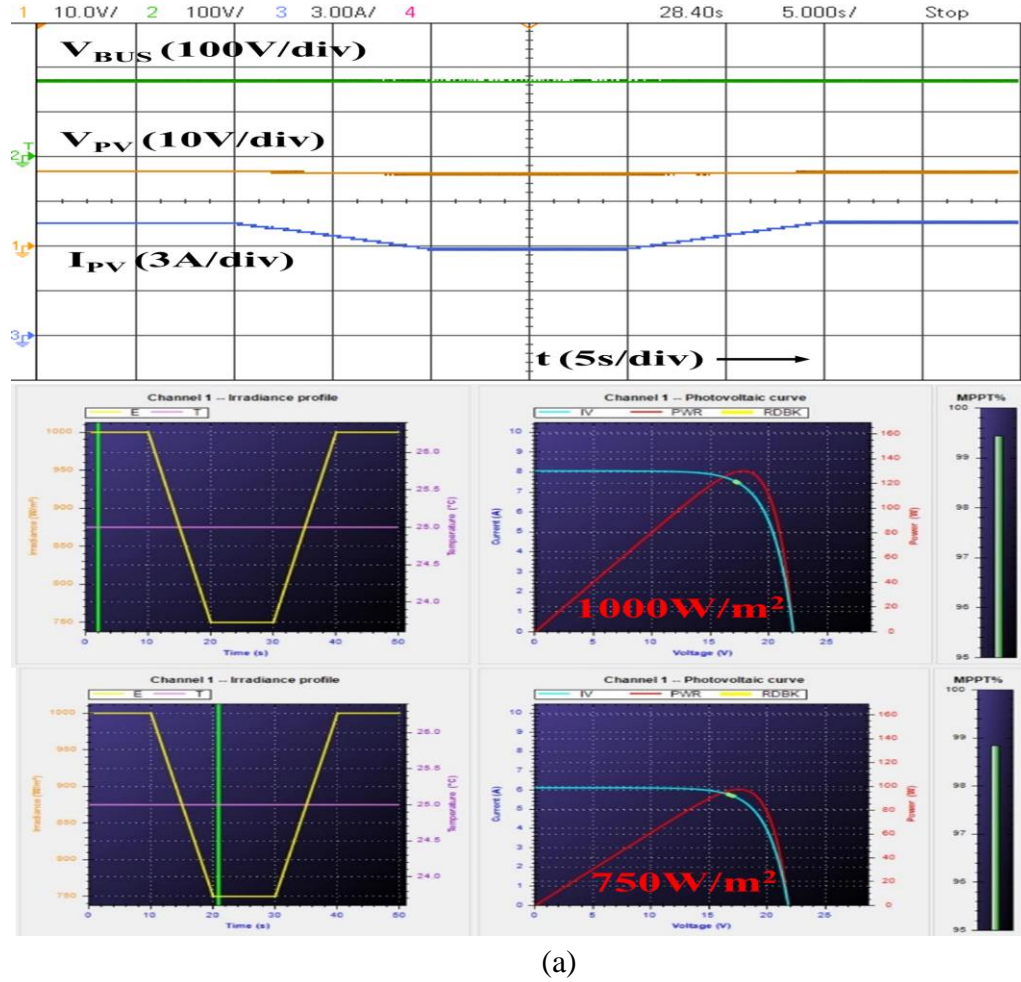


Fig.6.25. Experimental operation of CF-HGIIC based MLIC integrating PV simulator with section of 170V DC microgrid (a) DC bus voltage V_{BUS} (V), PV voltage V_{PV} (V) and PV current I_{PV} (A) (b) Load current I_{LOAD} (A), DC bus current I_{BUS} (A) and converter output current I_O (A)

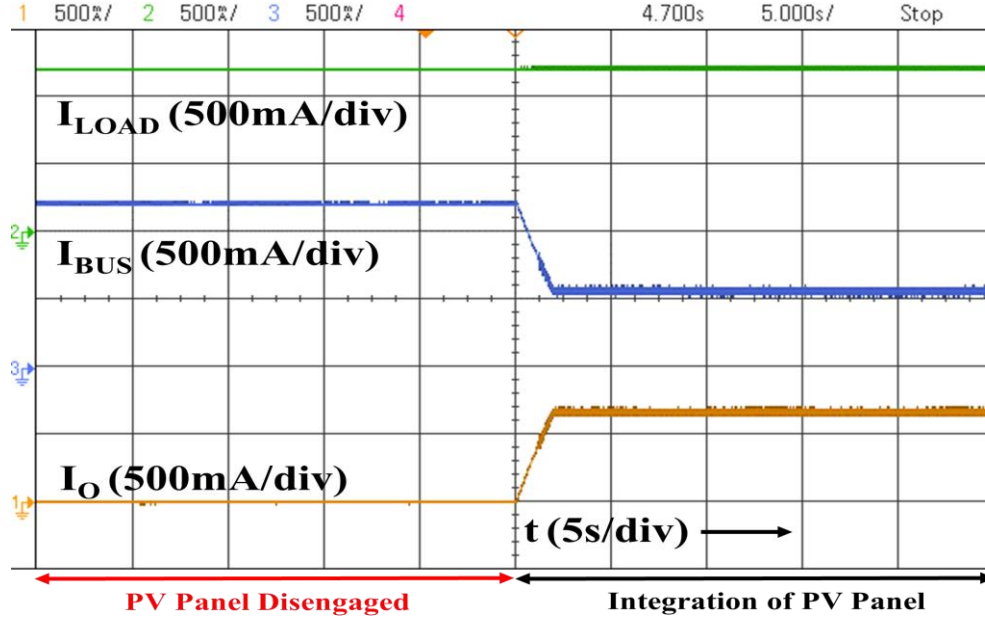
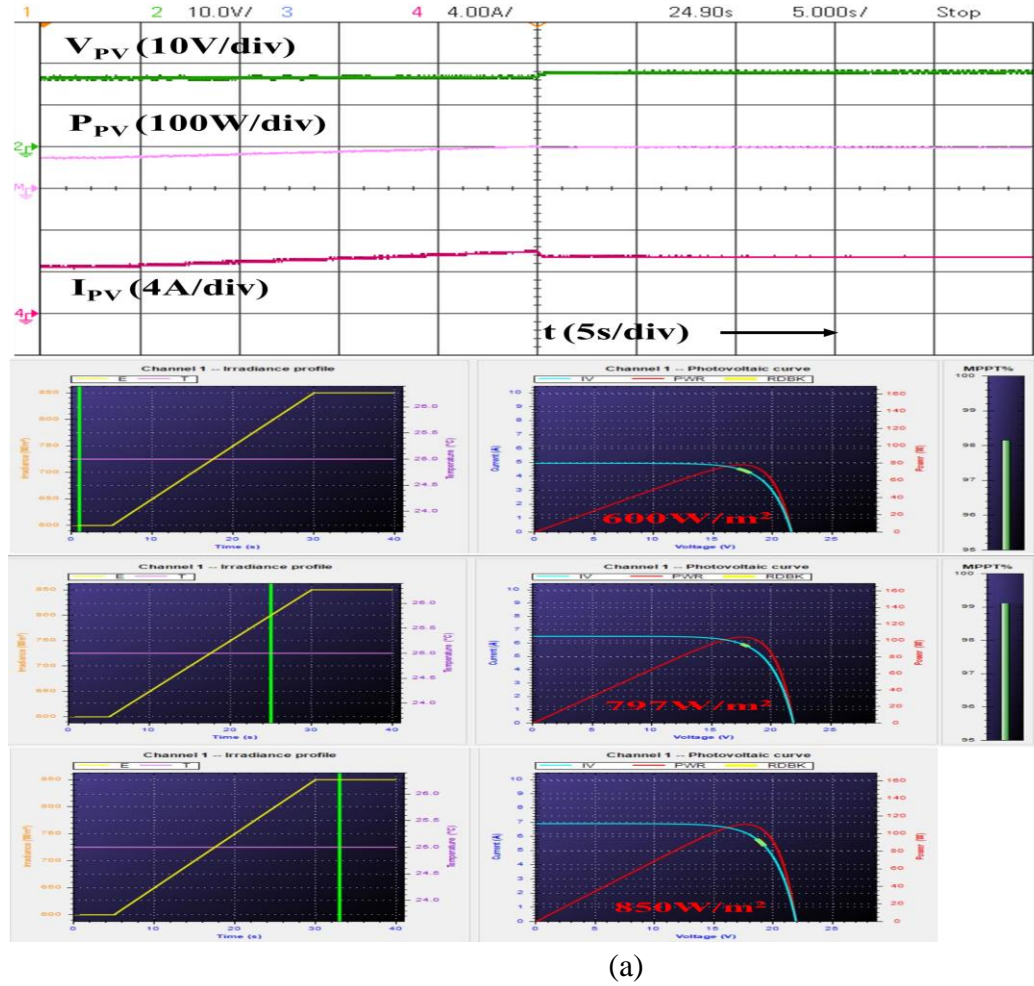


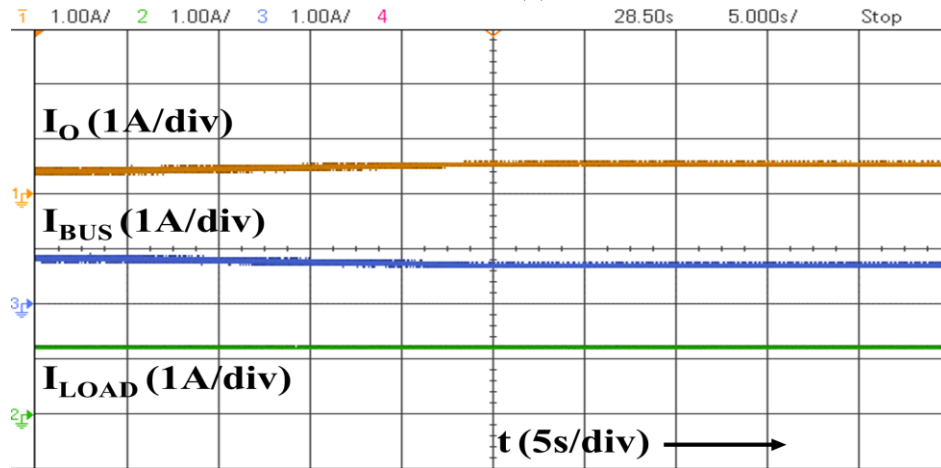
Fig.6.26. Experimental starting dynamics of system with integration of PV simulator with the section of 170V DC microgrid using CF-HGIIC at $t=25s$ having load current I_{LOAD} (A), DC bus current I_{BUS} (A) and converter output current I_O (A)

Moreover, the section of the DC microgrid comprises of 170V DC bus and 212W load such that both the PV simulator and DC bus cumulatively feed the load.

Fig.6.25 shows the experimental performance of the system utilizing the InC MPPT algorithm for insolation variations from $1000W/m^2$ to $750W/m^2$ and vice versa. Fig.6.25(a) shows the experimental PV side dynamics under insolation variations from $1000W/m^2$ to $750W/m^2$ from $t=10s$ to $t=20s$ and vice versa from $t=30s$ to $t=40s$. The results highlight the operating current of the PV simulator which experiences variation from 7.506A @ $1000W/m^2$ to 5.718A @ $750W/m^2$. Moreover, the maximum power is evacuated from the PV simulator with its value at $1000W/m^2$ of 129.32W which reduces to 97.2W at an insolation of $750W/m^2$. The PV simulator and DC bus voltages are also demonstrated from the results. Fig.6.25(b) shows experimental load side dynamics during the insolation variation where the output current (I_O) reduces from 0.714A @ $1000W/m^2$ to 0.625A



(a)



(b)

Fig.6.27. Experimental flexible power generation using CF-HGIIC based MLIC integrating PV simulator with section of 170V DC microgrid under insolation variation from 600W/m² to 850W/m² from $t = 5s$ till $t = 30s$ (a) PV voltage V_{PV} (V), PV power P_{PV} (W) and PV current I_{PV} (A) (b) Converter output current I_O (A), DC bus current I_{BUS} (A) and load current I_{LOAD} (A)

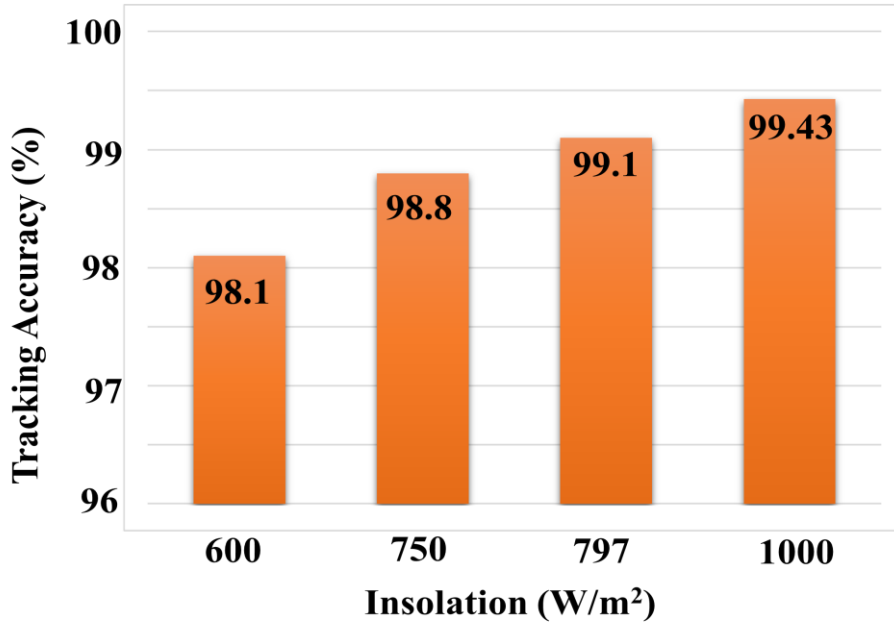


Fig.6.28. Tracking accuracy of InC MPPT and CPG-InC FPPT implemented on dsPIC33FJ16GS502 during different operating conditions.

@750W/m² while the DC bus current (I_{BUS}) simultaneously increases from 0.536A to 0.725A. Moreover, the converter and DC bus synchronously operate to regulate the load at 1.25A. The experimental starting dynamics of the system are shown in Fig.6.26 where the PV simulator is integrated into the system at $t=25s$. The result shows that when the PV panel is disengaged from the system, the DC bus is entirely feeding the load. Moreover, at $t=25s$, the PV panel is integrated into the system and starts feeding the load with its current increasing to 0.714A while the DC bus current falls to 0.536A. The InC algorithm implemented on the dsPIC controller observes significantly higher experimental tracking accuracy of 99.43% @1000W/m² and 98.8% @750W/m².

Fig.6.27 shows the experimental performance of the system exhibiting flexible power generation while utilizing the CPG-InC FPPT algorithm under insolation change from 600W/m² at $t=5s$ to 850W/m² at $t=30s$. Fig.6.27(a) shows the experimental PV side dynamics where the PV current operates at 4.59A @600W/m² and starts increasing from

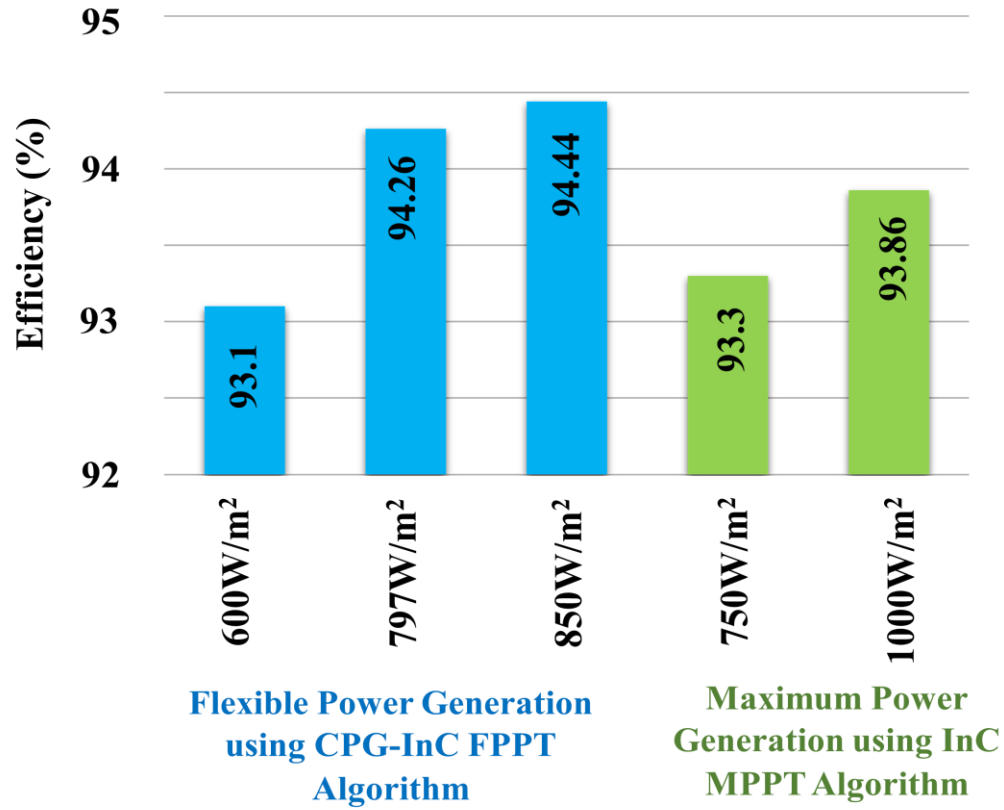


Fig.6.29. Efficiency of CF-HGIIC based MLIC under different operating conditions

t=5s as the insolation increases, demonstrating operation in MPPT mode. At t=25s, the operating PV current reaches 5.765A and subsequently transits from MPPT mode to CPG mode such that the PV current starts tracking the reference current and observing regulated current of 5.396A. Similarly, the PV power operating at 77.5W @ 600W/m^2 starts increasing at t=5s as the insolation starts rising and reaches the peak value of 104.06W at t=25s. The seamless transition in operating mode from MPPT to CPG mode is observed from the result at t=25s and further demonstrates the regulation of PV power at 102.63W while operating in CPG mode. The operating PV voltage also observes an increase from 16.88V at t=5s @ 600W/m^2 during MPPT mode to 19.02V at t=30s during CPG mode. Fig.6.27(b) shows the experimental load side dynamics during operation under flexible

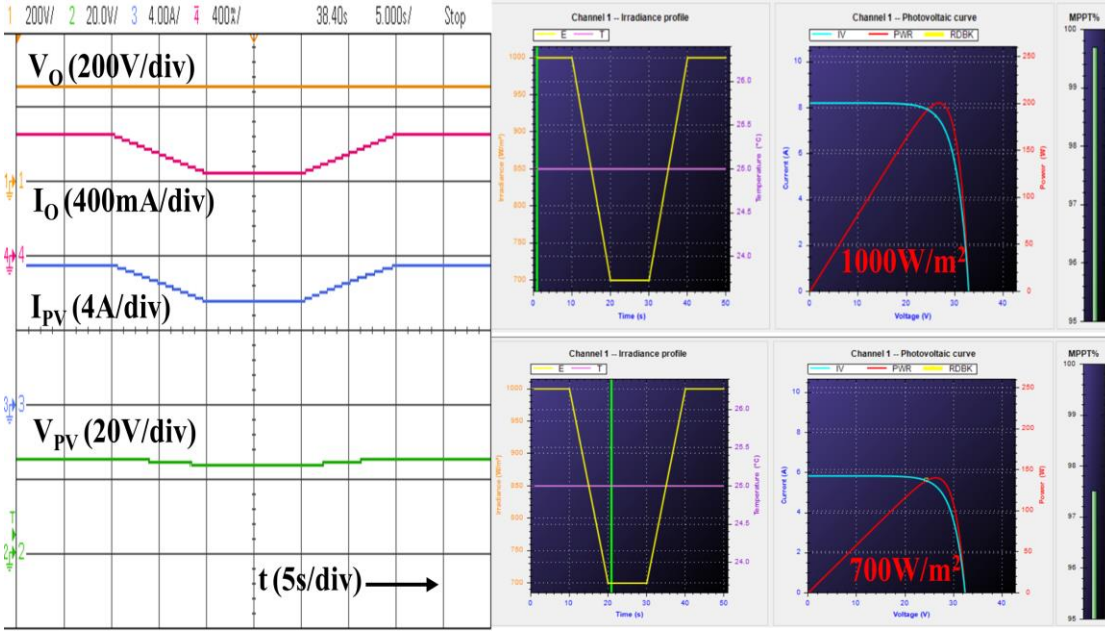


Fig.6.30. Experimental operation of MCF-HGIIC based MLIC integrating PV simulator with section of 270V DC microgrid under insolation variation from 1000W/m² to 700W/m² from t=10s till t=20s and vice versa from t=30s till t=40s with waveforms of output voltage V_O (V) and current I_O (A) of converter and PV current I_{PV} (V) and voltage V_{PV} (V)

TABLE 6.5: Experimental parameters of MCF-HGIIC based MLIC for MLPS system architecture	
Parameter	Value
PV Panel Kyocera KC200GT	Rated Power (P _{MPP}) – 200W (1000W/m ²)
	Rated Voltage (V _{MPP}) – 26.3V (1000W/m ²)
	Rated Current (I _{MPP}) – 7.61A (1000W/m ²)
PV Simulator	AMETEK TerraSaS 600/8
Nominal Voltage of DC Microgrid	270V
Number of PV panel units	1
Sampling of MPPT	1kHz
MCF-HGIIC	Refer to Table 4.5 for experimental parameters

power operation with mode transition from MPPT to CPG. The output and DC bus current initially operating at 0.429A and 0.821A respectively @600W/m² experiences insolation variation and reach the values of 0.577A and 0.673A respectively at t=25s. Subsequently,

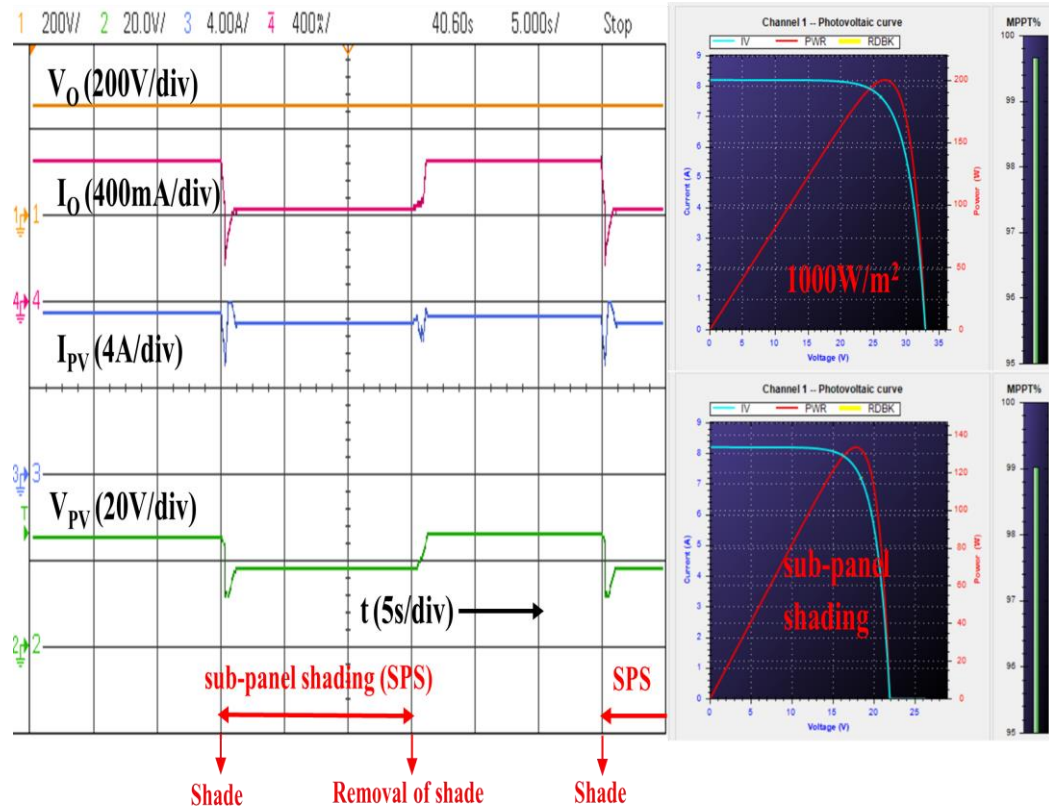


Fig.6.31. Experimental operation of MCF-HGIIC based MLIC integrating PV simulator with section of 270V DC microgrid under sub-panel shading at $t=15s$ and $t=45s$ and removal of shade at $t=30s$ with waveforms of output voltage V_O (V) and current I_O (A) of converter and PV current I_{PV} (V) and voltage V_{PV} (V)

the

mode transition from MPPT to CPG at $t=25s$ observes regulation of their currents at 0.57A and 0.68A respectively. Moreover, the converter and load currents operate synchronously to maintain the load current at 1.25A. The experimental tracking accuracy of the FPPT algorithm while operating in MPPT mode is 98.1% @600W/m² and 99.1% @797W/m². Fig. 6.28 shows the tracking accuracy of the InC MPPT and CPG-InC FPPT algorithm implemented on the dsPIC controller under different operating conditions and highlights their superior performance. The efficiency of CF-HGIIC based MLIC under different operating conditions is demonstrated in Fig.6.29.

B. MCF-HGIIC based MLIC for MLPS system architecture

The hardware setup of the 200W proposed system is developed in the laboratory based on the system parameters in Table 6.5. The proposed 200W MCF-HGIIC is utilized as MLIC and interfaces the AMETEK TerraSaS 600/8 PV simulator with the 270V DC microgrid. The characteristics of Kyocera KC200GT have been emulated on the PV simulator with a maximum power of 200W at an insolation of 1000W/m^2 .

Fig.6.30 demonstrates the experimental system dynamics under insolation change from 1000W/m^2 to 700W/m^2 from $t=10\text{s}$ to 20s and vice versa from $t=30\text{s}$ to $t=40\text{s}$. The dynamic transition in PV current and converter output current is observed during the insolation changes with their value reducing as insolation decreases from 1000W/m^2 to 700W/m^2 .

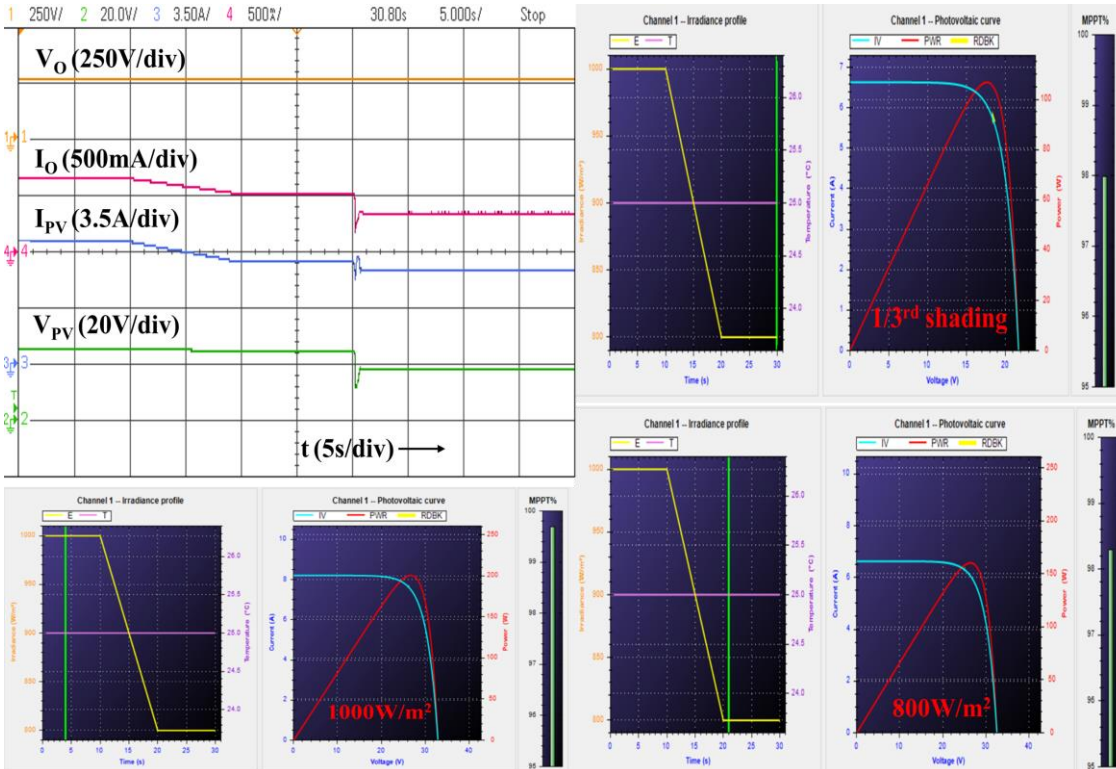


Fig.6.32. Experimental operation of MCF-HGIIC under insolation variation from 1000W/m^2 to 800W/m^2 from $t=10\text{s}$ till $t=20\text{s}$ and subsequent sub panel shading at $t=30\text{s}$ with waveforms of output voltage V_O (V) and current I_O (A) of converter and PV current I_{PV} (V) and voltage V_{PV} (V)

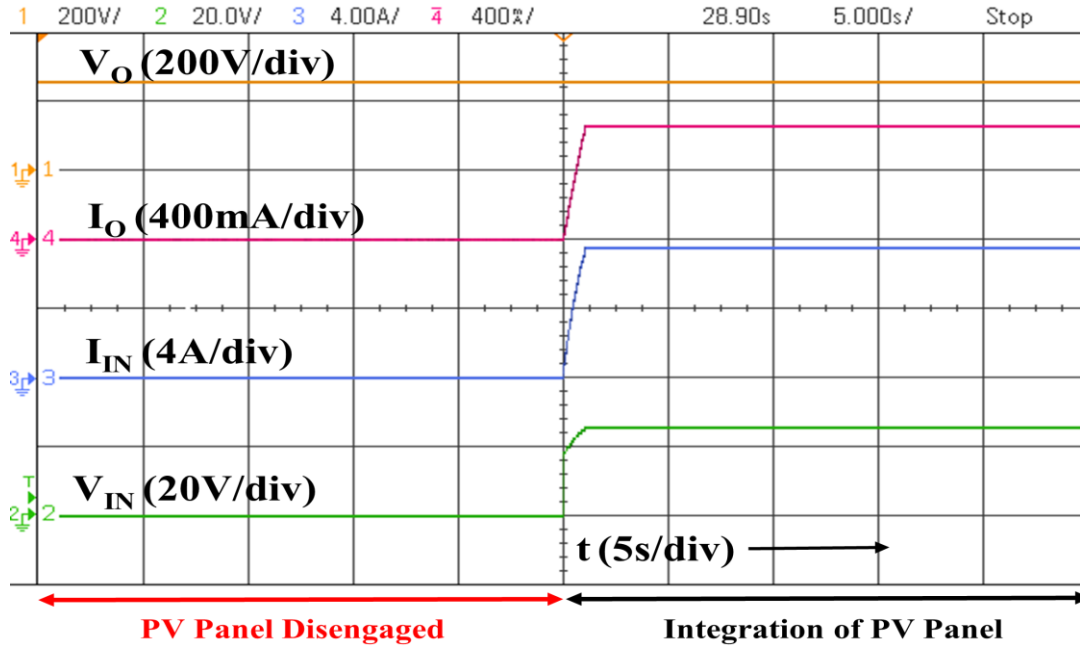


Fig.6.33. Experimental starting dynamics of system with integration of PV simulator with the section of 270V DC microgrid using MCF-HGIIC at $t=25s$ with waveforms of output voltage V_O (V), output current I_O (A), input current I_{IN} (A) and input voltage V_{IN} (V) of converter

Moreover, the PV voltage and output voltage of the converter are also shown in the result. The experimental dynamic response of the system during sub-panel shading and its subsequent removal is demonstrated in Fig.6.31. The PV panel voltage and output current of the converter observe reduction during sub-panel shading and subsequently return to their original value upon removal of the shade. Furthermore, a small dip in PV current is observed from the result because of the displacement from the maximum power point (MPP) and it ultimately settles back in the vicinity of I_{MPP} . The result demonstrates the high voltage gain capability of MCF-HGIIC with its experimental voltage gain of nearly 16 and also seamlessly meets the 53% increase in the gain demand, thus allowing fast response to wide variations in the voltage gain as necessitated during sub-panel shading conditions. The performance of the system is further tested under more stringent operating conditions where

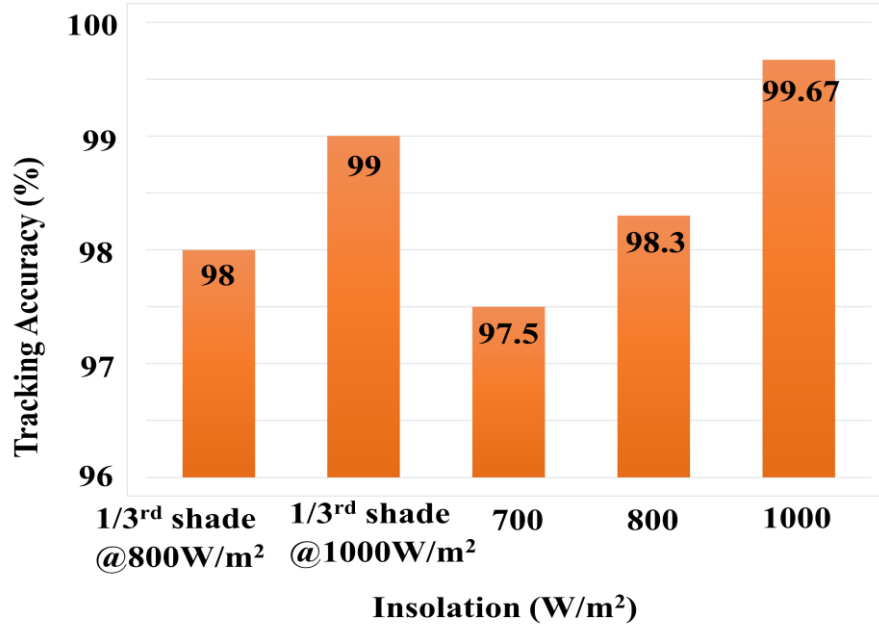


Fig.6.34. Tracking accuracy of InC MPPT implemented on dsPIC33FJ16GS502 during different operating conditions

both insolation variation and subsequent sub-panel shading are observed. Fig.6.32 observes a reduction in the insolation from 1000W/m^2 to 800W/m^2 from $t=10\text{s}$ till $t=20\text{s}$ and further observes sub-panel shading @ 800W/m^2 at $t=30\text{s}$. The PV current and output converter current observe a reduction from $t=10\text{s}$ to $t=20\text{s}$ as the insolation decreases from 1000W/m^2 to 800W/m^2 . Furthermore, during sub-panel shading at $t=30\text{s}$ @ 800W/m^2 observes a reduction in the output converter current and PV voltage whereas the PV current observes slight fluctuation and subsequently settles in the vicinity of I_{MPP} corresponding to the insolation of 800W/m^2 . The result also highlights the wide operating range of the converter. Fig.6.33 shows the starting experimental dynamics of the system with the insertion of a PV panel in the system. The result shows that the output converter current, input converter voltage, and input converter current are zero till $t=25\text{s}$ as the PV simulator is disengaged from the system. As the PV simulator is inserted into the system at $t=25\text{s}$, the converter input voltage and current increase to their corresponding V_{MPP} and I_{MPP} @ 1000W/m^2 .

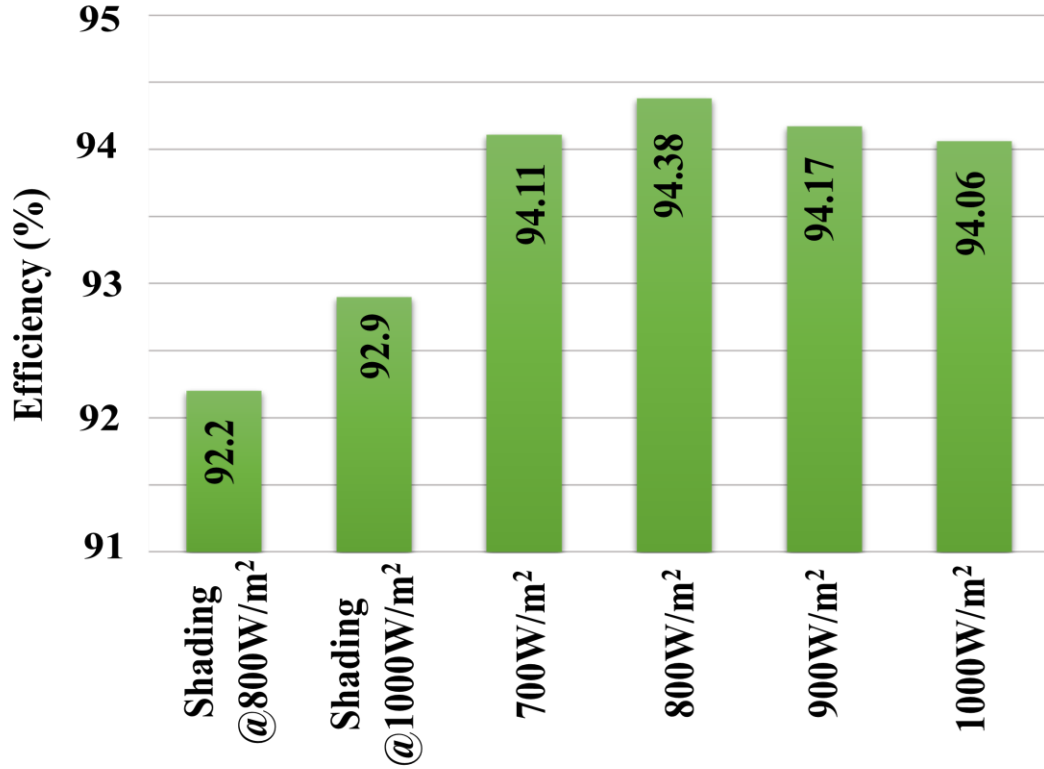


Fig.6.35. Efficiency of MCF-HGIIC based MLIC under different operating conditions

Moreover, the integration of the PV panel in the system also observes the increase in the output current of the converter. The tracking performance of InC MPPT implemented on the dsPIC controller for different operating conditions is shown in Fig.6.34. The overall high tracking accuracy of InC MPPT with 99.67% observed for the insolation of 1000W/m² and 99% during sub-panel shading highlights the superior performance of the InC MPPT. The efficiency of MCF-HGIIC based MLIC under different operating conditions is demonstrated in Fig.6.35.

6.7. Integration of Proposed Converters with DC Microgrid

The typical configurations of DC microgrid are grid connected and off-grid DC microgrids. In grid connected DC microgrid, AC grid acts as a master while providing

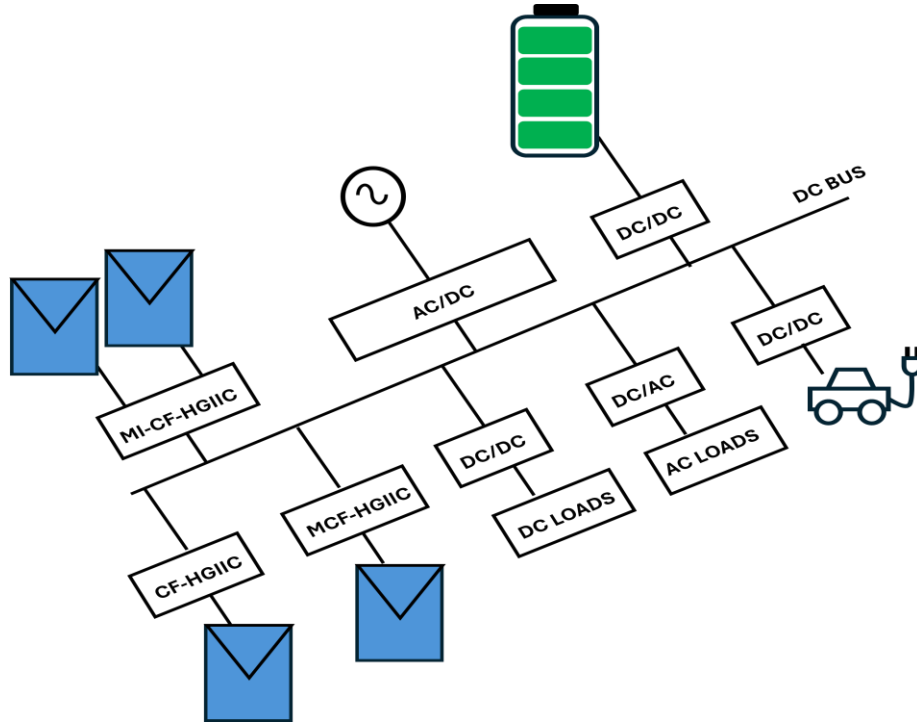


Fig.6.36. DC microgrid architecture with integration of proposed converters

voltage regulation via AC/DC converters. The renewable energy sources are integrated in slave mode while operating as a current source and feed the connected loads. Similarly, for off-grid DC microgrid, the energy storage system with voltage fed converter operates as a master and facilitates the voltage regulation, while the renewable energy sources operates in slave mode as a current source and feed connected loads. Fig.6.36 shows the DC microgrid architecture where MLPS incorporating PV fed proposed converters operates in slave mode as a current source and feed the connected loads.

6.8. Conclusion

This chapter presented different configurations of MLPS-based system architecture utilizing different interfacing converters and further discussed the merits and various applications of MLPS. The concept of dynamic sub-panel shading has been introduced in the chapter and delineated its challenges and performance limitations. The power

generation control algorithms viz, flexible power point tracking (FPPT) algorithm and fast MPPT algorithm have been proposed in this chapter to facilitate flexible power generation of the system and operation under fast shading variation during dynamic sub-panel shading conditions.

The simulated system has been further classified based on their interfacing converter and their performance has been evaluated under different operating conditions. The performance of MLIC-based MLPS system architecture demonstrated the seamless operation of each unit of PV-fed MLIC without impacting the performance of other units and observed no inter-converter circulating currents between the units. The results also highlighted the efficacy of the system operation under insolation variations, partial shading conditions, and sub-panel shading conditions with maximum power evacuation and superior power utilization of each PV panel. Furthermore, the high voltage gain capability of MLIC with its ability to meet wide gain variations during fast shading conditions has been demonstrated from the results. The plug-and-play operation of the system has been observed from the result and established its ability to dynamically increase the power capacity without interrupting the services. Moreover, the effectiveness of the system in achieving flexible power generation under different operating conditions has been evaluated from the results and emphasizes the high performance of the CPG-InC FPPT algorithm in realizing seamless transition between operating modes and preserving constant power generation of the panels. The flexible power operation of the system also mitigated the effects of partial shading conditions to a certain extent and supported the alleviation of the intermittency of PV. The performance of MMIC-based MLPS system architecture observed seamless operation under different operating conditions viz, partial shading, sub-

panel shading, and dynamic sub-panel shading. The system demonstrated the independent operation of the power modules of MMIC without any intermodular circulating currents. Furthermore, the high voltage gain capability of MMIC with a wide operating range and seamless operation under asymmetric operation where both modules have different operating duty cycles has been highlighted from the results. The outage of a power module of MMIC displayed the sustained operation of the system at reduced capacity and further prevented the interruption of the system. The results demonstrated the seamless operation of the system during dynamic sub-panel shading conditions and exhibited effective tracking of fast shading transitions with superior performance. Furthermore, the efficacy of the Fast-MPPT algorithm has been displayed with quick convergence and minimal power oscillations during fast shading variations.

The experimental performance of the system incorporating CF-HGIIC based MLIC has been comprehensively investigated and demonstrated seamless operation under insolation variations and further highlighted the effectiveness in facilitating flexible power generation. The seamless experimental performance of the system utilizing MCF-HGIIC based MLIC has been observed from the results and presented high voltage gain capability with a wide operating range and also the ability to meet the large voltage gain demand. The experimental results showed high tracking accuracy of algorithms under different operating conditions and highlighted the superior performance of conventional InC MPPT algorithm and CPG-InC FPPT algorithm which have been implemented on the dsPIC controller.

Consequently, the simulated and experimental performance of the system validated the salient features of MLPS and effectively emphasized its operational superiority under different operating conditions.

CHAPTER 7

CONCLUSION AND FUTURE SCOPE

7.1. Main Conclusion

The prime objective of the thesis is to focus on the study of DC/DC topologies for module-level interfacing converter (MLIC) and multi-input module interfacing converter (MMIC) to interface module-level PV systems (MLPS) and further investigate their performance under different operating conditions. The topologies of module-level interfacing converter and multi-input module interfacing converter have been conceptualized, mathematically analyzed, and designed with their performance comprehensively analyzed. The results presented unique findings and validated the superior performance of the topologies. The main conclusion of the thesis is presented below:

- The isolated current-fed high gain topology (CF-HGIIC) for module-level interfacing converter has been conceptualized and theoretically analyzed extensively with the mathematical study of its voltage gain characteristics, input current ripple, and component stress. The proposed converter has exhaustively been designed with a proper selection of its components based on their ratings. The proposed topology is comparatively studied with different state-of-the-art topologies and highlighted its salient features and merits which indicated its suitability for MLIC. The simulated results demonstrated the superior performance of the proposed converter with the high gain capability of the converter while utilizing the low turns ratio of the HF transformer. The results also highlighted the low input current ripple in the converter with mitigation of

leakage current at the output. Moreover, the natural voltage clamping in switches S_1 and S_2 of the converter has been affirmed by the results. The hardware prototype of the proposed converter has been developed and experimentally tested, with its performance corroborating with the theoretical analysis and design of the converter as well as simulated results. Moreover, the experimental results also demonstrated the operation of the converter at a gain of 10 with high efficiency during experimental study. The results further validated the merits of the converter and further highlighted its viability for MLIC.

- The topological structure of CF-HGIIC has been modified for enhanced and improved performance. The proposed MCF-HGIIC offered notable improvements over conventional CF-HGIIC viz, utilization of all low side switches and simplified gate drive with the elimination of additional isolated power supplies and lower EMI issues and mitigation of switching loss in S_3 and S_4 due to quasi-ZCS operation. A detailed theoretical analysis of the proposed converter has also been presented. The simulated results of the converter highlighted salient features and superior performance of the converter. Moreover, the experimental performance of the converter has been tested by developing the hardware prototype of the converter. The improvements in the performance and merits of MCF-HGIIC with inherited features of conventional CF-HGIIC have been affirmed by the results. Additionally, the wide operating range of the converter with its ability to seamlessly furnish high gain is established from the results. The experimental results demonstrated an experimental voltage gain of nearly 16 in MCF-HGIIC while operating at high efficiency. Furthermore, the

results validated the theoretical analysis and design of the converter and further established the suitability of the improved topology for MLIC.

- The multi-input approach of conventional CF-HGIIC has been studied and theoretically analyzed. The proposed MI-CF-HGIIC retained the salient features of conventional CF-HGIIC while achieving modular operational independence with low intermodular circulating currents and further facilitated the simultaneous integration and operation of dual sources. This has been validated through the simulated results and further highlighted the decoupled operation of the converter. The results also demonstrated the seamless converter operation under symmetric and asymmetric conditions without impacting the performance of the power modules of the converter. Moreover, the operational flexibility and wide operating range of the converter have been established from the results while also indicating the plug-and-play operational capability of the converter. The simulated results also encouraged the utilization of the proposed MI-CF-HGIIC topology for MMIC.
- The system integration of MLPS with the DC microgrid while utilizing the proposed converter topologies as interfacing converter has been comprehensively investigated. The applications of MLPS are extensively studied and the merits and viability of MLPS pertaining to the applications are delineated in detail. The dynamic sub-panel shading has been conceptually introduced and its challenges are discussed. Different power generation control algorithms are proposed with a detailed analysis of their operation. The simulated performance of the proposed system where the MLPS is integrated with a DC microgrid using MLIC and MMIC under different operating conditions has been extensively investigated.

The results demonstrated the superior performance of the system under insolation variations and shading conditions with no inter-converter circulating currents. Moreover, the high gain capability of MLIC and MMIC has been highlighted from the results while also demonstrating their wide operating range. Additionally, the plug-and-play operational capability of the MLPS-based system architecture has been highlighted from the results and allowed a dynamic increase in the power capacity of the system without interrupting the power generation, thereby conforming to the merit of the MLPS. The simulated results also showcased the efficacy of flexible power operation of the system under different operating conditions with the superior performance of the proposed CPG-InC FPPT algorithm. The results also supported the effective performance of MMIC under asymmetric operation with no intermodular circulating currents and independent operation of each power module. The robust, resilient, and reliable operation of the system is established from the simulated performance under the PV panel outage. Furthermore, the seamless operation of the system during dynamic shading conditions under fast shading variations validated the superior performance of the Fast-MPPT algorithm with fast convergence and minimal power oscillations. The experimental setup of the system is developed to test the performance experimentally and affirm the salient features of the MLPS. Moreover, the experimental results further highlighted the merits of the proposed converters CF-HGIIC and MCF-HGIIC and demonstrated superior performance during flexible power operation and under insolation variations and sub-panel shading conditions. Moreover, the experimental high gain capability of both converters has been displayed by the results. Additionally, the high tracking

accuracy of the InC MPPT and CPG-InC FPPT algorithm implemented on the dsPIC33FJ16GS502 controller is exhibited, highlighting high-performance operation. The salient features of MLPS discussed in the thesis have been effectively validated by the simulated and experimental performance of the system during different operating conditions.

7.2. Future Scope of Work

The study of interfacing DC/DC converter topologies and their capability in integrating MLPS with the DC microgrid conducted in the thesis is highly relevant in the present scenario where the major thrust of research is on photovoltaic systems. Based on the research conducted in the thesis, there is a potential for a wider scope of research to further enhance the performance.

The future scope of work is detailed below:

- The resonant tank can be introduced in the proposed converter topologies to provide complete soft-switching implementation. This will alleviate the switching losses in the converter topologies while allowing a power-dense solution with operation at significantly higher switching frequencies. Furthermore, for wider adoption of such converters in MLPS, the implementation of soft switching control on low-cost controllers is imperative.
- The present study has been focused on the unidirectional capability of the proposed converter topologies. Considering the salient features of the proposed

topologies, future research can focus on their bidirectional capabilities, allowing seamless integration of the battery storage system with the DC microgrid.

- Future research can be conducted on the hybrid current-fed and voltage-fed multi-port topologies utilizing the structure of the proposed converter. This will allow integration of both PV panel and battery storage system and present a power-dense and highly efficient solution.
- The implementation of FPPT and Fast MPPT algorithms utilizing machine learning and artificial intelligence algorithms will enable more robust and adaptive performance under diverse operating conditions and allow high-performance operation.

REFERENCES

- [1] <https://www.un.org/en/climatechange/>
- [2] <https://www.iea.org/reports/india-energy-outlook-2021/energy-in-india-today>
- [3] P. A. Owusu and S. A. Sarkodie, "A review of renewable energy sources, sustainability issues and climate change mitigation," *Cogent Engineering*, vol. 3, no. 1, p. 1167990, Apr. 2016
- [4] E. Erdiwansyah, M. Mahidin, H. Husin, N. Nasaruddin, M. Zaki, and Muhibbuddin, "A critical review of the integration of renewable energy sources with various technologies," *Protection and Control of Modern Power Systems*, vol. 6, no. 1, Feb. 2021.
- [5] A. Qazi *et al.*, "Towards Sustainable Energy: A Systematic review of renewable energy sources, technologies, and public opinions," *IEEE Access*, vol. 7, pp. 63837–63851, Jan. 2019.
- [6] W. Strielkowski, L. Civiń, E. Tarkhanova, M. Tvaronavičienė, and Y. Petrenko, "Renewable Energy in the Sustainable Development of Electrical Power Sector: A review," *Energies*, vol. 14, no. 24, p. 8240, Dec. 2021.
- [7] A. Azarpour, S. Suhaimi, G. Zahedi, and A. Bahadori, "A review on the drawbacks of renewable energy as a promising energy source of the future," *Arabian Journal for Science and Engineering*, vol. 38, no. 2, pp. 317–328, Dec. 2012.
- [8] <https://mnre.gov.in/en/>
- [9] <https://cea.nic.in/>
- [10] https://cag.gov.in/uploads/download_audit_report/2015/Union_Civil_Performance_Renewable_Energy_Report_34_2015_chap_3.pdf
- [11] <https://sungzu.com/advantages-disadvantages-photovoltaic-systems/>
- [12] <https://sites.lafayette.edu/egrs352-sp14-pv/technology/advantages-and-challenges-with-solar-pv/>
- [13] A. M. Soomar, A. Hakeem, M. Messaoudi, P. Musznicki, A. Iqbal, and S. Czapp, "Solar photovoltaic energy optimization and challenges," *Frontiers in Energy Research*, vol. 10, May 2022.
- [14] O. A. Al-Shahri *et al.*, "Solar photovoltaic energy optimization methods, challenges and issues: A comprehensive review," *Journal of Cleaner Production*, vol. 284, p. 125465, Feb. 2021.
- [15] <https://www.waaree.com/blog/solar-energy-in-india>
- [16] M. Hosenuzzaman, N. A. Rahim, J. Selvaraj and M. Hasanuzzaman, "Factors affecting the PV based power generation," *3rd IET International Conference on Clean Energy and Technology (CEAT) 2014*, Kuching, 2014, pp. 1-6.
- [17] A. Singla, K. Singh and V. K. Yadav, "Environmental effects on performance of solar photovoltaic module," *2016 Biennial International Conference on Power and*

- Energy Systems: Towards Sustainable Energy (PESTSE)*, Bengaluru, India, 2016, pp. 1-6.
- [18] K. B. Samal and A. Bisoyi, "Investigation of Environmental Effects on the Performance of Solar PV Modules," *2020 International Conference on Emerging Frontiers in Electrical and Electronic Technologies (ICEFEET)*, Patna, India, 2020, pp. 1-5.
 - [19] Y. A. Jieb and E. Hossain, "Photovoltaic systems: Fundamentals and Applications", Springer Nature, 2021.
 - [20] J. Imhoff, G. F. Rodrigues, J. R. Pinheiro and H. L. Hey, "A stand-alone photovoltaic system based on Dc-Dc converters in a multi string configuration," *2007 European Conference on Power Electronics and Applications*, Aalborg, Denmark, 2007, pp. 1-10.
 - [21] D. Riley, J. Stein and C. Carmignani, "Performance of Bifacial PV Modules with MLPE vs. String Inverters," *2018 IEEE 7th World Conference on Photovoltaic Energy Conversion (WCPEC) (A Joint Conference of 45th IEEE PVSC, 28th PVSEC & 34th EU PVSEC)*, Waikoloa, HI, USA, 2018, pp. 1745-1748.
 - [22] Y. Alharbi, A. Darwish, and X. Ma, "A Comprehensive Review of Distributed MPPT for Grid-Tied PV Systems at the Sub-Module Level," *Energies*, vol. 16, no. 14, p. 5468, Jul. 2023.
 - [23] U. Kunwar, A. Shupao, A. Tamrakar and A. Shrivastava, "Advantages And Challenges Of DC Standalone Decentralized Microgrid For Institutional Buildings: A Case Study Of The Installed Microgrid In Rewa Engineering College," *2023 3rd International Conference on Intelligent Technologies (CONIT)*, Hubli, India, 2023, pp. 1-5.
 - [24] S. Backhaus and G. W. Swift, "DOE DC microgrid scoping study - opportunities and challenges," *2015 IEEE First International Conference on DC Microgrids (ICDCM)*, Atlanta, GA, USA, 2015, pp. 43-44.
 - [25] G. S. Rawat and Sathans, "Survey on DC microgrid architecture, power quality issues and control strategies," *2018 2nd International Conference on Inventive Systems and Control (ICISC)*, Coimbatore, India, 2018, pp. 500-505.
 - [26] V. Chapparya, A. Dey and S. P. Singh, "A Novel Non-Isolated Boost-Zeta Interleaved DC-DC Converter for Low Voltage Bipolar DC Micro-Grid Application," *IEEE Transactions on Industry Applications*, vol. 59, no. 5, pp. 6182-6192, Sept. 2023.
 - [27] Z. Wang, Z. Chen and X. Wang, "Research of the DC microgrid topology," *2016 Chinese Control and Decision Conference (CCDC)*, Yinchuan, China, 2016, pp. 2855-2859.
 - [28] D. J. Becker and B. J. Sonnenberg, "DC microgrids in buildings and data centers," *2011 IEEE 33rd International Telecommunications Energy Conference (INTELEC)*, Amsterdam, Netherlands, 2011, pp. 1-7.

- [29] A. Kumar and N. A. Prabha, "A comprehensive review of DC microgrid in market segments and control technique," *Heliyon*, vol. 8, no. 11, p. e11694, Nov. 2022.
- [30] <https://new.abb.com/low-voltage/direct-current-systems/dc-summit/dc-microgrid-for-commercial-and-industrial-applications>
- [31] E. Marafante, L. Mackay, T. G. Hailu, G. R. C. Mouli, L. Ramirez-Elizondo and P. Bauer, "PV architectures for DC microgrids using buck or boost exclusive microconverters," *2015 IEEE Eindhoven PowerTech*, Eindhoven, Netherlands, 2015, pp. 1-6.
- [32] M. H. Rashid, "Power electronics - challenges and trends," *2017 International Conference on Innovations in Electrical Engineering and Computational Technologies (ICIEECT)*, Karachi, Pakistan, 2017, pp. 1-1.
- [33] Y. Wang, Ó. Lucía, Z. Zhang, S. Gao, Y. Guan, and D. Xu, "A review of high frequency power converters and related technologies," *IEEE Open Journal of the Industrial Electronics Society*, vol. 1, pp. 247–260, Jan. 2020.
- [34] S. M. S. H. Rafin, R. Ahmed and O. A. Mohammed, "Wide Band Gap Semiconductor Devices for Power Electronic Converters," *2023 Fourth International Symposium on 3D Power Electronics Integration and Manufacturing (3D-PEIM)*, Miami, FL, USA, 2023, pp. 1-8
- [35] M. Farsijani, S. Abbasian, H. Hafezi, M. T. Bina, and K. Abbaszadeh, "Design and implementation of a single Switch High Gain Boost Topology: Structure, ripple Control and ZCS," *IEEE Access*, vol. 11, pp. 2092–2104, Jan. 2023.
- [36] S. Khan et al., "A new transformerless ultra high gain DC–DC converter for DC microgrid application," *IEEE Access*, vol. 9, pp. 124560–124582, Jan. 2021.
- [37] S. Gopinathan, V. S. Rao, and S. Kumaravel, "Family of Non-Isolated Quadratic high gain DC–DC converters based on extended Capacitor-Diode network for renewable energy source integration," *IEEE Journal of Emerging and Selected Topics in Power Electronics*, vol. 10, no. 5, pp. 6218–6230, Oct. 2022.
- [38] B. Yuan, L. Liao, G. Ning, W. Xiong, and M. Su, "An expandable High Voltage-Gain resonant DC-DC converter with low semiconductor voltage stress," *IEEE Transactions on Circuits and Systems II-Express Briefs*, vol. 69, no. 9, pp. 3844–3848, Sep. 2022.
- [39] L. Chen, L. Tarisciotti, A. Costabeber, Q. Guan, P. Wheeler, and P. Zanchetta, "Phase-Shift modulation for a Current-Fed isolated DC–DC converter in more electric aircrafts," *IEEE Transactions on Power Electronics*, vol. 34, no. 9, pp. 8528–8543, Sep. 2019.
- [40] V. R. Vakacharla, A. K. Rathore, R. K. Singh and S. K. Mishra, "Analysis and Design of Current-fed LCL Series Resonant Converter with Capacitive Doubler," *2020 IEEE Industry Applications Society Annual Meeting*, Detroit, MI, USA, 2020, pp. 1-6.

- [41] M. Muñoz, M. Alonso-García, N. Vela, and F. Chenlo, "Early degradation of silicon PV modules and guaranty conditions," *Solar Energy*, vol. 85, no. 9, pp. 2264–2274, Sep. 2011.
- [42] X. C. Miow, Y. S. Lim, L. C. Hau, J. Wong and H. Patsios, "Impact of High Intermittent PV Systems on the System Frequency and Rate of Change of Frequency in Malaysia," *2022 IEEE PES Innovative Smart Grid Technologies - Asia (ISGT Asia)*, Singapore, Singapore, 2022, pp. 31-35.
- [43] K. Hasan, S. B. Yousuf, M. S. H. K. Tushar, B. Das, P. Das, and Md. S. Islam, "Effects of different environmental and operational factors on the PV performance: A comprehensive review," *Energy Science & Engineering*, vol. 10, no. 2, pp. 656–675, Dec. 2021.
- [44] J. D. Mondol, Y. G. Yohanis, and B. Norton, "The impact of array inclination and orientation on the performance of a grid-connected photovoltaic system," *Renewable Energy*, vol. 32, no. 1, pp. 118–140, Jan. 2007.
- [45] V. Prema and K. U. Rao, "Development of statistical time series models for solar power prediction," *Renewable Energy*, vol. 83, pp. 100–109, Nov. 2015.
- [46] J. M. Bright, O. Babacan, J. Kleissl, P. Taylor, and R. Crook, "A synthetic, spatially decorrelating solar irradiance generator and application to a LV grid model with high PV penetration," *Solar Energy*, vol. 147, pp. 83–98, May 2017.
- [47] K. Abdulmawjood, S. Alsadi, S. S. Refaat, and W. G. Morsi, "Characteristic study of solar photovoltaic array under different partial shading conditions," *IEEE Access*, vol. 10, pp. 6856–6866, Jan. 2022.
- [48] P. Bharadwaj and V. John, "Subcell modeling of partially shaded photovoltaic modules," *IEEE Transactions on Industry Applications*, vol. 55, no. 3, pp. 3046–3054, May 2019.
- [49] N. Ramachandra and R. Natarajan, "Productivity Enhancement of Total-Cross-Tied PV Array Under Static Shade Conditions," *IEEE Transactions on Power Electronics*, vol. 38, no. 3, pp. 4053-4060, March 2023.
- [50] A. Riaz, A. F. Murtaza, H. A. Sher, U. T. Shami, and S. Olalekan, "An analytical approach to study partial shading effects on PV array supported by literature," *Renewable & Sustainable Energy Reviews*, vol. 74, pp. 721–732, Jul. 2017.
- [51] M. Z. S. El-Dein, M. Kazerani, and M. M. A. Salama, "Optimal photovoltaic array reconfiguration to reduce partial shading losses," *IEEE Transactions on Sustainable Energy*, vol. 4, no. 1, pp. 145–153, Jan. 2013.
- [52] J. Ma, X. Pan, K. L. Man, X. Li, H. Wen, and T. O. Ting, "Detection and assessment of partial shading scenarios on photovoltaic strings," *IEEE Transactions on Industry Applications*, vol. 54, no. 6, pp. 6279–6289, Nov. 2018.
- [53] M. A. Ghasemi, H. M. Foroushani and M. Parniani, "Partial Shading Detection and Smooth Maximum Power Point Tracking of PV Arrays Under PSC," *IEEE Transactions on Power Electronics*, vol. 31, no. 9, pp. 6281-6292, Sept. 2016.

- [54] Z. Bi, J. Ma, K. Wang, K. L. Man, J. S. Smith and Y. Yue, "Identification of Partial Shading Conditions for Photovoltaic Strings," *IEEE Access*, vol. 8, pp. 75491-75502, 2020.
- [55] V. Verma and A. Narula, "Wide Operating Range, Continuous Input Current T-Impedance Boost Converter for PV Application," *IEEE Transactions on Industry Applications*, vol. 55, no. 6, pp. 7442-7451, Nov.-Dec. 2019.
- [56] H. Deboucha, M. Kermadi, S. Mekhilef and S. L. Belaid, "Ultra-Fast and Accurate MPPT Control Structure for Mobile PV System Under Fast-Changing Atmospheric Conditions," *IEEE Transactions on Sustainable Energy*, vol. 14, no. 4, pp. 2168-2176, Oct. 2023.
- [57] S. Raizada and V. Verma, "Step Up Gain Converter with fast MPPT control under moving partial shading for train rooftop PV-DC- μ G," *2018 IEEE International Conference on Electrical Systems for Aircraft, Railway, Ship Propulsion and Road Vehicles & International Transportation Electrification Conference (ESARS-ITEC)*, Nottingham, UK, 2018, pp. 1-6.
- [58] S. Verma, S. Mohapatra, S. Chowdhury, and G. Dwivedi, "Cooling techniques of the PV module: A review," *Materials Today: Proceedings*, vol. 38, pp. 253–258, Jan. 2021.
- [59] S. A. M. Said, G. Hassan, H. M. Walwil, and N. Al-Aqeeli, "The effect of environmental factors and dust accumulation on photovoltaic modules and dust-accumulation mitigation strategies," *Renewable & Sustainable Energy Reviews*, vol. 82, pp. 743–760, Feb. 2018.
- [60] M. S. Salim, J. M. Najim, and S. M. Salih, "Practical evaluation of solar irradiance effect on PV performance," *Energy Science and Technology*, vol. 6, no. 2, pp. 36–40, Nov. 2013.
- [61] S. A. M. Said, N. Al-Aqeeli, and H. M. Walwil, "The potential of using textured and anti-reflective coated glasses in minimizing dust fouling," *Solar Energy*, vol. 113, pp. 295–302, Mar. 2015.
- [62] H. Qasem, T. R. Betts, H. Müllejans, H. AlBusairi, and R. Gottschalg, "Dust-induced shading on photovoltaic modules," *Progress in Photovoltaics: Research and Applications*, vol. 22, no. 2, pp. 218–226, Jun. 2012.
- [63] A. Gok, E. Ozkalay, G. Friesen and F. Frontini, "The Influence of Operating Temperature on the Performance of BIPV Modules," *IEEE Journal of Photovoltaics*, vol. 10, no. 5, pp. 1371-1378, Sept. 2020.
- [64] T. Nordmann and L. Clavadetscher, "Understanding temperature effects on PV system performance," *3rd World Conference on Photovoltaic Energy Conversion, 2003*. Proceedings of, Osaka, Japan, 2003, pp. 2243-2246 Vol.3.
- [65] E. L. Meyer and E. E. Van Dyk, "Assessing the reliability and degradation of photovoltaic module performance parameters," *IEEE Transactions on Reliability*, vol. 53, no. 1, pp. 83–92, Mar. 2004.

- [66] I. M. Peters and A. M. Nobre, "On Module Temperature in Floating PV Systems," *2020 47th IEEE Photovoltaic Specialists Conference (PVSC)*, Calgary, AB, Canada, 2020, pp. 0238-0241.
- [67] M. M. Rahman, M. Hasanuzzaman, and N. A. Rahim, "Effects of various parameters on PV-module power and efficiency," *Energy Conversion and Management*, vol. 103, pp. 348–358, Oct. 2015.
- [68] A. Q. Malik and S. J. B. H. Damit, "Outdoor testing of single crystal silicon solar cells," *Renewable Energy*, vol. 28, no. 9, pp. 1433–1445, Jul. 2003.
- [69] S. Devakirubakaran, R. Verma, B. Chokkalingam and L. Mihet-Popa, "Performance Evaluation of Static PV Array Configurations for Mitigating Mismatch Losses," *IEEE Access*, vol. 11, pp. 47725-47749, 2023.
- [70] A. Demetriou, D. Buxton and C. A. Charalambous, "Stray Current DC Corrosion Blind Spots Inherent to Large PV Systems Fault Detection Mechanisms: Elaboration of a Novel Concept," *IEEE Transactions on Power Delivery*, vol. 33, no. 1, pp. 3-11, Feb. 2018.
- [71] A. A. Widayat, S. Ma'arif, K. D. Syahindra, A. F. Fauzi and E. A. Setiawan, "Comparison and Optimization of Floating Bifacial and Monofacial Solar PV System in a Tropical Region," *2020 9th International Conference on Power Science and Engineering (ICPSE)*, London, United Kingdom, 2020, pp. 66-70.
- [72] Y.-P. Huang and S.-Y. Hsu, "A performance evaluation model of a high concentration photovoltaic module with a fractional open circuit voltage-based maximum power point tracking algorithm," *Computers & Electrical Engineering*, vol. 51, pp. 331–342, Apr. 2016.
- [73] K. Anoop and M. Nandakumar, "A novel maximum power point tracking method based on particle swarm optimization combined with one cycle control," *2018 International Conference on Power, Instrumentation, Control and Computing (PICC)*, Thrissur, India, 2018, pp. 1-6.
- [74] H. H. H. Mousa, A. Youssef, and E. E. M. Mohamed, "State of the art perturb and observe MPPT algorithms based wind energy conversion systems: A technology review," *International Journal of Electrical Power & Energy Systems*, vol. 126, p. 106598, Mar. 2021.
- [75] V. R. Kota and M. N. Bhukya, "A novel linear tangents based P&O scheme for MPPT of a PV system," *Renewable & Sustainable Energy Reviews*, vol. 71, pp. 257–267, May 2017.
- [76] S. K. Kollimalla and M. K. Mishra, "A novel adaptive P&O MPPT algorithm considering sudden changes in the irradiance," *IEEE Transactions on Energy Conversion*, vol. 29, no. 3, pp. 602–610, Sep. 2014.
- [77] Y. C. Jiang, J. A. Abu Qahouq, and T. A. Haskew, "Adaptive step size with adaptive-perturbation-frequency digital MPPT controller for a single-sensor photovoltaic solar system," *IEEE Transactions on Power Electronics*, vol. 28, no. 7, pp. 3195–3205, Jul. 2013.

- [78] G. C. Hsieh, H. I. Hsieh, C. Y. Tsai, and C. H. Wang, "Photovoltaic power-increment-aided incremental-conductance MPPT with two-phased tracking," *IEEE Transactions on Power Electronics*, vol. 28, no. 6, pp. 2895–2911, Jun. 2013.
- [79] E. Kandemir, N. S. Çetin, and S. Börekçi, "A comprehensive overview of maximum power extraction methods for PV systems," *Renewable & Sustainable Energy Reviews*, vol. 78, pp. 93–112, Oct. 2017.
- [80] P. Bharadwaj and V. John, "Optimized Global Maximum Power Point Tracking of Photovoltaic Systems Based on Rectangular Power Comparison," *IEEE Access*, vol. 9, pp. 53602–53616, 2021.
- [81] A. Ali et al., "Investigation of MPPT Techniques Under Uniform and Non-Uniform Solar Irradiation Condition—A Retrospection," *IEEE Access*, vol. 8, pp. 127368–127392, 2020.
- [82] M. Kumar, K. P. Panda, J. C. Rosas-Caro, A. Valderrabano-Gonzalez and G. Panda, "Comprehensive Review of Conventional and Emerging Maximum Power Point Tracking Algorithms for Uniformly and Partially Shaded Solar Photovoltaic Systems," *IEEE Access*, vol. 11, pp. 31778–31812, 2023.
- [83] H. Patel and V. Agarwal, "Maximum Power Point Tracking Scheme for PV Systems Operating Under Partially Shaded Conditions," *IEEE Transactions on Industrial Electronics*, vol. 55, no. 4, pp. 1689–1698, April 2008.
- [84] E. Koutroulis and F. Blaabjerg, "A New Technique for Tracking the Global Maximum Power Point of PV Arrays Operating Under Partial-Shading Conditions," *IEEE Journal of Photovoltaics*, vol. 2, no. 2, pp. 184–190, April 2012.
- [85] Syafaruddin, E. Karatepe, and T. Hiyama, "Artificial neural network-polar coordinated fuzzy controller based maximum power point tracking control under partially shaded conditions," *IET Renewable Power Generation*, vol. 3, no. 2, p. 239, Jan. 2009.
- [86] N. Priyadarshi, F. Azam, A. K. Sharma, and M. Vardia, "An adaptive Neuro-Fuzzy inference System-Based intelligent Grid-Connected photovoltaic power generation," *Advances in intelligent systems and computing*, 2019, pp. 3–14.
- [87] V. V. Ramana and D. Jena, "Maximum power point tracking of PV array under non-uniform irradiance using artificial neural network," *2015 IEEE International Conference on Signal Processing, Informatics, Communication and Energy Systems (SPICES)*, Kozhikode, India, 2015, pp. 1–5.
- [88] C. Cabal, L. Martínez-Salamero, L. Séguier, C. Alonso, and F. Guinjoan, "Maximum power point tracking based on sliding-mode control for output-series connected converters in photovoltaic systems," *IET Power Electronics*, vol. 7, no. 4, pp. 914–923, Apr. 2014.
- [89] K. Sundareswaran, S. Peddapati, P. S. R. Nayak, S. P. Simon, and S. Palani, "Enhanced energy output from a PV system under partial shaded conditions through artificial bee colony," *IEEE Transactions on Sustainable Energy*, vol. 6, no. 1, pp. 198–209, Jan. 2015.

- [90] K. Ishaque and Z. Salam, "A Deterministic Particle Swarm Optimization Maximum Power Point Tracker for Photovoltaic System Under Partial Shading Condition," *IEEE Transactions on Industrial Electronics*, vol. 60, no. 8, pp. 3195-3206, Aug. 2013.
- [91] N. Kumar, I. Hussain, B. Singh and B. K. Panigrahi, "Rapid MPPT for Uniformly and Partial Shaded PV System by Using JayaDE Algorithm in Highly Fluctuating Atmospheric Conditions," *IEEE Transactions on Industrial Informatics*, vol. 13, no. 5, pp. 2406-2416, Oct. 2017.
- [92] J. Ahmed and Z. Salam, "A Maximum Power Point Tracking (MPPT) for PV system using Cuckoo Search with partial shading capability," *Applied Energy*, vol. 119, pp. 118–130, Apr. 2014.
- [93] S. Mohanty, B. Subudhi and P. K. Ray, "A New MPPT Design Using Grey Wolf Optimization Technique for Photovoltaic System Under Partial Shading Conditions," *IEEE Transactions on Sustainable Energy*, vol. 7, no. 1, pp. 181-188, Jan. 2016.
- [94] C. Huang, L. Wang, R. S. -C. Yeung, Z. Zhang, H. S. -H. Chung and A. Bensoussan, "A Prediction Model-Guided Jaya Algorithm for the PV System Maximum Power Point Tracking," *IEEE Transactions on Sustainable Energy*, vol. 9, no. 1, pp. 45-55, Jan. 2018.
- [95] M. Kermadi and E. M. Berkouk, "Artificial intelligence-based maximum power point tracking controllers for Photovoltaic systems: Comparative study," *Renewable & Sustainable Energy Reviews*, vol. 69, pp. 369–386, Mar. 2017.
- [96] C. Manickam, G. P. Raman, G. R. Raman, S. I. Ganesan and N. Chilakapati, "Fireworks Enriched P&O Algorithm for GMPPT and Detection of Partial Shading in PV Systems," *IEEE Transactions on Power Electronics*, vol. 32, no. 6, pp. 4432-4443, June 2017.
- [97] S. Mohanty, B. Subudhi and P. K. Ray, "A Grey Wolf-Assisted Perturb & Observe MPPT Algorithm for a PV System," *IEEE Transactions on Energy Conversion*, vol. 32, no. 1, pp. 340-347, March 2017.
- [98] M. Kermadi, Z. Salam, J. Ahmed and E. M. Berkouk, "A High-Performance Global Maximum Power Point Tracker of PV System for Rapidly Changing Partial Shading Conditions," *IEEE Transactions on Industrial Electronics*, vol. 68, no. 3, pp. 2236-2245, March 2021.
- [99] N. Kumar, I. Hussain, B. Singh and B. K. Panigrahi, "MPPT in Dynamic Condition of Partially Shaded PV System by Using WODE Technique," *IEEE Transactions on Sustainable Energy*, vol. 8, no. 3, pp. 1204-1214, July 2017.
- [100] Y. Wang, Y. Li and X. Ruan, "High-Accuracy and Fast-Speed MPPT Methods for PV String Under Partially Shaded Conditions," *IEEE Transactions on Industrial Electronics*, vol. 63, no. 1, pp. 235-245, Jan. 2016.

- [101] M. H. Mobarak and J. Bauman, "A Fast Parabolic-Assumption Algorithm for Global MPPT of Photovoltaic Systems Under Partial Shading Conditions," *IEEE Transactions on Industrial Electronics*, vol. 69, no. 8, pp. 8066-8079, Aug. 2022.
- [102] Y. Yang, H. Wang, F. Blaabjerg and T. Kerekes, "A Hybrid Power Control Concept for PV Inverters With Reduced Thermal Loading," *IEEE Transactions on Power Electronics*, vol. 29, no. 12, pp. 6271-6275, Dec. 2014.
- [103] H. Beltran, E. Bilbao, E. Belenguer, I. Etxeberria-Otadui and P. Rodriguez, "Evaluation of Storage Energy Requirements for Constant Production in PV Power Plants," *IEEE Transactions on Industrial Electronics*, vol. 60, no. 3, pp. 1225-1234, March 2013.
- [104] C. E. Okafor and K. A. Folly, "Sizing of Battery Energy Storage System (BESS) for Inertia Response Support," *2022 IEEE PES/IAS PowerAfrica*, Kigali, Rwanda, 2022, pp. 1-5.
- [105] A. Cabrera-Tobar, E. Bullich-Massagué, M. Aragüés-Peñalba, and O. Gomis-Bellmunt, "Review of advanced grid requirements for the integration of large scale photovoltaic power plants in the transmission system," *Renewable & Sustainable Energy Reviews*, vol. 62, pp. 971–987, Sep. 2016.
- [106] H. D. Tafti et al., "Comparative Analysis of Flexible Power Point Tracking Algorithms in Photovoltaic Systems," *2020 IEEE Energy Conversion Congress and Exposition (ECCE)*, Detroit, MI, USA, 2020, pp. 110-115.
- [107] A. Narang et al., "Dynamic Reserve Power Point Tracking in Grid-Connected Photovoltaic Power Plants," *IEEE Transactions on Power Electronics*, vol. 38, no. 5, pp. 5939-5951, May 2023.
- [108] V. D. Paduani, H. Yu, B. Xu and N. Lu, "A Unified Power-Setpoint Tracking Algorithm for Utility-Scale PV Systems With Power Reserves and Fast Frequency Response Capabilities," *IEEE Transactions on Sustainable Energy*, vol. 13, no. 1, pp. 479-490, Jan. 2022.
- [109] X. Li, H. Wen, Y. Zhu, L. Jiang, Y. Hu and W. Xiao, "A Novel Sensorless Photovoltaic Power Reserve Control With Simple Real-Time MPP Estimation," *IEEE Transactions on Power Electronics*, vol. 34, no. 8, pp. 7521-7531, Aug. 2019.
- [110] K. Ishaque, Z. Salam, M. Amjad and S. Mekhilef, "An Improved Particle Swarm Optimization (PSO)–Based MPPT for PV With Reduced Steady-State Oscillation," *IEEE Transactions on Power Electronics*, vol. 27, no. 8, pp. 3627-3638, Aug. 2012.
- [111] A. F. Hoke, M. Shirazi, S. Chakraborty, E. Muljadi and D. Maksimovic, "Rapid Active Power Control of Photovoltaic Systems for Grid Frequency Support," *IEEE Journal of Emerging and Selected Topics in Power Electronics*, vol. 5, no. 3, pp. 1154-1163, Sept. 2017.
- [112] C. -Y. Tang, Y. -T. Chen and Y. -M. Chen, "PV Power System With Multi-Mode Operation and Low-Voltage Ride-Through Capability," *IEEE Transactions on Industrial Electronics*, vol. 62, no. 12, pp. 7524-7533, Dec. 2015

- [113] A. Sangwongwanich, Y. Yang and F. Blaabjerg, "High-Performance Constant Power Generation in Grid-Connected PV Systems," *IEEE Transactions on Power Electronics*, vol. 31, no. 3, pp. 1822-1825, March 2016.
- [114] A. Sangwongwanich, Y. Yang, F. Blaabjerg and H. Wang, "Benchmarking of Constant Power Generation Strategies for Single-Phase Grid-Connected Photovoltaic Systems," *IEEE Transactions on Industry Applications*, vol. 54, no. 1, pp. 447-457, Jan.-Feb. 2018.
- [115] H. D. Tafti et al., "Extended Functionalities of Photovoltaic Systems With Flexible Power Point Tracking: Recent Advances," *IEEE Transactions on Power Electronics*, vol. 35, no. 9, pp. 9342-9356, Sept. 2020.
- [116] H. D. Tafti, A. Sangwongwanich, Y. Yang, J. Pou, G. Konstantinou and F. Blaabjerg, "An Adaptive Control Scheme for Flexible Power Point Tracking in Photovoltaic Systems," *IEEE Transactions on Power Electronics*, vol. 34, no. 6, pp. 5451-5463, June 2019.
- [117] W. A. Omran, M. Kazerani and M. M. A. Salama, "Investigation of Methods for Reduction of Power Fluctuations Generated From Large Grid-Connected Photovoltaic Systems," *IEEE Transactions on Energy Conversion*, vol. 26, no. 1, pp. 318-327, March 2011.
- [118] R. Gomez-Merchan et al., "Binary Search Based Flexible Power Point Tracking Algorithm for Photovoltaic Systems," *IEEE Transactions on Industrial Electronics*, vol. 68, no. 7, pp. 5909-5920, July 2021.
- [119] A. Kumaresan, H. D. Tafti, N. K. Kandasamy, G. G. Farivar, J. Pou and T. Subbaiyan, "Flexible Power Point Tracking for Solar Photovoltaic Systems Using Secant Method," *IEEE Transactions on Power Electronics*, vol. 36, no. 8, pp. 9419-9429, Aug. 2021.
- [120] A. Kumaresan, H. D. Tafti, G. G. Farivar, N. B. Y. Gorla, N. Beniwal and J. Pou, "Flexible Power Point Tracking Algorithm for Photovoltaic Systems Using the Newton's Method," *IECON 2021 – 47th Annual Conference of the IEEE Industrial Electronics Society*, Toronto, ON, Canada, 2021, pp. 1-6.
- [121] A. Kumaresan et al., "Improved Secant-Based Global Flexible Power Point Tracking in Photovoltaic Systems Under Partial Shading Conditions," *IEEE Transactions on Power Electronics*, vol. 38, no. 8, pp. 10383-10395, Aug. 2023.
- [122] H. D. Tafti, Q. Wang, C. D. Townsend, J. Pou and G. Konstantinou, "Global Flexible Power Point Tracking in Photovoltaic Systems Under Partial Shading Conditions," *IEEE Transactions on Power Electronics*, vol. 37, no. 9, pp. 11332-11341, Sept. 2022.
- [123] V. K. Kolakaluri, M. N. Aalam and V. Sarkar, "Metaheuristics Assisted Efficiency Maximizing Flexible Power Point Tracking of a Photovoltaic Array Under the Partial Shading," *IEEE Transactions on Energy Conversion*, vol. 38, no. 3, pp. 1576-1588, Sept. 2023.

- [124] H. W. Yan et al., "Battery Lifetime Extension in a Stand-Alone Microgrid With Flexible Power Point Tracking of Photovoltaic System," *IEEE Journal of Emerging and Selected Topics in Power Electronics*, vol. 11, no. 2, pp. 2281-2290, April 2023.
- [125] H. W. Yan, A. Narang, H. D. Tafti, G. G. Farivar, S. Ceballos and J. Pou, "Minimizing Energy Storage Utilization in a Stand-Alone DC Microgrid Using Photovoltaic Flexible Power Control," *IEEE Transactions on Smart Grid*, vol. 12, no. 5, pp. 3755-3764, Sept. 2021.
- [126] R. C. N. Pilawa-Podgurski and D. J. Perreault, "Submodule Integrated Distributed Maximum Power Point Tracking for Solar Photovoltaic Applications," *IEEE Transactions on Power Electronics*, vol. 28, no. 6, pp. 2957-2967, June 2013.
- [127] A. Chub, D. Vinnikov, R. Kosenko and E. Liivik, "Wide Input Voltage Range Photovoltaic Microconverter With Reconfigurable Buck–Boost Switching Stage," *IEEE Transactions on Industrial Electronics*, vol. 64, no. 7, pp. 5974-5983, July 2017.
- [128] H. M. Maheri, A. Chub, D. Vinnikov and A. Blinov, "Photovoltaic Microconverter with Integrated Sub-Modular Power Optimizer," *2021 IEEE 15th International Conference on Compatibility, Power Electronics and Power Engineering (CPE-POWERENG)*, Florence, Italy, 2021, pp. 1-6.
- [129] Y. -M. Chen, K. -Y. Lo and Y. -R. Chang, "Multi-string single-stage grid-connected inverter for PV system," *2011 IEEE Energy Conversion Congress and Exposition*, Phoenix, AZ, USA, 2011, pp. 2751-2756.
- [130] B. S. Revathi and M. Prabhakar, "Non isolated high gain DC-DC converter topologies for PV applications – A comprehensive review," *Renewable & Sustainable Energy Reviews*, vol. 66, pp. 920–933, Dec. 2016.
- [131] M. Lakshmi and S. Hemamalini, "Nonisolated High Gain DC–DC Converter for DC Microgrids," *IEEE Transactions on Industrial Electronics*, vol. 65, no. 2, pp. 1205-1212, Feb. 2018.
- [132] J. Anzola et al., "Review of Architectures Based on Partial Power Processing for DC-DC Applications," *IEEE Access*, vol. 8, pp. 103405-103418, 2020.
- [133] M. S. Agamy et al., "An Efficient Partial Power Processing DC/DC Converter for Distributed PV Architectures," *IEEE Transactions on Power Electronics*, vol. 29, no. 2, pp. 674-686, Feb. 2014.
- [134] K. A. Kim, S. Lertburapa, Chenyang Xu and P. T. Krein, "Efficiency and cost trade-offs for designing module integrated converter photovoltaic systems," *2012 IEEE Power and Energy Conference at Illinois, Champaign, IL*, 2012, pp. 1-7.
- [135] D. Vinnikov, A. Chub, E. Liivik and I. Roasto, "High-Performance Quasi-Z-Source Series Resonant DC–DC Converter for Photovoltaic Module-Level Power Electronics Applications," *IEEE Transactions on Power Electronics*, vol. 32, no. 5, pp. 3634-3650, May 2017.

- [136] D. Sha, J. Zhang and J. Wu, "A GaN-Based Microconverter Utilizing Fixed-Frequency BCM Control Method for PV Applications," *IEEE Transactions on Industrial Electronics*, vol. 65, no. 6, pp. 4771-4780, June 2018.
- [137] O. Khan, W. Xiao and M. S. E. Moursi, "A New PV System Configuration Based on Submodule Integrated Converters," *IEEE Transactions on Power Electronics*, vol. 32, no. 5, pp. 3278-3284, May 2017.
- [138] G. R. Walker and P. C. Sernia, "Cascaded DC-DC converter connection of photovoltaic modules," *IEEE Transactions on Power Electronics*, vol. 19, no. 4, pp. 1130-1139, July 2004.
- [139] S. Harb, M. Kedia, H. Zhang and R. S. Balog, "Microinverter and string inverter grid-connected photovoltaic system — A comprehensive study," *2013 IEEE 39th Photovoltaic Specialists Conference (PVSC)*, Tampa, FL, USA, 2013, pp. 2885-2890.
- [140] G. R. Walker and J. C. Pierce, "Photovoltaic DC-DC module integrated converter for novel cascaded and bypass grid connection topologies — Design and optimization," *2006 37th IEEE Power Electronics Specialists Conference*, Jeju, Korea (South), 2006, pp. 1-7.
- [141] W. -J. Cha, Y. -W. Cho, J. -M. Kwon and B. -H. Kwon, "Highly Efficient Microinverter With Soft-Switching Step-Up Converter and Single-Switch-Modulation Inverter," *IEEE Transactions on Industrial Electronics*, vol. 62, no. 6, pp. 3516-3523, June 2015.
- [142] T. Noguchi, S. Togashi and R. Nakamoto, "Short-current pulse-based maximum-power-point tracking method for multiple photovoltaic-and-converter module system," *IEEE Transactions on Industrial Electronics*, vol. 49, no. 1, pp. 217-223, Feb. 2002.
- [143] G. Spagnuolo, S. Kouro, and D. Vinnikov, "Photovoltaic module and submodule level power electronics and control," *IEEE Transactions on Industrial Electronics*, vol. 66, no. 5, pp. 3856–3859, May 2019.
- [144] A. Chub, D. Vinnikov, O. Korkh, M. Malinowski and S. Kouro, "Ultrawide Voltage Gain Range Microconverter for Integration of Silicon and Thin-Film Photovoltaic Modules in DC Microgrids," *IEEE Transactions on Power Electronics*, vol. 36, no. 12, pp. 13763-13778, Dec. 2021.
- [145] K. Alluhaybi, I. Batarseh and H. Hu, "Comprehensive Review and Comparison of Single-Phase Grid-Tied Photovoltaic Microinverters," *IEEE Journal of Emerging and Selected Topics in Power Electronics*, vol. 8, no. 2, pp. 1310-1329, June 2020.
- [146] M. Adly and K. Strunz, "Irradiance-Adaptive PV Module Integrated Converter for High Efficiency and Power Quality in Standalone and DC Microgrid Applications," *IEEE Transactions on Industrial Electronics*, vol. 65, no. 1, pp. 436-446, Jan. 2018.
- [147] N. Femia, G. Lisi, G. Petrone, G. Spagnuolo and M. Vitelli, "Distributed maximum power point tracking of photovoltaic arrays: Novel approach and system analysis,"

- IEEE Transactions on Industrial Electronics*, vol. 55, no. 7, pp. 2610-2621, July 2008.
- [148] R. Motamarri and N. Bhookya, "JAYA Algorithm Based on Lévy Flight for Global MPPT Under Partial Shading in Photovoltaic System," *IEEE Journal of Emerging and Selected Topics in Power Electronics*, vol. 9, no. 4, pp. 4979-4991, Aug. 2021.
 - [149] L. Gao, R. A. Dougal, S. Liu and A. P. Iotova, "Parallel-Connected Solar PV System to Address Partial and Rapidly Fluctuating Shadow Conditions," *IEEE Transactions on Industrial Electronics*, vol. 56, no. 5, pp. 1548-1556, May 2009.
 - [150] D. Vinnikov, A. Chub, R. Kosenko, V. Sidorov and A. Lindvest, "Implementation of Global Maximum Power Point Tracking in Photovoltaic Microconverters: A Survey of Challenges and Opportunities," *IEEE Journal of Emerging and Selected Topics in Power Electronics*, vol. 11, no. 2, pp. 2259-2280, April 2023.
 - [151] Y. Zhang, J. Xiong, P. He and S. Wang, "Review of power decoupling methods for micro-inverters used in PV systems," *Chinese Journal of Electrical Engineering*, vol. 4, no. 4, pp. 26-32, Dec 2018.
 - [152] Q. Li and P. Wolfs, "A Review of the Single Phase Photovoltaic Module Integrated Converter Topologies With Three Different DC Link Configurations," *IEEE Transactions on Power Electronics*, vol. 23, no. 3, pp. 1320-1333, May 2008.
 - [153] D. Kumar, F. Zare and A. Ghosh, "DC Microgrid Technology: System Architectures, AC Grid Interfaces, Grounding Schemes, Power Quality, Communication Networks, Applications, and Standardizations Aspects," *IEEE Access*, vol. 5, pp. 12230-12256, 2017.
 - [154] P. Silva and C. M. D. S. Medeiros, "A Promising Future To DC Power System: A Review," *IEEE Latin America Transactions*, vol. 15, no. 9, pp. 1639-1642, 2017.
 - [155] T. Hakala, T. Lahdeaho and R. Komsí, "LVDC Pilot Implementation in Public Distribution Network", *Proceeding of International Conference on Electrical Distribution*, CIRED 2015, June 2015.
 - [156] D. Gerber, V. Vossos, W. Feng, C. Marnay, B. Nordman, and R. E. Brown, "A simulation-based efficiency comparison of AC and DC power distribution networks in commercial buildings," *Applied Energy*, vol. 210, pp. 1167–1187, Jan. 2018.
 - [157] J. J. Justo, F. Mwasilu, J. Lee, and J. W. Jung, "AC-microgrids versus DC-microgrids with distributed energy resources: A review," *Renewable & Sustainable Energy Reviews*, vol. 24, pp. 387–405, Aug. 2013.
 - [158] J. -D. Park, J. Candelaria, L. Ma and K. Dunn, "DC Ring-Bus Microgrid Fault Protection and Identification of Fault Location," *IEEE Transactions on Power Delivery*, vol. 28, no. 4, pp. 2574-2584, Oct. 2013.
 - [159] A. El-Shahat and S. Sumaiya, "DC-MicroGrid system design, control, and analysis," *Electronics*, vol. 8, no. 2, p. 124, Jan. 2019.
 - [160] T. Dragičević, X. Lu, J. C. Vasquez and J. M. Guerrero, "DC Microgrids—Part II: A Review of Power Architectures, Applications, and Standardization Issues," *IEEE Transactions on Power Electronics*, vol. 31, no. 5, pp. 3528-3549, May 2016.

- [161] K. M. Bhargavi, N. S. Jayalakshmi, D. N. Gaonkar, A. Shrivastava and V. K. Jadoun, "A Comprehensive Review on Control Techniques for Power Management of Isolated DC Microgrid System Operation," *IEEE Access*, vol. 9, pp. 32196-32228, 2021.
- [162] P. Singh and J. S. Lather, "Power management and control of a grid-independent DC microgrid with hybrid energy storage system," *Sustainable Energy Technologies and Assessments*, vol. 43, p. 100924, Feb. 2021.
- [163] Z. Liu, J. Zhao, and Z. Zou, "Impedance modeling, dynamic analysis and damping enhancement for DC microgrid with multiple types of loads," *International Journal of Electrical Power & Energy Systems*, vol. 122, p. 106183, Nov. 2020.
- [164] O. D. Montoya, W. Gil-González, and L. F. Grisales-Noreña, "Solar photovoltaic integration in monopolar DC networks via the GNDO algorithm," *Algorithms*, vol. 15, no. 8, p. 277, Aug. 2022.
- [165] S. Rivera, R. Lizana F., S. Kouro, T. Dragičević and B. Wu, "Bipolar DC Power Conversion: State-of-the-Art and Emerging Technologies," *IEEE Journal of Emerging and Selected Topics in Power Electronics*, vol. 9, no. 2, pp. 1192-1204, April 2021.
- [166] N. Bayati, H. R. Baghaee, A. Hajizadeh and M. Soltani, "Localized Protection of Radial DC Microgrids With High Penetration of Constant Power Loads," *IEEE Systems Journal*, vol. 15, no. 3, pp. 4145-4156, Sept. 2021.
- [167] R. Mohanty and A. K. Pradhan, "Protection of Smart DC Microgrid With Ring Configuration Using Parameter Estimation Approach," *IEEE Transactions on Smart Grid*, vol. 9, no. 6, pp. 6328-6337, Nov. 2018.
- [168] C. Chakraborty, H. Ho-Ching Iu and D. Dah-Chuan Lu, "Power converters, control, and energy management for distributed generation," *IEEE Transactions on Industrial Electronics*, vol. 62, no. 7, pp. 4466-4470, July 2015.
- [169] X. Feng, K. L. Butler-Purpy, and T. Zourntos, "Real-time electric load management for DC zonal all-electric ship power systems," *Electric Power Systems Research*, vol. 154, pp. 503–514, Jan. 2018.
- [170] S. Anand and B. G. Fernandes, "Optimal voltage level for DC microgrids," *IECON 2010 - 36th Annual Conference on IEEE Industrial Electronics Society*, Glendale, AZ, USA, 2010, pp. 3034-3039.
- [171] V. Verma and G. G. Talpur, "Decentralized Master-Slave operation of microgrid using current controlled distributed generation sources," *2012 IEEE International Conference on Power Electronics, Drives and Energy Systems (PEDES)*, Bengaluru, India, 2012, pp. 1-6.
- [172] D. S. D'antonio, O. López-Santos, A. Navas-Fonseca, F. Flores-Bahamonde and M. A. Pérez, "Multi-Mode Master-Slave Control Approach for More Modular and Reconfigurable Hybrid Microgrids," *IEEE Access*, vol. 11, pp. 55334-55348, 2023.

- [173] X. Lu, J. Lai and G. -P. Liu, "Master–Slave Cooperation for Multi-DC-MGs via Variable Cyber Networks," *IEEE Transactions on Cybernetics*, vol. 52, no. 8, pp. 8425-8438, Aug. 2022.
- [174] V. F. Pires, A. Pires, and A. Cordeiro, "DC Microgrids: Benefits, Architectures, Perspectives and Challenges," *Energies*, vol. 16, no. 3, p. 1217, Jan. 2023.
- [175] A. Sannino, G. Postiglione and M. H. J. Bollen, "Feasibility of a DC network for commercial facilities," *IEEE Transactions on Industry Applications*, vol. 39, no. 5, pp. 1499-1507, Sept.-Oct. 2003.
- [176] J. Kathiresan, S. K. Natarajan, and J. Gnanavadeivel, "Energy management of distributed renewable energy sources for residential DC microgrid applications," *International Transactions on Electrical Energy Systems*, vol. 30, no. 3, Dec. 2019.
- [177] H. A. B. Siddique, S. M. Ali and R. W. De Doncker, "DC collector grid configurations for large photovoltaic parks," *2013 15th European Conference on Power Electronics and Applications (EPE)*, Lille, France, 2013, pp. 1-10.
- [178] D. Kumar and F. Zare, "Harmonic Analysis of Grid Connected Power Electronic Systems in Low Voltage Distribution Networks," *IEEE Journal of Emerging and Selected Topics in Power Electronics*, vol. 4, no. 1, pp. 70-79, March 2016.
- [179] E. Candan, P. S. Shenoy and R. C. N. Pilawa-Podgurski, "A Series-Stacked Power Delivery Architecture With Isolated Differential Power Conversion for Data Centers," *IEEE Transactions on Power Electronics*, vol. 31, no. 5, pp. 3690-3703, May 2016.
- [180] T. Tanaka, K. Hirose, D. Marquet, B. Sonnenberg and M. Szpek, "Analysis of wiring design for 380-VDC power distribution system at telecommunication sites," *Intelec 2012*, Scottsdale, AZ, USA, 2012, pp. 1-5 .
- [181] M. Tabari and A. Yazdani, "An Energy Management Strategy for a DC Distribution System for Power System Integration of Plug-In Electric Vehicles," *IEEE Transactions on Smart Grid*, vol. 7, no. 2, pp. 659-668, March 2016.
- [182] L. Xu et al., "A Review of DC Shipboard Microgrids—Part I: Power Architectures, Energy Storage, and Power Converters," *IEEE Transactions on Power Electronics*, vol. 37, no. 5, pp. 5155-5172, May 2022.
- [183] A. Verdicchio, P. Ladoux, H. Caron and C. Courtois, "New Medium-Voltage DC Railway Electrification System," *IEEE Transactions on Transportation Electrification*, vol. 4, no. 2, pp. 591-604, June 2018.
- [184] M. Mobarrez, D. Fregosi, G. Jalali, S. Bhattacharya and M. A. Bahmani, "A novel control method for preventing the PV and load fluctuations in a DC microgrid from transferring to the AC power grid," *2017 IEEE Second International Conference on DC Microgrids (ICDCM)*, Nuremburg, Germany, 2017, pp. 352-359.
- [185] X. Xiong and Y. Yang, "A Photovoltaic-Based DC Microgrid System: Analysis, Design and Experimental Results," *Electronics*, vol. 9, no. 6, pp. 941, Jun. 2020.
- [186] C. Correa-Betanzo, H. Calleja, C. Aguilar, A. R. Lopez-Nunez and E. Rodriguez, "Photovoltaic-based DC microgrid with partial shading and fault tolerance," *Journal*

- of Modern Power Systems and Clean Energy*, vol. 7, no. 2, pp. 340-349, March 2019.
- [187] M. Nasir, H. A. Khan, A. Hussain, L. Mateen and N. A. Zaffar, "Solar PV-Based Scalable DC Microgrid for Rural Electrification in Developing Regions," *IEEE Transactions on Sustainable Energy*, vol. 9, no. 1, pp. 390-399, Jan. 2018.
 - [188] M. Hamza, M. Shehroz, S. Fazal, M. Nasir and H. A. Khan, "Design and analysis of solar PV based low-power low-voltage DC microgrid architectures for rural electrification," *2017 IEEE Power & Energy Society General Meeting*, Chicago, IL, USA, 2017, pp. 1-5.
 - [189] S. Grace Sadhana, S. Ashok, N. Sasidharan, S. Rahman and S. Kumaravel, "Energy Management Strategy for a Standalone Solar PV based DC Community Grid," *2020 6th IEEE International Energy Conference (ENERGYCon)*, Gammarth, Tunisia, 2020, pp. 468-473.
 - [190] O. Abdel-Rahim, A. Chub, D. Vinnikov and A. Blinov, "DC Integration of Residential Photovoltaic Systems: A Survey," *IEEE Access*, vol. 10, pp. 66974-66991, 2022.
 - [191] K. Kanathipan, R. Emamalipour and J. Lam, "A Single-Switch High-Gain PV Microconverter With Low-Switch-Voltage-to-High-Voltage-Bus Ratio," *IEEE Transactions on Power Electronics*, vol. 35, no. 9, pp. 9530-9540, Sept. 2020.
 - [192] X. Zhang et al., "Novel High Step-Up Soft-Switching DC–DC Converter Based on Switched Capacitor and Coupled Inductor," *IEEE Transactions on Power Electronics*, vol. 35, no. 9, pp. 9471-9481, Sept. 2020.
 - [193] M. Forouzesh, Y. P. Siwakoti, S. A. Gorji, F. Blaabjerg and B. Lehman, "Step-Up DC–DC Converters: A Comprehensive Review of Voltage-Boosting Techniques, Topologies, and Applications," *IEEE Transactions on Power Electronics*, vol. 32, no. 12, pp. 9143-9178, Dec. 2017.
 - [194] Y. Qin, Y. Yang, S. Li, Y. Huang, S. -C. Tan and S. Y. Hui, "A High-Efficiency DC/DC Converter for High-Voltage-Gain, High-Current Applications," *IEEE Journal of Emerging and Selected Topics in Power Electronics*, vol. 8, no. 3, pp. 2812-2823, Sept. 2020.
 - [195] V. Karthikeyan, S. Kumaravel and G. Gurukumar, "High Step-Up Gain DC–DC Converter With Switched Capacitor and Regenerative Boost Configuration for Solar PV Applications," *IEEE Transactions on Circuits and Systems II: Express Briefs*, vol. 66, no. 12, pp. 2022-2026, Dec. 2019.
 - [196] M. Sagar Bhaskar et al., "Survey of DC-DC Non-Isolated Topologies for Unidirectional Power Flow in Fuel Cell Vehicles," *IEEE Access*, vol. 8, pp. 178130-178166, 2020.
 - [197] H. Tarzamni, H. S. Gohari, M. Sabahi, and J. Kyyrä, "Non-Isolated High Step-Up DC-DC Converters: Comparative Review and Metrics Applicability," *IEEE Transactions on Power Electronics*, pp. 1–41, Jan. 2023.

- [198] Qun Zhao and F. C. Lee, "High-efficiency, high step-up DC-DC converters," in *IEEE Transactions on Power Electronics*, vol. 18, no. 1, pp. 65-73, Jan. 2003.
- [199] T. S. Wu, Y. S. Lai, J. C. Hung, and Y. M. Chen, "Boost converter with coupled inductors and buck-boost type of active clamp," *IEEE Transactions on Industrial Electronics*, vol. 55, no. 1, pp. 154-162, Jan. 2008.
- [200] S. -W. Lee and H. -L. Do, "High Step-Up Coupled-Inductor Cascade Boost DC-DC Converter With Lossless Passive Snubber," *IEEE Transactions on Industrial Electronics*, vol. 65, no. 10, pp. 7753-7761, Oct. 2018.
- [201] Tsai-Fu Wu and Te-Hung Yu, "Unified approach to developing single-stage power converters," *IEEE Transactions on Aerospace and Electronic Systems*, vol. 34, no. 1, pp. 211-223, Jan. 1998.
- [202] J. Leyva-Ramos, M. G. Ortiz-Lopez, L. H. Diaz-Saldierna, and J. A. Morales-Saldaña, "Switching regulator using a quadratic boost converter for wide DC conversion ratios," *IET Power Electronics*, vol. 2, no. 5, pp. 605-613, Sep. 2009.
- [203] H. Xie and R. Li, "A Novel Switched-Capacitor Converter With High Voltage Gain," *IEEE Access*, vol. 7, pp. 107831-107844, 2019.
- [204] H. Lei, R. Hao, X. You and F. Li, "Nonisolated High Step-Up Soft-Switching DC-DC Converter With Interleaving and Dickson Switched-Capacitor Techniques," *IEEE Journal of Emerging and Selected Topics in Power Electronics*, vol. 8, no. 3, pp. 2007-2021, Sept. 2020.
- [205] M. S. Makowski, "A canonical switched capacitor DC-DC converter," *2014 IEEE 15th Workshop on Control and Modeling for Power Electronics (COMPEL)*, Santander, Spain, 2014, pp. 1-8.
- [206] A. Kushnerov, "Dual output sub-period interleaved step-up Fibonacci switched capacitor converters," *2014 IEEE Faible Tension Faible Consommation*, Monaco, Monaco, 2014, pp. 1-4.
- [207] Y. Tang, T. Wang and D. Fu, "Multicell Switched-Inductor/Switched-Capacitor Combined Active-Network Converters," *IEEE Transactions on Power Electronics*, vol. 30, no. 4, pp. 2063-2072, April 2015.
- [208] K. W. E. Cheng and Y. M. Ye, "Duality approach to the study of switched-inductor power converters and its higher-order variations," *IET Power Electronics*, vol. 8, no. 4, pp. 489-496, Apr. 2015.
- [209] M. E. Azizkandi, F. Sedaghati, H. Shayeghi and F. Blaabjerg, "A High Voltage Gain DC-DC Converter Based on Three Winding Coupled Inductor and Voltage Multiplier Cell," *IEEE Transactions on Power Electronics*, vol. 35, no. 5, pp. 4558-4567, May 2020.
- [210] K. R. Kothapalli, M. R. Ramteke, H. M. Suryawanshi, N. K. Reddi and R. B. Kalahasthi, "Soft-Switched Ultrahigh Gain DC-DC Converter With Voltage Multiplier Cell for DC Microgrid," *IEEE Transactions on Industrial Electronics*, vol. 68, no. 11, pp. 11063-11075, Nov. 2021.

- [211] L. Schmitz, D. C. Martins and R. F. Coelho, "Comprehensive Conception of High Step-Up DC–DC Converters With Coupled Inductor and Voltage Multipliers Techniques," *IEEE Transactions on Circuits and Systems I: Regular Papers*, vol. 67, no. 6, pp. 2140-2151, June 2020.
- [212] X. Liu, X. Zhang, X. Hu, H. Chen, L. Chen and Y. Zhang, "Interleaved high step-up converter with coupled inductor and voltage multiplier for renewable energy system," *CPSS Transactions on Power Electronics and Applications*, vol. 4, no. 4, pp. 299-309, Dec. 2019.
- [213] P. Mohseni, S. Mohammadsalehian, M. R. Islam, K. M. Muttaqi, D. Sutanto and P. Alavi, "Ultrahigh Voltage Gain DC–DC Boost Converter With ZVS Switching Realization and Coupled Inductor Extendable Voltage Multiplier Cell Techniques," *IEEE Transactions on Industrial Electronics*, vol. 69, no. 1, pp. 323-335, Jan. 2022.
- [214] X. Kong, L. T. Choi and A. M. Khambadkone, "Analysis and control of isolated current-fed full bridge converter in fuel cell system," *30th Annual Conference of IEEE Industrial Electronics Society, 2004. IECON 2004*, Busan, Korea (South), 2004, pp. 2825-2830 Vol. 3.
- [215] K. Wang, C. Y. Lin, L. Zhu, D. Qu, F. C. Lee and J. S. Lai, "Bi-directional DC to DC converters for fuel cell systems," *Power Electronics in Transportation (Cat. No.98TH8349)*, Dearborn, MI, USA, 1998, pp. 47-51.
- [216] Z. Zhang, M. Liao, D. Jiang, X. Yang, and S. Li, "High step-up isolated forward-flyback DC/DC converter based on resonance with pulse frequency modulation," *Journal of Power Electronics*, vol. 21, no. 2, pp. 483–493, Dec. 2020.
- [217] B. Pal and S. S. Saha, "A Novel Soft-switched Single-Switch Flyback Converter with Active Leakage Recovery Network," *2021 National Power Electronics Conference (NPEC)*, Bhubaneswar, India, 2021, pp. 1-6.
- [218] L. Jiang et al., "A New Push-Pull DC/DC Converter Topology With Complementary Active Clamped," *IEEE Transactions on Industrial Electronics*, vol. 69, no. 6, pp. 6445-6449, June 2022.
- [219] M. S. Rana, S. Suresh and S. K. Mishra, "A Voltage-Fed Soft-Switched Push–Pull Topology With Phase-Shifted Power Transfer Using Coupled LC Snubber," *IEEE Transactions on Power Electronics*, vol. 36, no. 12, pp. 13903-13916, Dec. 2021.
- [220] Q. Wu, Q. Wang, J. Xu and L. Xiao, "A Wide Load Range ZVS Push–Pull DC/DC Converter With Active Clamped," *IEEE Transactions on Power Electronics*, vol. 32, no. 4, pp. 2865-2875, April 2017.
- [221] H. Tarzamani, E. Babaei, F. P. Esmaelnia, P. Dehghanian, S. Tohidi and M. B. B. Sharifian, "Analysis and Reliability Evaluation of a High Step-Up Soft Switching Push–Pull DC–DC Converter," *IEEE Transactions on Reliability*, vol. 69, no. 4, pp. 1376-1386, Dec. 2020.
- [222] Z. Chen, Y. Chen and Q. Chen, "Isolated Series-Capacitor-Based Full-Bridge Converter With Reduced Circulating Losses and Wide Soft Switching Range,"

- IEEE Journal of Emerging and Selected Topics in Power Electronics*, vol. 7, no. 2, pp. 1272-1285, June 2019.
- [223] D. Liu, Y. Wang, F. Deng, Q. Zhang and Z. Chen, "Zero-Voltage Switching Full-Bridge T-Type DC/DC Converter with Wide Input Voltage Range and Balanced Switch Currents," *IEEE Transactions on Power Electronics*, vol. 33, no. 12, pp. 10449-10466, Dec. 2018.
 - [224] K. V. Ravi Kishore, B. F. Wang, K. N. Kumar and P. L. So, "A new ZVS full-bridge DC-DC converter for battery charging with reduced losses over full-load range," *2015 Annual IEEE India Conference (INDICON)*, New Delhi, India, 2015, pp. 1-6.
 - [225] T. -J. Liang, C. -H. Lin, W. -J. Tseng and Y. -M. Lin, "Design and Implementation of Half-Bridge Resonant Converter With Novel Primary-Side Control," *IEEE Transactions on Power Electronics*, vol. 35, no. 5, pp. 5408-5416, May 2020.
 - [226] Y. Li, F. Li, F. -W. Zhao, X. -J. You, K. Zhang and M. Liang, "Hybrid Three-Level Full-Bridge Isolated Buck–Boost Converter With Clamped Inductor for Wider Voltage Range Application," *IEEE Transactions on Power Electronics*, vol. 34, no. 3, pp. 2923-2937, March 2019.
 - [227] P. He and A. Khaligh, "Comprehensive Analyses and Comparison of 1 kW Isolated DC–DC Converters for Bidirectional EV Charging Systems," *IEEE Transactions on Transportation Electrification*, vol. 3, no. 1, pp. 147-156, March 2017.
 - [228] M. Schulz and S. Ditzel, "Analysis and Experimental Verification of an Isolated Half-Bridge Bidirectional DC–DC Converter," *IEEE Transactions on Power Electronics*, vol. 37, no. 5, pp. 5089-5106, May 2022.
 - [229] D. Cittanti, M. Gregorio, E. Vico, F. Mandrile, E. Armando and R. Bojoi, "High-Performance Digital Multiloop Control of LLC Resonant Converters for EV Fast Charging With LUT-Based Feedforward and Adaptive Gain," *IEEE Transactions on Industry Applications*, vol. 58, no. 5, pp. 6266-6285, September - October 2022.
 - [230] H. Tong, Z. Miao, H. Lin, W. Yao, W. Li and Z. Lu, "A Three-Level LLC Converter With Flexible Variable-Mode Control for Wide Gain Range Application," *IEEE Transactions on Power Electronics*, vol. 38, no. 4, pp. 4503-4519, April 2023.
 - [231] X. Wu, R. Li and X. Cai, "A Wide Output Voltage Range LLC Resonant Converter Based on Topology Reconfiguration Method," *IEEE Journal of Emerging and Selected Topics in Power Electronics*, vol. 10, no. 1, pp. 969-983, Feb. 2022.
 - [232] J. -Y. Lin, P. -H. Liu, H. -Y. Yueh and Y. -F. Lin, "Design and Analysis of LLC Resonant Converter With Valley Switching Control for Light-Load Conditions," *IEEE Journal of Emerging and Selected Topics in Power Electronics*, vol. 10, no. 5, pp. 6033-6044, Oct. 2022.
 - [233] C. -H. Chou, C. -Y. Hsiao and Y. -H. Liu, "Half-Bridge LLC Series-Resonant Converter With Hybrid Rectifier for LED Signage Backlighting Systems," *IEEE Transactions on Circuits and Systems II: Express Briefs*, vol. 70, no. 2, pp. 566-570, Feb. 2023.

- [234] N. -G. Kim, S. -W. Jo, B. Han, H. -H. Choi and M. Kim, "Highly Efficient Bidirectional Current-Fed Resonant Converter Over a Wide Voltage Gain Range," *IEEE Transactions on Industrial Electronics*, vol. 68, no. 11, pp. 10913-10927, Nov. 2021.
- [235] Q. Wu, Q. Wang, J. Xu, H. Li and L. Xiao, "A High-Efficiency Step-Up Current-Fed Push–Pull Quasi-Resonant Converter With Fewer Components for Fuel Cell Application," *IEEE Transactions on Industrial Electronics*, vol. 64, no. 8, pp. 6639-6648, Aug. 2017.
- [236] X. Zhang, H. S. H. Chung, X. Ruan, and A. Ioinovici, "A ZCS fullbridgeconverter without voltage overstress on the switches," *IEEE Transactions on Power Electronics*, vol. 25, no. 3, pp. 686–698, Mar. 2010.
- [237] Q. Li and P. Wolfs, "A Current Fed Two-Inductor Boost Converter With an Integrated Magnetic Structure and Passive Lossless Snubbers for Photovoltaic Module Integrated Converter Applications," *IEEE Transactions on Power Electronics*, vol. 22, no. 1, pp. 309-321, Jan. 2007.
- [238] Eun-Soo Kim, Kee-Yeon Joe, Hae-Young Choi, Yoon-Ho Kim and Yong-Hyun Cho, "An improved soft switching bi-directional PSPWM FB DC/DC converter," *IECON '98. Proceedings of the 24th Annual Conference of the IEEE Industrial Electronics Society (Cat. No.98CH36200)*, Aachen, Germany, 1998, pp. 740-743 vol.2.
- [239] T. Tanaka, T. Ninomiya and K. Harada, "Design of a nondissipative turn-off snubber in a forward converter," *PESC '88 Record., 19th Annual IEEE Power Electronics Specialists Conference*, Kyoto, Japan, 1988, pp. 789-796 vol.2.
- [240] F. J. Nome and I. Barbi, "A ZVS clamping mode-current-fed push-pull DC-DC converter," *IEEE International Symposium on Industrial Electronics. Proceedings. ISIE'98 (Cat. No.98TH8357)*, Pretoria, South Africa, 1998, pp. 617-621 vol.2.
- [241] T. C. Lim, B. W. Williams, S. J. Finney, H. B. Zhang, and C. Croser, "Energy recovery snubber circuit for a dc–dc push–pull converter," *IET Power Electronics*, vol. 5, no. 6, pp. 863–872, Jul. 2012.
- [242] H. Wang, Q. Sun, H. S. H. Chung, S. Tapuchi and A. Ioinovici, "A ZCS Current-Fed Full-Bridge PWM Converter With Self-Adaptable Soft-Switching Snubber Energy," *IEEE Transactions on Power Electronics*, vol. 24, no. 8, pp. 1977-1991, Aug. 2009.
- [243] C. Vartak, A. Abramovitz and K. Ma Smedley, "Analysis and Design of Energy Regenerative Snubber for Transformer Isolated Converters," *IEEE Transactions on Power Electronics*, vol. 29, no. 11, pp. 6030-6040, Nov. 2014.
- [244] En-Sung Park, Sung Jin Choi, J. M. Lee and B. H. Cho, "A soft-switching active-clamp scheme for isolated full-bridge boost converter," *Nineteenth Annual IEEE Applied Power Electronics Conference and Exposition, 2004. APEC '04.*, Anaheim, CA, USA, 2004, pp. 1067-1070 vol.2.

- [245] A. K. Rathore, A. K. S. Bhat and R. Oruganti, "Analysis, Design and Experimental Results of Wide Range ZVS Active-Clamped L-L Type Current-Fed DC/DC Converter for Fuel Cells to Utility Interface," *IEEE Transactions on Industrial Electronics*, vol. 59, no. 1, pp. 473-485, Jan. 2012.
- [246] Q. Wu, M. Wang, W. Zhou, C. Huang, G. Liu and X. Wang, "High Frequency Active-Clamped Zero-Current Switching Current-Fed Push-Pull Converter for Micro-Converter Applications," *2020 IEEE Energy Conversion Congress and Exposition (ECCE)*, Detroit, MI, USA, 2020, pp. 1273-1278.
- [247] V. K. Goyal and A. Shukla, "Isolated DC–DC Boost Converter for Wide Input Voltage Range and Wide Load Range Applications," *IEEE Transactions on Industrial Electronics*, vol. 68, no. 10, pp. 9527-9539, Oct. 2021.
- [248] V. K. Goyal and A. Shukla, "Two-Stage Hybrid Isolated DC–DC Boost Converter for High Power and Wide Input Voltage Range Applications," *IEEE Transactions on Industrial Electronics*, vol. 69, no. 7, pp. 6751-6763, July 2022.
- [249] K. -B. Park, G. -W. Moon and M. -J. Youn, "Two-Transformer Current-Fed Converter With a Simple Auxiliary Circuit for a Wide Duty Range," *IEEE Transactions on Power Electronics*, vol. 26, no. 7, pp. 1901-1912, July 2011.
- [250] J. -M. Kwon and B. -H. Kwon, "High Step-Up Active-Clamp Converter With Input-Current Doubler and Output-Voltage Doubler for Fuel Cell Power Systems," *IEEE Transactions on Power Electronics*, vol. 24, no. 1, pp. 108-115, Jan. 2009.
- [251] M. -K. Nguyen, T. -D. Duong, Y. -C. Lim and Y. -J. Kim, "Isolated Boost DC–DC Converter With Three Switches," *IEEE Transactions on Power Electronics*, vol. 33, no. 2, pp. 1389-1398, Feb. 2018.
- [252] B. Zhu, H. Wang, Y. Zhang and S. Chen, "Buck-Based Active-Clamp Circuit for Current-Fed Isolated DC–DC Converters," *IEEE Transactions on Power Electronics*, vol. 37, no. 4, pp. 4337-4345, April 2022.
- [253] Y. -H. Kim, S. -C. Shin, J. -H. Lee, Y. -C. Jung and C. -Y. Won, "Soft-Switching Current-Fed Push–Pull Converter for 250-W AC Module Applications," *IEEE Transactions on Power Electronics*, vol. 29, no. 2, pp. 863-872, Feb. 2014.
- [254] W. C. P. De Aragao Filho and I. Barbi, "A comparison between two current-fed push-pull DC-DC converters-analysis, design and experimentation," *Proceedings of Intelec'96 - International Telecommunications Energy Conference*, Boston, MA, USA, 1996, pp. 313-320.
- [255] J. -W. Lim, J. Hassan and M. Kim, "Bidirectional Soft Switching Push–Pull Resonant Converter Over Wide Range of Battery Voltages," *IEEE Transactions on Power Electronics*, vol. 36, no. 11, pp. 12251-12267, Nov. 2021.
- [256] D. A. Ruiz-Caballero and I. Barbi, "A new flyback-current-fed push-pull DC-DC converter," *IEEE Transactions on Power Electronics*, vol. 14, no. 6, pp. 1056-1064, Nov. 1999.
- [257] Q. Wu, Q. Wang, J. Xu and L. Xiao, "Implementation of an Active-Clamped Current-Fed Push–Pull Converter Employing Parallel-Inductor to Extend ZVS

- Range for Fuel Cell Application," *IEEE Transactions on Industrial Electronics*, vol. 64, no. 10, pp. 7919-7929, Oct. 2017.
- [258] J. -W. Lim, C. Bai, T. A. Wagaye, J. -H. Choi and M. Kim, "Highly Reliable Push–Pull Resonant DC/DC Converter for Medium-Power Applications," *IEEE Transactions on Industrial Electronics*, vol. 70, no. 2, pp. 1342-1355, Feb. 2023.
- [259] E. M. Miranda-Terán, F. L. Tofoli, G. V. Torrico Bascopé, and R. P. Torrico Bascopé, "Modified Active-Clamped Current-Fed DC–DC Push–Pull Converter," *Energies*, vol. 16, pp.6300, Aug. 2023.
- [260] T. -T. Le, S. Kim and S. Choi, "A Four-Phase Current-Fed Push–Pull DAB Converter for Wide-Voltage-Range Applications," *IEEE Transactions on Power Electronics*, vol. 36, no. 10, pp. 11383-11396, Oct. 2021.
- [261] R. L. Andersen and I. Barbi, "A ZVS-PWM Three-Phase Current-Fed Push–Pull DC–DC Converter," *IEEE Transactions on Industrial Electronics*, vol. 60, no. 3, pp. 838-847, March 2013.
- [262] S. Lee, J. Park and S. Choi, "A Three-Phase Current-Fed Push–Pull DC–DC Converter With Active Clamp for Fuel Cell Applications," *IEEE Transactions on Power Electronics*, vol. 26, no. 8, pp. 2266-2277, Aug. 2011.
- [263] A. Mousavi, P. Das and G. Moschopoulos, "A Comparative Study of a New ZCS DC–DC Full-Bridge Boost Converter With a ZVS Active-Clamp Converter," *IEEE Transactions on Power Electronics*, vol. 27, no. 3, pp. 1347-1358, March 2012.
- [264] D. Wu, Y. Wu, J. Kan, Y. Tang, J. Chen and L. Jiang, "Full-Bridge Current-Fed PV Microinverter With DLFCR Reduction Ability," *IEEE Transactions on Power Electronics*, vol. 35, no. 9, pp. 9541-9552, Sept. 2020.
- [265] M. Escudero, D. Meneses, N. Rodriguez and D. P. Morales, "Modulation Scheme for the Bidirectional Operation of the Phase-Shift Full-Bridge Power Converter," *IEEE Transactions on Power Electronics*, vol. 35, no. 2, pp. 1377-1391, Feb. 2020.
- [266] N. Yang, J. Zeng, R. Hu and J. Liu, "Analysis and Design of an Isolated High Step-Up Converter Without Voltage-Drop," *IEEE Transactions on Power Electronics*, vol. 37, no. 6, pp. 6939-6950, June 2022.
- [267] T. -T. Le, M. -K. Nguyen, T. -D. Duong, C. Wang and S. Choi, "Open-Circuit Fault-Tolerant Control for a Three-Phase Current-Fed Dual Active Bridge DC–DC Converter," *IEEE Transactions on Industrial Electronics*, vol. 70, no. 2, pp. 1586-1596, Feb. 2023.
- [268] D. Chen, D. Sha and T. Sun, "Three Phase Current-Fed Semi Dual Active Bridge DC–DC Converter With Hybrid Operating Mode Control," *IEEE Transactions on Power Electronics*, vol. 35, no. 2, pp. 1649-1658, Feb. 2020.
- [269] U. R. Prasanna and A. K. Rathore, "Small-Signal Modeling of Active-Clamped ZVS Current-Fed Full-Bridge Isolated DC/DC Converter and Control System Implementation Using PSoC," *IEEE Transactions on Industrial Electronics*, vol. 61, no. 3, pp. 1253-1261, March 2014.

- [270] S. Bal, D. B. Yelaverthi, A. K. Rathore and D. Srinivasan, "Improved Modulation Strategy Using Dual Phase Shift Modulation for Active Commutated Current-Fed Dual Active Bridge," *IEEE Transactions on Power Electronics*, vol. 33, no. 9, pp. 7359-7375, Sept. 2018.
- [271] L. Chen, L. Tarisciotti, A. Costabeber, F. Gao, P. Wheeler and P. Zanchetta, "Advanced Modulations for a Current-Fed Isolated DC–DC Converter With Wide-Voltage-Operating Ranges," *IEEE Journal of Emerging and Selected Topics in Power Electronics*, vol. 7, no. 4, pp. 2540-2552, Dec. 2019.
- [272] C. F. Moraes, E. G. Carati, J. P. da Costa, R. Cardoso and C. M. d. Oliveira Stein, "Active-Clamped Zero-Current Switching Current-Fed Half-Bridge Converter," *IEEE Transactions on Power Electronics*, vol. 35, no. 7, pp. 7100-7109, July 2020.
- [273] S. Salehi Dobakhshari, J. Milimonfared, M. Taheri and H. Moradisizkoohi, "A Quasi-Resonant Current-Fed Converter With Minimum Switching Losses," *IEEE Transactions on Power Electronics*, vol. 32, no. 1, pp. 353-362, Jan. 2017.
- [274] T. -T. Nguyen, H. Cha and H. -G. Kim, "Current-Fed Quasi-Z-Source Full-Bridge Isolated DC–DC Converter," *IEEE Transactions on Industrial Electronics*, vol. 68, no. 12, pp. 12046-12057, Dec. 2021.
- [275] T. -F. Wu, Y. -C. Chen, J. -G. Yang and C. -L. Kuo, "Isolated Bidirectional Full-Bridge DC–DC Converter With a Flyback Snubber," *IEEE Transactions on Power Electronics*, vol. 25, no. 7, pp. 1915-1922, July 2010.
- [276] J. B. Banu and M. B. Moses, "A current fed full bridge DC-DC converter with an active flyback and passive auxiliary circuits," *2016 International Conference on Energy Efficient Technologies for Sustainability (ICEETS)*, Nagercoil, India, 2016, pp. 382-387.
- [277] P. Xuwei and A. K. Rathore, "Naturally Clamped Zero-Current Commutated Soft-Switching Current-Fed Push–Pull DC/DC Converter: Analysis, Design, and Experimental Results," *IEEE Transactions on Power Electronics*, vol. 30, no. 3, pp. 1318-1327, March 2015.
- [278] P. Xuwei, A. K. Rathore, "Novel Bidirectional snubberless naturally commutated soft-switching current-fed full bridge isolated DC/DC Converter for fuel cell vehicles", *IEEE Transactions on Industrial Electronics*, vol. 61, no. 5, pp. 2307-2315, May 2014.
- [279] K. Khatun, V. R. Vakacharla, A. R. Kizhakkan and A. K. Rathore, "Small-Signal Analysis and Control of Snubberless Naturally Clamped Soft-Switching Current-Fed Push–Pull DC/DC Converter," *IEEE Transactions on Industry Applications*, vol. 56, no. 4, pp. 4299-4308, July-Aug. 2020.
- [280] S. Bal, A. K. Rathore and D. Srinivasan, "Naturally Clamped Snubberless Soft-Switching Bidirectional Current-Fed Three-Phase Push–Pull DC/DC Converter for DC Microgrid Application," *IEEE Transactions on Industry Applications*, vol. 52, no. 2, pp. 1577-1587, March-April 2016.

- [281] H. Kim, C. Yoon and S. Choi, "An Improved Current-Fed ZVS Isolated Boost Converter for Fuel Cell Applications," *IEEE Transactions on Power Electronics*, vol. 25, no. 9, pp. 2357-2364, Sept. 2010.
- [282] K. R. Sree and A. K. Rathore, "Impulse Commutated Zero-Current Switching Current-Fed Push–Pull Converter: Analysis, Design, and Experimental Results," *IEEE Transactions on Industrial Electronics*, vol. 62, no. 1, pp. 363-370, Jan. 2015.
- [283] S. Tandon and A. K. Rathore, "Analysis and Design of Series LC Resonance-Pulse Based Zero-Current-Switching Current-Fed Half-Bridge DC–DC Converter," *IEEE Transactions on Industrial Electronics*, vol. 68, no. 8, pp. 6784-6793, Aug. 2021.
- [284] S. Tandon and A. K. Rathore, "Novel Series LC Resonance-Pulse-Based ZCS Current-Fed Full-Bridge DC–DC Converter: Analysis, Design, and Experimental Results," *IEEE Transactions on Power Electronics*, vol. 36, no. 2, pp. 1844-1855, Feb. 2021.
- [285] F. Kardan, R. Alizadeh and M. R. Banaei, "A New Three Input DC/DC Converter for Hybrid PV/FC/Battery Applications," *IEEE Journal of Emerging and Selected Topics in Power Electronics*, vol. 5, no. 4, pp. 1771-1778.
- [286] B. A. Aghdam, P. H. Nia and D. Nazarpour, "A New Multi-port DC/DC Converter for PV/battery/DC grid Energy Systems," *2022 9th Iranian Conference on Renewable Energy & Distributed Generation (ICREDG)*, Mashhad, Iran, Islamic Republic of, 2022, pp. 1-8.
- [287] Gaurav, N. Jayaram, S. Halder, K. P. Panda and S. V. K. Pulavarthi, "A Novel Design With Condensed Component of Multi-Input High Gain Nonisolated DC–DC Converter for Performance Enhancement in Carbon Neutral Energy Application," *IEEE Journal of Emerging and Selected Topics in Industrial Electronics*, vol. 4, no. 1, pp. 37-49, Jan. 2023.
- [288] Z. Zhang, O. C. Thomsen and M. A. E. Andersen, "Soft-Switched Dual-Input DC–DC Converter Combining a Boost-Half-Bridge Cell and a Voltage-Fed Full-Bridge Cell," *IEEE Transactions on Power Electronics*, vol. 28, no. 11, pp. 4897-4902, Nov. 2013.
- [289] B. Zhu, Q. Zeng, Y. Chen, Y. Zhao and S. Liu, "A Dual-Input High Step-Up DC/DC Converter With ZVT Auxiliary Circuit," *IEEE Transactions on Energy Conversion*, vol. 34, no. 1, pp. 161-169, March 2019.
- [290] F. Davalos Hernandez, R. Samanbakhsh, P. Mohammadi and F. M. Ibanez, "A Dual-Input High-Gain Bidirectional DC/DC Converter for Hybrid Energy Storage Systems in DC Grid Applications," *IEEE Access*, vol. 9, pp. 164006-164016, 2021.
- [291] C. Shi, B. Miller, K. Mayaram and T. Fiez, "A Multiple-Input Boost Converter for Low-Power Energy Harvesting," *IEEE Transactions on Circuits and Systems II: Express Briefs*, vol. 58, no. 12, pp. 827-831, Dec. 2011.
- [292] M. Azizi, M. Mohamadian and R. Beiranvand, "A New Family of Multi-Input Converters Based on Three Switches Leg," *IEEE Transactions on Industrial Electronics*, vol. 63, no. 11, pp. 6812-6822, Nov. 2016.

- [293] L. Yu and H. Wang, "A Novel Dual-Input ZVS DC/DC Converter for Low-Power Energy Harvesting Applications," *IEEE Journal of Emerging and Selected Topics in Power Electronics*, vol. 7, no. 2, pp. 1197-1206, June 2019.
- [294] S. M. Hashemzadeh, V. Marzang, S. Pourjafar and S. Hossein Hosseini, "An Ultra High Step-Up Dual-Input Single-Output DC–DC Converter Based on Coupled Inductor," *IEEE Transactions on Industrial Electronics*, vol. 69, no. 11, pp. 11023-11034, Nov. 2022.
- [295] G. G. Kumar and K. Sundaramoorthy, "Dual-Input Nonisolated DC–DC Converter With Vehicle-to-Grid Feature," *IEEE Journal of Emerging and Selected Topics in Power Electronics*, vol. 10, no. 3, pp. 3324-3336, June 2022.
- [296] Z. Saadatizadeh, P. C. Heris, X. Liang and E. Babaei, "Expandable Non-Isolated Multi-Input Single-Output DC-DC Converter With High Voltage Gain and Zero-Ripple Input Currents," *IEEE Access*, vol. 9, pp. 169193-169219, 2021.
- [297] R. -J. Wai and B. -H. Chen, "High-Efficiency Dual-Input Interleaved DC–DC Converter for Reversible Power Sources," *IEEE Transactions on Power Electronics*, vol. 29, no. 6, pp. 2903-2921, June 2014.
- [298] G. -J. Su and L. Tang, "A Reduced-Part, Triple-Voltage DC–DC Converter for EV/HEV Power Management," *IEEE Transactions on Power Electronics*, vol. 24, no. 10, pp. 2406-2410, Oct. 2009.
- [299] H. Al-Atrash, M. Pepper and I. Batarseh, "A Zero-Voltage Switching Three-Port Isolated Full-Bridge Converter," *INTELEC 06 - Twenty-Eighth International Telecommunications Energy Conference*, Providence, RI, USA, 2006, pp. 1-8.
- [300] V. Karthikeyan and R. Gupta, "Multiple-Input Configuration of Isolated Bidirectional DC–DC Converter for Power Flow Control in Combinational Battery Storage," *IEEE Transactions on Industrial Informatics*, vol. 14, no. 1, pp. 2-11, Jan. 2018.
- [301] K. R and R. Kalpana, "An Isolated Dual-Input Half-Bridge DC–DC Boost Converter With Reduced Circulating Power Between Input Ports," *IEEE Canadian Journal of Electrical and Computer Engineering*, vol. 45, no. 1, pp. 68-76, winter 2022.
- [302] K. R and R. Kalpana, "Design and Development of Modular Dual-Input DC–DC Step-Up Converter for Telecom Power Supply," *IEEE Transactions on Industry Applications*, vol. 57, no. 3, pp. 2591-2601, May-June 2021.
- [303] C. -L. Shen and L. -Z. Chen, "Dual-Input Isolated Converter With Dual-Charge-Pump Cell for High Step-Up Voltage Ratio Achievement," *IEEE Transactions on Industrial Electronics*, vol. 67, no. 11, pp. 9383-9392, Nov. 2020.
- [304] S. M. Tayebi, H. Hu, S. Abdel-Rahman and I. Batarseh, "Dual-Input Single-Resonant Tank LLC Converter with Phase Shift Control for PV Applications," *IEEE Transactions on Industry Applications*, vol. 55, no. 2, pp. 1729-1739, March-April 2019.
- [305] Z. Zhang, O. C. Thomsen, M. A. E. Andersen and H. R. Nielsen, "A novel dual-input isolated current-fed DC-DC converter for renewable energy system," *2011*

Twenty-Sixth Annual IEEE Applied Power Electronics Conference and Exposition (APEC), Fort Worth, TX, USA, 2011, pp. 1494-1501.

- [306] A. H. Chander, L. K. Sahu and P. T. Bankupalli, "Review on General Architecture and Selection of Multiple Input Converters," *2020 First International Conference on Power, Control and Computing Technologies (ICPC2T)*, Raipur, India, 2020, pp. 240-245.
- [307] O. Balapanuru, M. M. Lokhande and M. V. Aware, "Dual-Input High Gain DC-DC Converter with Two Energy Storage Systems for Light EV Applications," *2023 International Conference on Future Energy Solutions (FES)*, Vaasa, Finland, 2023, pp. 1-6.
- [308] P. Gunawardena, N. Hou, D. Nayanassiri and Y. Li, "A Dual-Input Single-Output DC-DC Converter Topology for Renewable Energy Applications," *IEEE Transactions on Industry Applications*, vol. 59, no. 2, pp. 1995-2006, March-April 2023.
- [309] P. Gunawardena, D. Nayanassiri, N. Hou and Y. Li, "A Soft-Switched Current-Fed Dual-Input Isolated DC-DC Converter Topology," *IEEE Transactions on Industrial Electronics*, vol. 70, no. 5, pp. 4842-4853, May 2023.
- [310] N. K. Reddi, M. R. Ramteke, H. M. Suryawanshi, K. Kothapalli and S. P. Gawande, "An Isolated Multi-Input ZCS DC-DC Front-End-Converter Based Multilevel Inverter for the Integration of Renewable Energy Sources," *IEEE Transactions on Industry Applications*, vol. 54, no. 1, pp. 494-504, Jan.-Feb. 2018.
- [311] E. Karimi, B. M. Tehrani and E. Adib, "A Soft-Switching Double-Input Micro-Inverter," *IEEE Transactions on Industrial Electronics*, vol. 68, no. 8, pp. 6721-6728, Aug. 2021.
- [312] S. -Y. Yu and A. Kwasinski, "Analysis of Soft-Switching Isolated Time-Sharing Multiple-Input Converters for DC Distribution Systems," *IEEE Transactions on Power Electronics*, vol. 28, no. 4, pp. 1783-1794, April 2013.
- [313] M. Mohammadi, N. Safari, J. Milimonfared and J. S. Moghani, "Application of a new high step-up double-input converter in a novel module- integrated-inverter photovoltaic system," *The 6th Power Electronics, Drive Systems & Technologies Conference (PEDSTC2015)*, Tehran, Iran, 2015, pp. 53-58.
- [314] J. O. N. Wilson and T. T. Lie, "Off-grid EV charging stations to reduce the impact of charging demand on the electricity grid," *2022 7th IEEE Workshop on the Electronic Grid (eGRID)*, Auckland, New Zealand, 2022, pp. 1-5.
- [315] G. Rituraj, G. R. C. Mouli and P. Bauer, "A Comprehensive Review on Off-Grid and Hybrid Charging Systems for Electric Vehicles," *IEEE Open Journal of the Industrial Electronics Society*, vol. 3, pp. 203-222, 2022.
- [316] A. A. Wahedi and Y. Biçer, "Development of an off-grid electrical vehicle charging station hybridized with renewables including battery cooling system and multiple energy storage units," *Energy Reports*, vol. 6, pp. 2006-2021, Nov. 2020.

- [317] M. López, F. Soto, and Z. A. Hernández, “Assessment of the potential of floating solar photovoltaic panels in bodies of water in mainland Spain,” *Journal of Cleaner Production*, vol. 340, p. 130752, Mar. 2022.
- [318] M. R. A. Refaai, L. Dhanesh, B. P. Ganthia, M. Mohanty, R. Sasisekharan, and E. M. Anbese, “Design and implementation of a floating PV model to analyse the power generation,” *International Journal of Photoenergy*, vol. 2022, pp. 1–13, May 2022.
- [319] R. Claus and M. López, “Key issues in the design of floating photovoltaic structures for the marine environment,” *Renewable & Sustainable Energy Reviews*, vol. 164, p. 112502, Aug. 2022.
- [320] V. K. Viswambharan, V. Kumar, K. Amjad and A. Ghani, "A case study — Solar powered metro in UAE," *2018 5th International Conference on Renewable Energy: Generation and Applications (ICREGA)*, Al Ain, 2018, pp. 46-51.
- [321] <http://www.financialexpress.com/economy/indiasfirst-solar-powered-train-all-you-want-to-know-about-indian-railwaysgreen-initiative/264505/>.
- [322] M. J. Lencwe, S. P. Chowdhury and H. M. ElGohary, "Solar photovoltaic integration on locomotive roof top for South African railway industry," *2016 51st International Universities Power Engineering Conference (UPEC)*, Coimbra, 2016, pp. 1-5.

LIST OF PUBLICATIONS

JOURNALS

1. S. Raizada and V. Verma, "PV fed front-end isolated voltage multiplier converter for off grid EV charging infrastructure," in Journal of Power Electronics, vol. 22, pp. 1484–1495, 2022. <https://doi.org/10.1007/s43236-022-00464-4>
2. S. Raizada and V. Verma, "Front-End Current-Fed High Gain Isolated Converter with Flexible Power Point Tracking for Floating PV System," in Journal of Electrical Engineering and Technology, 2024. <https://doi.org/10.1007/s42835-023-01563-3>.

CONFERENCES

1. S. Raizada and V. Verma, "Isolated voltage multiplier converter for sustainable off-grid EV charging application," 2017 IEEE Transportation Electrification Conference (ITEC-India), Pune, India, pp. 1-5, 2017. <https://doi.org/10.1109/ITEC-India.2017.8356955>
2. S. Raizada and V. Verma, "Step Up Gain Converter with fast MPPT control under moving partial shading for train rooftop PV-DC- μ G," 2018 IEEE International Conference on Electrical Systems for Aircraft, Railway, Ship Propulsion and Road Vehicles & International Transportation Electrification Conference (ESARS-ITEC), Nottingham, UK, pp. 1-6, 2018. <https://doi.org/10.1109/ESARS-ITEC.2018.8607357>
3. S. Raizada and V. Verma, "Isolated High Gain Multi-Input Converter fed Floating PV System for DC Microgrid," 2018 13th IEEE International Conference on Industry Applications (INDUSCON), Sao Paulo, Brazil, pp. 312-318, 2018. <https://doi.org/10.1109/INDUSCON.2018.8627240>
4. S. Raizada and V. Verma, "Coupled Inductor based Isolated Voltage Multiplier Converter," 2018 IEEE 4th Southern Power Electronics Conference (SPEC), Singapore, pp. 1-7, 2018. <https://doi.org/10.1109/SPEC.2018.8635881>

5. S. Raizada and V. Verma, "Modular Multi-Input-Isolated Voltage Multiplier Converter for PV fed DC Microgrid," 2018 IEEE International Conference on Power Electronics, Drives and Energy Systems (PEDES), Chennai, India, pp. 1-6, 2018. <https://doi.org/10.1109/PEDES.2018.8707539>.
6. P. Bhatia, S. Mittal, S. Raizada and V. Verma, "Hybrid ANN based Incremental Conductance MPPT-Current Control Algorithm for Constant Power Generation of PV fed DC Microgrid," 2020 IEEE First International Conference on Smart Technologies for Power, Energy and Control (STPEC), Nagpur, India, pp. 1-7, 2020. <https://doi.org/10.1109/STPEC49749.2020.9297751>.

BIODATA

Name	Shirish Raizada
Date of Birth	24/11/1992
Place of Birth	Aligarh, UP, India
Nationality	Indian
Father's Name	Dr. Sumesh Raizada
Mother's Name	Mrs. Roli Raizada

Educational Qualifications

B.Tech.	Delhi Technological University
---------	--------------------------------

Area of Interest

DC/DC Converters, Photovoltaic Systems, Design and Modeling of converters, Control of DC/DC Converter, DC Microgrid